Graphene-reinforced MOFs-derived nanocomposites for electrochemical applications

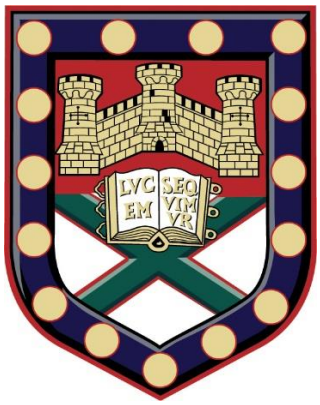

Submitted by Laicong Deng
to the University of Exeter as a thesis for the degree of
Doctor of Philosophy in Engineering
In November 2019

I certify that all material in this thesis which is not my own work has been identified and that no material has previously been submitted and approved for the award of a degree by this or any other University.

Signature: ……..

Abstract

Zeolitic imidazolate frameworks (ZIFs) are sub-family of metal organic frameworks with structures similar to traditional aluminosilicate zeolities. Consequently, ZIFs exhibit zeolite-type topologies with crystal structures, ultrahigh surface area, and excellent chemical and thermal stability, which makes ZIFs being an attractive candidate in various potential applications. Moreover, ZIF materials can act as outstanding templates or precursors to produce metal components on porous carbon nanocomposites, leading to a wide range of applications in energy storage and electrochemical utilisations. On the other hand, porous graphene could effectively avoid the stacking of graphene sheets, generating materials with high surface areas. Porous graphene can not only offer large aspect ratios which enhances the stability of porous frameworks to prevent collapse, but also provide the possibilities of multiple interactions with various species, both at the surface and through their porous frameworks, benefiting a rapid transportation of ions/molecules or charge carriers through the porous channels.

In this thesis, the synthesis of ZIFs and graphene oxide (GO) derived nanocomposites were demonstrated and fully characterised. Moreover, the renewable-energy-related applications of these functional nanostructured derivatives were also evaluated and analysed. In brief, the main findings are as follows:

1. Developed a facile approach to produce highly efficient graphene-based cobalt sulfide and porous carbon composites, converted from one-step *in-situ* synthesised GO/ZIF-67 composites *via* sulfurisation and carbonisation at high temperatures. Different characterisation techniques have confirmed the CoS nanoparticles were homogeneously dispersed in carbon matrix. Moreover, the obtained nanocomposites exhibit much improved electrochemistry performance comparing with the reference material without graphene, and the electrocatalytic activities of the composites can be tuned by adjusting graphene content in the composites.
2. Apart from single metal sulfide, explorative research work were also performed to understand the potential of bi-metallic ZIF-67 derived nanocomposites. Homogenously dispersed nickel promoted cobalt

sulfide/N, S co-doped carbon/graphene and iron promoted cobalt sulfide/N, S co-doped carbon/graphene have been successfully prepared *via* sulfurisation and carbonisation from Ni-substituted GO/ZIF-67 and Fe-substituted GO/ZIF-67, respectively. Due to the joint effect of graphene, N, S co-doped porous carbon and abundant metal-N moieties, the obtained nanocomposites exhibit not only remarkable OER catalytic activities with lowest onset/over potential, but also excellent HER activities with high current density and low onset potential, making them potential bifunctional electrocatalyst in water splitting.

3. Moreover, the derivatives of bi-metallic Fe-substituted GO/ZIF-67 have been further investigated. Iron promoted cobalt based nanoparticles homogeneously embedded in N-doped porous carbon and graphene *via* a facile one-step carbonisation of the *in-situ* as-synthesised composite. The obtained nanocomposites exhibit excellent electrochemical activities, which makes them promising electrode materials for catalysis and energy applications, owing to the increased surface area, hierarchical porous graphene and carbon structure, and bi-metal anchoring effect. Moreover, iron promoted cobalt oxide nanoparticles embedded in N-doped graphene and porous carbon by an efficient two-step carbonisation and oxidation of Fe-substituted GO/ZIF-67 has also been successfully developed. Due to the triple synergistic effect between iron oxide, cobalt oxides and N-doped porous graphene and carbon, the as-synthesised nanocomposites exhibit remarkable bifunctional activities towards both OER and HER in water splitting.
4. In addition, in all the studied mono- or bi-metallic component system, the effect of graphene oxide content as well as the sulfurisation/ carbonisation temperature have been well explored and optimised. It was found that the resultant nanocomposite sulfurised and carbonised at 800 °C, exhibited promising high-efficient catalytic activities. Meanwhile, owing to the introduction of a certain amount of graphene providing an increased electrical conductivity and more catalytic active sites, the optimum 5 wt% graphene contained nanocomposite shows the most remarkable electrochemical performance within the studied range of graphene content (up to 10 wt%).

Publications and Presentations

- Laicong Deng, Zhuxian Yang, Binling Chen, Xinglong Gou, Yanqiu Zhu, Yongde Xia. (2019) Graphene reinforced cobalt sulfide/N, S co-doped porous carbon nanocomposite as multifunctional electrocatalysts. Submitted
- Laicong Deng, Zhuxian Yang, Yanqiu Zhu, Yongde Xia. (2019) Metal-organic-framework-derived bi-metallic cobalt-iron sulfide on N, S co-doped porous carbon and graphene nanocomposites as superior electrocatalysts for overall water splitting. In preparation
- Cobalt sulfide-embedded in porous carbon and graphene derived from metal-organic-frameworks as electrocatalysts for oxygen reduction reaction, oxygen evolution reaction and hydrogen evolution reaction. The 12th International Conference on Materials Chemistry, York, UK, 2015
- A simple method to the synthesis of bi-metallic nickel promoted GO/ZIF-67 nanocomposites and electrocatalytic applications of their derivatives. The 23rd Joint Annual Conference of CSCST-SCI (Chinese Society of Chemical Science and Technology-Society of Chemical Industry) Conference. Nottingham, UK. 2016

Contents

List of Figures and Tables

Acknowledgement

I would like to express my very sincere appreciation to all the people who provided constant supports and helped me during the period of my Ph.D journey.

Frist and foremost, I would like to express my deepest gratitude to my best supervisor, Dr. Yongde Xia. His guidance, daily support and earnest supervision style has given me immense help over the five years of my PhD study, and his expert opinion is always the first thing I would look for whenever any problems encountered, no matter it is theoretical, experimental or just technical. During my preparation of the thesis, he has spent much time reading through each draft and provided me with inspiring advice. Without his patient instruction, insightful criticism and expert guidance, the completion of this thesis would not have been possible. I would also like to give big thanks to Prof. Yanqiu Zhu, my second supervisor, who provided me with beneficial help and offered me precious comments during the whole process of my PhD study. I wish to thank my mentor Prof. J Roy Sambles. He has always encouraged me to engage in different academic events and training sessions to enhance my research skills and he always believed in me and guided me throughout my studies.

I appreciate the constant help and friendship from my laboratory colleagues and friends: Dr. Zhuxian Yang, Dr. Binling Chen, Dr. Bahareh Yazdani, Dr. Nannan Wang, Dr. Ke Bao, Dr. Cheng Liu, Ms Zheng Huang, Mr Mian Zahid Hussain, Mr Yu Chen, Mr Cheng Shi, Mr Peng Tian, Mr Xiao Chen and many others.

I am also thankful to Dr. Hong Chang for XRD, SEM, TEM and other technical support from Harrison imaging suite; Dr. Ellen Green for Raman spectroscopy characterisation from Physics; Dr. David Morgan for XPS characterisation support from Cardiff Catalysis Institute, Cardiff University.

I would like to acknowledge the EPSRC Centre for Doctoral Training (CDT) in metamaterials, University of Exeter, for the provision of scholarship.

Last but not least, I will express my deepest gratitude to my parents and my girlfriend for their love, caring, understanding and moral support. They are the most important people in my world and I dedicate this thesis to them. Many thanks again!

List of symbols and abbreviations

2D	Two-dimensional
3D	Three-dimensional
BET	Brunauer-Emmett-Teller
CNTs	Carbon nanotubes
EDX	Energy-dispersive X-ray spectroscopy
FTIR	Fourier-transform infrared spectroscopy
G	Graphene
HER	Hydrogen evolution reaction
MOF	Metal organic framworks
MS	Mass spectrometry
OER	Oxygen evolution reaction
ORR	Oxygen reduction reaction
PVD	Physical vapour deposition
SAED	Selected area electron diffraction
SEM	Scanning electron microscope
STEM	Scanning transmission electron spectroscopy
TEM	Transmission electron microscopy
TGA	Thermogravimetric analysis
UV-Vis	Ultraviolet–visible spectroscopy
XPS	X-ray photoelectron spectroscopy
XRD	X-ray diffraction

Chapter 1: Introduction

Metal organic frameworks (MOFs), as a class of typical porous materials that are made up of metal ions and organic ligands [1-3], have shown tuneable structures, versatile functionalities and other fascinating properties. Specifically, zeolitic imidazolate frameworks (ZIFs) are sub-family of MOFs and have attracted increased interests in past years. Generally, ZIFs consist of M-Im-M bonds where M is Co or Zn and Im is imidazolate or derives, with the bridging angle of 145°, which is coincident with Si-O-Si angle in zeolites. Therefore ZIFs are similar to traditional aluminosilicate zeolities, in a way where M and Im play the role of Si and O respectively [3]. Consequently, ZIFs exhibit zeolite-type topologies like crystal structures, ultrahigh surface area, and excellent chemical and thermal stability, making ZIFs attractive precursors or excellent sacrificial templates for the preparation of porous carbon based nanocomposites [1, 3].

Recently, as one of the most important electrocatalytic material systems, porous carbon-based materials have attracted a lot of attention. The materials feature advantages like variable structures, large surface area, tunable porosity while remaining affordable. Various electrocatalysis processes including oxygen reduction reaction (ORR), oxygen evolution reaction (OER), hydrogen evolution reaction (HER) and water splitting [4-6] have been developed to utilise these materials. Particularly, many MOF-derived porous carbon based materials have been developed as active electrocatalysts. Therefore, ZIFs could generate multiple extended 3D open frameworks whose topologies are similar to those already identified in aluminosilicate zeolites [7]. In addition, ZIFs share many advantages with zeolites including their exceptional ultrahigh chemical stability (a result of their metal–nitrogen bonds), and tuneable pore size and surface area (realised by simply modifying Im), which distinguish them from most other MOFs. Moreover, metal sulfides/oxides could also be formed from ZIF precursors under certain treatment conditions. Consequently, ZIFs and their derivatives have emerged as the best candidates for electrochemical applications.

On the other hand, since the discovery of graphene in 2004, significant efforts have been made to exploit its application in almost every field of science, including physics, chemistry, materials sciences and life science [8-10]. Graphene

oxide (GO) has been widely considered an excellent precursor for graphene. Graphene is a two-dimensional single layered material with free-standing graphene sheets showing low chemical activity [11-12]. Graphene and GO have been the subject of extensive research of electrochemistry related technologies with great expectation for future electrochemical applications, due to their high electric conductivity, large surface area and high electron transfer rate. Furthermore, porous graphene have attracted much attention owing to its 3D unique porous structure in addition to the intrinsic properties of graphene. Compared to the original free-standing graphene sheet, porous graphene offers inherent properties of graphene and also exhibits outstanding properties including large surface to volume ratio, high electrical conductivity and low cytotoxicity and tremendous flexibility [13-14].

Traditionally, ZIFs can be synthesised from organic solvents [15-21], which are sources of some environmental concerns as most of organic solvents are toxic and flammable. On the other hand, homogeneous dispersion of nanoparticles in carbon matrix is always a challenge, because nanoparticles constantly tend to agglomerate. Thus, synthesis of ZIFs *via* green, low-cost and efficient methods is highly desirable.

Moreover, after the carbonisation process of ZIFs, the derivatives from ZIFs normally show low electrical conductivity and slow electron transfer due to the low graphitised carbon. In order to improve the electrical conductivity, GO can be introduced into the precursor ZIFs as GO are expected to be converted to porous graphene during the carbonisation process. As result, novel synthesis method for the preparation of GO containing ZIFs is highly desirable.

Most importantly, water splitting into oxygen and hydrogen has been considered as a potential solution of the global energy crisis for some time [22-25]. However, the slow rate of water splitting is inefficient and energy-consuming, thus, highly efficient electrochemical catalysts are extensively sought to accelerate the reactions rates (for both half-reactions). Pt-group and Ir-/Ru-based noble metal materials are good candidates as they are highly effective catalysts for HER and OER respectively. However, their high price, poor durability and scarce reserve prevent their large-scale applications. Consequently, it is highly desirable to explore the possibility of utilising transition metals or bi-transition

metals based new cost-effective electrocatalysts for those important energy storage and conversion electrochemical reactions.

Therefore, the main objectives of this thesis are:

1. To explore the generation of homogeneously dispersed transition metal compounds in functional porous carbon and graphene from a single precursor and to insight into the relationship between their structures and properties;
2. To design facile approaches to produce bi-metallic (nickel or iron promoted) GO/ZIF-67 nanocomposites and study the fundamental synthesising parameters on each system;
3. To investigate the electrocatalytic applications of ZIF-67 derivatives in relevant electrochemical reactions field.

This thesis has been presented as seven main Chapters. Chapter 1 introduces the inspiration, the motivation and the organisation of this thesis. Chapter 2 provides the background and literature review for (a) the basic microstructure of ZIFs and different synthesis methods for ZIFs and ZIF derivatives, properties and potential applications of ZIFs and ZIF derivatives in gas separation, catalysis, electrocatalytic activities and supercapacitors; (b) the synthesis strategies and properties of porous graphene. Its attractive applications in electrocemical devices, fuel cell and lithium ion batteries in recent years are fully discussed and reviewed. Chapter 3 briefly describes the synthesis methods to produce ZIFs and converted ZIF derivatives. Moreover, the detailed experimental processing and property characterisation techniques were also described. Chapter 4 describes the use of one-step *in-situ* synthesised GO/ZIF-67 nanocomposites to produce their derivative CoS-C-G *via* the simultaneously sulfurisation and carbonisation of GO/ZIF-67. Moreover, the electrocatalytic activities including ORR, OER and HER of cobalt sulfide/N doped carbon/graphene have all been demonstrated and discussed. Additionally, Chapter 4 also explores a simple method for the preparation of cobalt-nickel sulfide/N, S co-doped nanoporous carbon/graphene nanocomposite derived from Ni-substituted GO/ZIF-67. Their applications in OER and HER have been studied and the effect of GO content on the electrochemistry performance has also been investigated. Chapter 5 presents a facile way to produce homogeneously dispersed cobalt-iron/N doped nanoporous carbon/graphene

derived from Fe-substituted GO/ZIF-67. Their electrochemistry applications of resulting nanocomposites have been presented and the effect of GO content towards water splitting has also been researched. Furthermore, a simple preparation process of bimetallic cobalt-iron oxide/N doped nanoporous carbon/graphene derived from Fe-substituted GO/ZIF-67 has also been demonstrated. The electrocatalytic performance of the produced oxidation nanocomposites has been presented in Chapter 5 as well. Chapter 6 further provides an efficient method for the preparation of bi-metallic cobalt-iron sulfide/N, S co-doped nanoporous carbon/graphene nanocomposite derived from Fe-substituted GO/ZIF-67. Their applications towards waters splitting such as OER and HER were all showed and the effect of GO content on the electrochemistry performance has also been investigated. Finally, the main conclusions of this thesis work and some recommendations for future studies are summarised in Chapter 7.

Chapter 2: Literature Review

2.1 ZIFs and ZIF-derivatives materials

2.1.1 Introduction

During the past decades, porous materials have been widely investigated owing to their permanent porosity, relatively high thermal and chemical stability[26]. In 1995, Yaghi *et al.* first introduced and synthesised metal–organic frameworks (MOFs). Since then MOFs materials were rapidly developed with the aim to find new structures and explore new gas sorption and electro-catalytic properties and so on.

In recent years, a lot of efforts have been devoted to develop a new class of porous materials based on hybrid metal–organic frameworks. Among them, a series of MOFs with zeolitic architectures have attracted much attention and were synthesised as hybrid frameworks successfully. Zeolitic imidazolate frameworks (ZIFs) are a class of porous crystals with extended three-dimensional structures constructed from tetrahedral metal ions (e.g., Co, Zn) bridged by imidazolate (Im). These ZIFs (M–Im–M) and conventional aluminasilicate zeolites (Si–O–Si) have similar structures (shown in Figure 2.1), in which Co^{2+} or Zn^{2+} ions play the role of silicon and the imidazolate anions form bridges that mimic the role of oxygen in zeolites with the angle of 145° [27-28]. Compared with other MOFs, ZIFs are advantageous in structural topologies and coordination factors, and show exceptional thermal and chemical stability. Therefore, ZIFs hold great promise as porous materials for a variety of applications.

Recently, as one of the most important electrocatalytic material systems, porous carbon-based materials have attracted a lot of attention in electrochemical applications due to their advantages of variable structures, large surface area, tunable porosity and affordable price. Actually, porous carbon-based materials have been developed for various electrocatalysis applications including Oxygen Reduction Reaction (ORR), Oxygen Evolution Reaction (OER), Hydrogen Evolution Reaction (HER) and water splitting [4-5, 29-30]. Particularly, in the past years, many MOF-derived porous carbon based materials have been developed as active electrocatalysts in different areas such as Li-O_2 batteries,

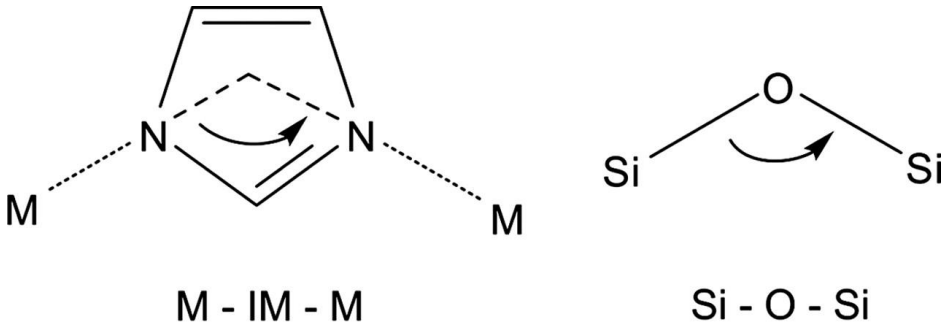

Figure 2. 1 Bridging angles in metal IMs and zeolites [15]

CO_2 reduction, HER, OER, and ORR. ZIFs, as a sub-class of MOFs with unique structure, can generate multiple extended 3D open frameworks with topologies that are similar to those have been already identified in the aluminosilicate zeolites [7]. In addition, it has been demonstrated that ZIFs share many virtues of zeolites, which distinguish them from many other MOFs, such as the exceptional mechanical stability, ultrahigh chemical stability results from the metal–nitrogen bonds, tuneable pore size and surface area by simply modifying the Im its interaction with electrolytes and reactants. Moreover, metal sulfides/ oxides could also be formed from ZIF precursors under certain controlled synthesis conditions. All these outstanding characteristics have made ZIFs and their derives as promising candidates for electrochemical application and stable electrocatalysts.

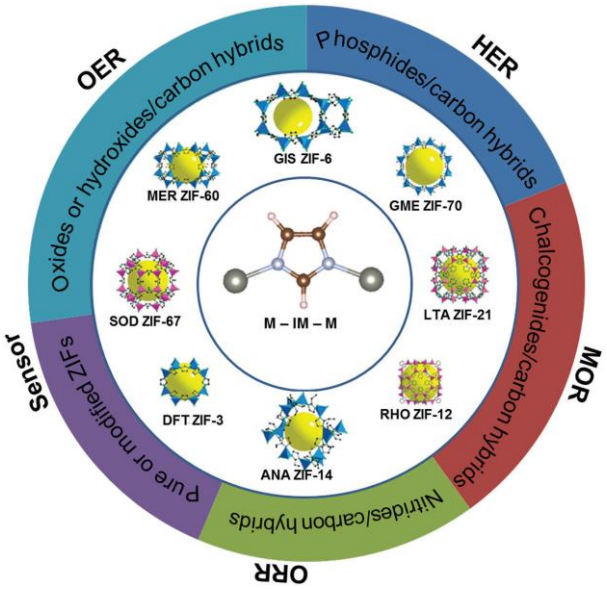

Figure 2. 2 The illustration of typical topologies of ZIFs and ZIF-derived materials as electrocatalysts in various areas [31]

In the first section of this literature review part, we will summarise and analyse the structures, synthesis methods, and applications of ZIFs material. Meanwhile, their derived porous N-doped carbon-based materials for electrochemistry would also be analysed and the relationship between the various derives systems and different applications in electrocatalytic reactions, such as ORR, OER, HER, molecule oxidation reactions (MOR) and sensor. (Figure 2.2).

2.1.2 Microstructures and characteristics of ZIFs and ZIF derivatives

Table 2.1 shows a comprehensive list of the topologies and the structural properties of common species of ZIFs. Structure properties of a specific ZIF mainly depend on the type of imidazolate and the solvents used during the synthesis process, and therefore a variety of ZIFs with different structures could be obtained by using functional imidazolates in different solvents. By using different imidazolate ligands and solvents, the obtained ZIFs can have multiple structures and can be classified into several classes according to their topologies (as shown in Figure 2.3), such as Linde Type A sodalite (LTA), zeolite rho (RHO), gmelinite (GME), merlinoite (MER), gismondite (GIS), analcite (ANA) and ZIF-3 framework structure type (DFT, a tetrahedral form with a space group $P4_2mnm$), which are traditional topologies of standard zeolites [3]. Nowadays, hundreds of ZIFs materials have been successfully synthesised. The crystal size in ZIF materials can be continuously tuneable in a range *via* using mixed linkers. In contrast, for the single linker ZIFs material, only discrete changes could be obtained. For instance, a series of ZIF-8-90 zeolites with tunable crystal size ranging from <0.5 μm to about 100 μm were synthesised through adjusting the ratio of 2-methylimidazole and carboxyaldehyde-2-imidazole [32]. When ZIFs are used in many different applications such as gas separation/ adsorption, molecular sensing, heterogeneous catalysis, etc., their porous structures will be inevitably subjected to different kinds and degrees of mechanical stresses and strains, which in turn sometimes damage their structures and then lower their efficiencies. Therefore, the stiffness and hardness properties of the synthesised ZIFs, which are definitely influenced by imidazolate-type linkers, are keys to determining their suitability for practical applications.

Recently, many ZIFs with different topologies were developed to achieve huge pores [2]. In the application of gas sorption, both ZIF-11(d=14.6 Å) and ZIF-8

(*d*=14.6 Å) materials possess large pores, nearly twice larger than their corresponding zeolites. It should be shocked that the Langmuir surface area of ZIF-8 is 1810 m^2 g^{-1} for the hydrogen uptake based on bar high pressure [2].*Park et a*l found. [15] research, they found that the fully exposed faces and edges of the organic links in the ZIF materials result in the large surface areas and pores. These works illustrated that surface areas and pore volumes of ZIFs are superior to those of traditional crystalline porous materials such as zeolites and mesoporous silica, and comparable with some of the highly porous MOF compounds [15].

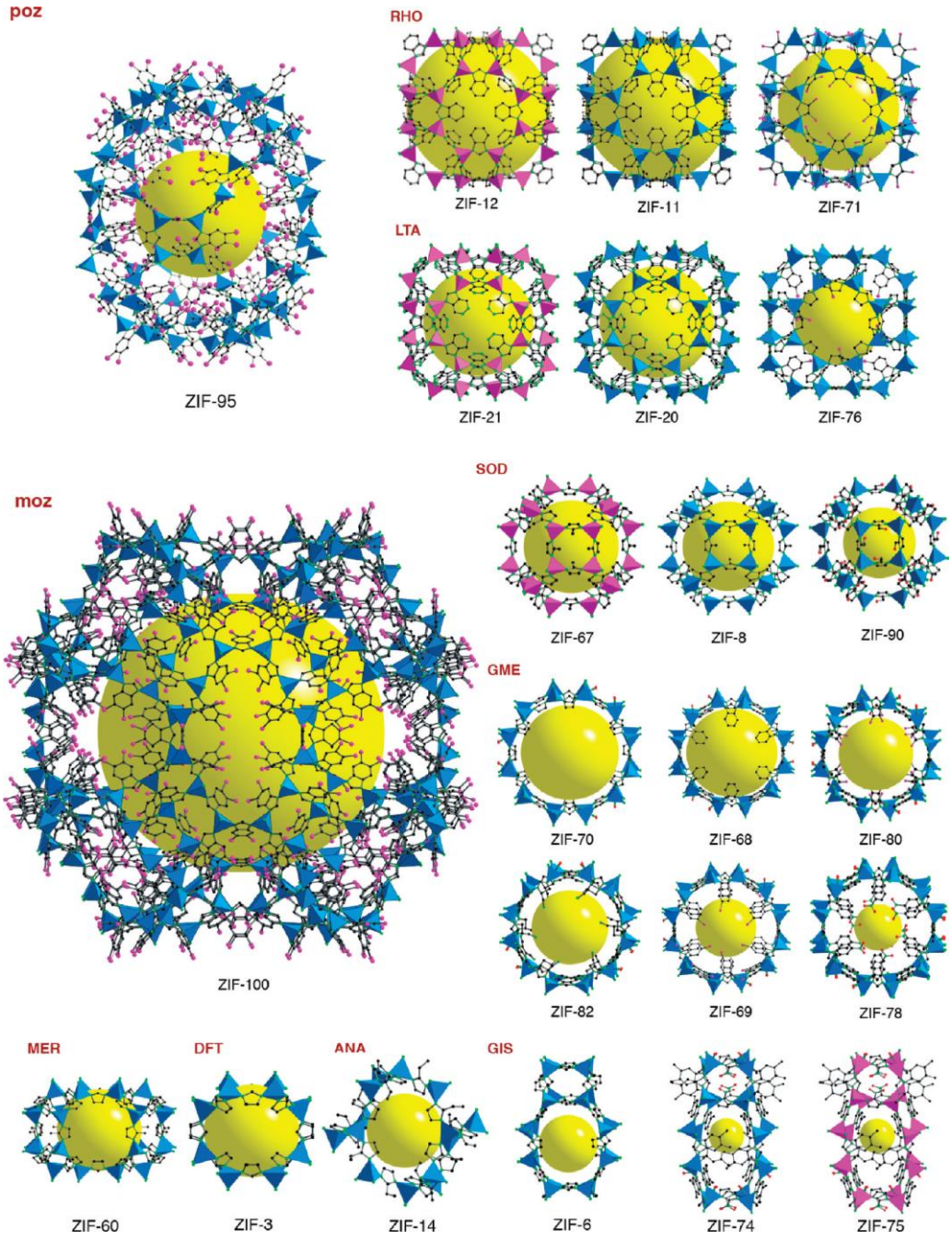

Figure 2. 3 Different topologies and crystal structures of ZIFs [3]

In addition, ZIFs materials possess an exceptional thermal and chemical stability owing to their unique structural characteristics: ZIFs consist of strong metal-nitrogen bonds, therefore, they show very high resistance to organic and alkaline solvent [15, 33]; another reason is that the MN_4 units are not influenced by solvents, thus, the framework and surface structure cannot be broken. For instance, both ZIF-11 and ZIF-8 were carried out in water and sodium hydroxide solvent at 50°C for seven days. The XDR results show that both ZIFs could retain their structure in those two solvents [15].

Table 2. 1 List of topologies and microstructural properties of common ZIFs

Name	Molecular structure	Topology	Density of metal Atoms (T/nm^3)	Ref.
ZIF-3	$Zn_2(Im)_2$	DFT	2.66	[15]
ZIF-6	$Zn\ (Im)_2$	GIS	2.31	[15]
ZIF-8	$Zn(mIm)_2$	SOD	2.45	[34]
ZIF-11	$Zn(bIm)_2$	RHO	3	[15]
ZIF-12	$Co(bIm)_2$	RHO	3	[15]
ZIF-14	$Zn(eIm)_2$	ANA	2.57	[35]
ZIF-20	$Zn(pur)_2$	LTA	2.04	[36]
ZIF-21	$Co(pur)_2$	LTA	2.04	[36]
ZIF-60	$Zn_2(Im)_3(mIm)$	MER	2.24	[35]
ZIF-67	$Co(mIm)_2$	SOD	3.4	[35]
ZIF-68	Zn(bIm)(nIm)	GME	2.11	[35]
ZIF-69	Zn(cIm)(nIm)	GME	2.10	[35]
ZIF-70	$Zn(Im)_{1.13}(nIm)_{0.87}$	GME	2.11	[35]
ZIF-71	$Zn(dcIm)_2$	RHO	2.06	[35]
ZIF-74	Zn(mbIm)(nIm)	GIS	2.67	[35]
ZIF-75	Co(mbIm)(nIm)	GIS	2.67	[35]
ZIF-76	Zn(Im)(cbIm)	LTA	1.03	[35]
ZIF-78	Zn(nbIm)(nIm)	GME	2.08	[37]
ZIF-80	Zn(dcbIm)(nIm)	GME	2.07	[37]
ZIF-82	Zn(cnIm)(nIm)	GME	2.09	[37]
ZIF-90	$Zn(Ica)_2$	SOD	3.5	[38]
ZIF-95	$Zn(cbIm)_2$	POZ	1.51	[2]
ZIF-100	$Zn_{20}(cbIm)_{39}(OH)$	MOZ	1.29	[2]

2.1.3 Synthesis of ZIFs and ZIF derivatives

2.1.3.1 Powder-based ZIFs

During the past years, solvothermal and hydrothermal synthesis methods in organic solvents or water have been used for preparing ZIF-based materials. The reaction temperature varies from room temperature to 200°C and reaction duration could be from a couple of hours to three days.

Multiple synthesis methods have been developed to generate ZIF-based materials (as shown in Figure 2.4) with different pore size and morphologies. Undoubtedly, ZIFs can be synthesised in the form of either a powder or a membrane.

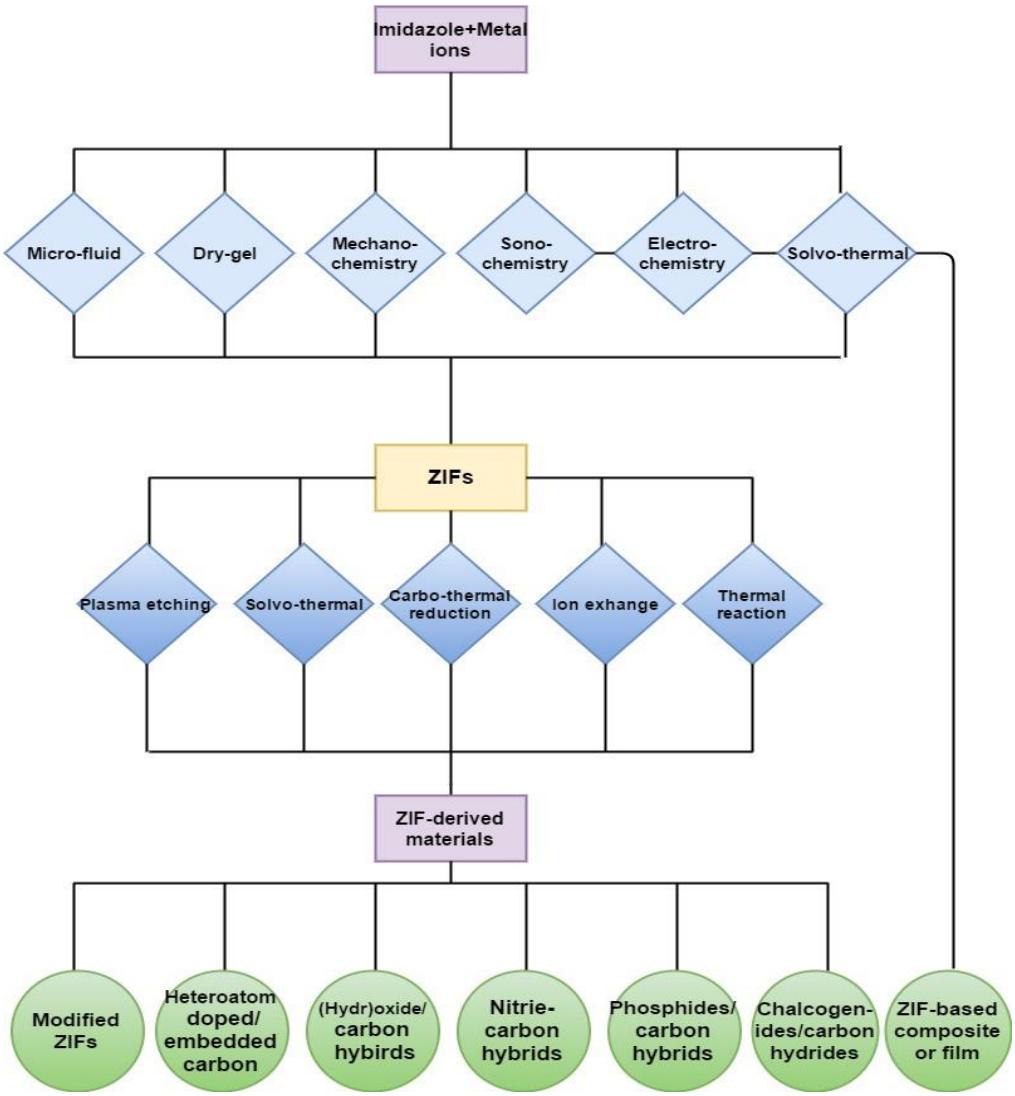

Figure 2. 4 Summary of different synthesis methods for ZIFs and ZIF-derived materials

Solvent-based synthesis

Commonly, ZIFs materials can be prepared *via* a solvent-based or solvent free synthesis methods where selected organic solvents acted as the reaction medium. In 2006, Park *et al.* [15] successfully synthesised ZIF-1 to ZIF-12 in different amide solvent systems such as N, N-dimethylformamide (DEF), N-methylpyrrolidine (NMP) and N, N-dimethylformamide (DMF), which were regarded as agents and could be removed after the reaction. In the same year, a mixed system of DEF/NMP/DMF was also acted as solvents to synthesise ZIF materials such as ZIF-95 to ZIF-100, ZIF-78 to ZIF-82 and ZIF-60 to ZIF-77 [35-37]. Methanol, being regarded as another important organic solvent, was also widely used in the synthesis of ZIFs. Huang's group [16] successfully synthesised three different kinds of crystal structures in methanol medium. Zhang and co-workers [39] obtained ZIF-8 crystals by using methanol as reaction medium mixed with aqueous ammonia. Later on, many researchers used similar approaches and solvents to synthesise many new ZIF materials.

In order to improve the formation of ZIFs, the methanol/ethanol-based system was promoted by additives, such as pyridine, trimethylamine, and sodium hydroxide, which were added to the organic solvent systems during the synthesis process to control the crystal sizes and nanocrystal structures of ZIF materials [40-41]. For instance, the nanocrystal size of ZIF-8 was controlled *via* employing sodium formate/1-methylimidazole and n-butylamine in methanol solution [42]. After the use of additives, the crystal size of ZIF-8 could vary from 10 to 65 nm. Meanwhile, the modulated ligand sodium could accelerate the crystal formation at room temperature. In addition, Nune's group [18] synthesised nano-sized ZIF-8 with hexagonally shaped by using agent of poly (diallyldimethyl ammonium chloride) as a stabilizer in methanol. Since 2-methylimidazolate could stop the growth and stabilize the positively charged nanocrystals, Peralta *et al.* [41] synthesised uniform ZIF-8 nanocrystals without any auxiliary agents but with excess 2-methylimidazole in the precursor. Thus, shapes and sizes could be successfully controlled *via* adding N-heterocycle, alkalamine, poly and sodium formate into the methanol-based medium.

Hydrothermal synthesis

Considering the safety and environment friendly issue, large amount of flammable and expensive organic solvent could cause serious pollution to environment in the early state of synthesis researches. To avoid the above problem, much effort has been devoted to find green and efficient methods to synthesise ZIF materials in recent years. In Pan's research [43], ZIF-8 with controllable size and high surface area was successfully synthesised at room temperature by adjusting the ratio of 2-methylimidazole and zinc nitrate. ZIF-67 was obtained from the molar ratio of Co^{2+}: MIm: H_2O=1: 58: 1100 in aqueous solutions at room temperature [44].

Using ammonium hydroxide or TEA as the deprotonating agent could reduce the use of ligand MIm and initiate the formation of ZIFs. Thanks to the action of TEA, it was found that the ratio of metal ion: MIm decreased to 1: 4 for the preparing of ZIF-67 and ZIF-8 at room temperature in Gross's research [45]. Yao's group [46] reported the preparation of ZIF-8 in the presence of ammonium hydroxide with the molar ratio of Zn^{2+}: MIm: NH_4^+: H_2O=1: 4: 16: 547. Additionally, ZIF materials could be also obtained in the presence of other additives in aqueous such as triblock copolymer and polyvinylpyrrodlidone (PVP), which can attract metal ions during the reaction. For example, both ZIF-67 and ZIF-8 were prepared in aqueous ammonia systems in the presence of the triblock copolymer surfactant, which could promote the formation of porous ZIF-67 and ZIF-8 due to the electrostatic attraction to the metal ions [46]. Furthermore, in Shieh's report [47], smaller particles of ZIF-90 were successfully obtained *via* adding a certain amount of alcohol and polyvinylpyrrolidone in aqueous solution.

Other solvent synthesis

To avoid the competing interactions between the solvent-framework and the template-framework that are present in the hydrothermal synthesis process, an ionothermal method was developed using green solvents (ionic liquids), where ionic liquids are used as both the templates and solvents during the synthesis [38, 48-49]. The first use of ionic liquid for the synthesis of ZIFs was from Morris's group [50], reporting ZIFs nanostructure were obtained by using 1-ethyl-3-methylimidazolium bis-(trifluoromethyl)sulfonylimide, where ZIF-8 was

successfully synthesised. Apart from ionothermal synthesis, the sonochemical synthesis method has attracted much attention in recent years. During the sonochemical synthesis process, the formation of nucleation was promoted and become much more homogeneously. From Seoane's report [51], ZIFs were generated under ultrasound irradiation. The resultant ZIFs crystals were much smaller with narrower particle sizes comparing to the conventional oven heating synthesised materials.

Solvent-minimisation and solvent-free method

Although the synthesis of ZIFs in the aqueous-based system is environmental friendly and cost-effective compared with those in the organic solvents-based system, some problems such as the use of excessive imidazole sources and massive solvent washing still make the aqueous synthesis method inefficient. Thus, solvent-minimisation methodology has been developed to eliminate the annoying washing procedure in solvent based systems [51]. For instance, Shi and co-workers [52] found a conventional method of using a steam-assisted/ vapor-assisted/ heating-assisted to fabricate porous ZIF-67 and ZIF-8. Compared with conventional hydrothermal synthesis approaches, solvent-minimisation method can not only reduce the amount of solvent significantly, but also increase the transformation rate from the solid reagents.

Moreover, many ZIFs materials could be also successfully generated *via* solvent-free methods according to some very recent researches. For example, porous ZIF-8 have been successfully produced from the oxide/hydroxide-based solvent-free reaction without any by-product by Lin and co-workers [53]. Cliffe *et al.* [54] successfully synthesised ZIFs using a low energy and solvent-free "accelerated aging" method. Then, ZIF-4, ZIF-67, ZIF-8 and ZIF-20 were all generated following the similar process. It is noteworthy that many different kinds of ZIFs could be formed using grinding the organic linker with the specific metal oxide [55-56]. By using ZnO reaction with liquid-assisted and ion-assisted grinding, ZIFs with different kinds of topologies such as RHO, Quartz, and ANA can be obtained [57].

2.1.3.2 Pure ZIFs film and membranes

The well-defined and tunable porous structures of ZIFs allow them to achieve adsorption, gas separation and gas storage with a high selectivity due to the

molecular sieving effect [58]. The pore size of ZIFs is usually less than 5 Å, which is in the suitable range of small gas molecular and liquids. The surface area and pore size of ZIFs were determined by using different linkers, which is versatility of imidazolate linkers. Therefore, different multiple synthesis approaches have been considered to fabricate ZIFs membranes for gas separation and chemical sensors, such as gas purification, carbon dioxide capture, and liquid separation *via* pervaporation. Similar to zeolite membranes, ZIF membranes are also generated by growing a thin ZIF layer on porous substrates, which could provide mechanical support and exhibit minimal permeation resistance. Although a wide range of materials could be considered as substrates such as stainless steel tubes, polymer sheets and porous ceramics, the quality of the fabricated membranes is mainly determined by the nature characteristic such as surface roughness, pore size and chemical composition [58]. Currently, techniques for the synthesis of ZIF-based membranes can be roughly classed as direct synthesis and secondary growth [1].

Direct synthesis

In the direct synthesis process, a porous membrane substrate without surface modification is immersed in a ZIF synthesis solution, where a layer of ZIF grows directly on the substrate [59-60]. For example, ZIF-8 membrane was prepared on titania support by microwave-assisted solvothermal synthesis [61]. Firstly, immersing a dried and clean titania support into the precursor solution and leaving it for about 25 minutes. Then, the solution with the support was transferred into a 200 ml Teflon autoclave and heated in a microwave oven at 100°C for 4 hours to complete the membrane preparation. Moreover, ZIF-8 was also synthesised *via* a one step *in situ* method, in which sodium formate was introduced and played a critical role in the formation of ZIF-8 membrane [62]. So far, although many ZIF membranes have been successfully formed, the quality of resultant ZIF membranes with many intercrystal voids were not good because it is difficult to control ZIF crystallisation on an unmodified substrate.

Secondary growth

In order to control the growth speed, orientation, and the thickness of the synthesised ZIF films efficiently, the secondary growth, which is also named as seeded growth, has been developed in recent years. In the secondary synthesis

process, ZIF crystals are first directly deposited on the substrate, which could provide seeds to promote ZIF crystallisation. Afterwards, crystals are generated on the substrate during growth through initial functionalisation of the surface of the substrate by organic linkers [63-64], infiltration of precursors into porous substrates [65-66], or deposition of the precursor solutions on the substrate separately. For instance, porous zinc oxide support was acted as reactive seeding to generate ZIF-78 membranes during the hydrothermal synthesis process, and the secondary seeded growth was then carried out to crystallise a ZIF-78 layer on the support. Compared with the direct synthesis method, the secondary growth exhibits remarkable advantages of controlling the crystal orientation and thickness of the ZIF membrane [66].

2.1.3.3 ZIFs-derived carbons

Thanks to the porous structures with extra high surface and large pore volumes, ZIFs have been used as templates or precursors to generate porous carbon materials in recent years. For instance, ZIF-8, as a member of ZIFs family, is emerging as the best candidate to prepare metal-free nitrogen doped porous carbon due to the evaporation of zinc oxides during the pyrolysis. The resultant of nitrogen-doped carbons exhibits high ORR activity and stability [67-68]. Moreover, other members of ZIFs family such as ZIF-68, ZIF-69 and ZIF-7 have been also developed as candidates for the generation of porous carbon materials. Their synthesis processes are similar to ZIF-67 by using heating treatment in inert atmosphere. Porous carbons were obtained after washing the high temperature processed resultant materials by acid.

2.1.3.4 ZIFs derived sulfides/phosphides and porous carbon

The earth's abundant resources, cost effective and the synergistic effects between the metal and chalcogenide parts make transition-metal chalcogenides with heterogeneous structure as promising candidates in electrochemistry area [69]. Among them, ZIF-derived metal sulfides were most attractive owing to their large amount of active edge sites. Our group utilised ZIF-67 to synthesise cobalt sulfide/porous carbon nanocomposite by direct sulfurisation and carbonisation in hydrogen sulfide and argon atmosphere [1]. In the first step, ZIF-67 materials were heated to the target temperature (600-1000°C) for carbonisation. Then, the hydrogen sulfide was introduced with flow rate of 5 ml/min and held for one

hour. After cooling down to the room temperature, the black powder was obtained. In addition, the cobalt sulfide/ porous carbon were also obtained by directly reacting ZIF-67 with thioacetic acid during the refluxing, under the inert atmosphere [70]. In order to increase the electrochemistry performance of the ZIF derived sulfides, nickel/cobalt bimetallic sulfides were prepared. In the synthesis process of ZIF-67 powder, Nickel Nitrate Hexahydrate ($Ni(NO_3)_2{\cdot}6H_2O$) was introduced into solution with Co: Ni mol= 2: 1 and 4: 1. Then, using the same process as above, the bimetallic sulfides/ porous carbon were obtained.

Very recently, many researches focused on the transition metal phosphides, which were used as HER catalysts owing to the facts that the negative charge of P sites can attract protons and the slightly positively charged metal sites of the transition metal phosphides can facilitate the bonding of atomic H. The cobalt phosphide/porous carbon were successfully synthesised *via* one step method. Generally, the mixture of a certain amount of ZIF-67 and sodium dihydrogen phosphate (weight ratio=1:4) were placed in the tube, followed by heating to the target temperature (300, 600 and 800°C) and was held for one hour in the argon atmosphere. After cooling down, the resulting powders were collected and then washed by ethanol and distilled water three times. Moreover, bimetallic phosphides were also obtained by introducing nickel such as Ni_2P-CoP and NiCoP [71-72].

2.1.3.5 ZIF derived oxide(s) and porous carbon hybrids

Transition metals or metal oxides are one of the attractive electrocatalysts for OER. However, the single transition metal oxide could not exhibit a good conductivity. The special configuration of ZIF materials, provides a strategy to generate well-dispersed metal oxide in the N-doped porous carbon composite to overcome its poor conductivity. For example, a recent report demonstrated that finely dispersed Co_3O_4/ porous carbon hybrid materials can be synthesised by a two-step thermal conversion of ZIF-67 in different atmosphere [73]. As shown in Figure 2.6, ZIF-67 powder was treated *via* carbonisation in argon atmosphere, converted to Co/ porous carbon. In the annealing process, the powder was held for 2 hours and then cooled down to room temperature. In the second step, the obtained powder was heated to 350°C in the air for two hours and finally, the resultant of Co_3O_4/ N-doped porous carbon were obtained. In addition, a complicated method of producing carbon-cobalt/ cobalt oxide composites was

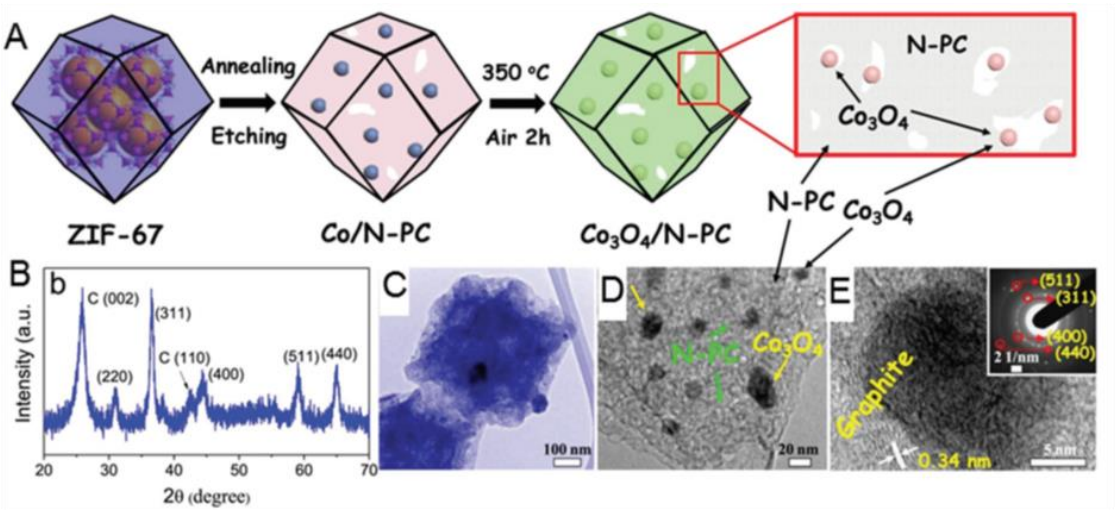

Figure 2. 5 (A) Synthesis procedure and schematic diagram and (B) XRD pattern (C, D) TEM images and (E) HRTEM image of Co_3O_4/NPC [74]

also developed. In details, the first step is as same as above thermal pyrolysis of ZIF-67, followed by dispersing products in 2M H_2SO_4 solution for 12 hours to remove metallic cobalt with large particle size. The resultant materials were annealed at 350°C for one hour in air atmosphere and finally carbon-cobalt oxide nanocomposites were obtained [75]. Moreover, our group first develop a green and facile one-step approach by using water steam at high temperatures with the utilisation of ZIF-8 as a precursor to generate atomically homogeneous dispersed ZnO/nanoporous N-doped carbon composites [76].

In summary, many synthesis methods for preparing ZIFs and ZIF derivatives have been introduced and reviewed. For ZIFs powder materials, most common synthesis methods such as solvothermal and hydrothermal methods have been widely used. Moreover, other approaches, including ionothermal and sonothermal methods have also been applied for ZIF production. Additionally, solvent-minimisation and solvent-free methods have been successfully developed and were regarded as novel trend in the future. For the ZIF film/membranes materials, two synthesis techniques, direct synthesis and secondary growth methods have been developed in the past years. Regarding to the ZIF derivatives, ZIF-derived carbon-based materials with different properties and structures have attracted much attention. Among all synthesis methods, the *in situ* approach is the most popular to achieve a well dispersion of metals or metal compounds particles in porous carbon. Owing to the rapid improvement of synthesis strategies, there is no doubt that novel synthesis

methods with cost-effective, environment friendly and large scaled ZIFs and ZIF derivatives production will be developed in the future.

2.1.4 Properties and applications of ZIFs and ZIF derivatives

Due to the properties of high surface area, adjustable compositions and controllable structures, ZIF materials have been considered as promising adsorbents, catalysts, electrical sensors and drug deliveries. Moreover, given the fact that ZIF derivatives of carbon, metal-carbon and metal composite-carbon could be obtained by heat treatment under different conditions, ZIF derivatives are attracting much attention owing to their porous structure and electrically conductivity properties. Therefore, many ZIF derivatives could be used as electrocatalysts and supercapacitors in typical electrochemical reactions.

2.1.4.1 Gas separation

Due to the increased global climate problem, both natural gas purification and carbon dioxide capture are attracting increased attentions. Developing novel materials with green and cost/energy efficient is the most urgent research topic in recent years. Similar to zeolite structures, ZIFs exhibit permanent porosities, variable structures, highly thermal and chemical stabilities, as a result, ZIFs have been considered as good candidates for gas separation applications. In Figure 2.5, a summarised gas separations illustrate both ZIFs and ZIF-based polymer mixed matrix membranes (MMMs) have been widely developed. Owing to the good potential in practical applications of ZIF membranes in these fields, ZIF membranes exhibit remarkable performance in both carbon dioxide and hydrogen gas separation. Among all ZIF materials, ZIF-8 is the most promoting porous membrane, which showed an excellent separation performance of H_2 from other large gases [58], such as separation of H_2/CH_4 [59] and separation of C_2-C_3 hydrocarbon mixtures [77]. In addition, ZIF-7/PBI MMMs and ZIF-8/PBI MMMs exhibited extra high separation of H_2/CO_2 and CO_2/CH_4, respectively.

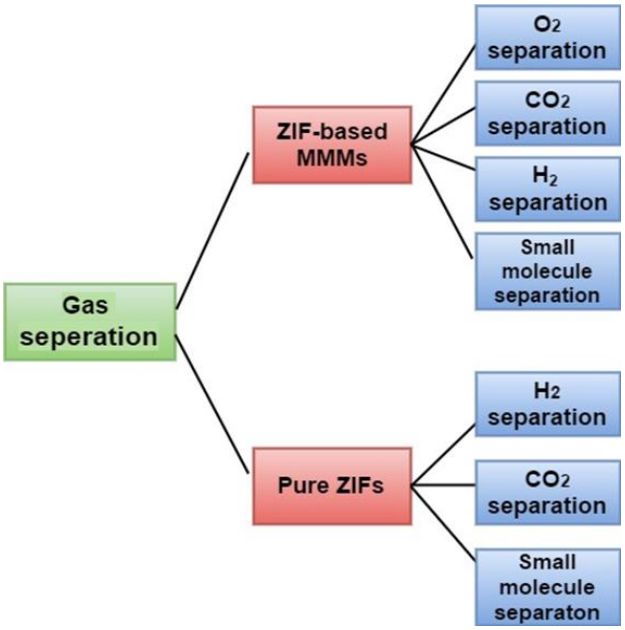

Figure 2. 6 Summary of gas separations for both ZIFs and ZIF-based polymer mixed matrix membranes

2.1.4.2 Catalysts

Due to its similarity to aluminosilicate zeolites which are typical porous materials and also key commercially available catalytic materials [78], ZIFs and ZIF-based materials can also be efficient catalysts for a number of reactions, such as transesterification [79], the Knoevenagel reaction [80], Friedel-Crafts acylation [81] and oxidation and epoxidation [82] etc. In a recent research, both ZIF-9 and ZIF-10 show a promoting performance to form benzylidene malononitrile, acting as efficient catalysts in the Knoevenagel reaction [83]. In addition, ZIF-8 has been explored as an efficient catalyst in Friedel-Crafts acylation reactions between benzoyl chloride and anisole [79]. Furthermore, ZIF-8 was also shown excellent catalytic activity in hydrogen production [84] and ZIF-8/ZIF-9 demonstrated abilities as catalysts for oxidation [85] and epoxidation reactions [82].

2.1.4.3 Drug delivery & electronic devices

Due to the excellent chemical and thermal stabilities, good porous structure and pH sensitive properties, ZIFs have been used as platform for drug deliveries [86]. For example, ZIF-8 showed a remarkable loading capacity for the anticancer drug 5-fluorouracil owing to its porous structure [87]. Thanks to the its pH sensitive advantage, ZIF-8 was also used as drug delivery vehicle in medical treatment [87]. In addition, in recent reports, ZIF-8 was also found to be an agent

to control the release of caffeine and protect the drug molecules in high temperature [88].

For their excellent tuneable diameters and good functionalisation capabilities, ZIF materials can also be applied in electronic devices. For instance, ZIF materials including ZIF-7, ZIF-8, ZIF-67, ZIF-68 and ZIF-70 used as a matrix respectively for co-immobilising electrocatalysts methylene green and glucose dehydrogenase on the electrode surface, and the as-fabricated ZIF-based biosensors demonstrated a high selectivity and sensitivity to glucose in the cerebral system [89]. Moreover, due to the porous structure, ZIF-8 is sensitive to Cu^{2+} and Cd^{2+} ions, and thus it can be used as luminescent probes to detect metal ions [90].

Properties and applications of ZIF materials have shown a great development in the past years. The properties of these materials can be chemically tuned for different applications and has unlocked many opportunities for researchers to exploit ZIFs for their structure, thermal and chemical stabilities. However, scientists should pay attention to the nature of the functional groups pending on the imidazolate rings, since their chemical environment may change drastically the stabilisation and influences the activity and selectivity. It is believed that ZIFs are yet to unleash their whole potential, other challenges and novel developments would make ZIF materials highly attractive supports.

2.1.4.4 Electrocatalysts

Since the tetrahedral centres of ZIFs are connected by tuneable organic ligands and the porous structures of pure ZIFs could shorten the diffusion length of the electrolyte and therefore expose more active edge sites, many pure ZIFs have been synthesised and used as electrocatalysts [7, 91]. Co-ZIF-9 is a theoretically promising candidate that can be used as an OER electrocatalyst because it can activate water molecules with low activation barriers. In Wang's research [92], Co-ZIF-9 can deliver efficient OER performance in the whole pH range, and the onset potential is only 0.4 V with the Tafel slope of 193 mV dec^{-1} in neutral solution. Apart from Co-ZIF-9, Co-ZIF-67 is also used as an excellent OER electrocatalyst in all pH range. A current density of 4 mA cm^{-2} was measured in a certain potential with a slope of -97 mV dec^{-1}/pH from pH=13 to pH=2 [93]. Since the combination of ZIFs' structure and cobalt centres located close to

vicinity, cobalt contained ZIFs could act as promising OER electrocatalyst with high catalytic activity and stability [94].

Multiple ZIFs can be thermally treated to obtain conductive ZIF derivatives as electrocatalysts. Recently, nitrogen-doped carbon exhibits high ORR activities since the pyridinic-N will activate the adjacent carbon, enhancing its adsorption and activation toward oxygen during catalysis. Therefore, ZIFs materials were considered as good precursors to prepare nitrogen-doped carbons. For example, ZIF-8 is the best precursor to generate metal-free nitrogen-doped carbon among all ZIFs material [95] and therefore can be used as a template in the presence of furfuryl and NH_4OH, which acted as additional precursors of carbon and nitrogen [96]. The obtained resultants exhibit onset potential of 0.83 V (vs RHE) in O_2 saturated 0.1M KOH solution and demonstrate a four-electron reduction pathway to produce H_2O as the dominant product [96]. Due to the active sites provided by porous structure, the resulting carbon exhibits an exchange current density of 0.063 mA cm^{-2} in 0.5M H_2SO_4 in HER and also shows a remarkable performance in OER. Beside these, ZIF-8 derived carbon also shows a high surface area of 923 m^2 g^{-1} and pore volume of 1.58 cm^3 g^{-1} [96]. In addition, ZIF-67 was also a good candidate precursor to prepare metal composite carbon. The four nitrogen atom coordinated and uniformly dispersed metal ions (M-N_4) in the ZIFs are considered as the active sites for the ORR [97]. Therefore, Xia's group obtained nitrogen-doped carbon nanotube frameworks (NCNTFs), which retains the original morphology of the initial ZIF-67 particles. The resulting NCNTFs exhibit outstanding ORR activity with the half-wave potential of 0.87 V (vs RHE) and an excellent OER activity with the overpotential of 1.6 V (vs RHE) at the current density of 10 mA cm^{-2}.

Many ZIF-derived sulfides are also synthesised and exhibited considerable electrocatalytic activity toward the OER, ORR, and HER [98-99]. In our research, ZIF-67 was used as precursor to generate metal sulfide *via* a heating treatment in hydrogen sulfide atmosphere [98]. The obtained cobalt sulfide nanoparticles embedded in nitrogen-doped porous carbon exhibit outstanding OER and HER performance with the overpotential of 1.86 V and 0.3 V (vs RHE) at the current density of 10 mA cm^{-2}, respectively. In order to increase the electrochemical performance, the combination of two metal sulfides or one metal with double-shelled nanocages were explored. For example, in my research,

CoS@NiS@carbon nanocomposites were successfully synthesised and exhibit potential of 1.6 V and 0.39 V (vs RHE) at the current density of 10 mA cm^{-2}, respectively. Besides that, different kinds of hybrids such as Co_9S_8/NC@MoS_2 [72], Co_3S_4@MoS_2 [100] and CoNC@MoS_2 CNF [101] were all developed and used as electrocatalysts. Not only metal sulfides show good electrochemical performance, but also the combination of metal sites and phosphorus sites exhibit outstanding conductivity and superior stability in both acid and alkali environment. Thus, ZIFs can be used as precursors to generate metal phosphides embedded in N-doped porous carbon as electrocatalysts toward the OER and HER [102-103]. For instance, the bimetallic phosphides Ni_2P-CoP matrix and NiCoP were successfully prepared. The obtained nanocomposite possesses superior OER activity and exhibits excellent HER performance.

In addition, transition metal oxides embedded in nitrogen-doped porous carbons were also well developed in recent years. For example, Co_3O_4@carbon nanocomposites, which were derived from ZIF-67, exhibited good OER performance with the overpotential of 1.52 V (vs RHE) at the current density of 10 mA cm^{-2}. To further increase the performance of the composites, Xu and co-workers [93] improved the Co_3O_4 with oxygen vacancies.

2.1.4.5 Supercapacitors

So far the most representative ZIF materials which are studied for usage in supercapacitor applications are ZIF-8 and ZIF-67 [104], thus ZIF-8 and ZIF-67 derivatives also receive most research interests in this field.

A promising type of materials for supercapacitor applications is nanoporous carbon (NPC), due to their large specific surface areas, good electric and thermal conductivities, and excellent porosity. All these are particularly optimistic for being used as electrode material in high-performance supercapacitor. Thus, it is understandable that ZIF-8 and ZIF-67 were considered to be promosing precursors to produce multi-structured carbon systems for potential use in supercapacitors.

As early as in 2011, there was already report about unexpected high surface area and electrochemical properties as electrode for NPC material prepared from ZIF-8 and furfuryl alcohol [105]. This early research clearly indicated the potential of ZIF derived materials in supercapacitors, which was soon followed

by a number of researches of different processes for ZIF. In 2012, Yamauchi *et al.* [104, 106-107] performed a series of experiments to produce NPC system from ZIF-8 and ZIF-67 *via* one-step direct carbonisation processes at different temperatures (T = 600-1000 °C for ZIF-8, 800 °C for ZIF-67). In their results, they discovered although the surface areas of the got samples increased with increasing carbonisation temperature, it is the Z-900 sample that achieved the highest capacitance performance (214 F g^{-1} at 5 mVs^{-1}) among all ZIF-8 derived samples. Furthermore, the NPC derived from ZIF-67 through simple thermal decomposition process (which was carried out under an inert atmosphere and followed by thorough removal of cobalt nanoparticles with an acid wash) displayed even better capacitance performance (238 F g^{-1} at 20 mVs^{-1} in 0.5M H_2SO_4) than all ZIF-8 derived systems.

Researchers have also made high-performance asymmetric supercapacitor (ASC, to distinguish from symmetric supercapacitor, which is SSC) with ZIF-8-derived NPC as negative electrode materials. One interesting research was conducted by Wang *et al.* [108], in which the NPC was prepared with ZIF-8-derived porous carbon polyhedrons (PCPs), and the produced aqueous-electrolyte based ASC showed an excellent high capacitance value of 245 F g^{-1} at 1 A g^{-1} as well as outstanding energy storage capacity of 25.4 $Wh.kg^{-1}$ at 400 W kg^{-1}, plus excellent capacitance retaining property (93% retained after 10000 cycles). The researchers pointed out the polyhedral shape of the NPC could be the main factor of the enhanced capacitance, higher rate capabilities and electrode volumetric energy densities. For another instance, Zhang *et al.* [109] tried a MOF-NPC/MnO_2 hybrid as anode material while ZIF-8-derived NPC still as cathode. As a result, they observed encouragingly high energy storage capacities (maximum energy density and maximum power density are 76.02 W h kg^{-1}/2.20 kW kg^{-1} and 49.56 W h kg^{-1}/22.00 kW kg^{-1} for their MNCMn60//MNCMn950 samples respectively). This can be considered as further evidence of derived NPC to be one of the best candidates as electrode material of ASC.

On the basis of earlier work, researchers pointed out that in order to further improve electrode material properties, NPCs must be prepared with high graphic structures and possess high N content at the same time [105, 110-112]. Unfortunately, the two requirements are conflicting with each other, because

normally the graphitisation process will significantly reduce N contents. As a result, the NPCs' porosity was reduced [107, 113-115]. As an early effort to overcome this problem, Yamauchi *et al.* [116] performed a pioneer research in which a functionalised nanoporous hybrid carbon material (NC@GC) that was derived from core-shell ZIF-8@ZIF-67 structures was synthesised. The product showed a capacitance of 270 F g^{-1} at 2 A g^{-1}, which is an encouraging result for an early attempt for this type of new process. The fabrication of the material involves three basic steps: synthesis of the ZIF-8 seed core, growth of ZIF-67 shell surrounding the ZIF-8 seed and the final carbonisation step. The end product is a selectively functionalised nanoporous nitrogen-doped carbon@graphitic core-shell structure with a well-defined rhombic deodecahedral morphology. The structure features a NC core with relatively larger surface area and higher N content, and a GC shell with higher graphitisation level. The result of this research proves a balance between pore size distribution, pore volume, N content, surface area and graphitisation level is crucial to obtain high performance supercapacitors, which could be achieved with creative structure and functionalising process design.

Supercapacitor applications of ZIF-67 and its derived materials are heavily investigated in this work. They are particularly advantageous because ZIF-67, as a precursor, can produce not only N-doped NPCs (which is good cathode material, as aforementioned) but also nanoporous Co_3O_4 which can play the role of anode and possess high theoretical capacitance (3560 Fg^{-1}) and high electrochemical stability. In addition, from the point of view of practical application, cobalt oxides are cost-effective and environmentally-friendly.

Based on these advantages, researchers considered ZIF-67 and derivatives are superior supercapacitor material [117-118] and attempted to simplify the fabrication process of supercapacitor. One of the prominent work was performed by Yamauchi *et al.* [119] at 2015, in which they tried a so-called "two for one" strategy to produce NPCs and nanoporous Co_3O_4 through different thermal treatment process from ZIF-67. More specifically, the NPCs were produced by annealing in nitrogen atmosphere while nanoporous Co_3O_4 were in air. Both materials were proven to retain the original polyhedral morphology and were used to fabricate both SSCs and ASCs. For the SSCs, both electrodes are made up of same material (either NPCs or Co_3O_4) while the ASCs are with NPC cathode

and Co_3O_4 anode. The results, as expected, showed relatively low specific energy densities for the SSCs (carbon//carbon ~7 W h kg^{-1}, Co_3O_4// Co_3O_4 ~8 W h kg^{-1}), and in contrary, high energy densities of 36 W h kg^{-1} for the ASCs. The fact that both electrodes are made up of materials produced from the precursor, not only makes the fabrication process simple, but also provides a highly accessible surface area for electron transfer due to both electrodes retain the precursor's original polyhedral morphology.

This pioneering work was followed by Xia *et al.* [120] who developed a similar approach based on the "two for one" concept as well, in which shrinking carbon shells and hollow Co_3O_4 were prepared from ZIF-67 with the assistance of graphene aerogels. The as-synthesised N-doped graphene aerogels (NG-A) was proven to be an excellent catalyst for the reduction-oxidation reaction (Redox), while further derivative (C/NG-A) exhibited both high capacitance (421 Fg^{-1} at 1 Ag^{-1}, and be able to retain 305 Fg^{-1} when current increased to 50 Ag^{-1}) and rate capability. The C/NG-A also displayed an impressive power density of 500 W kg^{-1} at an energy density of 33.89 W h kg^{-1} and was able to retain 25000 W kg^{-1} at 24.86 W h kg^{-1} [121-126]. On the other hand, some researchers attempted other novel concept like "Ball-in-Cage" structure [127], in which a ZIF-67 polyhedron structure was integrated into a three-dimensional carbon network. The structure is considered beneficial to electrochemical properties because the carbon network was thought to provide nucleation sites for ZIF-67 particles, thus supplying more active sites to the electron conducting pathways.

ZIF materials have also been used to produce hollow nanostructures for supercapacitor applications. One prominent example is, Hu *et al.* [128] used ZIF-67/Ni-Co layered double hydroxide (ZIF-67/Ni-Co LDH) yolk-shelled structures to prepare $Co_3O_4/NiCo_2O_4$ double-shelled nanocages (DSNCs) by first dispersing ZIF-67 particles into an ethanol solution containing $Ni(NO_3)_2$ then annealing in air. The $Co_3O_4/NiCo_2O_4$ DSNCs displayed high specific capacitance (972 Fg^{-1} at 5 Ag^{-1}, and retain 92.5% of its after 12000 cycles) as electrode of pseudo-capacitance. The $Co_3O_4/NiCo_2O_4$ DSNCs, as name indicates and proven by energy-dispersive X-ray spectroscopy results, consist of an inner shell mainly composed of Co_3O_4 and an outer shell made up of $NiCo_2O_4$. Both shells remain stable and intact during repetitive anodic and cathodic sweeps, producing several distinct redox peaks, thus demonstrated

that the excellent surface pseudo-capacitance performance is originated from the surface redox reactions. In a following work [70], the same group produced a similar double-shelled nanocage structure from ZIF-67@CoS for efficient redox reactions.

Hu *et al.* [129] also made an interesting attempt to synthesise double-shelled hollow structures derived from ZIF-67 naocubes, which owns high surface area. In this work, after a two-step chemical treatment process, the core of the original nanocubes were transformed into CoS nanoparticles while shell become CoS nanosheets. These structures were found to successfully improve charge transport and help facilitate electrochemical reactions. In their prototype supercapacitors, these nanoboxes were used as anode material while activated carbon as cathode, and the hybrid device displayed an impressively high capacitance of 980 F g^{-1} at 1 A g^{-1} and 585 F g^{-1} at as high as 20 A g^{-1}. The system also demonstrated good stability of running through a voltage range of 1.6 V, and retained 88% of its capacitance after 10000 cycles.

In conclusion, a lot of attentions have been paid to using ZIFs-based materials to prepare nitrogen-doped porous carbon. However, the carbon obtained from ZIFs tends to be microporous in nature and the lacking of larger pores is disadvantageous for the performance of these materials in many targeted applications such as electrocatalysts and supercapacitors, as the transport of molecules and ions along the narrow microporous passages is expected to be sluggish. Many efforts have been devoted to develop new strategy such as ultrasonic preparation, simultaneous solvent evaporation or etching in an NH_3 environment. However, these methods result in the formation of carbons with pore size in the macropore range. Therefore, novel methods based on carbonisation of ZIFs and graphite oxide (GO) is investigated in this work to achieve uniform sized mesopores. After the high temperature treatment, the porous graphene, converted from GO, provides more pathway for electron transportation and further improve the electron transport rate of ZIF-derived electrode materials. Therefore, in the following section, the recent research developments on synthesis, properties and applications of porous graphene will be reviewed and summarised.

2.2 Porous graphene

2.2.1 Introduction

Since the discovery of graphene in 2004, significant efforts have been made to exploit its application in almost every field of science, including physics, chemistry, materials sciences and life science [8-10]. Graphene is a two dimensional single layered material, which behaves like semi-metals. The applications of graphene in electronics and electrochemistry are restricted due to its zero band gap nature [130]. Graphene can be also used in the field of energy storage and catalyst, while free-standing graphene sheets shows low chemical activity. Therefore, the activation of graphene sheets (*e.g.* for energy storage and catalysis) attracts a lot of attentions recently. For example, porous graphene was explored to increase the effective surface area for energy storage [131-133]. Porous graphene is a 3D structure built by few-layered graphene sheets with few carbon vacancies in 3D plane [131] and it can be micropore (pore diameter < 2 nm), mesopore (2 nm <pore diameter < 50 nm), and macropore (pore diameter > 50 nm), depending on the different fabrication techniques [132-133]. Compared to the original free-standing graphene sheet, porous graphene has unique porous structure combined with the inherent properties of graphene and exhibits outstanding properties of large surface to volume ratio, good biocompatibility, low cytotoxicity and tremendous flexibility [134-135] . Furthermore, porous graphene nanocomposites with unified systems are much more electrically and mechanically stable comparing with other graphene monolayer [136]. For these reasons, porous graphene has been demonstrated with good performances for various applications, including optoelectronics [137-138], sensors [139-140], devices for energy storage [141-142], lithium ion batteries [143-145], fuel cells [145-146] and biological applications [144].

Many techniques/ routes were developed to produce porous graphene such as in-situ reduction assembly techniques [147], template growth [148], non-template growth [149], and other chemical vapour deposition [150]. However, there are still some challenges in the production of porous graphene such as how to achieve structural conductivity and stability of porous graphene, how to control the pore size/shape for different applications and how to produce large scale porous graphene with low cost [151]. Therefore, this section would focus on the recent

research developments on the synthesis and applications of porous graphene, and further to discover its performance in energy storage and catalysis

2.2.2 Synthesis of porous graphene

Porous graphene materials have attracted much attention in recent years due to the unique pore structure. In the following parts, two main synthesis methods are introduced and reviewed, namely, self-assembly methods and chemical vapour depositions methods (templated and non-templated growth approaches). Besides, some other methods producing porous graphene would be discussed as well.

2.2.2.1 Self-assembly methods

Self-assembly of pristine graphene and graphene sheets is an important method to manufacture a variety of graphene nanocomposites for valuable industrial and commercial applications such as nano-sheets grown on substrates and other analogues of graphene. Xu *et al.* [151] formed a self-assembled graphene hydrogel through an expedient hydrothermal technique and the product graphene hydrogel could be used as a good electricity conductor, which exhibits a durable and thermal stability with a good capacitance. Chen *et al.* [152] established another technique to fabricate 3D graphene wrapping nanoparticles into the system. A magnetic graphene/Fe_3O_4 aerogel was synthesised by one-step reduction and followed by mixing GO in Fe_3O_4 nanoparticles. The obtained gel was superparamagnetic, permeable and having large surface to volume ratio of electrochemistry ability. Chen *et al.* [147] successfully fabricated porous graphene architecture *via* a self-assembly of graphene equipped by chemical reduction at 95 °C under the atmospheric pressure without stirring. In addition, Cong *et al.* [153] reported graphene/ Fe_3O_4 hydrogels with robust unified porous networks, can be efficiently induced by Fe (II) ions at different pH values under several circumstances. Liu *et al.* [154] reported a route to prepare large-scale graphene sponges using a speed vacuum concentrator. Depending on the temperature and other parameters, water soluble graphene oxide sheets were designed to create their sponges by using the centrifugal evaporation process. In this way, GO film thickness can be controlled at around 200 nm [154]. Worsley and co-workers [11] found a synthesising method of low density porous graphene sheets which

demonstrates high electrical conductivities and larger surface-to-volume ratios. Functionalised and surface-enhanced designs of porous graphene were extensively examined for the oxides-based nanomaterials and carbon related materials. This method is frequently restricted to multiphase materials, organic and inorganic hybridised materials. Moreover, Wang's group [155] reported a novel approach to build well-ordered metal oxide graphene nanocomposites. This technique can be also used to synthesise free-standing, flexible metal oxide graphene nanocomposite films and electrodes. Figure 2.7 presented the schematic illustrations of the ternary self-assembly approach to ordered metal oxide graphene nanocomposites was reported [155].

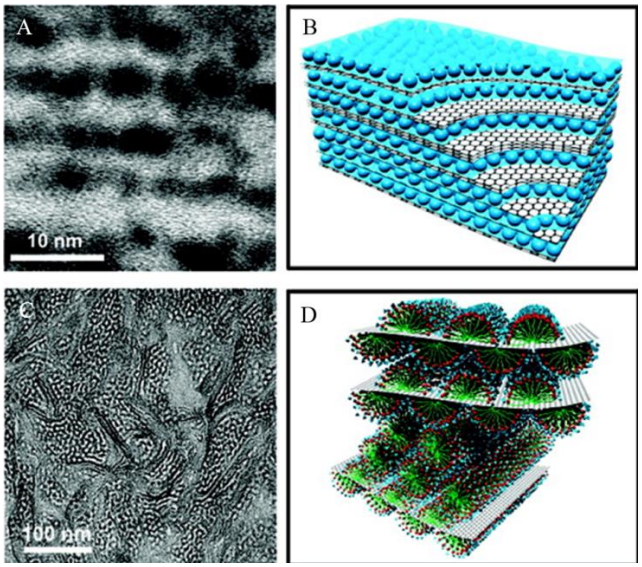

Figure 2. 7 Schematic illustrations of the ternary self-assembly approach to ordered metal oxide graphene nanocomposites. (A) Graphene or graphene stacks, which are used as the substrate instead of graphite. Adsorption of surfactant hemi micelles on the surfaces of the graphene or graphene stacks causes its dispersion in surfactant micelles in an aqueous solution. (B) The self-assembly of anionic sulfonate surfactant on the graphene surface with oppositely charged metal cation species and the transition into the lamella mesophase toward the formation of SnO_2 graphene nanocomposites, where hydrophobic graphenes are sandwiched in the hydrophobic domains of the anionic surfactant. (C) Metal oxide graphene layered nanocomposites composed of alternating layers of metal oxide nanocrystals and graphene/graphene stacks after crystallisation of metal oxide and removal of the surfactant. (D) Self-assembled hexagonal nanostructure of metal oxide precursor with nonionic surfactants on graphene stacks. Reprinted from [155]

2.2.2.2 Chemical vapour depositions (CVDs)

Template-based CVDs and non-template-based CVDs are two typical and significant techniques to fabricate 3D porous graphene. In the following parts, both two approaches will be introduced and discussed.

Template growth method

Cao *et al.* [156] developed a porous graphene network, which was fabricated *via* a facile CVD process with ethanol as the carbon source. The obtained resultant may serve as a useful platform to construct graphene and several metal oxide composites for energy storage applications. Chen's group [150] reported a template-based CVD method for the synthesis of porous graphene foams (GFs) using nickel as templates. Graphene sheets in the GFs are faultlessly consistent into a porous flexible network. The unique network structure, large specific surface area and the electrical and mechanical characteristics of GFs/composites make them particularly useful in several applications including lithium ion batteries and supercapacitors, catalysts and biomedical supports. Therefore, this template-based CVD method is versatile and scalable, and it could be used for the fabricating a broad class of porous graphene structures with different firm shapes and tremendous properties. In addition, Li *et al.* [157] developed fibers based on graphene with porous and monolithic structure fabricated from CVD films. The surface and evaporation behaviour of solvent plays important role in film growth. The obtained graphene fibers demonstrate not only high electrical and thermal properties, but also a uniform pore size distribution. In Wang's research [158], the porous graphene was designed to be grown on the surface of a porous graphene scaffold, which was known as the micro-graphene nanotube. Furthermore, Yoon *et al.* [159] reported a CVD method to fabricate porous graphene composites without using substrates. Throughout the experimentation, mono- and multi-layered graphene was precipitated on the surface of the reduced iron, whose dimension can be efficiently adjusted by familiarising the creation of nano-systems [160]. Significantly, the subsequent porous graphene could be further shifted onto any random substrate for flexible devices.

Non-template growth method

Apart from the template growth method, porous graphene can also be synthesised from non-templated growth methods. Commonly, KOH is the best chemical activation agent in the preparation of porous carbon materials. Ruoff *et al.* [161] synthesised porous graphene with the pore size of micro-pore and meso-pore from the exfoliated graphene oxide. The obtained porous graphene displays a good electrical conductivity and could be considered as the best electrode material for supercapacitor with an ultrahigh energy density. Chen *et al.* [162] synthesised porous graphene by using the precursor (e.g. biomass and polyvinyl alcohol), followed by the KOH activation from the graphene based material. The prepared porous graphene material exhibits an ultrahigh surface area and excellent capacitance with a high energy density. However, the strong KOH reagent used in the industry may cause an environment concern, and therefore, in recent Peng's research [163], carbon dioxide was used to reduce graphene oxide. Throughout the method, strong KOH activation process can be avoided and organic materials were removed from water. On the other hand, a few researchers put their efforts into developing the synthesis method by using HNO_3 oxidation of graphene oxide. Zhao and co-workers [164] reported that the porous graphene was prepared using nitric acid oxidation and ultrasonic vibration of graphene oxide and followed by thermal reduction. The advantage of this method is that the pore size can be controlled by changing the ultrasonic time and the acid concentration. The pores size increased from 7 to 600 nm with the increase of the acid concentration [164]. Additionally, the catalytic oxidation is also a good non-template synthesise growth method in which metal [165] and metal oxide [166] are used to prepare the porous graphene. The pore size can be controlled from 5 nm to tens of nanometres by changing the Ag loading level [165].

Currently, non-templated growth methods for the synthesis of porous graphene is easier compared with templated growth methods. However, it is difficult to control the geometries, pore size distribution and the defects in the porous graphene structures. Therefore, chemical agents or reaction methods need to be optimised to achieve porous graphene with low defects in the further.

2.2.2.3 Other methods

Local strain in graphene sheet could change its electronic and transport properties. In this regard, Li *et al.* [167] reported an accessible strain-engineering technique to yield porous graphene structures. The procedure could be surmounted up to roll graphene by changing laser beam size and scanning speed. Freeze casting is an additional template-free approach for the production of graphene sponge. Xie *et al.* [168] recommended a suitable and comprehensive process to adjust the characteristics of porous graphene. Using this tailored casting process, the pore size and wall thickness of the resulting graphene could be gradually tuned from 10 to 800 nm and 20 to 80 nm, respectively. The corresponding properties of porous graphene were then changed from hydrophilic to hydrophobic and the Young's Modulus varied by 15 times. To combine the excellent properties of both carbon nanotubes (CNTs) and graphene simultaneously, Zhu, *et al.* [169] formulated a sandwich structure using graphene and CNTs through covalent bonds. As shown in Figure 2.8, graphene was grown on a copper foil by decomposing CH_4 or PMMA at 1000 ˚C. Then the iron catalyst and alumina buffer layer were deposited on the graphene in series by electron beam evaporation. During this process, iron catalyst and alumina buffer layer were lifted up and the CNT carpet was grown directly out of the graphene.

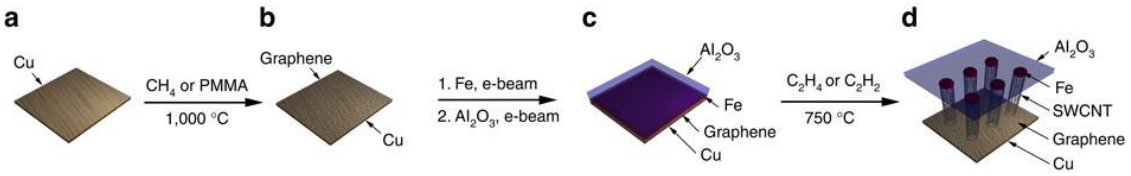

Figure 2. 8 (a) Copper foil substrate. (b) Graphene is formed on the copper foil by chemical vapour deposition (CVD) or solid carbon-source growth. (c) Iron and alumina are deposited on the graphene-covered copper foil by using e-beam evaporation. (d) A CNT carpet is directly grown from graphene surface. The iron catalyst and alumina protective layer are lifted up by the CNT carpet as it grows [169]

Li *et al.* [170] reported a one-step ion-exchange/activation method to construct porous graphene-based materials using a metal ion exchange resin as a carbon precursor at low temperature which resulted in porous graphene-like network structures. In addition, Liu *et al.*, [171] fabricated polyaniline (PANI)- graphene composites by *in situ* chemical oxidative polymerisation. Such kind of

polymerisation could be initiated by amino groups on graphene. The resultant composite showed high capacitance and excellent cycling and thermal stability.

2.2.3 Properties of porous graphene

Owing to the unique pore structure, porous graphene and graphene-based materials exhibits different properties. For instance, the microstructure properties offer large surface-to-volume ratio and porous graphene behaves like semiconducting nanocrystal because of the excellent electronic properties. In addition, doping of porous graphene can also improve the mechanical properties.

2.2.3.1 Microstructure properties

Depending on fabrication routes, porous graphene has various structural features in terms of porosity and size distribution. Recently, two dimensional polyphenylene, a porous graphene with pore size distribution within one atomic range, has been magnificently synthesised [172-173]. The obtained porous graphene can be considered as pure graphene with a crystallinity of hexagonal atomic arrangements. Then, similar results of porous graphene have been also reported [174]. Fischbein *et al.* [175] presented the generation of nanopores into graphene, claiming that thoroughly filled nanopores can be accomplished by utilizing an electron beam of a transmission electron microscope (TEM). Additionally, other groups also demonstrated that the production of pores into graphene sheets is a pronounced idea using TEM [176]. Bieri [172] and co-workers successfully fabricated porous graphene with systematic dispersed holes/pores, which were in two-dimensional polyphenylene and homogeneously distributed with an identical width. Due to the structure of the precursor, the cyclohexa-m-phenylene (CHP) is quite like graphene with phenyl rings periodically missed. Graphene unit cell comprises two carbon atoms while two dimensional polyphenylene contains a supercell with the unit cell linked with a carbon-carbon bonding [173]. The width of pores is determined by the various fabrication routes depending on the functional groups, crystal structures, electron mobility and lateral constraints.

2.2.3.2 Electronic properties

Electronic properties of porous graphene have been studied using density functional theory (DFT) [173, 177] and crystal orbital methods (COM) [178].

Computational results showed that porous graphene behaves like semiconducting nanocrystal with a bandgap which significantly varies with different techniques. The COM gives a wider band gap compared to DFT simulations [173]. DFT ordinarily gives an understanding on the band gap and thus it requires experimental verifications [177]. Porous graphene is particularly attractive owing to the band gap, which could be made open [178-181]. As there are nanopores in the crystalline arrangements of porous graphene, the electronic characteristics need to be optimised. The main restriction of pristine graphene is zero band gap, limiting its applications in optoelectronics [177, 182]. Thus, to have a band gap is the key feature of semiconductor materials and it plays a vital role in electronic configurations and structures [183]. For this reason, many researches carried out a lot of explorations to create a band gap in pristine graphene by several ways, such as surface modifications, doping [184-185], functionalisation [186] through a lateral dimension reduction and the formation of pores [185]. Many simulation and modelling works [187-189] indicated that the band opening in graphene can be induced by introducing holes/ pores into the graphene. The creation of bandgap in graphene could contribute to its variety of applications [187]. By introducing pores into graphene, porous graphene could have a wide bandgap owing to its weird aromatic structure. Different modelling works can provide various band gap values. For example, Brunetto *et al.* [190] demonstrated a band gap value of 3.3 eV using DFT, which is approximately 21% smaller than that reported by Pierre. This is maybe due to the different understanding of band gap values in generalised gradient approximation (GGA) function. On contrary, hydrogen fluoride (HF) were generally verified by experimental values [191]. Du *et al.* [177] gave a bandgap of 3.2 eV for porous graphene with a hybrid functional. Regardless inconsistency of band gap values in these studies, porous graphene has a bandgap owing to the presence of pores. Due to these indicative results, many studies have been carried out for the potential application of porous graphene [177].

2.2.3.3 Mechanical properties

Pure graphene, as discussed before, exhibits several fascinating characteristics and the presence of bandgap in graphene offers excellent mechanical and magnetic properties [187, 192]. Its mechanical characteristics were demonstrated by Lee *et al.* [187], indicating that porous graphene can be used as the strongest

material that exhibits hardening and strengthening features as well as the highest thermal conductivity at room temperature [188-189, 193-194]. Fabricated from pristine graphene, the porous graphene has benefits of excellent properties as well as the pristine graphene performance. As a result, many researches were carried out to investigate the properties of graphene with some functionalisation and conjugations. In addition, these performances need to be controlled through the doping and functionalizing agent. Different characteristics of graphene oxides were studied with various functionalizing agents. For the mechanical properties, doping/functionalisation can improve the tensile strength by adding several functional groups into graphene nanocomposites. A further increase of these functional groups can lead to a decline in tensile strength of GO. This can be caused by some defects in the nanostructure formed due to the aggregation of GO layers. On the other hand, for functionalised GO, the tensile strength is significantly increased when there is no aggregation of GO layers [195]. Extra work is therefore still needed to further explore the mechanism of relative tensile and mechanical properties, magnetic properties, edge structures and valence states.

By far, it has shown several extraordinary properties of porous graphene such as lower mass density [196], large surface to volume ratio [162], and a larger surface capacitance [130]. Consequently, porous graphene has been used in several applications in a variety of fields, including lithium batteries, energy storage [197] and supercapacitors [198], and nano-electronics [197].

2.2.4 Applications

Porous graphene has a variety of applications in the field of physics, chemistry, biosciences, material science and electronics engineering. Owing to its excellent mechanical and electrochemical properties, porous graphene has been found extremely useful in supercapacitors, Li-ion batteries, hydrogen evolution, fuel and solar cells, electrochemical sensors, as well as nano-electronic devices and DNA sequencing.

2.2.4.1 Electrocemical devices

From the last decade, electrochemical devices such as supercapacitors were considered as fascinating candidates in the field of energy storage owing to their long life cycle, high surface to area ratio, mechanical stability and cost

effective features [199-201]. Hence, they have been extensively explored in numerous fields such as nano-electronics devices [201]. Carbon based materials such as pure carbon [202], single-walled and multi-walled carbon nanotubes [202-204], stimulated carbon [205], metallic oxides and metalloids [206-207], could be used as electrode materials of supercapacitors. The capacitance characteristic relies on electrolyte, pore size distribution and conductivity. Qu [204] found those carbons with superior number of pores were more suitable for the supercapacitor applications owing to their high energy storage capacities [204]. In recent years, many research groups considered graphene related materials as promising candidate for capacitors [208-209] due to their large surface-to-volume ratios and other mechanical and electronic features [208]. Many studies have been focused on the practical applications of supercapacitors [210]. Additionally, porous graphene gives a higher capacitance than stimulated graphene due to its pore size, structure and dispersion. These properties make them good electrochemical materials as they have fast electron transfer rates on their surfaces. Zhang *et al.* [210] also reported the same result that the reduced porous graphene has good efficiency in supercapacitors in terms of fast electron transfer rate. They compared reduced porous graphene thin films with porous carbon thin films where porous graphene demonstrated a higher specific surface area of 2400 m^2g^{-1} [210]. Graphene related materials are promising candidates for portable energy devices and electronics vehicles. Especially combined with nanoparticles, it is able to gain ultrahigh specific capacitance depending on the Faradaic response on the electrode surface. Li *et al.* [211] reported a solid-state supercapacitor fabricated by graphene fibers restrained with MnO_2 nanoparticles. It presented an excellent capacitance (42.02 mF cm^{-2}), which was much higher than that of pure graphene fibers (GF) (2.13 mF cm^{-2}) [211]. The device showed an outstanding electrochemical and mechanical stability without sacrificial electron onto the surface for long and short term electrochemical and mechanical cycles. GFs displayed potentials for malleable, bendable and corrosion resistant electronic devices by textile electrodes which were fabricated by joining GF–carbon nanotubes fibers (CNTFs). It has been revealed that the superlative supercapacitor properties have been accomplished through refining electrodes with hierarchical nanostructures and larger porosity owing to the improved accessible surface area of porous graphene.

2.2.4.2 Fuel cells

Graphene related materials are very attractive for their applications on hydrogen evolution, oxygen reduction cathodic catalysis, water purification and filtration due to their fast electron transfer rates which are able to generate high power

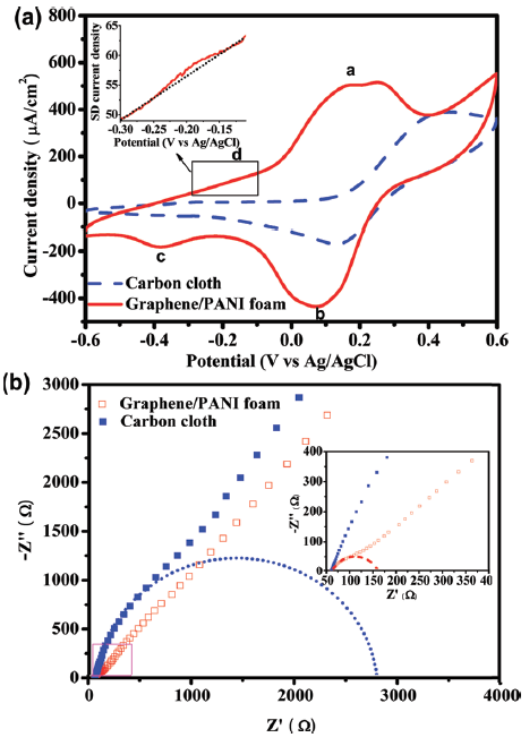

Figure 2. 9 Electrochemical Characterisations of carbon cloth anode and graphene/PANI anode in MFC [205]

electricity. By using electrochemical layer-by-layer (LBL) method, associated RGO/ GO/ PG/ GFs/ GNPs and RGO/ PDDA (polydiallyldimethylammonium chloride) film has been designed for the oxygen reduction reactions catalysis. For example, due to the chemical interaction between the reduced GO and Polydiallyldimethylammonium chloride (PDDA), graphene provides an improved oxygen reduction reaction ability with a blue-shifted potential and current density. In addition, 3D nitrogen-doped graphene/ Fe_3O_4 aerogel has been synthesised by a hydrothermal process and displayed a more positive potential of -0.19 V and higher current density of -2.56 mA cm^{-2} than those of nitrogen doped graphene/ Fe_3O_4 powder (-0.26 V and -1.46 mA cm^{-2}, respectively) [212]. The prepared 3D catalyst displayed a 100 mV negatively-shifted onset potential of -0.6 V and three times higher current density of 183 mA cm^{-2} compared with those of the commercial Pt/C electrode of -0.5 V and 55 mA cm^{-2} [212]. Linear sweep voltammetry, rotating ring-disk electrode and electrochemical impedance

spectroscopy demonstrated that oxidation/ reduction current of graphene hydrogel is superior to the commercialised catalyst, indicating its high stability for oxidation process. In recent years, microbial fuel cell (MFC) has attracted pronounced attentions in the field of renewable energy for converting bacterial metabolised power into electricity. Yong *et al.* [205] reported MFC has distinct effects in green energy foundations to yield electricity with numerous carbon-based substances. Despite of the low microbial stacking volume and little cellular electron transference proficiency amongst microorganisms, anode frequently bounds its applications. Figure 2.9 shows the electrochemical Characterisations of carbon cloth anode and graphene/PANI anode in MFC.

2.2.4.3 Lithium ion batteries

Excellent characteristics of porous graphene also make them fascinating for Li-ion batteries applications where it can be used to accomplish rising loads in the field of current electronic devices (e.g. portable communication devices and mobile electronic devices). Graphene combined with nanoparticles used as electrodes have shown high capacity, long cycling life and high stability in electrochemical applications. For instance, graphene honeycomb film was demonstrated to be an improved batteries enactments with an adjustable bulk (1614 $mAhg^{-1}$) and a flexible maintenance ability (71%) when compared with the traditional graphene film due to its large pore sizes and electrochemical and mechanical compatibility [213]. The graphene paper fabricated by mechanical exfoliating and disintegrating graphene aerogel displays excellent charge capacities of 864 $mAhg^{-1}$ (coulombic efficiency of 79.2%, higher than the other reported work and also enhanced to 97.5% in several cycles) [213], which is better than those demonstrated by other research groups earlier. Additionally, graphene paper showed a good cyclic stability of 99% of the capacitance remaining a high current density of 20 Ag^{-1} after 40000 cycles owing to the folding structure [214]. Such unique structure provide more access to the Li-ion insertion active spots and improve the ability of electrolytes in electrode materials. The sandwiched graphene/ Fe_3O_4 paper indicated a larger definite capacity of 940 $mAhg^{-1}$, compared to pristine Fe_3O_4 (200 $mAhg^{-1}$) and the traditional graphene/ Fe_3O_4 electrode (400 $mAhg^{-1}$), respectively [214]. Three-dimension graphene-based macroscopic assemblies with interconnected networks displayed distinctive pluses in exploring novel lithium-ion battery

electrode materials with improved capabilities. Owing to the large surface area of porous graphene, its assemblies are also favourable for electrochemical applications and speedy Li-ion dispersion.

2.2.4.4 Solar cells

Porous graphene has also been intensively researched in the field of solar cells owing to its cyclic stability, electrochemical performance and other electrical parameters. Joseph and co-workers [215] demonstrated the application of doped/ functionalised graphene sheets onto the counter electrode having oxygen species spots and their activity was excellent, which is comparable to platinum. To reveal the elctrocatalytic performance of functionalised graphene sheets regarding to the fast reduction of triiodide, they proposed an electrochemical impedance spectroscopy corresponding route that matches the experiential spectral parameters to understand their real mechanism. In addition, they have demonstrated that a functionalised graphene sheets based ink can be used as an electrocatalytic and malleable conductive counter electrode. Yen and co-workers [216] fabricated 3D hybrid materials (graphene and acid-treated multi-walled carbon nanotubes) by using a solution-based technique. The absorption of multi-walled carbon nanotubes on graphene sheets shrinks the p–p interface amongst graphene sheets ensuing from steric interruption and limitation. In addition, Li *et al.* [217] reported the synthesis of Schottky joints which is cost effective and low maintenance. It is expected that carbon-based photovoltaic cells may become more practicable than silicon-based cells with their novel fabrication process.

2.2.4.5 Other applications

Graphene is an exceptional and attractive material for biochemical sensors due to the fact that all atoms are exhibited to the environment for the adsorption of molecules and provided an extremely large sensing area [218]. The simplest and mostly applied configurations of graphene based sensors are either chemi-resistors or field effect transistors (FETs). In both cases, the electrical resistance from the interaction between the analyte and graphene was measured using a simple ohmmeter. Additionally, sequencing the human genome in DNA can improve our understanding of physiology, disease, medicine, genetics, and human development. An ideal technique for DNA

sequencing should be simple, fast and cost-effective. Among all techniques, nanopore graphene for DNA sequencing is unique because it is potential to meet above requirements [219]. Hence, membranes used for this are required to be robust, durable, and as thin as possible to differentiate the sign of two contiguous nucleobases.

Pure gases are important for manufacture applications and technical research, and they are usually gained by old-fashioned separation approaches such as distillation and adsorption by using high pressure. In comparison with these techniques, membrane separation has several advantages including low maintenance costs, small capital investments and mechanical stability [220]. Actually, membranes play a vital role in selective gas separation and show a substantial part in gas and chemical purifications. Size-defined pores of the membrane could selectively allow smaller molecules to pass through while blocking the larger molecules [221]. Graphene is a naturally existing excellent starting material for developing membranes with its high mechanical stability and chemical inertness. However, pristine graphene is impermeable to standard gases including helium because of densely packed honeycomb crystal lattice. Therefore, graphene membranes are becoming excellent candidates in gas purifications.

On the other hand, the shortage of water resources is recognised as a present and future threat to human activity and, consequently there is an increasing demand of developing alternative water resources. Desalination is one of the most promising methods to get new drinking water for human use due to the abundance of seawater. In contrast to the classical reverse osmosis (RO) membranes, nanoporous graphene membranes allow water to flow across well-defined channels rapidly. Molecular dynamics studies have shown that nanoporous graphene is a promising material for water desalination [222]. They found the relationship between the desalination dynamics with the size and chemistry of pores and the applied hydrostatic pressure [223]. These calculations proposed that functionalisation of porous graphene with hydroxyl groups is an efficient strategy as the hydroxyl groups can generate a strong energy barrier for Cl^- ions. It was also pointed out that a combination of electrostatic and hydration influences and defines the presentation of a nanoporous graphene membrane for water purification. The theoretical predictions described a

beautiful picture of using nanoporous graphene as a membrane for desalination in the future.

In conclusion, graphene has been a fascinating material to study due to its excellent thermal and mechanical stability, large surface to volume ratio, large surface area, and excellent electrical and mechanical properties. There are a variety of analogues of graphene, such as porous graphene, 3D graphene foam, graphene oxide, graphene quantum dots and others. Porous graphene is a kind of graphene sheet in which some carbon atoms are missing. Therefore, porous graphene exhibits different properties from pristine graphene owing to its unique pore structure. This is the reason that porous graphene is a suitable material for energy storage.

2.3 Summary

In summary, we have reviewed the development and the recent progress of ZIF materials/ZIF derivative materials and porous graphene materials. Thanks to the advantages of high carbon content, rich metal centres, and intrinsic porous nature, ZIFs are a class of versatile crystalline porous materials and their porous structures and tunable compositions provide a platform to prepare ZIF-derived nanomaterials with the desired catalytic active sites and can be used as various electrocatalysts. Duo to the limitation of intrinsic property, graphene-based materials with a high surface area, have been introduced and used as catalytic support to further improve the electrical conductivity and electrochemical stability. Because graphene embedded ZIF-based electrocatalysts are carbon-based nanocomposites derived from heating treatment of ZIFs/GO, further studies would focus on the developing and synthesising of bi-metal or trilateral-metal ZIF derivatives with controllable active sites used for electrocatalysis. The new concepts, new methods and new applications of ZIFs/ZIF derivatives/graphene are expected to be further expanded.

Chapter 3：Experimental methodology

3.1 Raw materials and chemicals

2-Methylimidazole (99%, MIm), $Co(NO_3)_2 \cdot 6H_2O$ (99%), $Ni(NO_3)_2 \cdot 6H_2O$ (99%), $Fe(NO_3)_2 \cdot 9H_2O$ (99%), Argon, Hydrogen sulfide, Graphite power, Concentrated suffuric acid, $KMnO_4$ and 30% H_2O_2. All chemicals were obtained from Sigma-Aldrich.

3.2 Synthesis of ZIF-67 and ZIF-67 based composites

3.2.1 Preparation of ZIF-67

ZIF-67 was synthesised from cobalt nitrate hexahydrate and 2-Methylimidazole (MIm) in water through an established approach. Briefly, 55 g of 2-Methylimidazole was dissolved in 200mL of deionised water; meanwhile, 4.5 g of cobalt nitrate hexahydrate ($Co(NO_3)_2 \cdot 6H_2O$) was also dissolved in 30 mL of deionised water and the two solutions were mixed together under further stirring at room temperature for 24 hrs. The molar ratio of the synthesis mixture is Co^{2+}: MIm: H_2O = 1: 58: 1100. Then the purple product was collected after being filtered and washed with deionised water for several times. Finally, the composites were air-dried in a fume cupboard at room temperature for 48 hrs before being subjected to further characterisations.

3.2.2 Preparation of Ni-substituted ZIF-67

Firstly, Ni-substituted ZIF-67 was solvothermal synthetised using requisite amount (1, 2, and 4 mmol) of nickel nitrate hexahydrate ($Ni(NO_3)_2 \cdot 6H_2O$) together with 4 mmol $Co(NO_3)_2 \cdot 6H_2O$ and 300 mmol 2-Methylimidazole. These chemicals were dissolved in 100 mL deionised water, the whole solution was then stirred continuously at room temperature for 24 hrs. The parental precursors were finally collected after filtration and being washed with 15 mL deionised water for three times, followed by drying at room temperature for 48 hrs. The obtained product was designed as xZIF-67-yNi, where x and y stand for the molar ratio of $n_{(Co)}/n_{(Ni)}$ in the Ni-substituted ZIF-67.

3.2.3 Preparation of Fe-substituted ZIF-67

The bimetallic composites were synthetised from the Fe-substituted ZIF-67 crystals. Typically, Fe-substituted ZIF-67 was solvothermally synthetised using requisite amount (1, 2, 4 and 8 mmol) of iron nitrate nonahydrate ($Fe(NO_3)_2 \cdot 9H_2O$) together with 4 mmol $Co(NO_3)_2 \cdot 6H_2O$ and 300 mmol 2-Methylimidazole. They were then dissolved in 100 mL deionised water, and the whole solution was stirred continuously at room temperature for 24 hrs. The parental composites were collected after being filtered and washed with 15 mL deionised water for three times, followed by drying at room temperature for 48 hours. Finally, the pristine obtained Fe-substituted ZIF-67 parental composite was designed as xZIF-67-yFe, where x and y stand for the molar ratio of $n_{(Co)}/n_{(Fe)}$ in the Fe-substituted ZIF-67.

3.2.4 Preparation of GO/ZIF-67

GO/ZIF-67 composites were synthesised *via* the same method for pristine ZIF-67 with slight modification. Briefly, requisite amount of GO was dispersed in deionised water and sonicated for 1 h, followed by the addition of requisite amount of 2-Methylimidazole under stirring. Then, combine it with $Co(NO_3)_2 \cdot 6H_2O$ solution under further stirring at room temperature for 24 hrs. The molar ratio of synthesis mixture is Co^{2+}: MIm: H_2O = 1: 58: 1100. After filtering and washing with deionised water several times, the purple product was collected. Finally, the composites were air-dried in a fume cupboard at room temperature for 48 hrs.

3.2.5 Preparation of Ni-substituted GO/ZIF-67

First, Ni-substituded GO/ZIF-67 was solvothermally synthetised using requisite amount (1, 2, and 4 mmol) of $Ni(NO_3)_2 \cdot 6H_2O$ together with 4 mmol $Co(NO_3)_2 \cdot 6H_2O$, 300 mmol 2-Methylimidazole and different amount of GO which were prepared *via* a slightly modified Hummers Method. These chemicals were first dissolved in 100 mL deionised water, the whole solution was then stirred continuously at room temperature for 24 hrs. The parental precursors were finally collected after filtering and washing with 15 mL deionised water for three times, followed by drying at room temperature for 48 hrs. The produced composites were named as xZIF-67-yNi-zGO where x, y stands for the molar ratio of Co and Ni in parental precursors and z stands for the weight percentage

of graphene oxide. Therefore, the precursor composite with a molar ratio $n_{(Ni)}/n_{(Co)}$ of 1/4 and a 5% graphene oxide is named as 4ZIF-67-Ni-5GO.

3.2.6 Preparation of Fe-substituted GO/ZIF-67

Fe-substituted GO/ZIF-67 composites were synthetised following the same procedure with Ni-substituted GO/ZIF-67. The obtained composites were named as xZIF-67-yFe-zGO where x, y stands for the molar ratio of Co and Fe in parental precursors and z stands for the weight percentage of graphene oxide. Thus, the precursor composite with a molar ratio $n_{(Co)}/n_{(Fe)}$ of 1/1 and a 5% graphene oxide is named as ZIF-67-Fe-5GO.

3.3 Synthesis of ZIF-67 derivatives

3.3.1 Cobalt/ nanoporous carbon/graphene composites derived from GO/ZIF-67

The composites were prepared by temperature programmed pyrolysis of the ZIF-67 in the Ar atmosphere. 0.3g dried parental composites were loaded into the tube furnace on an alumina boat. The furnace was set to a target temperature (600, 800 or 1000 °C) with a ramp rate of 10 °C/min in Ar atmosphere. After the furnace reaching the target temperature, maintained at the target temperature for one hour, then turned it off while remaining Ar gas on. The product was taken out of the furnace after the furnace was gradually cooled to room temperature. The collected composites were named as Co-zG-T, where z stand for the weight percentage of graphene oxide introduced and T is the target pyrolysis temperature. Therefore, the sample with a 5% graphene obtained at pyrolysis temperature of 800 °C will be named as Co-5G-800. For comparison, pristine parental composites were also carbonised following the same procedure and named as Co-800.

3.3.2 Cobalt, Iron/ nanoporous carbon/ graphene composites derived from Fe-substituted GO/ZIF-67

The air-dried bi-metallic Fe-substituted GO/ZIF-67 precursors were high temperature heat treated directly in the Ar atmosphere. The Fe substituted composites were also carbonised following the same procedure. The produced composites were named as xCo-yFe-zG-T, where x, y stands for the molar ratio of Co and Fe in bi-metallic precursors, z stands for the weight percentage of

graphene oxide introduced and T is the target pyrolysis temperature. Therefore, the sample with a molar ratio $n_{(Co)}/n_{(Fe)}$ of 1:1 and a 5% graphene obtained *via* heat treatment at 800 °C is named as Co-Fe-5G-800. For comparison, pristine parental composites is marked as Co-Fe-800.

3.3.3 Cobalt sulfide/ N, S co-doped nanoporous carbon/graphene composites derived from GO/ZIF-67

The air-dried GO/ZIF67 composites and pristine ZIF-67 were sulfurised directly in the presence of hydrogen sulfide (H_2S) atmosphere. Typically, 0.3g dried parental precursors were loaded into the tube furnace on an alumina boat. The furnace was set to a target temperature with a ramp rate of 10 °C/min in Ar atmosphere. After the furnace reaching the target temperature, H_2S gas flow with flow rate 20 mL/min was introduced to the tube and remained at the target temperature for one hour. The H_2S gas supply was then switched off while the Ar was kept on. After the furnace was gradually cooled down to room temperature, the product was collected from the alumina boat. The obtained product with a 5% graphene *via* heat treatment at 800 °C is labelled as CoS-5G-800 and the sample without graphene is named as CoS-800.

3.3.4 Nickel promoted cobalt sulfide/ N, S co-doped nanoporous carbon/ graphene composites derived from Ni-substituted GO/ZIF-67

The air-dried bi-metallic Ni-substituted GO/ZIF-67 precursors were prepared *via* a one-step direct carbonisation and sulfurisation process in the presence of hydrogen sulfide. Following the same treatment procedure with cobalt sulfide, the bi-metallic product was collected and labelled as xCoS-yNiS-zG-T, where x and y stand for the molar ratio $n_{(Co)}/n_{(Ni)}$ in the parental Ni-substituted GO/ZIF-67, and z stands for the weight percentage of graphene oxide introduced and T stand for the sulfurisation and carbonisation temperature. Therefore, the 5% graphene contained sample obtained at 800 °C with molar ratio $n_{(Ni)}/n_{(Co)}$=1/4 was labelled as 4CoS-NiS-5G-800.

3.3.5 Iron promoted cobalt sulfide/ N, S co-doped nanoporous carbon/ graphene composites derived from Fe-substituted GO/ZIF-67

The bi-metallic porous nanocomposites were carbonised and sulfurised directly in the presence of hydrogen sulfide atmosphere. The whole procedure is the same as the preparation of nickel promoted cobalt sulfide. After the treatment,

the obtained product was labelled as xCoS-yFeS-zG-T, where x and y stand for the molar ratio $n_{(Co)}/n_{(Fe)}$ in the parental Fe-substituted GO/ZIF-67, and z stands for the weight percentage of graphene oxide introduced and T stand for the sulfurisation and carbonisation temperature. Thus, the 5% graphene contained sample obtained at 800 °C with molar ratio $n_{(Fe)}/n_{(Co)}$=1/2 was labelled as 2CoS-FeS-5G-800.

3.3.6 Iron promoted cobalt oxide/ N doped nanoporous carbon/ graphene composites derived from Fe-substituted GO/ZIF-67

Typically, 0.3 g produced Co-Fe-zG-800 series samples were loaded into an alumina boat and sat at the centre of a tube furnace in the presence of air flowing through the tube. The temperature of furnace was set to 350 °C with a ramp rate of 10 °C/min. After reaching the target temperature, the furnace was kept at this temperature for one hour, then turned off. After the oxidation, the composites were named as CoO-FeO-zG-350, where z stand for the weight percentage of graphene oxides in the initial precursor.

3.4 General Characterisation techniques

In order to gain the crystalline phase structures, morphologies, interface features and elemental and chemical valence status of ZIFs and ZIF derivatives composites, a series of complementary characterisation techniques, including X-Ray diffraction (XRD), X-ray photoelectron spectroscopy (XPS), Scanning electron microscopy (SEM), transmission electron microscopy (TEM), energy dispersive X-ray analysis (EDX), Fourier transform infrared spectroscopy (FTIR) and Raman spectroscopy have been utilised. In addition, the textural properties of nanoporous composites were measured by Brunauer-Emmett-Teller method (BET) and thermophysical characterisation of the materials was carried out by thermogravimetric analysis (TGA) coupled with Mass Spectrometry (MS).

3.4.1 Powder X-ray Diffraction (XRD)

XRD technique is a method used to identify the crystallographic structure and crystallite size of the materials. X-rays can produce constructive interference upon reflection of atomic planes within the crystalline materials. A crystal is a regular arrangement of atoms. When the X-rays (Kα produced by electron beams on a metal source) fall on a crystal, the beam propagates in many distinct directions depending on the crystal structure. The atoms scatter (diffract)

part of the beam and form secondary spherical waves. A three-dimensional image of the electron density in the crystal can be obtained by measuring angles and intensities of the diffracted rays. During this diffraction, a regular atomic array can produce a regular array of spherical waves. The relationship between the incident and reflected X-rays can be expressed by Bragg's formula:

$$n\lambda = 2d\sin\theta \qquad (3.1)$$

where n is any positive integer, λ is the wavelength of X-ray, d is the inter-lattice spacing, and θ the incident angle of the X-rays.

Crystalline size can be assessed by measuring the peak breadth in an X-ray diffraction pattern, which can be explained by Debye-Scherrer equation:

$$t = K\lambda / B\cos\theta \qquad (3.2)$$

where t is the crystallite size and K is the crystalline shape factor, λ is the wavelength of incident X-rays, B is the breath of the peak at half maximum intensity of a specific plane (hkl) in radians.

In this thesis, all the XRD patterns were obtained using a Bruker D8 Advanced X-ray diffractometer. XRD patterns were recorded with Cu Kα radiation (40 kV-40 mA) at step time of 1 s and step size of 0.02°.

3.4.2 Scanning Electron Microscopy (SEM) and Energy-Dispersive X-ray Spectroscopy (EDS)

Scanning Electron Microscopy (SEM) is a powerful tool to characterize the surface morphology under high magnification. During SEM analysis, many types of electrons are generated when a focused electron beam scans the surface of the sample. The backscattered electrons are the electrons reflected from the sample after multiple collisions, including elastic and inelastic backscattered electrons. Secondary electrons are released from the sample by the action of the incident electrons. X-rays may also be emitted due to the transitions between the internal energy levels in the atoms of the sample. During this transition process, the generated energy can also excite other electrons, resulting in the release of secondary electrons, which is called Auger electrons. Among these electrons, the secondary electrons and backscattered electrons are generally used to produce SEM images. The number of secondary electrons depends on the angle of incidence of the electron beam

and on the surface structure of the sample. Then, the secondary electrons are collected by a detector and synchronised with the electronic beam position information to construct an image. Images obtained with backscattered electrons show a three-dimensional structure and reflect the surface structure of the sample. Secondary electrons are therefore used more frequently in SEM imaging. In contrast, the backscattered electrons are less sensitive to surface topography, but can be used to image variations in surface chemistry in the sample.

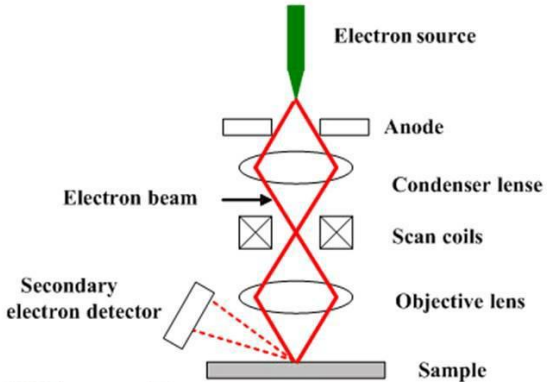

Figure 3. 1 Schematic demonstration of SEM [224]

In order to verify the exact elemental feature of a phase accurately, Energy-dispersive X-ray spectroscopy (EDS) were used to analyse the X-rays produced from the interactions between the accelerated electrons and the target sample surface. X-ray spectra with element-specific emission lines was emitted from absorbed incoming electrons of sample atoms. Normally, the X-ray generated from the top 2 μm of a sample, may reach the detector. Either single spectra from specific spots or EDX maps representing spatial distributions of chemical elements can be acquired.

In our work, SEM images were taken by a Toshiba JSM-6390LV machine in a high vacuum mode. In experiments, a small amount of powder were dropped on one side of carbon double-sided sticky tape. Then, samples were coated by Au to enhance the surface conductivity. Typically, the thin coating layer is 10 nm.

3.4.3 Transmission Electron Microscopy (TEM)

TEM (shown in Figure 3.2) works on the same principles as optical microscope, but uses electrons instead of light as source of illumination. Electrons are scattered when an electron beam passes through a thin sample. A

sophisticated system of electromagnetic lenses focuses the scattered electrons into an image or a diffraction pattern. The electrons beam emitted from the electron gun is focused by condenser lens into a tiny, thin, and coherent one. This beam is restricted by the condenser aperture, which excludes high angle electrons. Then, the beam strikes the specimen and parts of it are transmitted depending upon the thickness and electron transparency of the specimen. This transmitted portion is focused by the objective lens into an image on phosphor screen or charge coupled device camera. The image then passed down the column through the intermediate and projector lenses, is enlarged all the way. Selective Area Electron Diffraction (SEAD) has been used to identify crystal structural, crystal orientation of the samples.

In this work, a JEM2100, TEM (LaB6, 200 kV) was used to characterise the crystallinity of the composites. Typically, a tiny amount of powder sample were dispersed in 20 mL deionised water and carried out sonication for 30 minutes. Then, a drop of solution dispersed on the copper-supported carbon film.

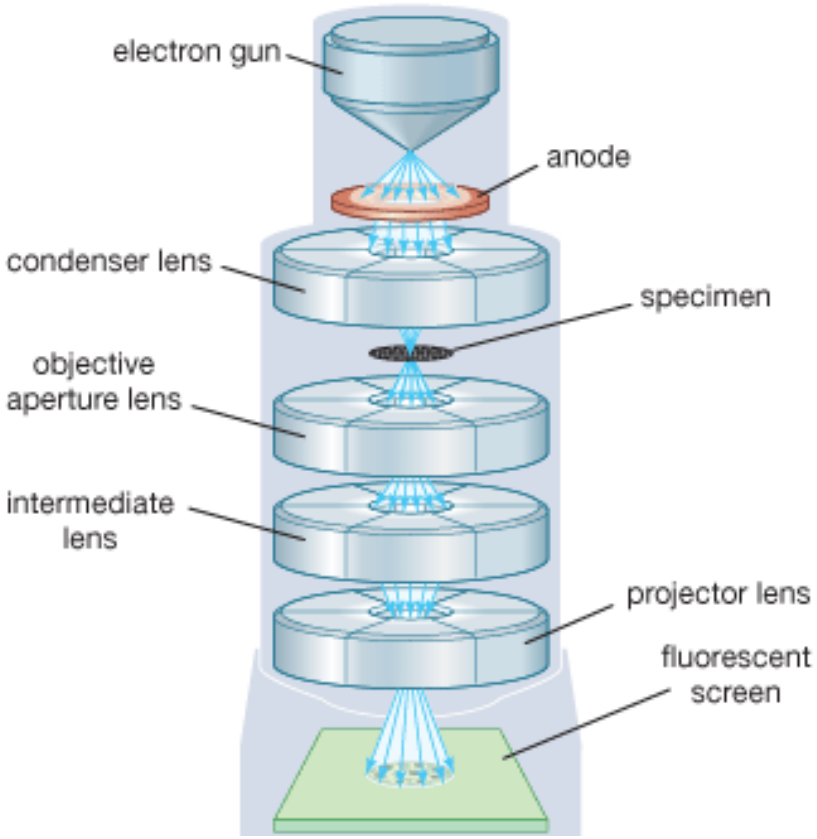

Figure 3. 2 Schematic diagram of the basic components of TEM [225]

3.4.4 X-ray Photoelectron Spectroscopy (XPS)

XPS is a sensitive quantitative technique used for measuring the elemental composition of the surface of a material, and it also can be used to determine the binding states of the elements. In an XPS, X-rays (typically Al Kα or Mg Kα) are incident on a surface in vacuum. An incident photon could come into collision with a core electron with its energy simultaneously transferred. The electron, now possess higher energy than its orbital, would emit from its original state with a kinetic energy (apparently dependent on both the incident photon and its binding energy). The emitted photoelectrons are then subjected to energy and intensity analysis to identify all the elements present, and their corresponding concentration. Typical XPS penetration is less than 10 nm, meaning all obtained information only reflect elemental composition within this depth. In this thesis, all XPS spectra were analysed with an exciting source of Al Ka, at Harwell XPS centre, Cardiff University. All samples were powder and a tiny amount of each sample were prepared. For the results analysis, Casa XPS software was carried out and a binding energy of C1s at 284.6 eV was used to calibrate all the XPS results.

3.4.5 Fourier Transform Infrared Spectroscopy (FTIR)

FTIR is a powerful spectroscopy used to obtain infrared spectra of absorption, emission, photoconductivity of a solid, liquid or gas. When IR (infra-red) radiation are incident through a sample of finite thickness, not all of the radiation are transmitted because a certain part of it are absorbed. The absorption/ transmittance spectrum is characteristic to the sample, and shows the unique molecular finger-print of the sample's material as well. Normally FTIR measurement can spread through the whole infrared frequency range. Subsequently, a spectrum analysis can be performed (mostly with the assistance of corresponding software nowadays) to deduce the wanted information of the sample.

3.4.6 Thermogravimetric Analysis (TGA)

In order to investigate thermophysical properties of materials, TGA and differential thermal analyses (DTA) are powerful methods designed to measure physical and chemical property changes of the material. TGA reflects the changes in weight of the sample as a function of increasing temperature. The

DTA shows the heat difference in temperature between the actual sample and the reference sample. In this thesis, all TGA measurements were carried out on a TA SDT Q600 instrument in a continuous air flow of 100 mL/min at a heating rate of 10 °C/min.

3.4.7 Mass Spectrometry (MS)

Mass spectrometry (MS) is an efficient tool to perform molecular compositional analysis to a substance, by taking advantage of the fact that mass-to-charge-ratio are characteristic for most elements. To start an MS analysis, a small portion of an unknown chemical is ionised (by one of the various ionisation techniques, for example, heating). The produced ions are then extracted and pulled to go through a mass analyser and finally received by a detector. The ions are sorted and measured according to their mass-to-charge-ratios during the process, to produce a comprehensive compositional result. In our study, a Hiden QGA gas analysis MS (coupled with a TA SDT Q600 instrument) to determine the compositions of exhaust emission.

3.4.8 Raman Spectroscopy

Raman spectroscopy is a powerful technique used to characterise crystalline molecular vibration on the basis of analysing information obtained from Raman scattering process. As shown in Figure 3.3, for a molecule or crystal, when excited with light, most photons are elastically scattered, which means energy are preserved during the scattering event. Consequently, the incident wavelength remains unchanged, and such process is called Rayleigh scattering. However, for a small fraction of scattering (approximately 1 in 107 photons), the scattered electrons possess frequencies different from (and usually lower) than the incident frequency. This inelastic scattering process is defined as Raman scattering. After a Raman scattering event happens, a molecule would be in either a different rotational or vibrational energy. Therefore, certain amounts of different “energy-shifted” scattered light can be detected by the spectroscope, and further plotted against frequency to generate the Raman spectrum of a sample with plural peaks at their characteristic frequency/wave number. These peaks represent different Raman scattering processes, which create or annihilate phonons of different momentum. The positions, widths and shapes of these peaks deliver plenty of information from the crystalline structure, which

are extremely useful for sample identification and quantification. In addition, Raman spectroscopy is particularly useful to investigate carbonaceous material. In general, all carbon crystalline allotropes display two feature peaks in their Raman spectrum: the G peak and the D peak. The G peak appears at around 1590 cm^{-1} indicates a certain amount of nanocrystalline carbon and a high percentage of sp^2 bonds due to graphitisation, while D peak at 1340cm^{-1} is related to sp^3 hybridisation and represents less disordered carbon.

The Raman instrument used throughout the work of this thesis is Renishaw RM1000 Raman microscope (Wooton-under-egde, UK), equipped with a 1200-line/mm grating providing a spectral resolution of 1 cm^{-1}, a diode laser providing excitation at 532 nm/ 785 nm with up to power 300 mW, and a 40X magnification objective lens. Powder samples were spread flatly onto a Si wafer surface, then placed under the microscope. The system was normally calibrated with the silicon peak of 520 cm^{-1}. The instrument is normally set at backscattering arrangement, 532 nm excitation wavelength under 6 mW power. Data were recorded with Renishaw v.1.2 WiRe software.

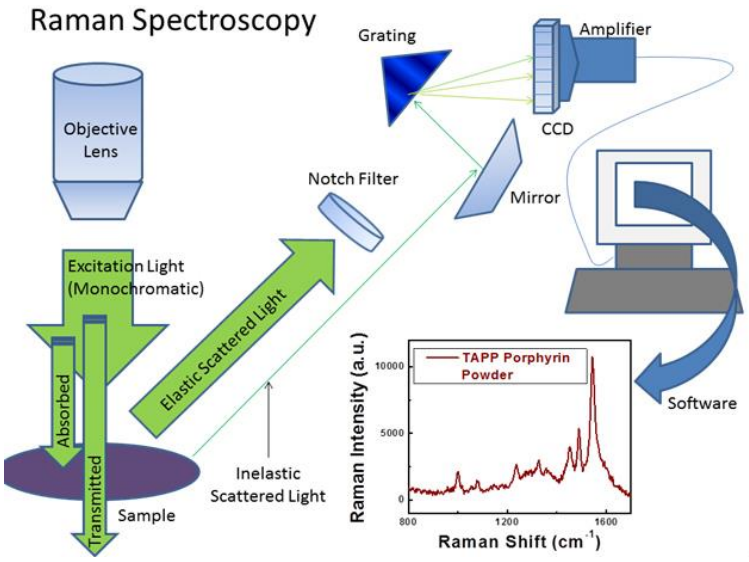

Figure 3. 3 Scheme for Raman spectroscopy [226]

3.4.9 Brunauer-Emmett-Teller method (BET)

BET equation is used for determining the physical adsorption of gas molecules on a solid surface by calculating the amount of adsorbate gas corresponding to a monomolecular layer on the surface, which serves as the basis of an important analysis technique for the measurement of the specific surface area

of materials, especially for porous materials. Physical adsorption results from relatively weak forces (van der Waals forces) between the adsorbate gas molecules and the adsorbent surface area of the test powder. The determination is usually carried out at the temperature of liquid nitrogen. The amount of gas adsorbed can be measured by a volumetric or continuous flow procedure. In this study, a Quantachrome Autosorb-iQ instrument was used to obtain N_2 gas sorption isotherms and textural properties. Since graphene or graphene oxide samples always contain absorbed water from ambient environment, all samples must be evacuated at 110°C for over 6 hrs to remove moisture before analysis. The analysis starts with admitting a small amount of sample powder into a cleaned tube and then have the stopper inserted. Followed by calculating the weight of the sample and then attaching the sample tube to the volumetric apparatus. Raise a Dewar vessel containing liquid nitrogen at -196°C up to a predefined point marked on the sample cell. Admit a certain volume of adsorbate gas to produce the lowest sufficient relative pressure. The surface area is calculated with the BET method, based on adsorption data in the partial pressure (P/Po) range of 0.02-0.22. The total pore volume can be calculated based on the amount of nitrogen adsorbed at P/Po of ca. 0.99.

3.5 Elctrocatalytic measurements

A three-electrode electrochemical cell was used to carry out electrocatalytic performance analysis of the catalysts including cyclic voltammograms (CV), linear sweep voltammograms (LSV) and chronoamperometry. The cell was at the same time connected to a computer which controls potentiostat CHI 660D coupling with a rotating disk electrode (RDE) system. The diagram of this electrochemical set up is shown in Figure 3.4. A platinum wire and a saturated calomel electrode (SCE) were used as the counter electrode and the reference electrode, respectively (Figure 3.5). On the other hand, the working electrode is made up of a 3 mm-diameter bare glassy carbon electrode (GCE) or modified GCE with the material to be studied. The GCE must be polished before experiment, which is performed by dropping 0.05 µm alumina on chamois leather and subsequently polishing the GCE for 15 min until a mirror-like surface shows up. The polished GCE should then be washed with ethanol and distilled water by sonication for 5 min, followed with natural drying process.

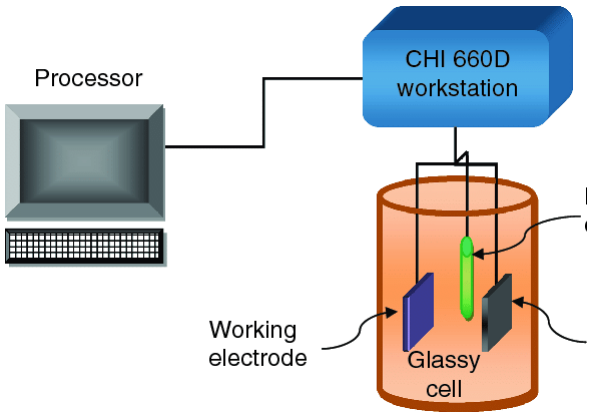

Figure 3. 4 Schematic diagram of the electrochemical set up [227]

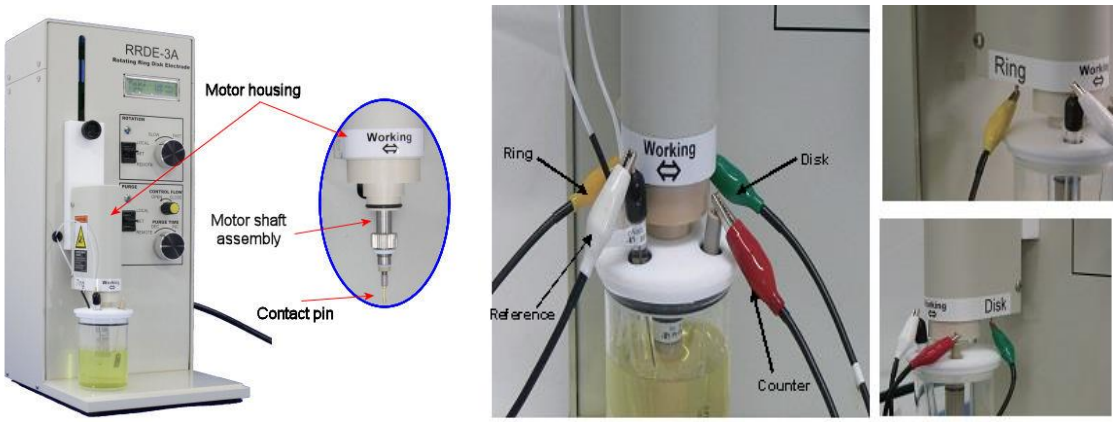

Figure 3. 5 Pictures of rotating disk electrode system. ©*Copyright by ALS Co., Ltd*

Moreover, if a modified GCE is desired, then a 5 µL aliquot of the catalyst ink should be casted onto the freshly polished surface of the newly prepared GCE and left to be dried to form a uniform thin film. The catalyst ink was obtained by ultrasonically dispersing 1mg of the catalyst into 0.5 mL 0.05 wt% of alcohol Nafion solution. The loaded amount of each catalyst can be kept as 141.5 µg cm^{-2} by applying this method. For oxygen reduction reaction (ORR), the electron process of ORR is different for different materials. Hence, the reaction can be written in:

Alkaline media:

$$O_2+2H_2O+4e^- \rightarrow 4OH^- \text{ (Four-electron process)} \quad (3.3)$$

$$O_2+H_2O+2e^- \rightarrow HO_2^-+OH^- \text{ (Two-electron process)} \quad (3.4)$$

$$H_2O+HO_2^-+2e^- \rightarrow 3OH^- \quad (3.5)$$

Acid media:

$$O_2+4H^++4e^- \rightarrow 2H_2O \text{ (Four-electron process)} \quad (3.6)$$

$$O_2+2H^++2e^- \rightarrow H_2O_2 \text{ (Two-electron process)} \quad (3.7)$$

$$H_2O_2+2H^++2e^- \rightarrow 2H_2O \quad (3.8)$$

For oxygen evolution reaction (OER), the experiments were carried out at room temperature in 1 M KOH and 0.5 M H_2SO_4 solution, the reaction can be written in:

Alkaline media:

$$4OH^- \rightarrow O_2+2H_2O+4e^- \quad (3.9)$$

Acid media:

$$2H_2O \rightarrow O_2+ 4H^++4e^- \quad (3.10)$$

For hydrogen evolution reaction (HER), The HER performance were evaluated using a three-electrode system in 0.5 M H_2SO_4 electrolyte and a commercial Pt/C (20 wt% Pt on carbon black) was examined as a reference. The reaction can be shown as:

$$2H_2O++2e^- \rightarrow H_2+2OH^- \quad (3.11)$$

The electrode potential reported in this thesis is relative to the reversible hydrogen electrode (RHE) potential, which can be converted by using Nernst equation:

$$E_{RHE} = E_{Ag/AgCl} + 0.059*pH + 0.197 \quad (3.12)$$

The *K-L* equations are shown as:

$$1/J = 1/J_K+1/B\omega^{1/2} \quad (3.13)$$

$$B = 0.62nFC_0D_0^{2/3}\upsilon^{-1/6} \quad (3.14)$$

Where J is current density, J_K is the kinetic current density, ω is the angular velocity of the rotating electrode, B is the Levich constant, n is the overall number of electron transferred in the ORR process, F is the Faraday constant, C_0 is the bulk concentration of O_2 (1.2×10^{-6} mol cm^{-3}), D_0 is the diffusion coefficient of O_2 (1.9×10^{-5} cm^2 s^{-1}) and υ is the kinematic viscosity of the electrolyte.

The peroxide percentage and electron transfer number can be analysed as following:

$$H_2O_2(\%) = 200 \times \frac{\frac{Ir}{N}}{Id+\frac{Ir}{N}} \quad (3.15)$$

$$n = 4 \times \frac{Id}{Id+\frac{Ir}{N}} \quad (3.16)$$

Where I_r is ring current, I_d is disk current and N is the current collection efficiency of the Pt ring.

Tafel plot, can be drawn representing the relationship between the overpotential and the logarithmic current density.Generally, the potential (η) is logarithmically related to the current density (i) and the linear portion of the Tafel plot is fit to the Tafel equation:

$$\eta = a \pm b\ log i \quad (3.17)$$

Where b is the Tafel slope.

Chapter 4: Bi-metallic cobalt and nickel sulfides/ N, S co-doped porous carbon/ graphene composites and their electrocatalytic applications

4.1 Introduction

Increasing demand for sustainable energy has stimulated intense research on energy conversion and storage systems that are highly efficient, low cost, and environmentally friendly [228-229]. Currently, ORR is the ubiquitous cathode reaction in fuel cells, and Pt are the most active ORR catalysts [230-231]. On the other hand, OER and HER on an anode lies at the heart of electrochemical water splitting and metal-air batteries, and Ir/Ru oxides are the best OER/HER catalysts [232-233]. However, either Pt or Ir/Ru oxides are among the rarest elements on earth, and thus hinder their large-scale application. Therefore, development of highly-efficient, non-precious metal catalysts with multifunctional catalytic activities in the same electrolyte is highly required for energy applications such as full water splitting to generate O_2 and H_2 [234-236].

Recently, cobalt active species contained carbon materials with heteroatom (*e.g.* N, S, P) doping/co-doping have demonstrated outstanding multifunctional catalytic activities of ORR/OER/HER [235, 237-239]. Tremendous synthesis methods have been developed to fabricate carbon-based electrocatalysts with cobalt active species. Among them, ZIFs as precursor materials is a facile and effective method to fabricate high performance carbon-based electrocatalysts. Since ZIF contains rich N content and transition metal species on the framework, carbonisation of ZIFs can lead to N doped on porous carbon materials with exposed homogenous metal species on the surface [238]. From our previous work, we successfully synthesised atomically homogeneous dispersed cobalt sulfide/N, S co-doped porous carbon nanocomposites by a facile one-step sulfurisation and carbonisation of ZIF-67 simultaneously [238].

For ORR/OER/HER, graphene-based materials have been widely used as catalytic support. However, the efficient attachment of catalytic active species with a uniform distribution remains a big challenge for graphene-based materials. In this respect, a composite of ZIF derivatives and graphene could

offer excellent charge mobility, high surface area and highly dispersed metal species for ORR/OER/HER. Moreover, the carbonisation of ZIFs and GO mixtures can lead to porous and N-doped carbon materials as well as N-doped graphene with improved electrical conductivity and active sites.

Additionally, the low electrical conductivities of cobalt sulfide together with its complicated preparation procedures usually lead to unsatisfactory catalytic durability. In order to accelerate all the reactions simultaneously, recent findings revealed that compounds like bi-metallic sulfides showed bi-functionality and thus be able to accelerate OER and HER at the same time [240-241]. Nickel (Ni), as another low-cost and abundant resource in nature, can be readily introduced to CoS. Since Ni and Co sulfides can form a unique structure in which Co ions occupy octahedral and tetrahedral sites while Ni ions partially distribute and replace Co ions at the octaherdral sites [242-243], the resulting binary metallic sulfides offer much richer redox chemistry which can result in a higher efficiency.

In the first part of this chapter, a simple method for the preparation of the cobalt sulfide embedded in N, S co-doped porous carbon and graphene from the simultaneously sulfurisation and carbonisation of GO/ZIF-67 has been presented. Various techniques were used to investigate the influence of the chemical and physical properties of CoS-G-800 after the introduction of graphene. Compared to the composite without graphene, this work demonstrates that the prepared composite showed improved ORR/OER/HER activities and superior ORR durability and good methanol tolerance in alkaline media. In the second part of this chapter, a simple method for the preparation of Co-Ni sulfide nanoparticles embedded in N, S co-doped porous carbon and graphene *via* the simultaneously sulfurisation and carbonisation of Ni-substituted ZIF-67 and graphene oxide (GO) in hydrogen sulfide atmosphere has been developed. Since Ni-substituted ZIF-67 is rich in Ni-N and Co-N moieties, it could be used as excellent precursor for the preparation of Co-Ni sulfides. Remarkably, the resultant nanocomposite 4CoS-NiS-5G-800 not only exhibits the best OER catalytic activities with lowest onset/over potential, but also shows good HER activities with high current density and low onset potential in water splitting

4.2 Characterisations of cobalt sulfides/ N, S co-doped porous carbon/ graphene composites

Generally, all the composites were composed of numerous cobalt sulfides nanoparticles in irregular shape with very small size, as shown in Figure 4.1a & c. No single CoS particle can be easily found and most CoS particles were well embedded in composite and surrounded with carbon. It should be noted that the graphene could be served as a bridge between cobalt sulfide contained porous carbon materials. Moreover, high resolution TEM images exhibited some pore channels that were visible at the edge of composite, maybe due to the presence of porous carbon. The lattice for CoS nanocrystals can also be seen in the dark area from the Figure 4.1d. The selected area electron diffraction (SAED) patterns, shown in inset of Figure 4.1a & c, clearly suggest that the bright scattered dots contributed from the crystalline cobalt sulfide nanoparticles while the dimmed diffraction rings were from the amorphous porous carbon matrix.

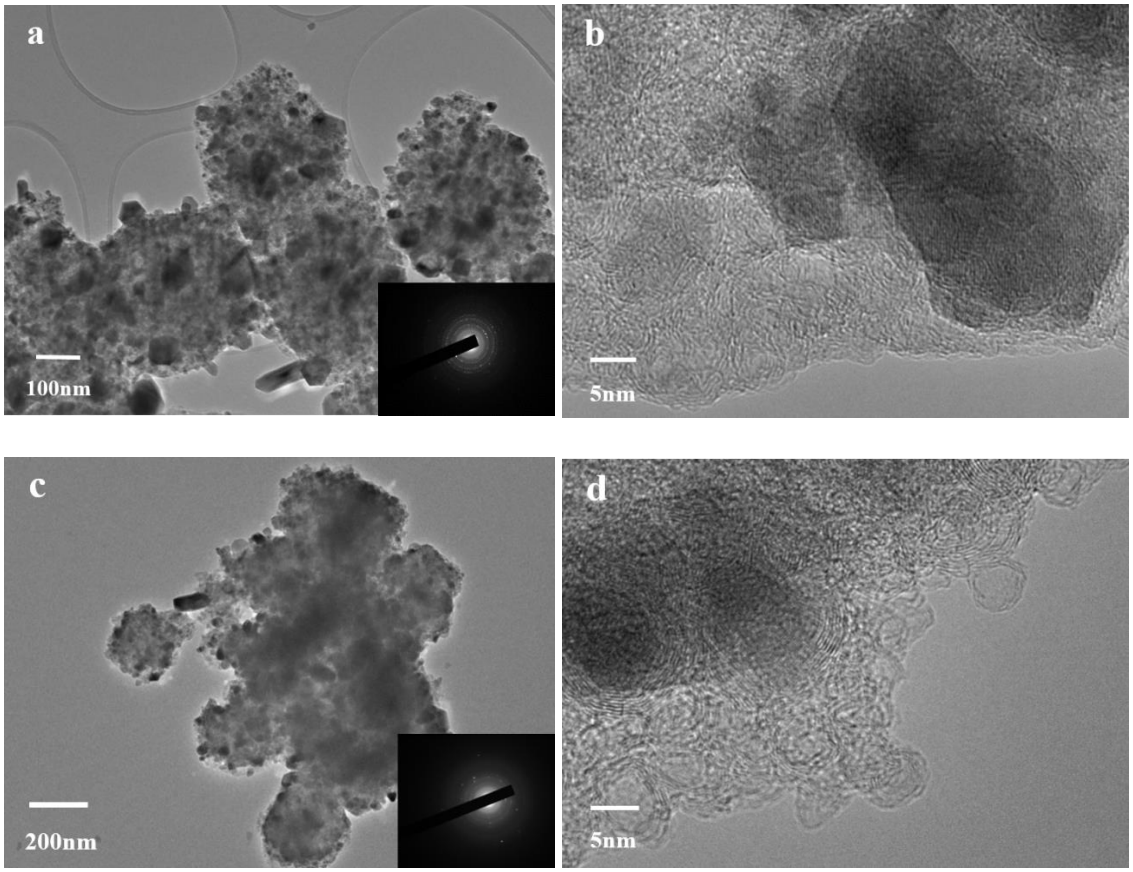

Figure 4. 1 TEM images of (a and b) CoS-800, (c and d) CoS-G-800, Inset in (a and c) is SAED patterns for corresponding sample

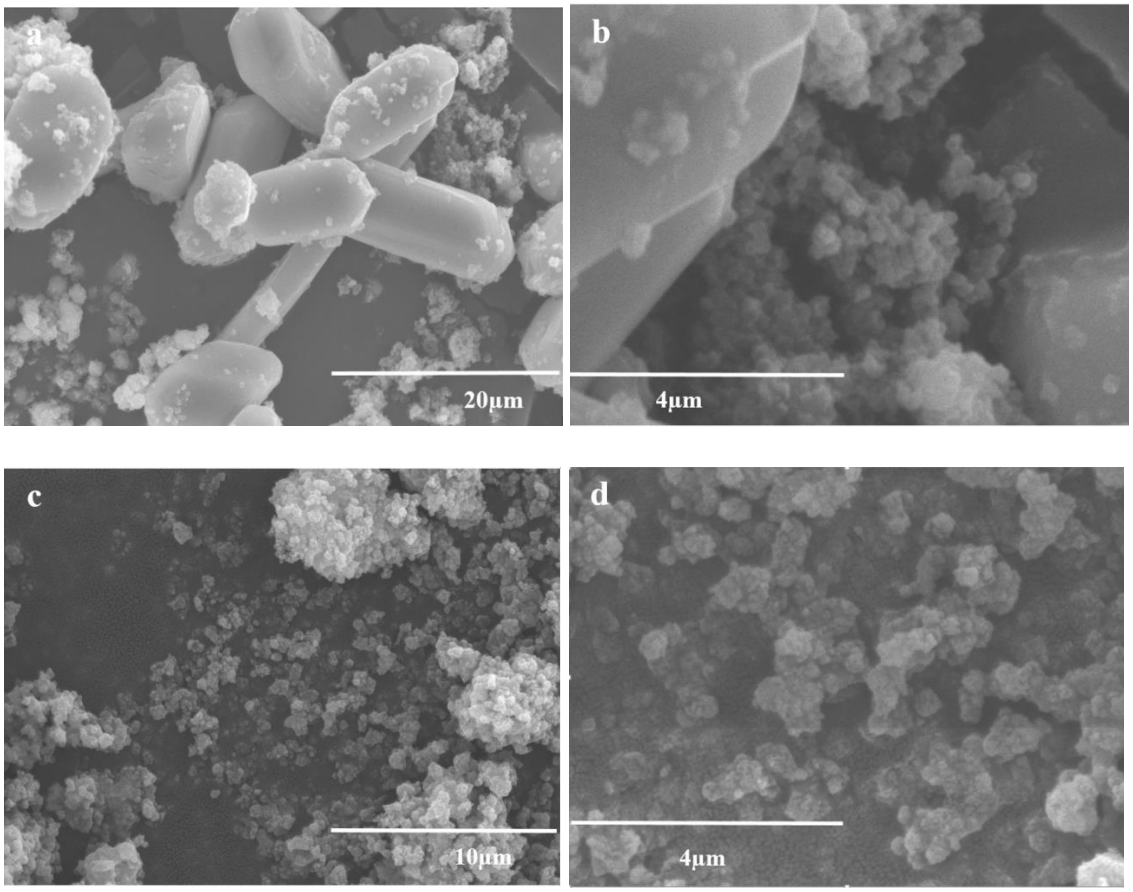

Figure 4. 2 SEM images of (a and b) CoS-800, (c and d) CoS-G-800

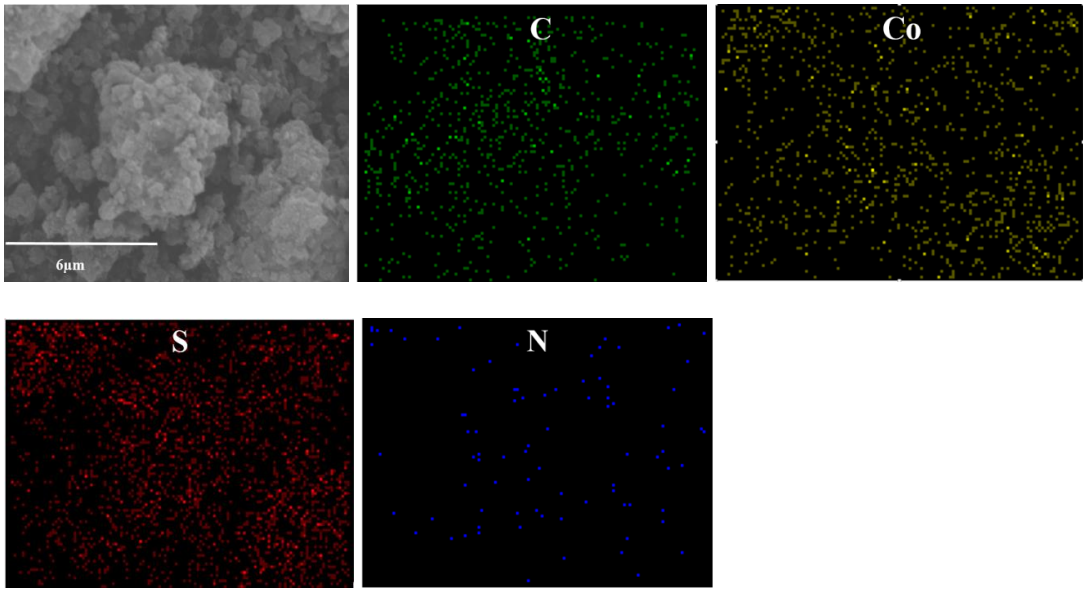

Figure 4. 3 SEM images and element mapping for sample CoS-G-800

The low/high magnification SEM images of CoS-800 and CoS-G-800 are shown in Figure 4.2a-d. Both of their particles were nanocrystal with polyhedral shape, with average size of CoS particle of 0.2 µm. In order to investigate the distribution of CoS particles in the nanocomposites, CoS-G-800 was measured by elemental mapping. As shown in Figure 4.3, all elements C, Co, S and N

exhibited similar mapping patterns in the selected area, which implies that uniform dispersion in CoS-800 and CoS-G-800 particles were homogeneous. Moreover, small amount of N element were detected, further indicating N-doped carbon matrix were contained in both samples.

XRD results of the *in-situ* synthesised pristine ZIF-67, GO/ZIF-67 and GO composites are all showed in Figure 4.4a. Obviously, GO showed a characteristic strong peak at 2θ of 10.5°, which is corresponding to the average interlayer spacing of 8.4 Å. XRD result of pristine ZIF-67 exhibited some strong peaks at 10.2°, 12.5°, 14.5°, 16.4°, 18°, 24.5°, 25.8°, 26.9°, corresponding to (002), (112), (022), (013), (222), (223), (224) and (134) planes, respectively, which implies the formation of pure sodalite (SOD)-type crystal structures [244]. However, the *in-situ* synthesised GO/ZIF-67 composite showed similar XRD peaks from pristine ZIF-67, which indicates that the introduction of GO into the synthesis gel did not damage the inherent crystalline structure of ZIF-67 and there was no GO peaks can be observed, maybe due to the overlapping the XRD peaks of GO with ZIF-67. XRD results of CoS-800 and CoS-G-800 are presented in Figure 4.4b. As shown, both samples exhibited a wide inter-plane (002) diffraction peak at around 25°, can be attributed to carbon or graphene [245-246]. Moreover, the XRD spectrum of both composites indicated that they mainly contain $Co_{1-x}S$ (ICDD PDF# 42-0826) with the hexagonal structure in P63/mmc space group (no. 194) [238]. Also, CoS-G-800 exhibited more intense and sharper XRD peaks than CoS-800, which implies a better growth of crystallite and crystallinity improvement of cobalt sulphite.

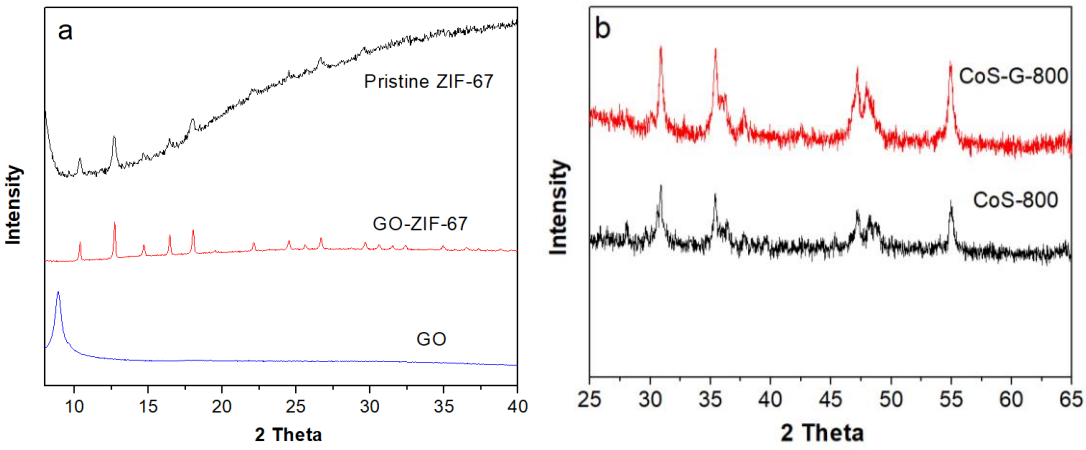

Figure 4. 4 XRD patterns of (a) as-synthesised pristine ZIF-67, GO/ZIF-67 and GO (b) CoS-G-800 and CoS-800 composites

The FTIR spectra of CoS-800 and CoS-G-800 are displayed in Figure 4.5a. Both samples exhibited weak peak at 1610 cm^{-1}, assigning to the C=C stretching vibration [247]. A strong peak around 1100 cm^{-1} and a few weak peaks at 700 cm^{-1} were related to the C=S stretch and C-S stretch, respectively. [247-248] Two peaks were found at 1625 and 1080 cm^{-1}, which is an indication of adsorbed and sulphated water in the composites. In addition, two small peaks at around 610 and 760 cm^{-1} came from Co-S bond vibration in the cobalt sulfide nanoparticles, confirming that both composites indeed contain $Co_{1-x}S$ nanocrystals and carbon/graphene species [247]. The C=S peak of CoS-G-800 shifted to higher wavenumber than CoS-800, which may be owing to the graphene contained in the composite [247].

The Raman Spectrum of CoS-800 and CoS-G-800 are shown in Figure 4.5b. Both of two samples showed two bands at 1380 cm^{-1} and 1580 cm^{-1} corresponding to the D band of disordered carbon and G band of sp^2 hybridised graphitic carbon, respectively. A peak located at 2690 cm^{-1} (2D band) in

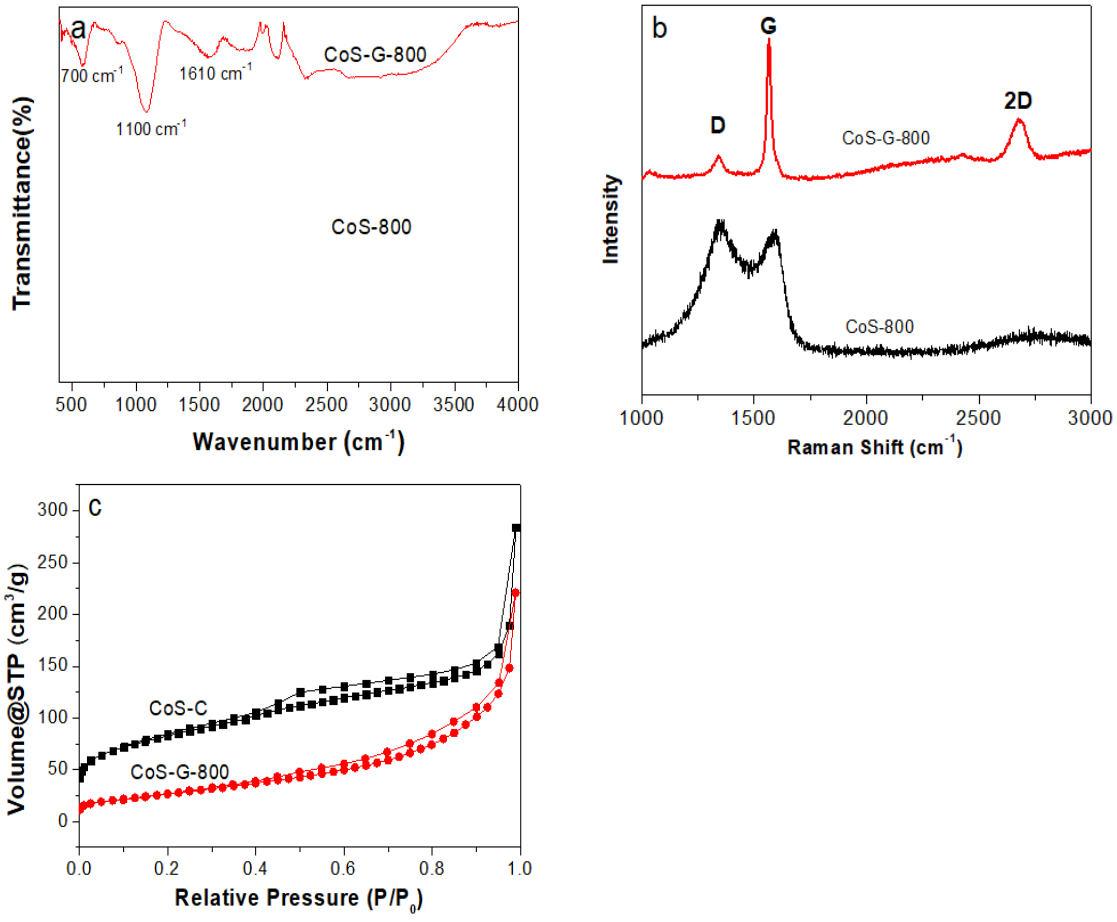

Figure 4. 5 (a) FTIR, (b) Raman spectroscopy and (c) Nitrogen sorption isotherms for CoS-G-800 and CoS-800 composites

CoS-G-800, however, could not be found in CoS-800, indicating the existence of graphene and the presence of a graphitised nanostructure in CoS-G-800. In addition, the intensity ratio (I_D/I_G) of CoS-G-800 was much lower than that of CoS-800 and the ratio values are 0.1 and 1.08, respectively. This value reflect the graphitisation degree of the composites, therefore, the Raman spectrum confirmed the presence of a highly graphitised nanostructure in CoS-G-800.

The textural properties of CoS-G-800 and CoS-800 composites can be obtained from N_2 sorption measurement, as shown in Figure 4.5c. Both samples exhibited type IV isotherms with an obvious hysteresis loop between the adsorption and desorption branches, indicating some mesopores existed in these composites. The surface area of CoS-G-800 and CoS-800 were 105 and 277 m^2 g^{-1} and pore volumes were 0.34 and 0.71 cm^3 g^{-1}, respectively. The surface area and pore volume of CoS-G-800 had a significant decrease comparing to the CoS-800, probably due to the partially blocking the pore channel of formed porous carbons.

The XPS survey spectrum of CoS-G-800 and CoS-800 displayed the binding energy peaks at 162, 284, 400, 530 and 778eV (Figure 4.6a), which can be assigned to S 2p, C 1s, N 1s and Co 2p, respectively [107, 249]. The strong peak with binding energy at 284.6 eV was observed in the high-resolution C 1s XPS spectrum (Figure 4.6b), which arose from the formation of sp^2 graphitic structure [249]. The peaks located at 284.9, 285.9 and 288.8 eV were attributed to C=C, C-S and C-N, respectively [250-253]. The Figure 4.6c displays Co 2p spectrum. Two peaks at 782.8 and 798.3 eV indicated the existence of Co^{2+} oxidation state in the composite while another two peaks were found at 778.8, 793.5 eV, implying the existence of Co^{3+} oxidation state [188, 254]. Therefore, both CoS-800 and CoS-G-800 possessed mixed oxidation states of Co^{2+} and Co^{3+}. In addition, some satellite features (802.9 eV) were also found, maybe owing to the 2^+ and 3^+ states. In S 2p spectrum shown in Figure 4.6d, two spine-orbit peaks at 161.4 and 162.5 eV were found that implies the spin-orbit in metal sulfide [255]. The peaks at 168.9 and 169.5 eV indicated tri*via*l amount of cobalt sulfide compounds were formed during the sulfurisation process [256]. In N 1s spectra (shown in Figure 4.6e), two peaks at 397.8 and 401.8 eV can be attributed to the doped pyridinic and quaternary nitrogen species, respectively [249, 257]. Two peaks at 399.1 and 400.1 eV were corresponded to Co-N and

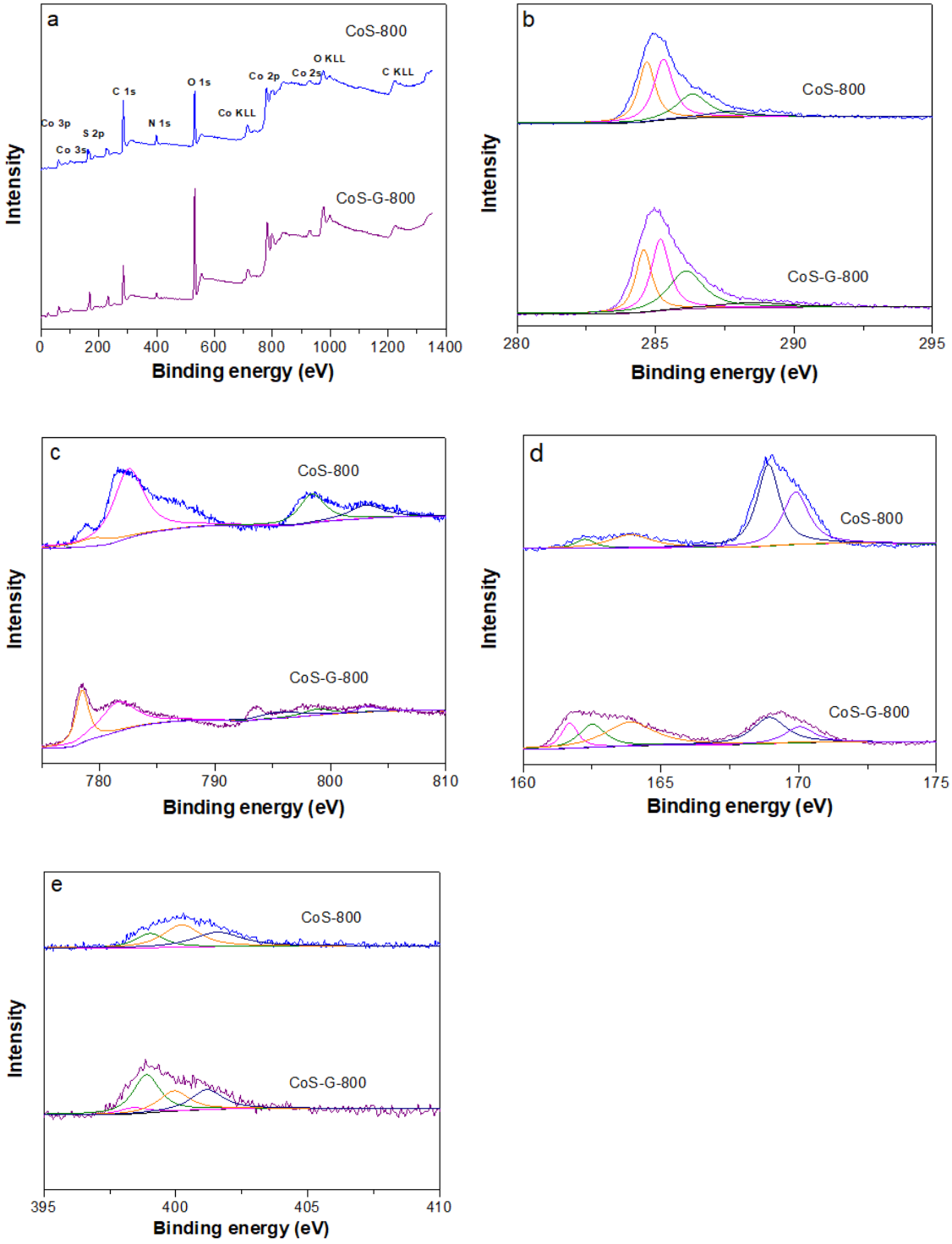

Figure 4. 6 (a) Element survey by XPS and high resolution XPS spectrum of (b) C 1s (c) Co 2p (d) S 2p (e) N 1s for CoS-G-800 and CoS-800 composites

pyrrolic-N [257-258], respectively, that indicates nitrogen was successfully doped in the graphene.

TGA and corresponding MS signal of CoS-G-800 and CoS-800 are shown in Figure 4.7. Firstly, both of two composites exhibited similar weight changes events around 100 ^{o}C, which is corresponding to the H_2O loss event. Then, they

displayed a weight gain in the temperature range of 400-460 ^{o}C due to the transferring of the formed low oxidation state cobalt sulfide to high oxidation state, followed by two weight loss events between 460-500 and 730-820 ^{o}C, which can be contributed to the combustion of the formed amorphous carbons composites and the oxidation of cobalt sulfide in air with emission of CO_2, SO_2 and NO_2 (Figure 4.7b-d). Compared with CoS-800, the weight loss temperatures of the CoS-G-800 shifted to high temperature, probably due to the relative higher burn off temperature for graphene than amorphous carbons.

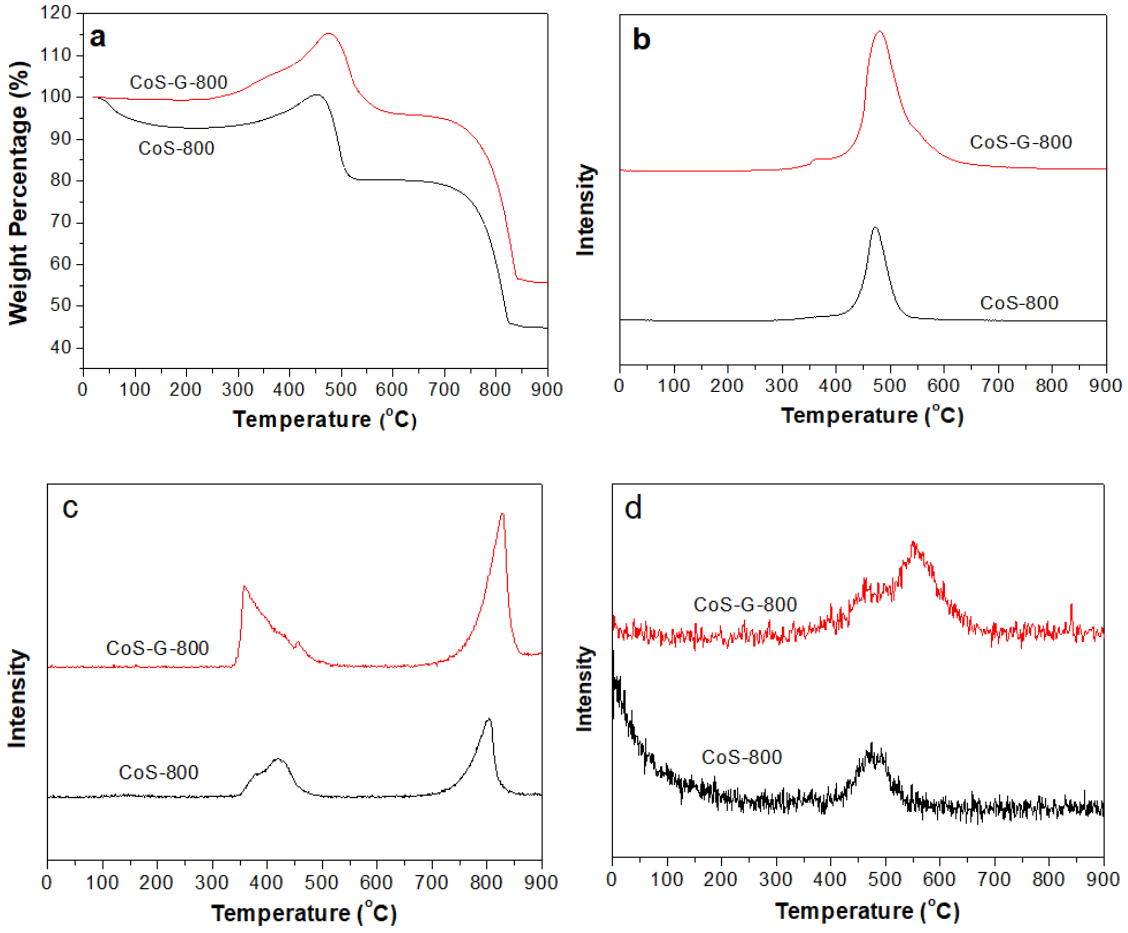

Figure 4. 7 (a) TGA and their corresponding MS curves of (b) CO_2 (c) SO_2 and (d) NO_2 for CoS-G-800 and CoS-800 composites

4.3 ORR / OER / HER performance

To evaluate the electrocatalytic activity of CoS-G-800 and CoS-800 in the ORR, the CV was performed in O_2- and N_2- saturated 0.1 M KOH solution at 25 ˚C. As shown in Figure 4.8a, no obvious redox peaks for both samples were observed in N_2- saturated KOH solution. When the solution was saturated with O_2, they exhibited remarkable ORR activity associated with a peak potential of ~0.782 V

(vs. reversible hydrogen electrode (RHE)). However, CoS-G-800 revealed a significant higher peak current (-2.89 mA cm^{-2}) than that of CoS-800 (-1.7 mA cm^{-2}), which indicates the enhanced ORR activity for CoS-G-800 compared to CoS-800.

In order to get further insight into the ORR kinetics of CoS-G-800 and CoS-800 composites, the rotating disk electrodes were measured. Both samples showed an increase of current density with the increase of rotation speed (Figure 4.8b & d), which is due to the enhanced diffusion of electrolyte at higher rotation rate. The Koutecky–Levich (K-L) curves were plotted using the inverse of rotation against the inverse of current density. The current density would get large due to the diffusion of oxygen at electrode surface, with the increasing electrode rotation speed, showing in Figure 4.8c & e. Comparing with CoS-G-800 and CoS-800, the K-L plot of graphene contained composite showed good linearity and parallelism properties, indicating that graphene have a benefit with oxygen reaction and have a good impact of electron transfer numbers (*n*) for ORR at various potentials.

Based on the K-L plots, the electron transfer number of CoS-G-800 in the ORR process was calculated to be 3.77 to 3.94 in the potential range from 0.23 to 0.63 V. In contrast, the *n* value for the CoS-800 composite varied from 3.56 to 3.73. The *n* and J_k value results for the CoS-G-800 and CoS-800 were displayed in Figure 4.8f. The *n* value results of two composite indicate that ORR processed through a four-electrode pathway and suggest that graphene have a good effect achieve high *n* value, which was measured by the rotating disk electrode tests. Furthermore, the *Jk* value for CoS-G-800 was 15.5-15.7 mA cm^{-2}, which is much higher than CoS-800 (7.2-9.5 mA cm^{-2}), indicating that graphene contained in the composite improved electron transfer kinetics of oxygen reduction. As shown in Figure 4.8g & h, the measured HO_2- yields were below 22% and 5.8% for CoS-800 and CoS-G-800, respectively. Through the potential range of 0.23-0.63 V, the corresponding electron transfer numbers are calculated to be 3.56-3.64 for CoS-800 and 3.88-3.90 for CoS-G-800, which is well in consistent with the results obtained from the K-L plots based on rotating disk electrode results.

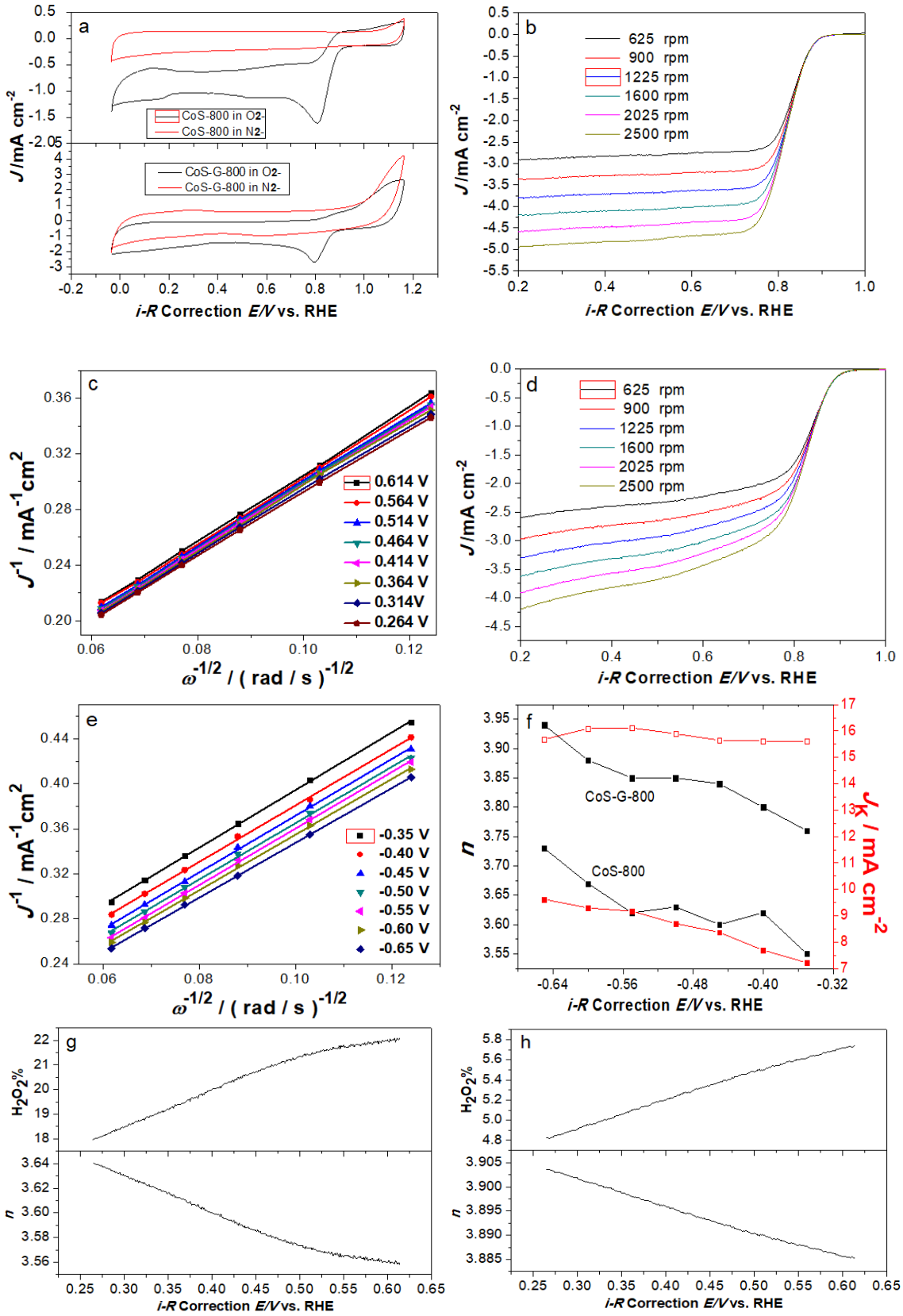

Figure 4. 8 (a) CV curves of CoS-800 and CoS-G-800 composites in N_2- or O_2-saturated 0.1M KOH; (b), (d) ORR polarisation curves of CoS-G-800 and CoS-800 at different rotating speeds, respectively;(c), (e) *K-L* plots of CoS-G-800 and CoS-800 at different potential; (f) Electron transfer number (*n*) and the corresponding kinetic current density (*Jk*) of CoS-G-800 and CoS-800 as a function of the electrode potentials; (g), (h) H_2O_2 yield and corresponding electron transfer number (*n*) for CoS-800 and CoS-G-800

The ORR polarisation curves for CoS-G-800, CoS-800 and commercial Pt/C at 1600 rpm in 0.1M KOH are shown in Figure 4.9a. Sample CoS-G-800 and CoS-800 hold very similar onset potential (0.87 and 0.86V, respectively) to the Pt/C onset potential (0.95 V), suggesting that both of two CoS contained composites are promising alternative catalyst for the cathodic ORR. However, the cathodic current density of CoS-G-800 (-4.2 mA cm^{-2}) was higher than that of CoS@C (-3.7 mA cm^{-2}), showing CoS-G-800 superior activity and it also indicates that graphene contained in the composite have an improvement to the composites conductivity. Moreover, the sample CoS-G-800 exhibited a superior electrochemical stability at a constant polarizing potential of -0.15 V in 0.1M KOH, with a very small current decay (2%) over 17500 s of continuous running, as shown in Figure 4.9b. In contrast, CoS-800 and Pt/C catalyst exhibited a 13% and 26% decay, respectively. Methanol tolerance was also investigated for CoS-G-800 and CoS-800 under the same conditions as Pt/C, which is shown in Figure 4.9c. The results showed that the introduction of methanol caused a sharp decrease in the current density for the Pt/C. In contrast, methanol had negligible effect on the performance of CoS-G-800 and CoS-800 at the cathode. The remarkable catalytically activity, high durability and good methanol tolerance suggest that CoS-G-800 is a promising electrocatalyst for the cathodic ORR.

Besides ORR activities, CoS-G-800 also exhibited good performance in OER test. As shown in Figure 4.10a, in order to reach current density 10 mA cm^{-2}, a high overpotential was required for Pt/C, suggesting it was not a good OER catalyst. However, the current density of 10 mA cm^{-2} can be achieved for the CoS-G-800 at a small overpotential of 1.68 V, which is much lower than 1.86 V of CoS-800 and only 0.1 V higher than that of IrO_2 (1.58 V). The improved OER performance of CoS-G-800 can be contributed to the contained graphene in the composite providing more access pathway and promoting the electron transfer between the catalyst surface and reaction intermediates. Furthermore, the chronoamperometric test was also carried out and shown in Figure 4.10b. The CoS-G-800 exhibited excellent durability with insignificant performance loss (15%) after 15000s continuous running.

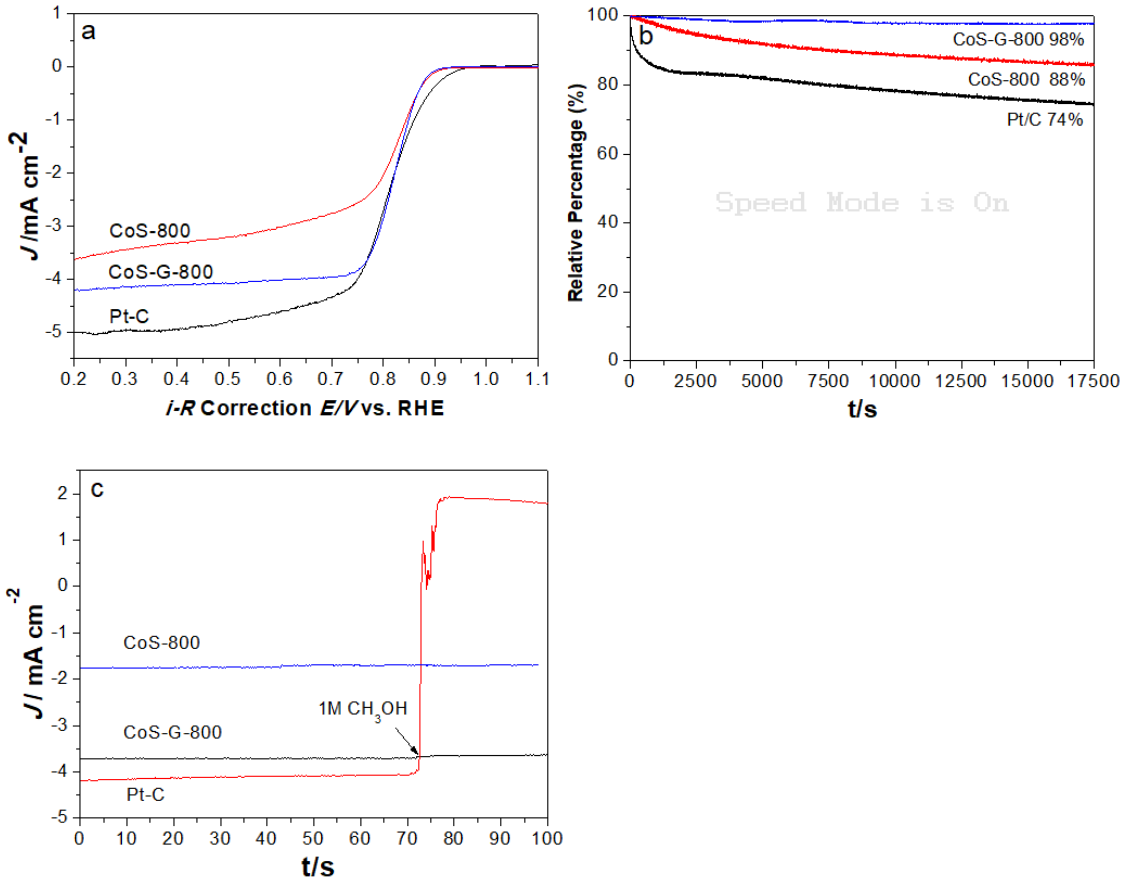

Figure 4. 9 (a) ORR polarisation curves of CoS-G-800, CoS-800 and Pt/C at 1600 rpm; (b) Chronoamperometric responses of CoS-G-800, CoS-800 and Pt/C in O_2- saturated 0.1M KOH electrolyte (1600 rpm); (c) Chronoamperometric responses of CoS-G-800, CoS-800 and Pt/C at -0.15 V in O_2- saturated 0.1M KOH electrolyte (1600 rpm) with the addition of 1M methanol

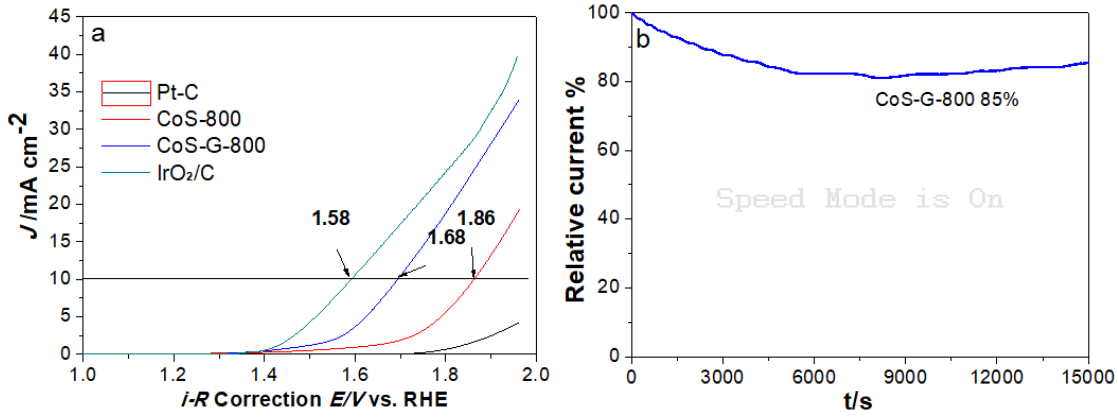

Figure 4. 10 (a) Linear sweep voltammetry polarisation curves of CoS-G-800, CoS-800 and Pt/C; (b) Current-time chronoamperometric responses of CoS-G-800. Measured in 0.1M KOH electrolyte

Apart from the ORR and OER activities, both samples have also been measured for their HER activities. The HER performance of CoS-800 and CoS-G-800 were evaluated using a three-electrode system in 0.5M H_2SO_4 electrolyte

(pH=0). For comparison purpose, the commercial Pt/C was examined as reference. As shown in Figure 4.11a, the polarisation curve recorded with CoS-G-800 exhibited an onset potential of 0.28 V, which is lower than 0.3 V of CoS-800. To reach a current density of 10 mA cm^{-2}, the overpotential of 0.45 V was needed for CoS-800, whereas, only 0.42 V required for CoS-G-800. The remarkable HER activities were also presented in the comparison in Tafel plot (shown in Figure 4.11b). The CoS-G-800 displayed a slope value of 80 mV/dec, which is much lower than 93 mV/dec for sample CoS-800, that is an indication of the graphene contained composite exhibited a remarkable HER performance in alkaline media due to the excellent conductivity of graphene

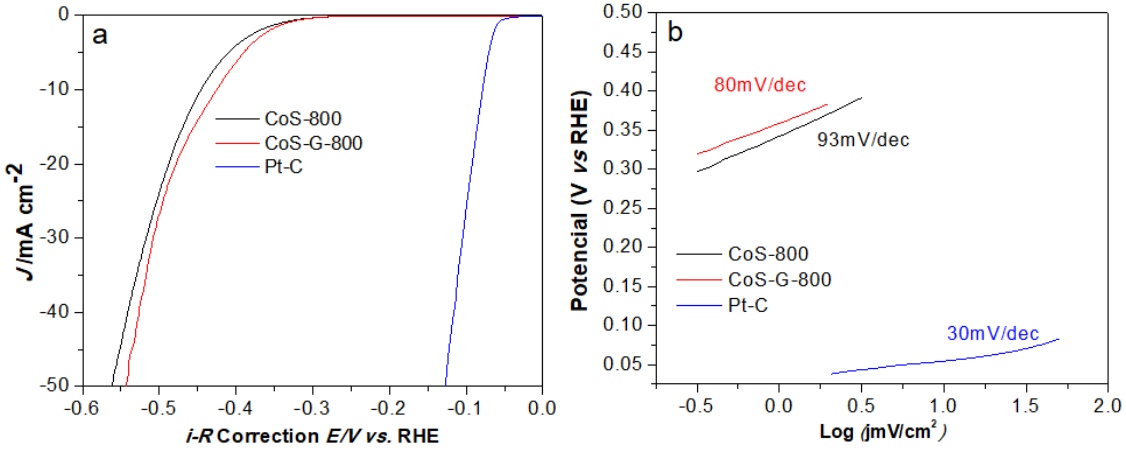

Figure 4. 11 (a) Polarisation curves for HER on CoS-G-800 and CoS-800 and Pt/C (b) corresponding Tafel plots. Measured in 0.5 M H_2SO_4 electrolyte

From above electrochemical results, obviously, the CoS-G-800 exhibited superior electrochemical activities, including ORR, OER and HER. The good electrocatalytic performance may be attributed to the N, S co-doped carbon, which was obtained from one step *in-situ* method using ZIF-67 and GO as precursor, can offer an improvement to the electron transport and promote structural stability. Moreover, the graphene achieved from GO under the high temperature treatment in H_2S atmosphere, will provide more access pathways and improve electron transfers between the catalyst surface and reaction intermediates.

4.4 Characterisations of the bi-metallic cobalt and nickel sulfides/ N, S co-doped porous carbon/ graphene composites

The crystal structures of the as-synthesised ZIF-67 and Ni-containing hybrid material with different amount of GO were investigated by XRD. As shown in Figure 4.12a, the pristine ZIF-67 exhibited some strong peaks at 10.2°, 12.5°, 14.5°, 16.4°, 18°, 24.5°, 25.8°, 26.9°, corresponding to (002), (112), (022), (013), (222), (223), (224) and (134) planes, respectively, which implied the formation of well-defined ZIF-67 crystal structures [244]. For all the Ni-containing composites, they all displayed similar diffraction patterns with pristine ZIF67, which indicates that the introduction of nickel ions and GO into the synthesis gel did not damage the inherent crystalline structure of ZIF-67. It is interesting to note that GO peaks could not be found in XRD patterns, maybe due to the low amount of GO adding to the composites or the peak of GO was overlapped with ZIF-67 at 2θ of 10.2°. After the heat treatment at 800^{o}C in H_2S atmosphere, the XRD patterns of the 4CoS-NiS-G-800 series composites are presented in Figure 4.12b. All the composites showed a wide diffraction peak at around 25°, which is attributed to the inter-plane (002) of carbon or graphene [244]. Moreover, the XRD patterns of all the composites indicated mainly $Co_{1-x}S$ (ICDD PDF# 42-0826) with the hexagonal structure in P63/mmc space group (no. 194) in samples [259]. In addition, two small diffraction peaks located at 2θ of 36.5° and 48.5°, which may correspond to nickel sulfide or nickel carbide. The XRD patterns of 4CoS-NiS-5G-T series composites which were obtained *via* heat treatment of the precursor 4Co-Ni-5GO in H_2S at different temperatures were presented in Figure 4.12c. All the resulting samples exhibited similar diffraction patterns owing to the existence of CoS and NiS, and their main diffraction peaks became sharper with increasing heat treatment temperature, implying the good crystallinity of CoS and NiS particles were obtained under higher heat treatment temperature. In addition, the diffraction peaks at 2θ of 26° for 4CoS-NiS-5G-800 and 4CoS-NiS-5G-1000 were more intense than the one in 4CoS-NiS-5G-600, indicating the formation of graphitised carbon at high temperature, which is beneficial to the electrochemical activities.

The thermal stability of as-synthesised 4CoS-NiS-zG-800 series composites heated in air atmosphere were measured by TGA-MS (Figure 4.13). Both 4CoS-NiS-5G-800 and 4CoS-NiS-10G-800 have a slight weight loss at around

50 °C due to the loss of adsorbed water in the composites. There were weight increases at around 400 °C and the weight increase peaks centred at 470 °C that may be due to the oxidation of both cobalt sulfide and nickel sulfide in air in all composites, followed by weight losses at around 450-550 °C, due to the burning of carbon and graphene in the air. These observations were confirmed by the detection of the emission of CO_2 in MS signals (shown in Figure 4.13b).The weight loss event above 700 ^{o}C for all the composites may be due to the transformation of metastable metal oxides to stable high oxidation state oxides. The TGA-MS results of 4CoS-NiS-5G-T series composites obtained under different heat treatment temperatures were also shown in Figure 4.14. The composite 4CoS-NiS-5G-600 displayed similar weight loss and CO_2 emission at similar temperature with 4CoS-NiS-5G-800. However, 4CoS-NiS-5G-1000 showed a different weight loss event between 400-700°C, maybe due to the formation of alloy or metallic carbide that can be evidenced by emission of CO_2 at rather higher temperature, as shown in Figure 4.14b.

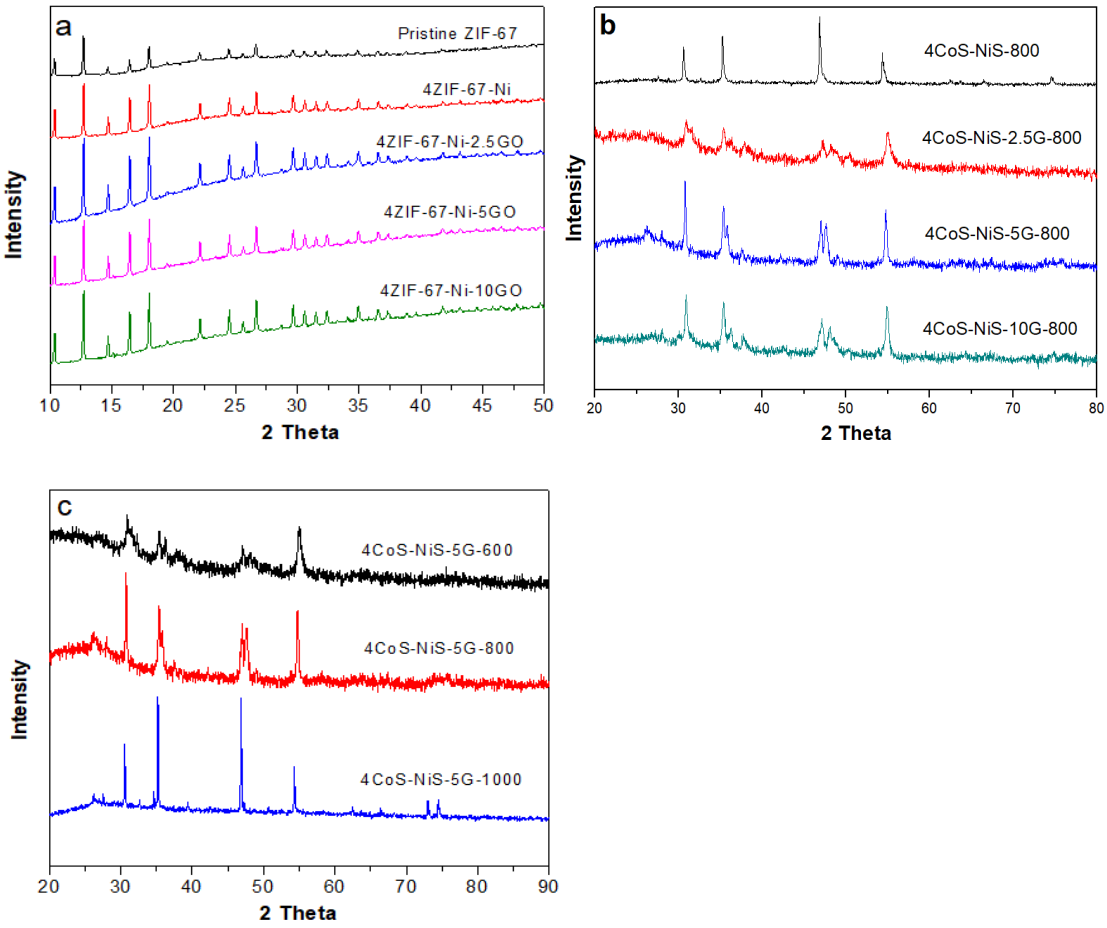

Figure 4. 12 XRD patterns of (a) as-synthesised 4ZIF-67-Ni-zGO series composites; (b) 4CoS-NiS-zG-800 and (c) 4CoS-NiS-5G-T series composites

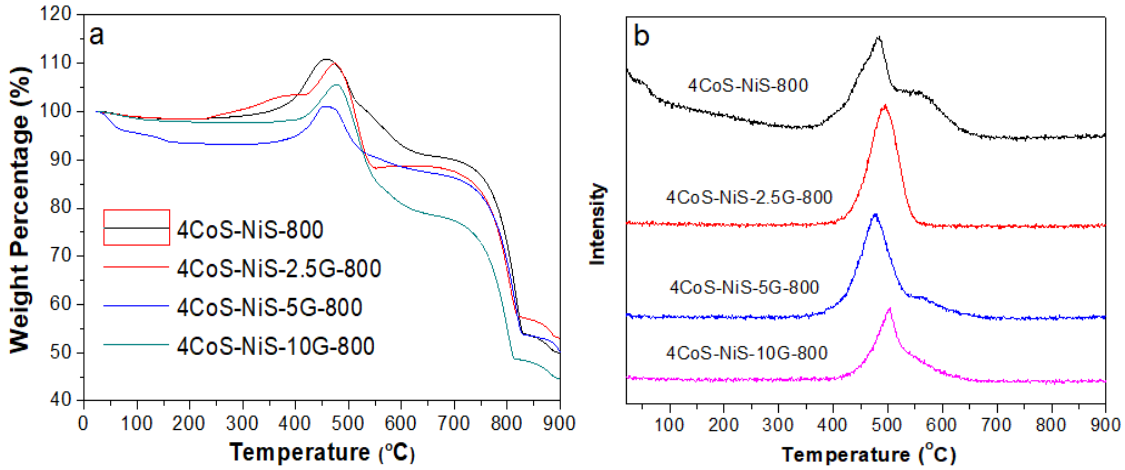

Figure 4. 13 (a) TGA and their corresponding MS curves of (b) CO_2 for the 4CoS-NiS-zG-800 series composites

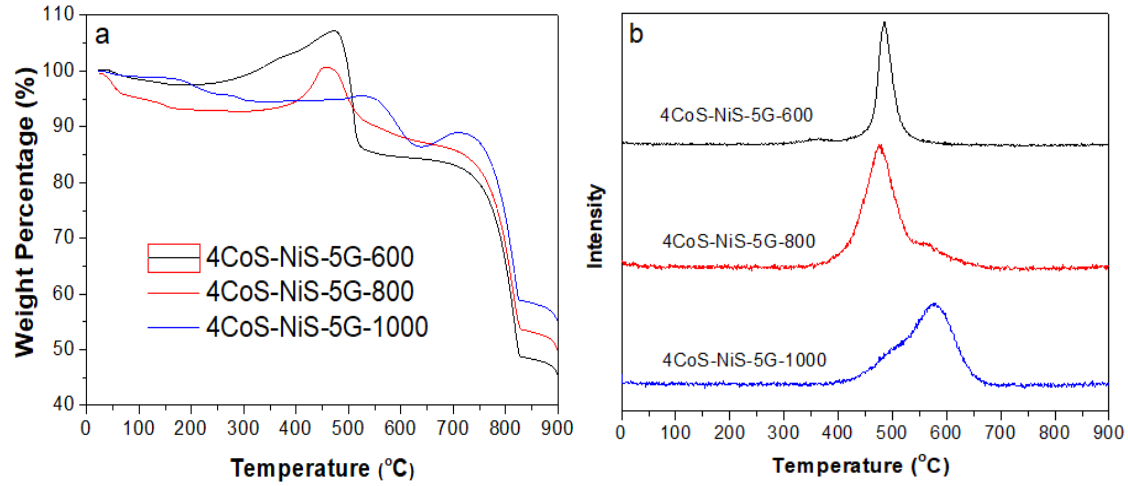

Figure 4.14 (a) TGA and their corresponding MS curves of (b) CO_2 for the 4CoS-NiS-5G-T composites

X-ray photoelectron spectroscopy (XPS) was applied to investigate the elements and their chemical state of the as-synthesised representative 4CoS-NiS-5G composite. As shown in Figure 4.15a, element survey indicates the presence of C, Co, Ni, S and N in the representative 4CoS-NiS-5G sample. The XPS spectra for each element are presented in Figure 4.15b-f. A strong peak with binding energy at 284.7eV was observed in the high-resolution C 1s XPS spectrum (Figure 4.15b), indicating the formation of sp^2 graphitic structure [260], which can improve the electron transfer and be beneficial to the electrochemical activities. In addition, three peaks located at 285.6, 286.8 and 289.9 eV may attribute to C=C, C-S and C-N, respectively [250-253]. The Co 2p spectrum shown in Figure 4.15c exhibited the presence of two doublets at 781.1 and 796.3 eV, which implied the dominance of Co^{2+} oxidation state in the sample. Moreover,

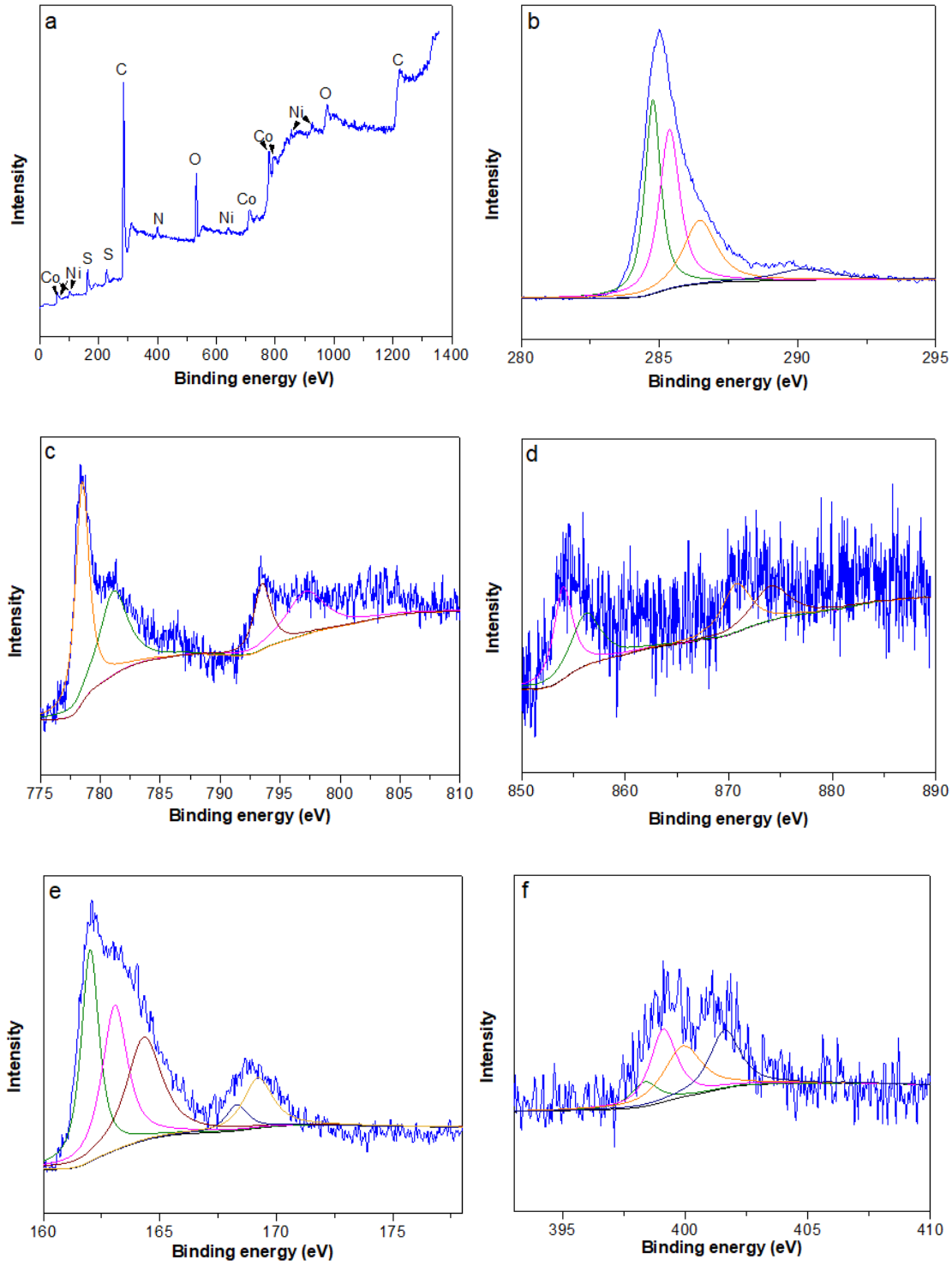

Figure 4. 15 (a) Element survey by XPS and XPS spectrum of (b) C 1s, (c) Co 2p, (d) Ni 2p, (e) S 2p and (f) N 1s for 4CoS-NiS-5G-800

another two peaks appeared at 778.4 and 793.6 eV, indicating that not only Co^{2+} oxidation state, but also Co^{3+} oxidation state exist in 4CoS-NiS-5G-800 [254, 261]. Interestingly, the same phenomenon was also happened in Ni 2p spectrum shown in the Figure 4.15d. Two peaks were found at 854.9 and 873.8 eV, which corresponds to Ni $2p_{3/2}$ and Ni $2p_{1/2}$ of Ni^{2+} state [262-263]. Apart from that, another two peaks located at 856.5 and 871 eV were also observed and they

correspond to Ni 2p $_{3/2}$ and Ni 2p $_{1/2}$ of Ni^{3+} state respectively. These observations indicate the existence of both Ni^{2+} and Ni^{3+} in sample 4CoS-NiS-5G-800 [264-265]. In S 2p spectrum (shown in Figure 4.15e), 4CoS-NiS-5G-800 displayed two deconvoluted peaks at 162.4 and 163.6 eV that are corresponding to the S 2p $_{3/2}$ and S 2p $_{1/2}$ doublets with a binding energy separation of 1.1 eV, corresponding to the S^{2-} species of metal sulfides.[256, 266]. And the peak located at 162.8 eV may be due to the formation of S-C bonding [252, 267]. In addition, binding energy at 168.3 and 169.4 eV are assigned to the S 2p $_{3/2}$ and S 2p $_{1/2}$ peaks of oxidised S species, such as sulfate groups [268] which could be due to the partially oxidation of sulfur in air [269]. The N 1s spectrum can be deconvoluted into four peaks located at 397.5, 399.4, 400.3 and 401.6 eV, corresponding to the pyridinic-N, Co-N, pyrrolic-N and graphitic-N, respectively [257-258]. Owing to the volatility of N and S species at high temperature treatment, the content of N and S in the composite remains low. From XPS results, it is clear that 4CoS-NiS-5G composite composes of Co^{2+}, Co^{3+}, Ni^{2+}, Ni^{3+} and S^{2-} states. These XPS analysis results indicate that Co-Ni sulfide with graphene and carbon composites have been successfully prepared *via* one-step carbonisation and sulfurisation process and CoS/NiS nanoparticles were supported on S, N co-doped carbon and/or graphene matrices.

The textural properties of the as-synthesised 4CoS-NiS-zG-800 series composites were analysed by N_2 sorption at -196 °C. As shown in Figure 4.16a, all the samples exhibit small hysteresis loops between their adsorption and desorption branches, indicating the existence of mesopores due to the voids between particles. The relevant surface area and pore volume are summarised in Table 4.1. The composite 4CoS-NiS-800, 4CoS-NiS-2.5G-800, 4CoS-NiS-5G-800 and 4CoS-NiS-10G-800 possess specific surface area of 175.9, 178.4, 103.3 and 192.6 $m^2\ g^{-1}$, and pore volume of 0.33, 0.24, 0.21and 0.24 $cm^3\ g^{-1}$, respectively. Interestingly, with increasing the amount of graphene in composites, the surface areas decrease at first and then increase, maybe due to the formed porous graphene in the composites with higher graphene content. By comparing nitrogen sorption isotherms of the 4CoS-NiS-5G-T obtained under three different treatment temperatures (shown in Figure 4.16b), it is obvious that the hysteresis loops between the adsorption and desorption branches for 600 and 800 ^oC samples were very clear, indicating the existence of mesopores in these composites. However, for the 1000 ^oC sample, the

hysteresis loop almost disappeared. Moreover, with increase of the heat treatment temperature, the pore volume and surface area of the resulting samples decrease, maybe due to the much higher heat treatment temperature leading to the increased crystallinity of the materials.

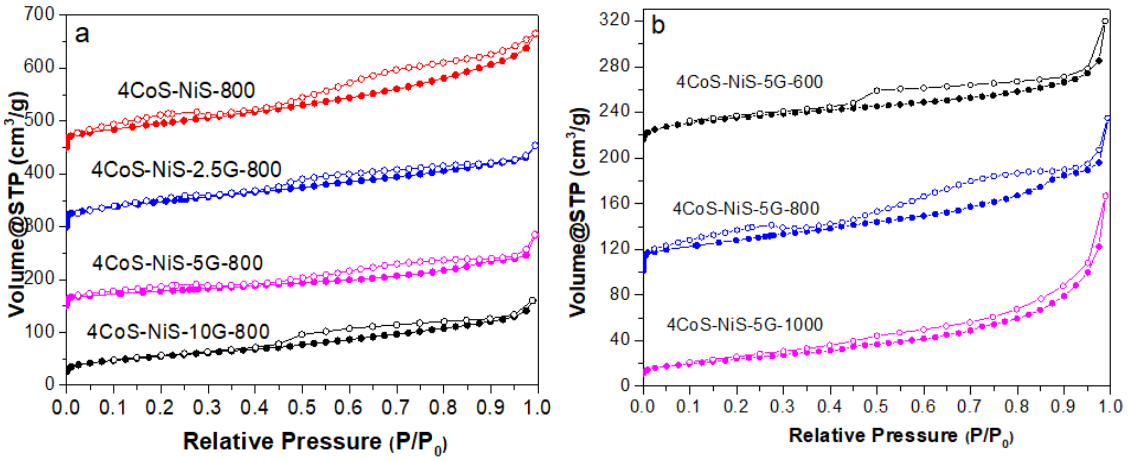

Figure 4. 16 N_2 sorption isotherms of (a) 4CoS-NiS-zG-800 and (b) 4CoS-NiS-5G-T series composites

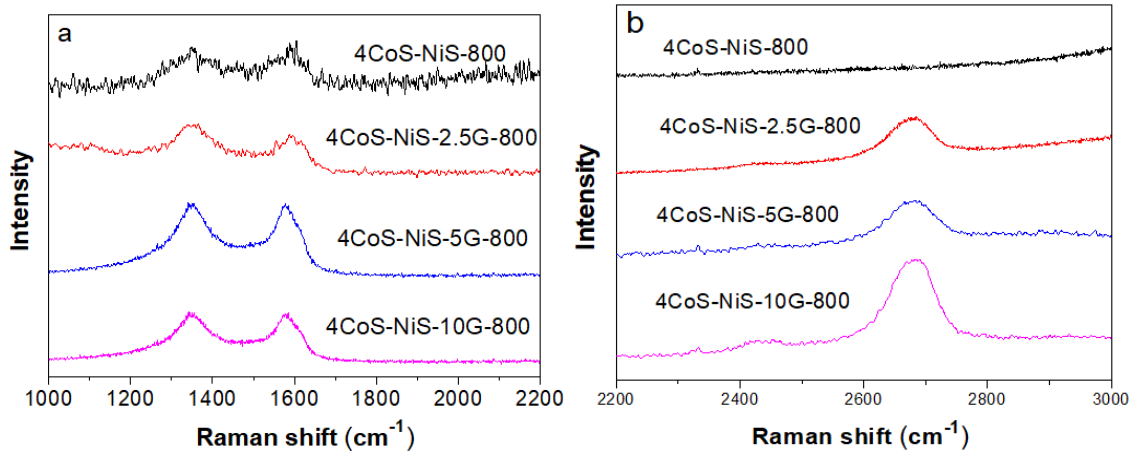

Figure 4. 17 Raman spectra (a) D and G bands (b) 2D band of 4CoS-NiS-zG-800 series composites

The 4CoS-NiS-zG-800 series composites were investigated by Raman spectroscopy (Figure 4.17). The D band at 1350 cm^{-1} is corresponding to disordered amorphous carbon and the G band at 1595 cm^{-1} is an indication of nanocrystalline graphitic carbon (Figure 4.17a). Both D band and G band appeared in all the composites, implying amorphous nature of the carbon with abundant defects [270]. Meanwhile, the appearance of 2D band at around 2690 cm^{-1} (shown in Figure 4.17b) for sample 4CoS-NiS-2.5G, 4CoS-NiS-5G and 4CoS-NiS-10G, suggests that the graphene oxide introduced in the precursor was well converted to graphene after the heating treatment, which clearly

evidences the existence of graphene in the composites that derived from the GO-containing precursors.

Table 4. 1 Textual properties of the 4CoS-NiS-zG and 4CoS-NiS-5G-T series composites

Composite	Surface area ($m^2 g^{-1}$)	Pore volume ($cm^3 g^{-1}$)
4CoS-NiS-800	175.9	0.33
4CoS-NiS-2.5G-800	178.4	0.24
4CoS-NiS-5G-800	103.3	0.21
4CoS-NiS-10G-800	192.6	0.25
4CoS-NiS-5G-600	126.2	0.19
4CoS-NiS-5G-1000	86.8	0.15

The morphologies of 4CoS-NiS-zG-800 series composites were investigated by scanning electron microscopy (SEM). As shown in Figure 4.18a-h, the particles are nanocrystal with polyhedral shape. The average particle size of 4CoS-NiS-800 is around 0.15 μm and particle sizes for graphene-contained composites ranged from 0.2 μm to 0.45 μm. Actually, the particle sizes of graphene-containing samples increased with increase of graphene content in the composites. From TGA and Raman spectra results, both of them have shown the graphene exist in the composites. Meanwhile, GO or graphene layers were not observable in the composites, may indicating GO was mostly converted to graphene and graphene was well embedded in the composites.

To further investigate the morphologies and structures of the samples, transmission electron microscopy (TEM) was utilised to characterise 4CoS-NiS-zG-800 series composites. As shown in Figure 4.19, all the composites had a sphere-like shape with an average single particle size of 10-20 nm. Interestingly, the metal sulfide particles in graphene contained composites were better embedded, which may due to the GO introduced in the precursor that can assist the dispersion of the metal sulfide particles. No single CoS or NiS particles can be easily observable and most of the CoS and NiS particles are well embedded in composites and surrounded with carbon layers. Actually, all the elements

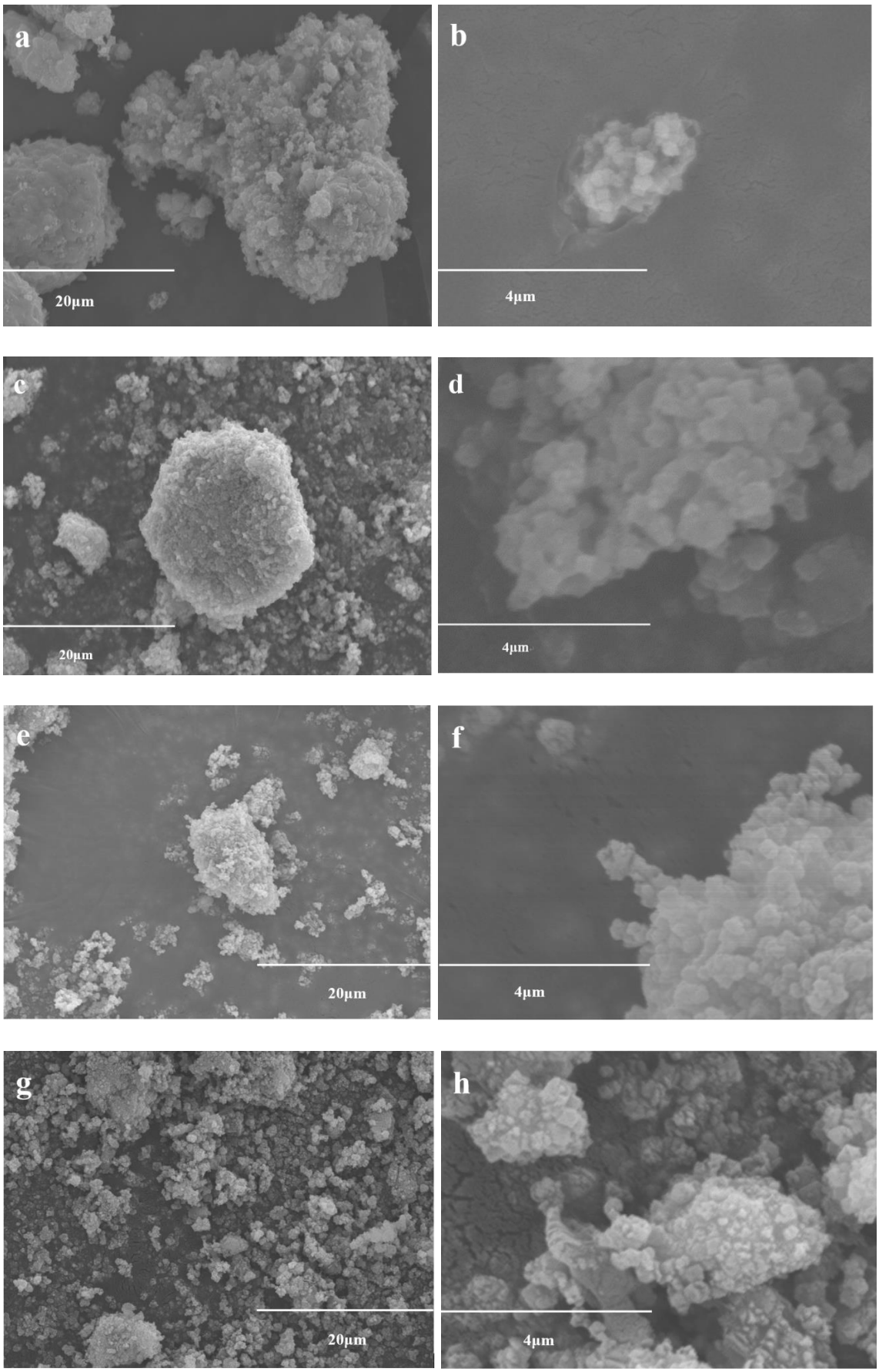

Figure 4. 18 SEM images of the (a, b) 4CoS-NiS-800; (c, d) 4CoS-NiS-2.5G-800; (e, f) 4CoS-NiS-5G-800 and (g, h) 4CoS-NiS-10G-800

including C, Co, Ni, S and N in the sample were homogeneous distributed in the composite, as demonstrated by element mapping results shown in Figure 4.20. It is interesting to note that the interlayer spacing for pure CoS is 0.194 nm, however, it changed to 0.182 nm in Ni-contained composites, which implies that nickel has been successfully partially substituting cobalt in the composite due to the ionic size of Ni ions are smaller than that of Co ions. Meanwhile, both carbon shells and carbon onions were found in all composites because of the catalytic effect of cobalt and nickel metal particles which formed from the reduction of the metal ions by the in-situ formed carbon particles, and the variety of formed carbons combined with the formed graphene coming from the GO, offer more electron transfer pathways and active sites to improve electrochemical activities. The selected area electron diffraction (SAED) patterns, shown in inset of Figure 4.19a, c, e and g, clearly suggest that the bright scattered dots contributed from the crystalline cobalt sulfide/nickel sulfide nanoparticles while the dimmed diffraction rings were from the amorphous porous carbon matrix.

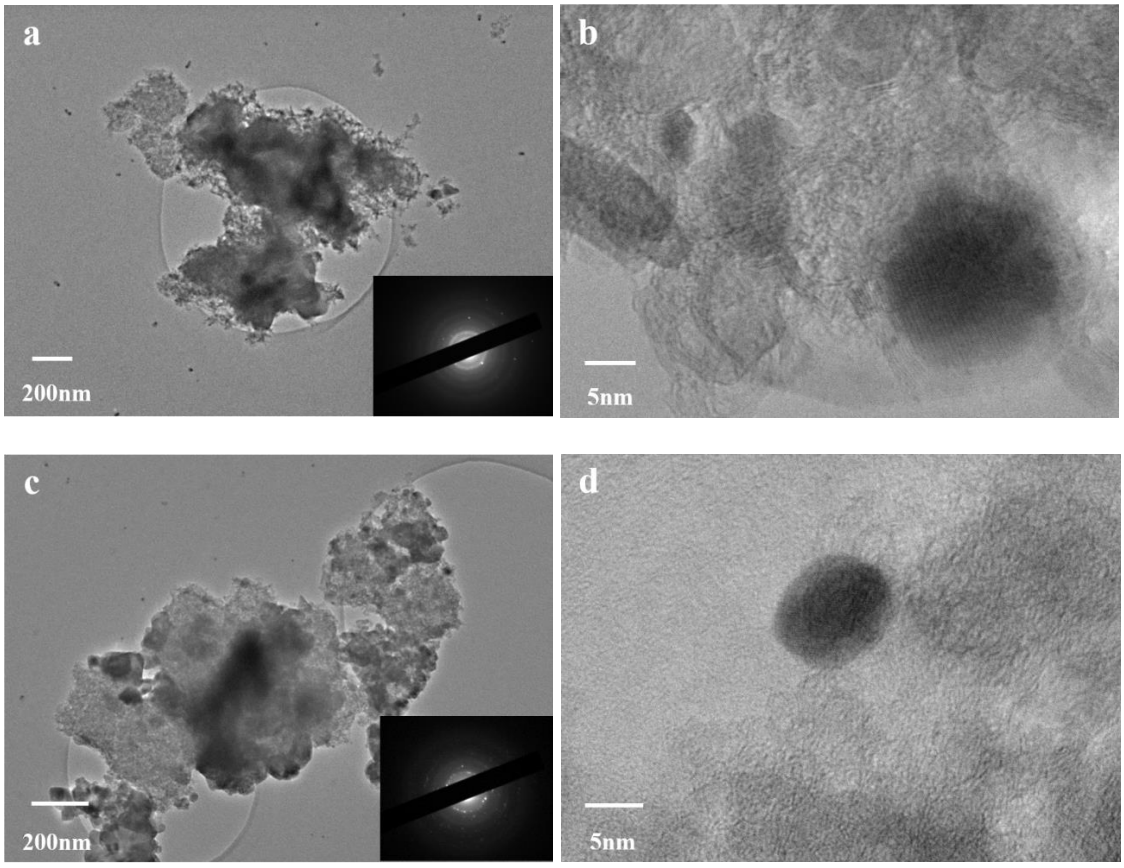

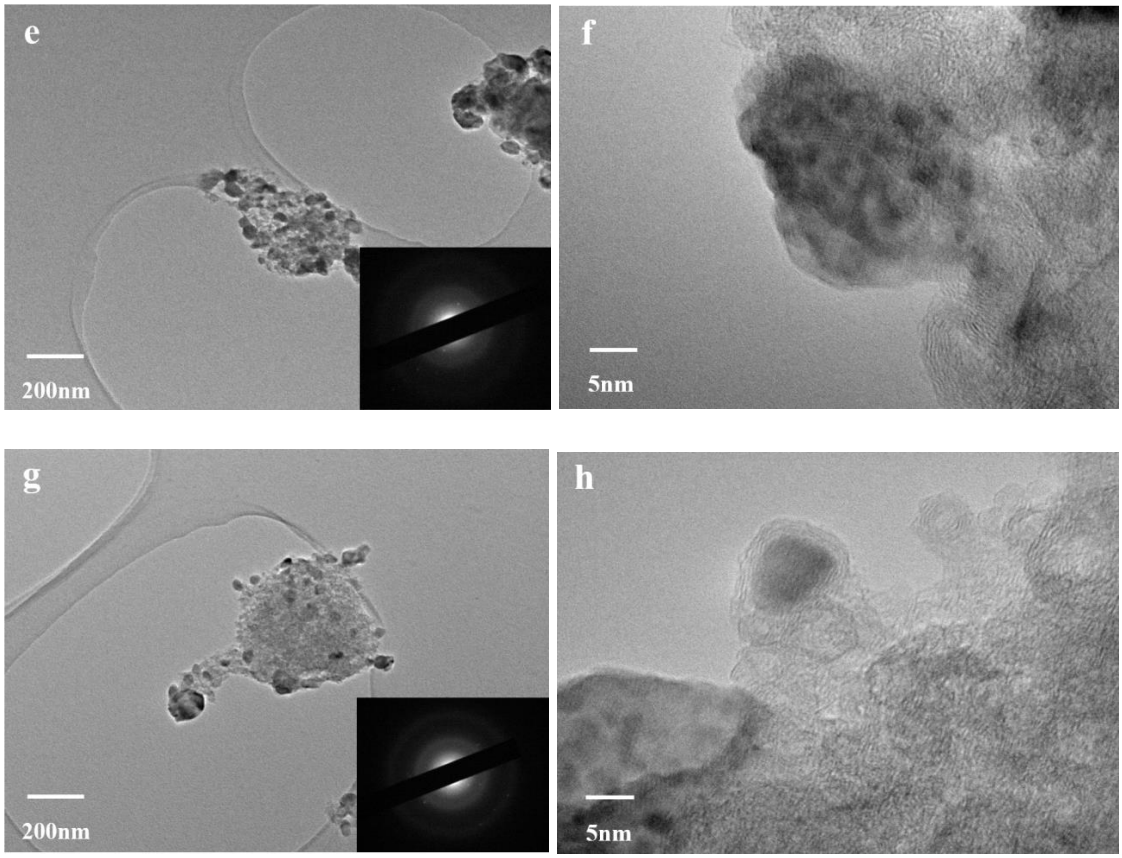

Figure 4. 19 TEM images of (a & b) 4CoS-NiS-800, (c & d) 4CoS-NiS-2.5G-800, (e & f) 4CoS-NiS-5G-800 and (g & h) 4CoS-NiS-10G-800. Inset in (a, c, e, and g) are SAED patterns for corresponding composites

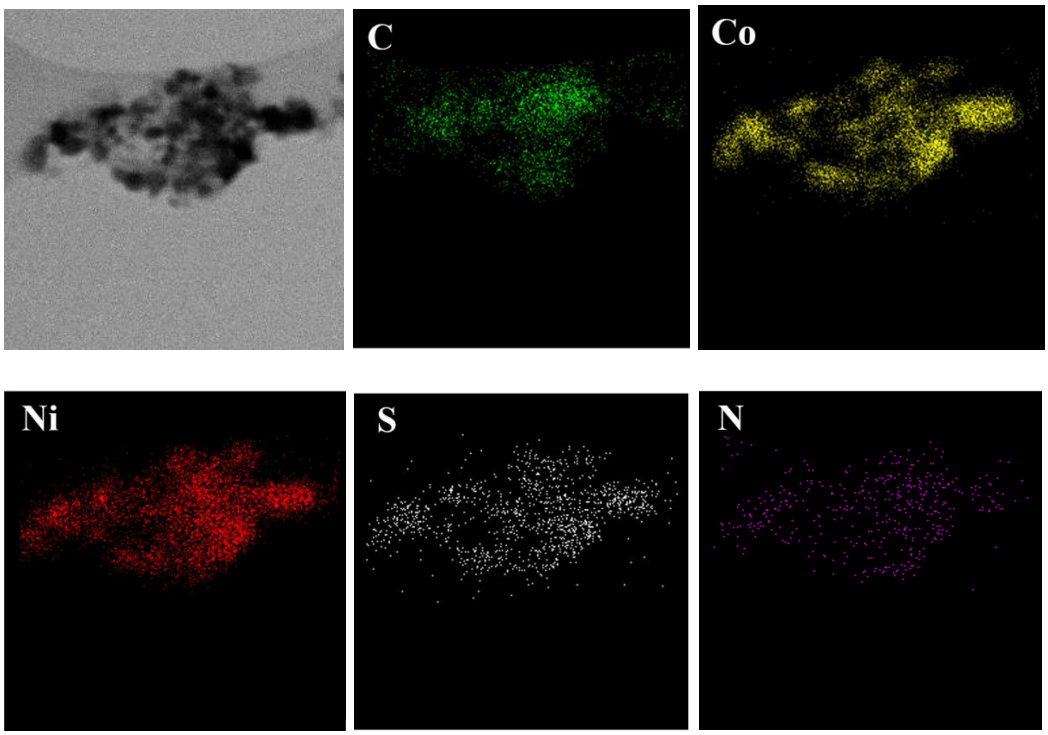

Figure 4. 20 TEM images and element mappings (C, Co, Ni, S and N) for sample 4CoS-NiS-5G-800

4.5 Electrocatalytic performance

The electrocatalytic activities of the as-synthesised xCoS-yNiS-zG-T composites for oxygen evolution reaction (OER) were evaluated in O_2-saturated 1 M KOH (pH=14) electrolyte by using three electrodes system with a scan rate of 5 mV s^{-1}. Owing to the effect of ohmic resistance (iR), the as-measured current was not the intrinsic behaviour of the tested samples. Therefore, before OER measurement, all the samples were subjected to initial current for iR correction. The OER performance of catalytic materials derived from Co: Ni ratio at 1: 1, 2: 1 and 4:1 with a fixed graphene content of 10 wt% and carbonisation/sulfurisation at 800 °C were first measured, and results are shown in Figure 4.21a. CoS-NiS-10G-800, 2CoS-NiS-10G-800 and 4CoS-NiS-10G-800 exhibited the onset potential of 1.62, 1.6 and 1.45 V for OER, respectively. To reach the current density of 10 mA cm^{-2} which is typically used to compare the performance for different materials, the potential of 1.71, 1.65 and 1.52 V were required for sample CoS-NiS-10G-800, 2CoS-NiS-10G-800 and 4CoS-NiS-10G-800 respectively. Comparing the onset potential and the overpotential to achieve current density of 10 mA cm^{-2} of these three catalysts with reference IrO_2/C, one can easily found that the ratio of Co: Ni =4: 1 with fixed graphene show a much better OER activities than the reference and other catalysts. Based on these results, the OER performances of 4CoS-NiS-zG-T series catalysts were further evaluated. The polarisation curve of 4CoS-NiS-5G-T and IrO_2/C are shown in Figure 4.21b. It can be found that 4CoS-NiS-5G-800 exhibit much enhanced OER activities with an onset potential of 1.41 V, which is far lower than 1.5 V of IrO_2/C, followed by 1.61 V and 1.65 V of 4CoS-NiS-5G-1000 and 4CoS-NiS-5G-600, respectively. The potential to achieve 10 mA cm^{-2} for 4CoS-NiS-5G-800 is 1.46 V, which is much lower than the value for IrO_2/C (1.61 V), 4CoS-NiS-5G-1000 (1.69 V) and 4CoS-NiS-4G-600 (>1.8V). Comparing with other catalysts (600 °C and 1000 °C samples), 4CoS-NiS-5G-800 sample exhibited remarkable current density in the whole potential range, which indicates this bi-metallic Co-Ni sulfides composite obtained *via* sulfurisation at 800 °C is a promising OER electrocatalyst with superior OER activities.

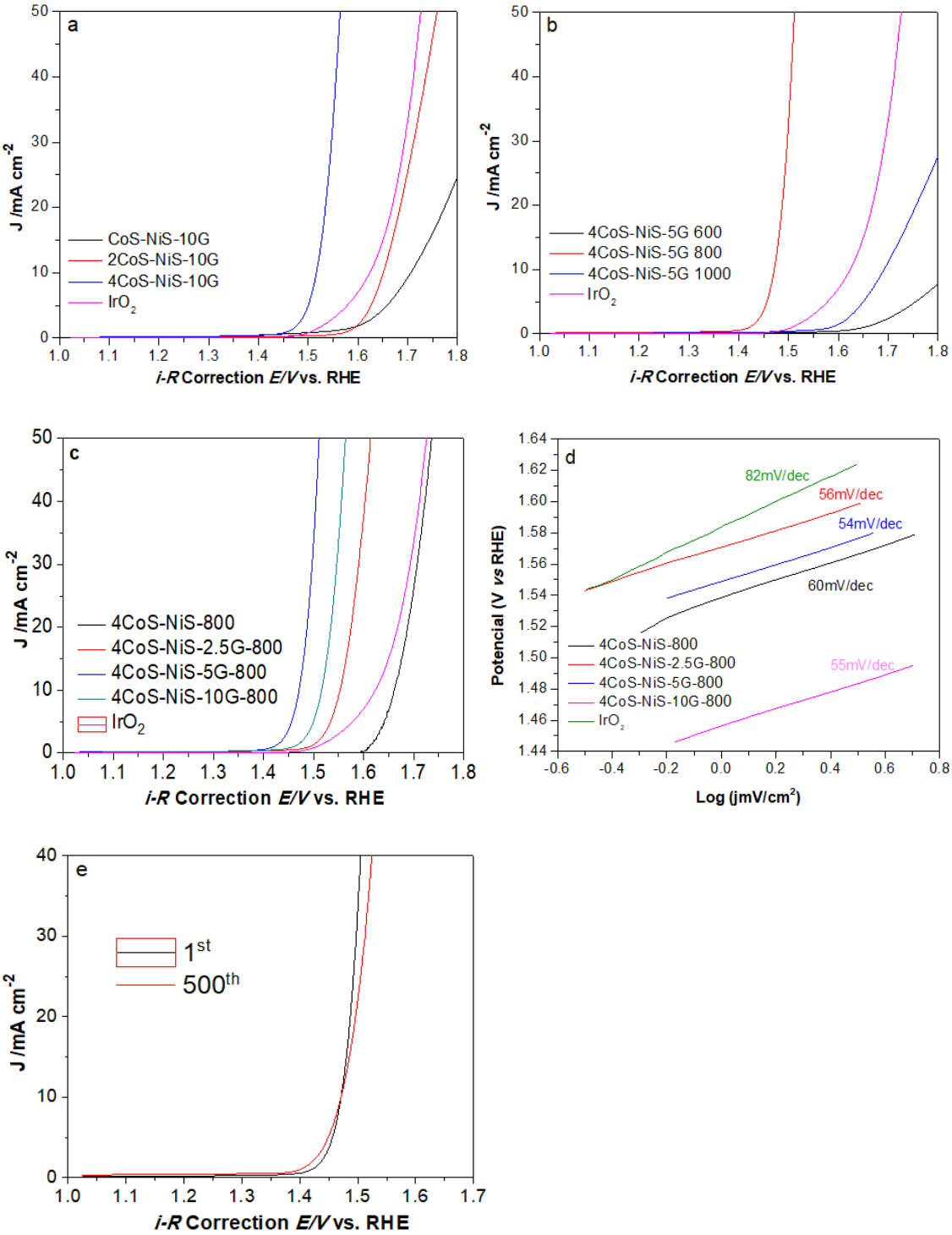

Figure 4. 21 Polarisation curves for OER on (a) xCoS-NiS-10G-800 series composites and IrO_2/C. (b) 4CoS-NiS-5G-T series composites and IrO_2/C. (c) 4CoS-NiS-zG-800 series composites and IrO_2/C. (d) Tafel plot of 4CoS-NiS-zG-800 series composites. (e) durability test

Besides the sulfurisation temperature, the amount of graphene in the samples is another important factor that can influence the OER activities. The as-synthesised 4CoS-NiS-800 and 4CoS-NiS-zG-800 (z= 2.5, 5 and 10) catalysts that contains different graphene content were all evaluated in 1 M KOH electrolyte solution and the results were presented in Figure 4.21c. It can be

found that the onset potential of 4CoS-NiS-5G is 1.41V, which is lower than that of 4CoS-NiS-10G (1.45 V), 4CoS-NiS-2.5G (1.49 V), 4CoS-NiS (1.6 V) and IrO_2/C (1.5 V), respectively. Both 4CoS-NiS and 4CoS-NiS-zG catalysts exhibited a sharp rise of anodic current, and the current density of 10 mA cm^{-2} could be achieved for 4CoS-NiS-5G at a potential of 1.46 V, which is lower than that for 4CoS-NiS-10G (1.51 V), followed by 1.54 V, 1.61 V and 1.67 V for 4CoS-NiS-2.5G, IrO_2/C and 4CoS-NiS, respectively. In addition, the kinetics of these catalysts were examined by Tafel plot (Figure 4.21d), which are derived from the polarisation curves for OER. A low Tafel slope of 54 mV dec^{-1} is observed for 4CoS-NiS-5G, which is smaller than 55, 56, 60 and 82 mV dec^{-1} for 4CoS-NiS-10G, 4CoS-NiS-2.5G, 4CoS-NiS and IrO_2/C, respectively. This further confirms that sample 4CoS-NiS-5G-800 is the most active electrocatalyst in OER among all the studied materials. Moreover, the catalyst durability is evaluated and displayed in Figure 4.21e. The 4CoS-NiS-5G-800 sample showed a similar I-V curve after 500 times scan with a scan rate of 5 mVs^{-1}, while the 500^{th} curve displayed the same overpotential at the current density of 10 mA cm^{-2} and even a litter lower than onset potential than the initial cycle. The superior durability of 4CoS-NiS-5G-800 may be due to that only tiny parts of CoS/NiS were oxidised to CoO/NiO during the initial electrochemical process and the rest of particles were protected by the graphene and carbon matrix.

The introduction of graphene promoted the electron transfer between the surfaces of 4CoS-NiS-5G catalyst and the reaction media, it is therefore an efficient OER process which can achieve high current density readily. The OER process produces H_2O and O_2 in the electrolyte media, following the reaction of $4OH^- \rightarrow 2H_2O+O_2+4e^-$. The OER performances of all the evaluated catalysts are listed in Table 4.3. The improved OER performance of 4CoS-NiS-xG was contributed to the existence of graphene in the samples, which provides more access pathways and promotes the electron transfer between the catalyst surface and the electrolyte. However, it is worth noting that the addition of too much graphene into composites plays an adverse effect since too much graphene can block the pore of the materials. Consequently, the weight content of graphene in the composites should be optimised.

Table 4. 2 OER performances of different composites

Catalyst	OER onset overpotential (mV vs. RHE)	OER overpotential (mV vs. RHE) @ 10 mA cm^{-2}
CoS-NiS-10G-800	162	171
2CoS-NiS-10G-800	160	165
4CoS-NiS-10G-800	145	152
4CoS-NiS-5G-600	165	183
4CoS-NiS-5G-1000	161	169
4CoS-NiS-800	160	167
4CoS-NiS-2.5G-800	149	154
4CoS-NiS-5G-800	141	146
4CoS-NiS-10G-800	143	151
IrO_2/C	150	161

According to previous results on activities, since catalysts with the ratio of Co: Ni =4: 1 sulfurised in 800 °C exhibited superior electrochemical performance in OER, 4CoS-NiS-zG series catalysts were further measured as electrocatalysts for hydrogen evolution reaction. From the polarisation curves shown in Figure 4.22a, the Pt/C displayed a negligible onset potential, while 4CoS-NiS-5G exhibited an onset potential of 0.26 V, which is higher than the onset potential of 0.245 V, 0.25 V and 0.24 V (lowest) for 4CoS-NiS-800, 4CoS-NiS-2.5G-800 and 4CoS-NiS-10G-800, respectively. In order to reach a current density of 10 mA cm^{-2}, 4CoS-NiS-10G needed an overpotential of 0.37 V, which is nearly the same voltage as 4CoS-NiS-800 and slightly lower than that of 4CoS-NiS-2.5G-800, whereas a high overpotential of 0.425 V was required for 4CoS-NiS-5G-800. In additional, an overpotential of 0.515V was needed to drive current density of 100 mA cm^{-2} for 4CoS-NiS-2.5G-800, slightly lower than that of 4CoS-NiS-800. These observations may suggest that 4CoS-NiS-2.5G-800 performs slightly better than other samples for HER in acid electrolyte. But in general, graphene-containing samples did not show obvious advantages over graphene-free sample and all the samples actually exhibited more or less comparable HER performances in acidic electrolyte media. The iR-corrected

Tafel plots are displayed in Figure 4.22b. The slope value of 4CoS-NiS-2.5G-800 is 91 mV/dec, which is lower than that of 95 mV/dec, 102 mV/dec and 103 mV/dec for 4CoS-NiS-800, 4CoS-NiS-10G-800 and 4CoS-NiS-5G-800, respectively.

However, when the HER catalytic activities of 4CoS-NiS-zG-800 were also evaluated in 1M KOH electrolyte and the iR corrected linear sweep voltammetry curves are shown in Figure 4.23a, the same composites demonstrate different HER performances in alkaline media. One can easily find that the HER activities of all the 4CoS-NiS-zG-800 samples were better than that of 4CoS-NiS-800, indicating that the introduction of graphene can remarkably improve the HER performance of the composites in alkaline media. The onset potential for 4CoS-NiS-2.5G-800 was 0.24 V, which is 20 mV lower than that for 4CoS-NiS-800 sample. In order to reach a current density of 10 mA cm^{-2}, the sample 4CoS-NiS-2.5G showed the best performance with an overpotential of 0.335V, which is lower than 0.358V, 0.355V and 0.388V for 4CoS-NiS-5G-800, 4CoS-NiS-10G-800 and 4CoS-NiS-800, respectively. Moreover, LSV curves of 4CoS-NiS-10G-800 and 4CoS-NiS-5G-800 displayed a dramatic drop in overall activities comparing with the others, with an overpotential much lower than that of 4CoS-NiS-800 at a current density of 100 mA cm^{-2}. The different HER performances of those samples in alkaline media can be also found in their iR- corrected Tafel plots (shown in Figure 4.23b) with slope values ranging from 90 to 121 mV/dec for 4CoS-NiS-10G-800, 4CoS-NiS-2.5G-800, 4CoS-NiS-5G-800 and 4CoS-NiS-800, which is an indication of that the graphene contained nanocomposite catalysts exhibited a remarkable HER performance in alkaline media, owing to the excellent conductivity of graphene that could improve the electron transfer between the catalyst surface and reaction intermediates. All the HER performances both in acidic and alkaline media for 4CoS-NiS-zG and IrO_2/C samples are summarised in Table 4.4.

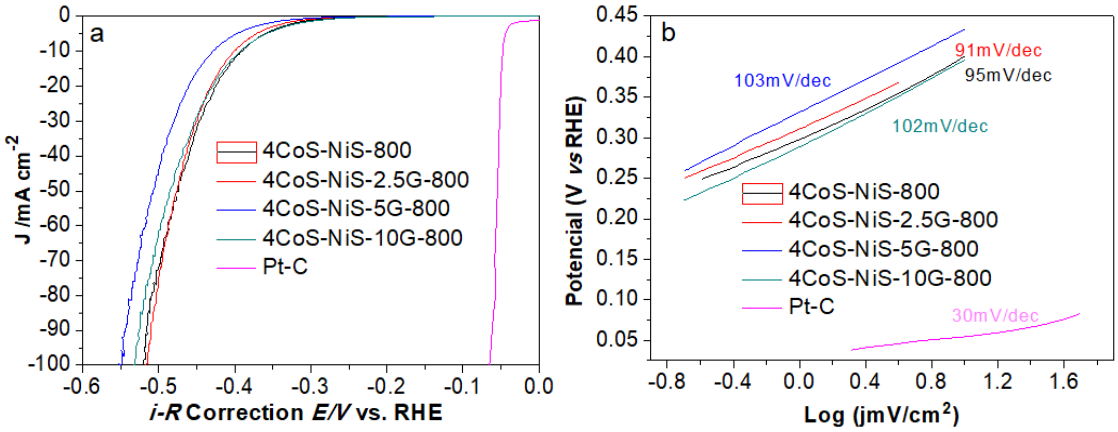

Figure 4. 22 (a) Polarisation curves for HER on 4CoS-NiS-zG-800 series composites and Pt-C and (b) corresponding Tafel plots. Measured in 0.5 M H_2SO_4 electrolyte

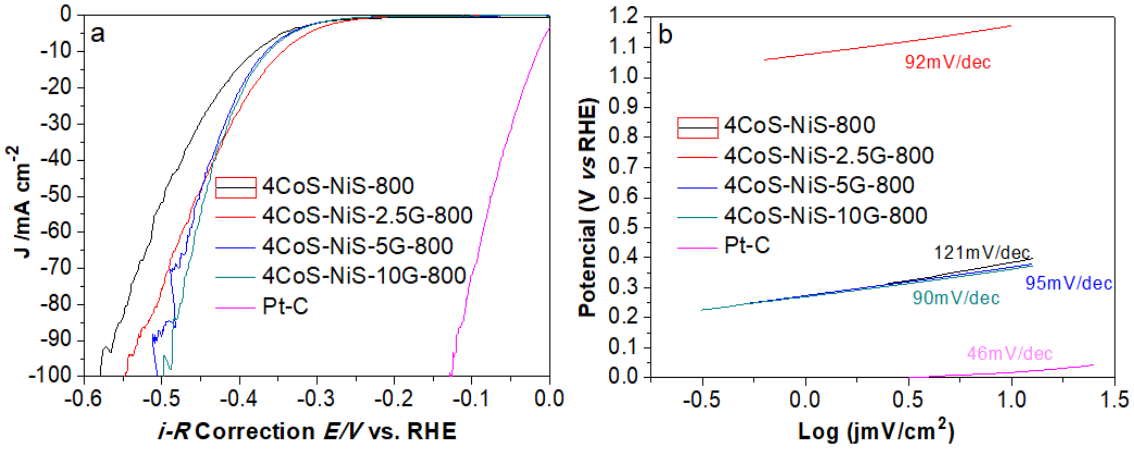

Figure 4. 23 (a) Polarisation curves for HER on the 4CoS-NiS-zG-800 series composites and Pt-C and (b) corresponding Tafel plots. Measured in 1 M KOH electrolyte

Table 4. 3 HER performances of different composites

Catalyst	Onset potential (mV vs. RHE)		Over potential (mV vs. RHE)@ 10 mA cm^{-2}		Tafel slope (mV dec^{-1})	
	0.5 M H_2SO_4	1 M KOH	0.5 M H_2SO_4	1 M KOH	0.5 M H_2SO_4	1 M KOH
4CoS-NiS-800	245	260	370	388	95	121
4CoS-NiS-2.5G-800	251	241	380	335	91	92
4CoS-NiS-5G-800	260	251	425	358	103	95
4CoS-NiS-10G-800	240	249	371	355	102	90
Pt-C	61	10	62	30	30	46

From the above OER and HER results, one can find that the as-prepared 4CoS-NiS-5G-800 can be used as a good electrocatalyst for overall water splitting. The potential reasons may be :(1) the outstanding OER performance can be attributed to the uniform dispersion of the bi-metal sulfides in porous carbon structure which can provide more exposure of edge sites which is beneficial to achieve excellent OER activities; (2) the good HER performance is originated from the introduction of nickel promoted cobalt sulfides which improves the adsorption abilities of H^+ on carbon by optimizing the electronic structure, thus enhancing HER activities both in acidic and alkaline electrolyte media; (3) the nanocomposites with incorporated porous carbon produced from *in-situ* sulfurisation/ pyrolysis method can greatly improve the electron transport, thus promoting the structural stability; (4) the porous carbon and graphene are doped with heteroatoms such as N and S during the carbonisation and sulfurisation process, which could not only offer more active sites for catalytic reaction, but also provide anchoring sites for the deposition of catalytic nanoparticle. Meanwhile, the introduced graphene itself can also provide more access pathway and promote the electron transfer between the catalyst surface and reaction intermediates.

Chapter 5: Electrocatalytic performance of bi-metallic derivatives derived from Fe substituted GO/ZIF-67

5.1 Introduction

As one of the most ideal, environmental friendly and zero carbon emission gas, hydrogen (H_2) energy resource has attracted great interest in fuel cells, renewable system and metal-air batteries [22, 271-272]. Overall water splitting into oxygen and hydrogen has been considered as a promising solution to the global energy crisis and hydrogen generation [22-23, 25, 273]. However, the slow rate of water splitting is efficiency limited, therefore, a high performance electrochemical catalyst is required to accelerate the two half reactions rates in order to overcome this bottleneck. Currently, a lot of efforts have been devoted to investigate bifunctional electrocatalysts that have efficient performance both in OER and HER. In Tian's research [274], self-supported NiMo nanorods were used as bifunctional catalyst and those materials could achieve current density of 10 mA cm^{-2} for water splitting with a very low voltage of 1.64 V. Liu *et al.* [275] discovered that amorphous CoSe films (with CoSe electrodeposited in Ti mesh) were also excellent bifunctional electrocatalyst for water splitting and only 1.65 V was needed to realise the current density of 10 mA cm^{-2}. Furthermore, two widely used metals Ni-Fe alloys and their nitrides exhibited great performance on water splitting [276-278]. However, for Co and Fe, which are known to have dramatic performance on the OER and HER activities, very limited researches have been exploring their bifunctional performances for overall water splitting.

In this chapter, we use a facile strategy for the preparation of Co-Fe based nanoparticles homogeneously embedded in N-doped porous carbon *via* a one-step carbonisation of the *in-situ* synthesised composite Fe-substituted ZIF-67/graphene oxide (GO) simultaneously. The obvious advantages of using this particular composite as the precursor are as follows: (1) the nanostructured products after high temperature heat treatment can increase the active surface area of the materials; (2) doping with heterogeneous elements can alter the electronic structure of the pristine active species, therefore can optimise its catalytic activity; (3) the bimetallic nanoparticles with graphene and porous carbon, which was achieved by heating treatment in argon atmosphere, could

effectively improve the conductivity of the electrocatalyst. In addition, this type of composites can not only offer large surface area to support active sites for catalytically reactions, but also prevent the accumulation of active species because of the anchoring effect. In this work, the resulting composite Co-Fe-5G-800 exhibited good electrochemical activities with onset potential of 1.41 V in alkaline electrolyte for OER. Particularly, Co-Fe-5G-800 showed remarkable HER activities over a wide pH range, which is better than most of noble metal free catalysts and comparable to that of Co-Fe-800. The increased electrical conductivity, active sites and the improved connectivity between cobalt and iron particles containing porous carbon and N-doped graphene enable the Co-Fe-5G-800 is a promising electrode material for catalysis and energy applications.

However, there are rare researches were done on bi-metallic oxide nanoparticles embedded with graphene and porous carbon, especially based on cobalt and iron element. Although a few studies reported single Co_xO_y [279] and Fe_xO_y [280] as electrocatalyst for OER with relative low activities, to the best of our knowledge, there is no such research that investigating on the synergistic effects between cobalt and iron oxide. Moreover, the combination of Co-Fe oxides with N-doped graphene and porous carbon could also offer triple synergistic effect. The existence of these synergistic effects in the nanocomposites may increase the electrocatalytic activities of the composites compared to the single transition metallic oxide. Additionally, graphene in the nanocomposites can improve the conductivities and enhance water splitting ability. Consequently, in this chapter, a facile strategy was also used to prepare Co-Fe based oxide nanoparticles embedded in N-doped graphene and porous carbon by a two-step carbonisation and oxidation of Fe-substituted ZIF-67 with GO. Due to the triple synergistic effect in the nanocomposites, the resulting samples exhibited remarkable OER and HER activities in alkaline media.

5.2 Characterisation of cobalt-iron/ N-doped porous carbon composites

The morphologies of the as-synthesised composites were investigated by scanning electron microscopy (SEM). As shown in Figure 5.1a-h, the crystal size of composites can be controlled by adjusting the ratio of Co: Fe and treatment temperature. The average crystal size decreased with the increase of the iron content and it is difficult to find any single cobalt particle with octahedral crystal shapes in samples. The crystal size of resulting Co-Fe-800 is only about 1/3 scale of Co-800, indicating particle sizes of the as-synthesised composites were affected by iron content in the samples due to the synergistic effect between cobalt and iron. The SEM images of Co-Fe-600 and Co-Fe-1000 are shown in Figure 5.1e-f and Figure 5.1g-h, separately. Comparing with sample Co-Fe-800, sample Co-Fe-600 displayed the similar crystal size with much more aggregate particles, implying the poor crystallisation of metal particles in the sample. While Co-Fe-1000 exhibited a larger crystal size, suggesting both cobalt and iron convert to metal particles during the high temperature treatment in Argon.

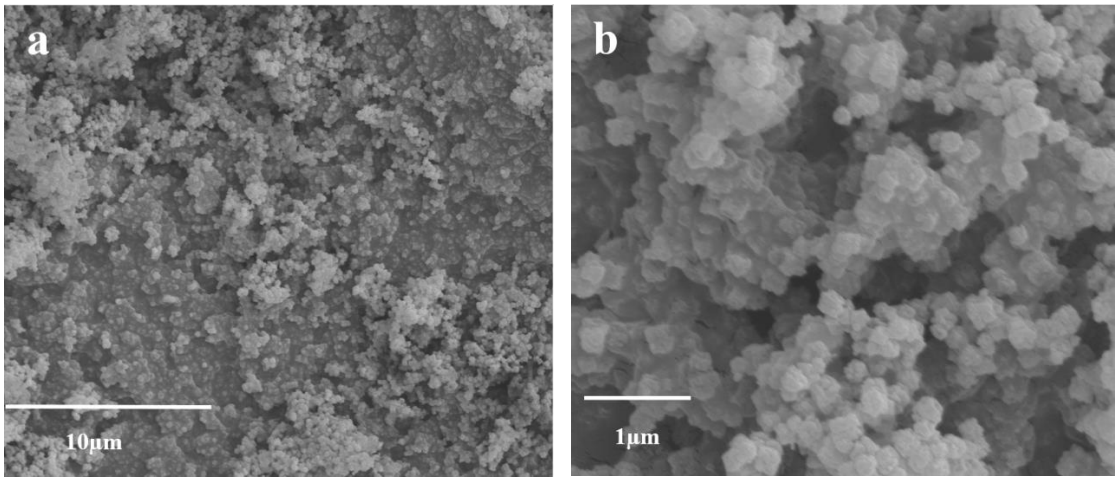

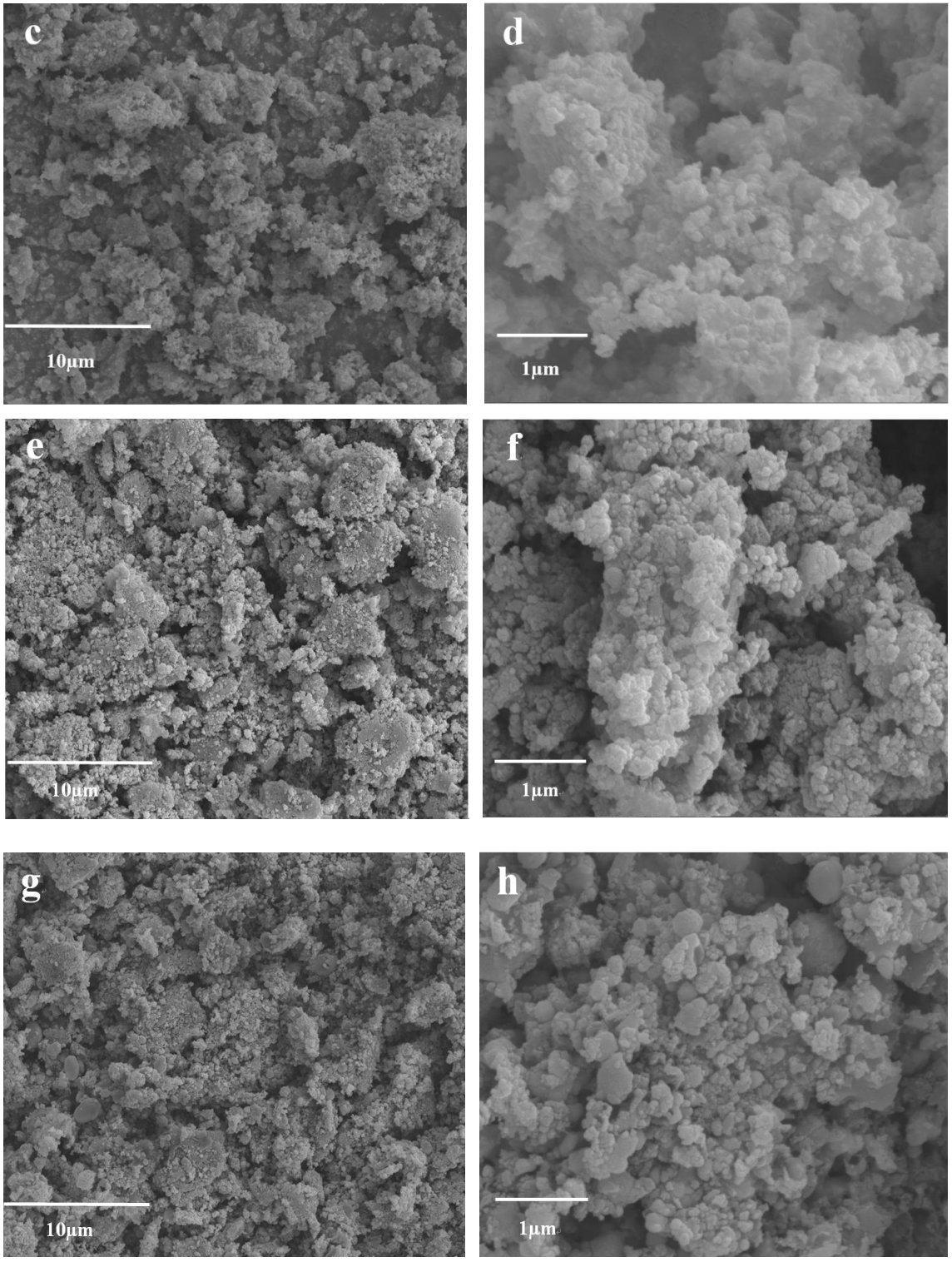

Figure 5. 1 SEM images of the (a, b) Co-800; (c, d) Co-Fe-800; (e, f) Co-Fe-600 and (g, h) Co-Fe-1000

To further investigate the morphologies and the local structure of the prepared materials, transmission electron microscopy (TEM) was used to characterise the representative samples Co-800 and Co-Fe-800. In Figure 5.2, both composites exhibited spherical-like particles after the carbonisation at 800 °C. From the low magnification TEM images, the average particle size is 20-40 nm

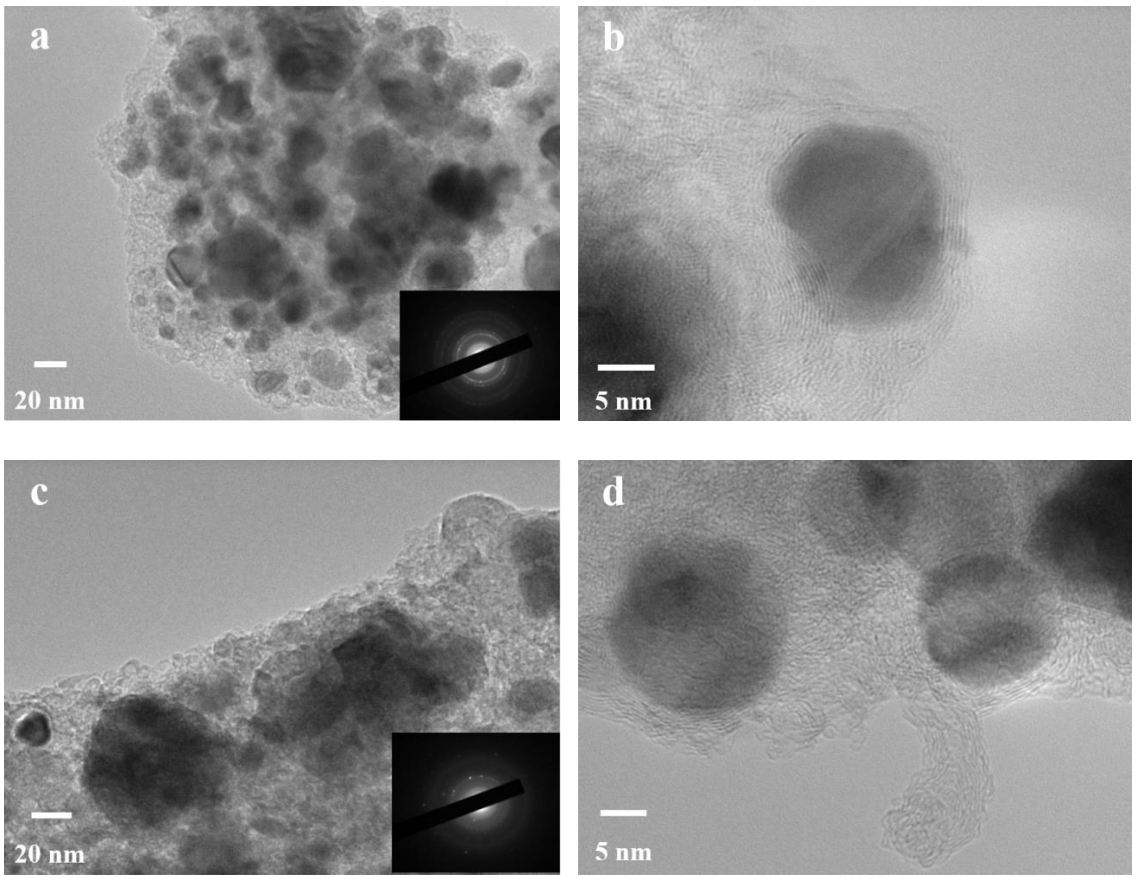

Figure 5. 2 TEM images of (a, b) Co-800 and (c, d) Co-Fe-800. Inset in (a, c) is SAED patterns for corresponding composites

for Co-800; however, the particle size is 15-20 nm for Co-Fe-800, maybe due to the effect of iron existence in the composite. Interestingly, it is easy to see there was around 15 nm long nanotube in the high resolution image of Co-Fe-800, which is *in-situ* formed from carbon due to the catalytic effect of cobalt and iron particles, and these nanotubes can offer more electron transfer pathways and active sites to improve electrochemical activities. Moreover, as shown in Figure 5.2b & d, some carbon onions can be also found with the diameter around 8-15 nm, which were in agreement with the Raman spectrum results and further confirmed that both composites contain graphitised nanostructure. The selected area electron diffraction (SAED) patterns, shown in the inset of Figure 5.2a & c, clearly showed the bright scattered dots contributed from the crystalline metal nanoparticles while the dimmed diffraction rings are from the amorphous porous carbon matrix. In order to ascertain the distribution of cobalt and cobalt/ iron particles in Co-800 and Co-Fe-800, the elemental mapping of those two samples were measured. In Figure 5.3, the element mapping for cobalt exhibited similar pattern with dark area in TEM images, implying the well dispersion of cobalt particles in the composite. Also, the element mapping for

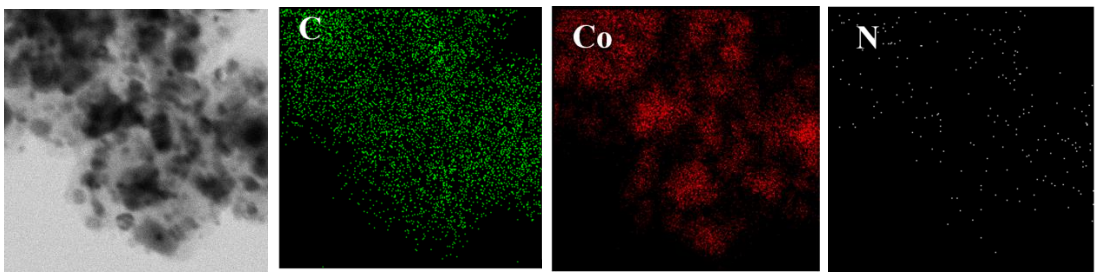

Figure 5. 3 TEM images and element mappings (C, Co and N/ C, Co, Fe and N) for Co-800

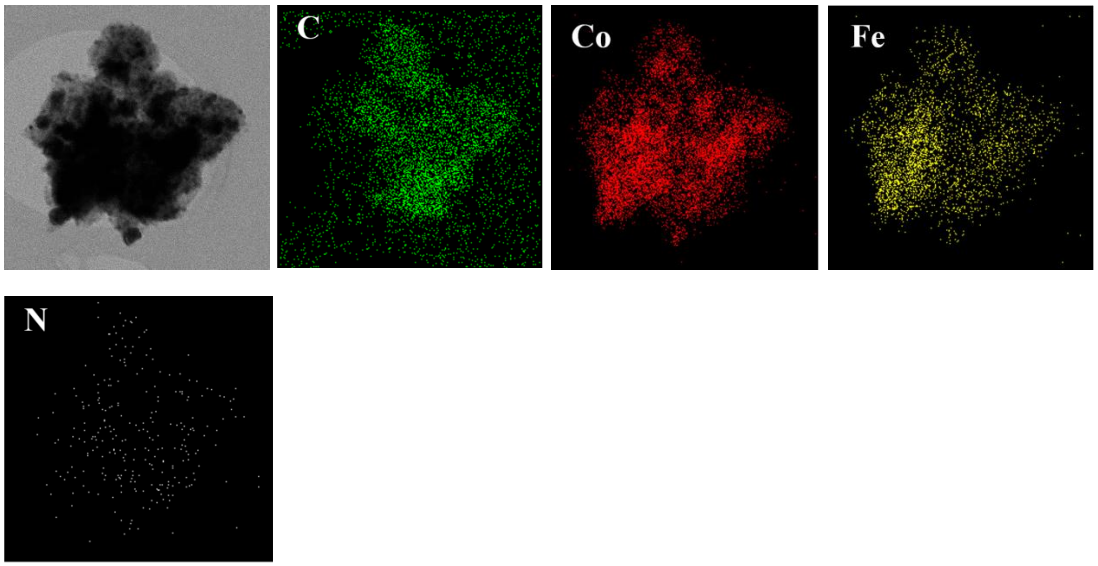

Figure 5. 4 TEM images and element mappings (C, Co and N/ C, Co, Fe and N) for Co-Fe-800

both cobalt and iron exhibited the similar patterns with the dark area in the selected TEM image (Figure 5.4), indicating both cobalt and iron were uniformly distributed in the composite of Co-Fe-800. In addition, the cobalt and cobalt/ iron core-shell structure was formed in Co-800 and Co-Fe-800, respectively.

X-ray photoelectron spectroscopy (XPS) was used to investigate the chemical environment and compositions of the as-synthesised representative composites of Co-Fe in three different heat treatment temperatures. The element surveys shown in Figure 5.5a clearly state the presence of element C, Co, Fe, and N in all the representative samples. In the high-resolution spectrum of C 1s (Figure 5.5b), a main peak centred at 284.5 eV in all the three samples, indicating a sp^2 hybridised graphitic structure was formed which can efficiently improve its electroconductivity [260]. The spectrum can be also deconvoluted into two peaks located at 285.3 and 286.4 eV, which may correspond to C=N and C-O/ C-N, respectively [252, 281-282]. A very weak peak appeared at 290.1 eV both in Co-Fe-800 and Co-Fe-1000, attributed to metal carbide. The high-resolution Co 2p and Fe 2p spectra of the Co/Fe carbide indicated the presence of different bonding

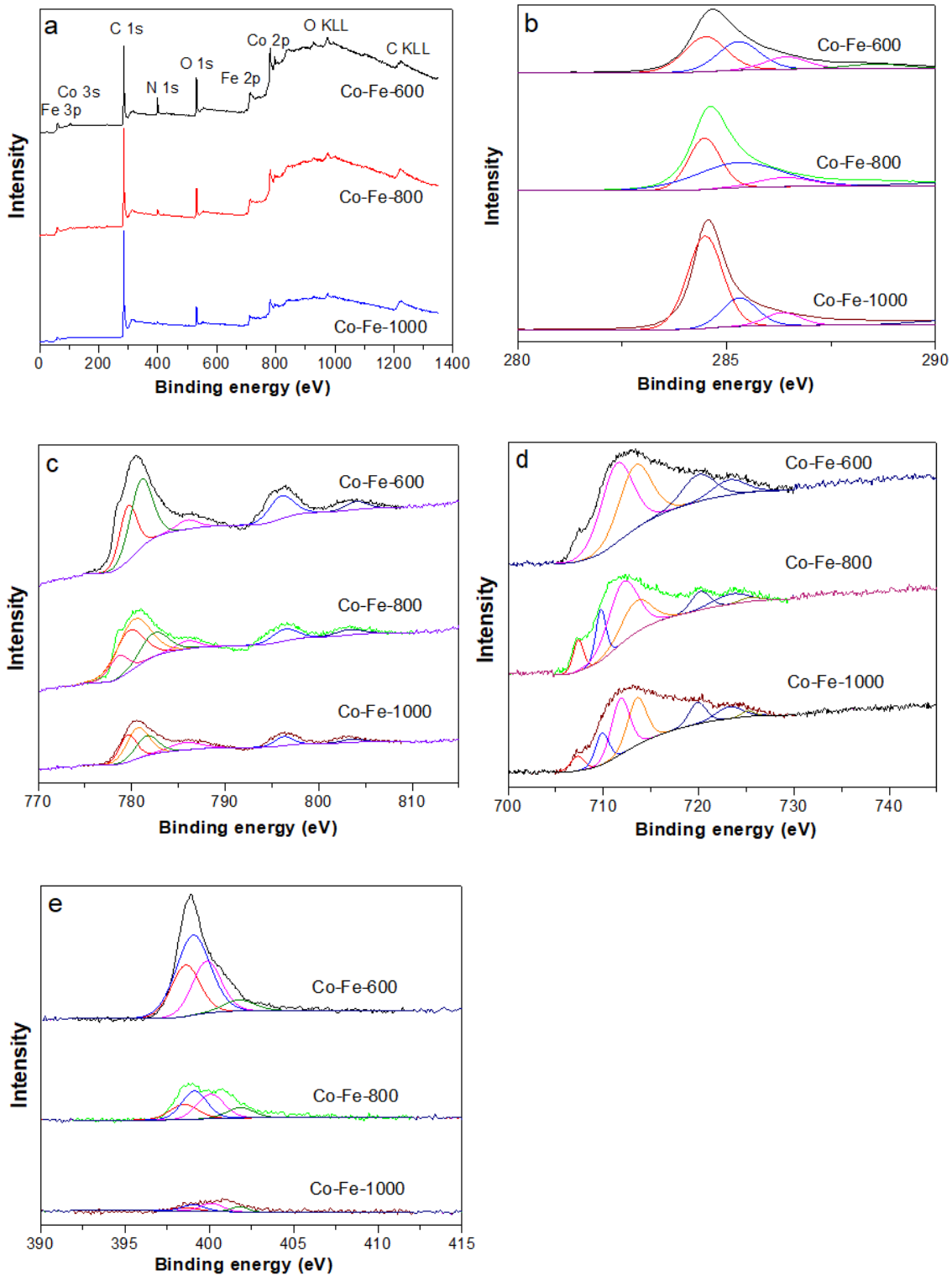

Figure 5. 5 (a) Element survey by XPS and XPS spectrum of (b) C 1s, (c) Co 2p, (d) Fe 2p, (e) N 1s for Co-Fe-T series composites

states of Co and Fe atoms (Figure 5.5c&d). The Co 2p spectra of Co-Fe-600 was deconvoluted into doublets at 779.7, 781. 2 and 796.2 eV, which were consistent with Co $2p_{3/2}$, while two peaks located at 786 and 803.2 eV were consistent with Co $2p_{1/2}$ satellite components [283]. The Fe 2p spectrum (Figure 5.5d) can be deconvoluted into three different peaks located at 711.8, 713.6

and 725.3 eV, which were consistent with Fe 2p $_{3/2}$ [283]. For both Co-Fe-800 and Co-Fe-1000, three doublets at 707.5, 709.8 and 723.4 eV could be found, corresponded to Fe 2p $_{1/2}$ and satellite components [283]. In particular, the presence of Co-C at 781.9 eV and Fe-C at 707.5 and 723.4 eV, respectively, was attributed to the formation of stoichiometric cobalt iron carbides during high-temperature annealing process [284-286]. Moreover, N 1s spectrum (shown in Figure 5.5e) for all samples deconvoluted into four different peaks at 392.8, 399.1, 400.1 and 401.8 eV, which are corresponding to pyridinic-N, Co-N, pyrrolic-N and graphitic-N, respectively [258, 287]. It has been found that the N-doped carbon materials can enhance electrochemical properties and the onset potential in OER and HER.

To identify the synergistic effect in the composite, another series of composites Co-800, Co-Fe-800 and Co-Fe-5G-800 have been analysed by XPS (Figure 5.6). The spectrum of C 1s (shown in Figure 5.6b) for all the three composites obtained at the same carbonisation condition of 800 °C displayed four deconvoluted peaks at 284.5, 285.3, 286.4 and 290.1 eV, which corresponds to sp^2 hybridised graphitic [260], C=N, C-O/ C-N and C-N/metal carbide [252, 281-282], respectively. Similar to previous analysis, carbon with sp^2 hybridised graphitic doped by N, will benefit electrons transfer and the enhancement of the OER and HER activities. The spectrum of Co 2p (Figure 5.6c) exhibited four peaks at 779.7, 781.2, 786 and 796 eV, which were corresponding to Co $2p_{3/2}$ in all samples [283]. In addition, a peak located at 803.2 eV attributed to Co 2p $_{1/2}$ satellite components is a symbol of bivalent oxidation state [283]. The Fe 2p spectrum only appeared in Co-Fe-800 and Co-Fe-5G-800 (shown in Figure 5.6d) can be deconvoluted into the same peaks located at 709.8 and 723.4 eV that is consistent of Fe $2p_{1/2}$ and satellite components [283], while other doublets were found at 711.8, 713.6, 720 and 725.3 eV, which were corresponding to Fe 2p $_{3/2}$ [283] in these two samples. Comparing Co-Fe-800 and Co-Fe-5G-800 with Co-800, two peaks were found at 781.9 and 707.5 eV, which represents Co-C and Fe-C, respectively, was attributed to the formation of stoichiometric cobalt iron carbides during high-temperature annealing process [284-286]. This phenomenon may be due to the synergistic effect between cobalt and iron atoms in the samples. Additionally, the N 1s spectrum (shown in Figure 5.6e) exhibited similar peak positions as discussed above. All samples containing graphitic-N

(401.8 eV) and pyrrolic-N (400.1 eV) may have enhanced electrochemical abilities [258, 287].

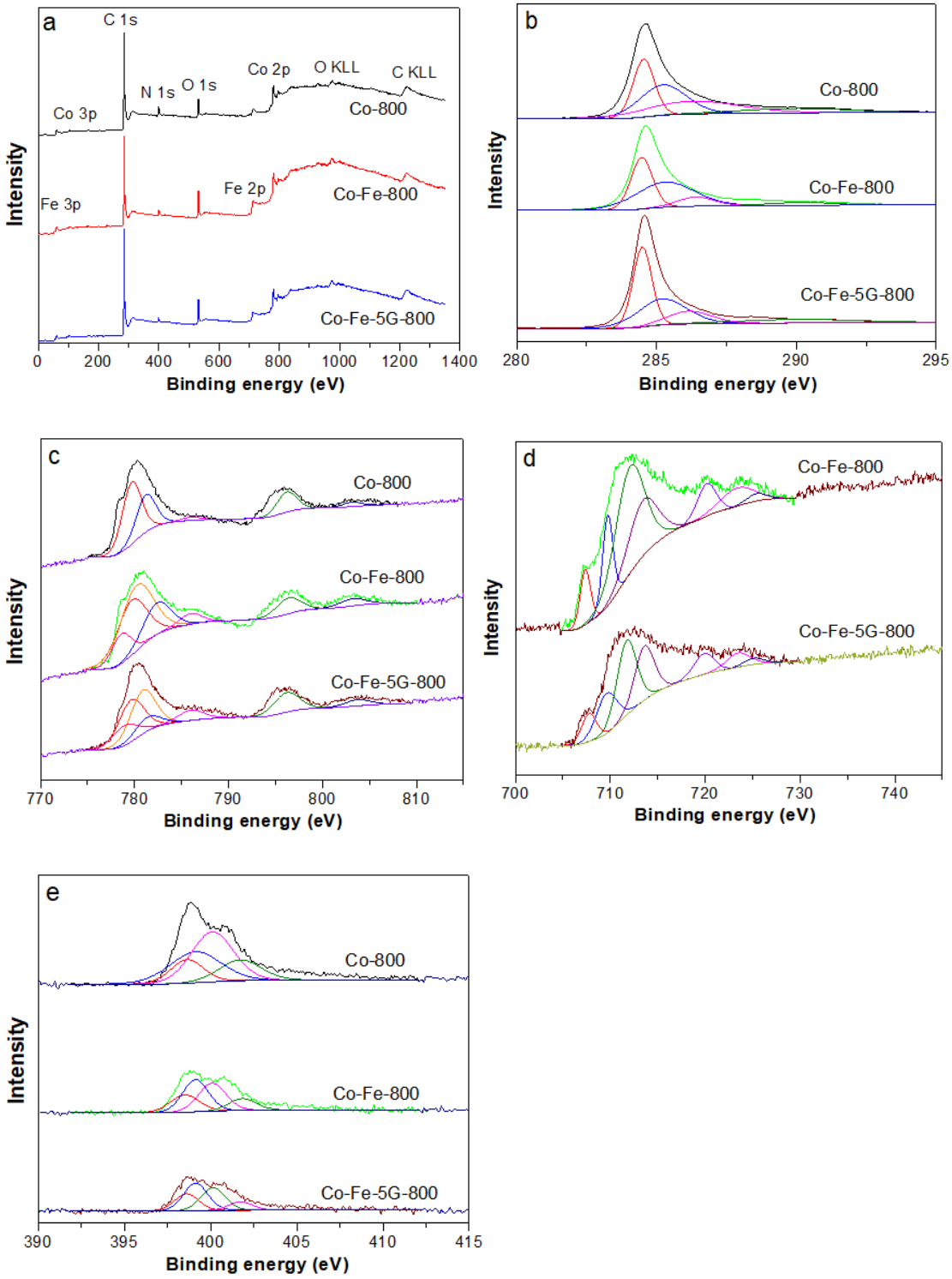

Figure 5. 6 (a) Element survey by XPS and XPS spectrum of (b) C 1s, (c) Co 2p, (d) Fe 2p, (e) N 1s for Co-800, Co-Fe-800 and Co-Fe-5G-800

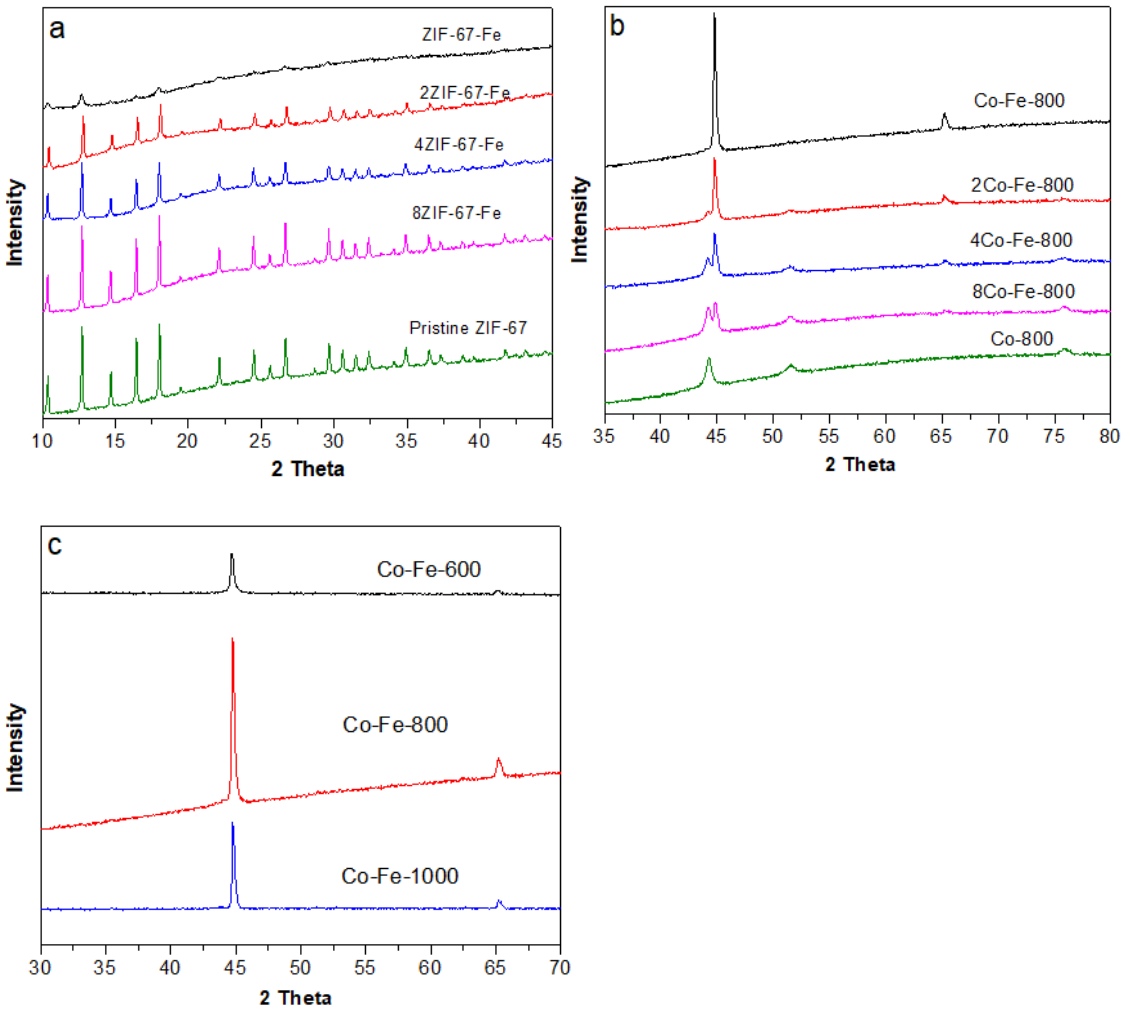

Figure 5. 7 XRD patterns of (a) Fe-substituted ZIF-67 composites (b) xCo-yFe-800 series composites and (c) Co-Fe-T series composites

The crystal structures of the as-synthesised Fe-substituted ZIF-67 with different ratio of cobalt to iron, were investigated by XRD (shown in Figure 5.7a). All precursor composites exhibited same peaks located at 10.2°, 12.5°, 14.5°,16.4°, 18°, 24.5°, 25.8°, 26.9°, corresponding to (002), (112), (022), (013), (222), (223), (224) and (134) planes [244], respectively. The XRD spectra of xCo-yFe-800 series samples are shown in Figure 5.7b. Three peaks appeared at 44°, 52° and 76.5°, corresponding to the diffraction planes of cobalt (111), (200) and (220) (JCPDS 15-0806) [288], respectively, which could be found in Co-800 sample. The diffraction intensity of these three peaks become weaker and blunter with the increase ratio of Fe: Co, while gradually the diffraction peaks are dominated with the metallic Fe phase, suggesting the existence of a synergistic effect between iron and cobalt in the hybrid composites. Eventually, only two peaks located at 44.5° and 65.5°, corresponding to the diffraction planes (110) and (200) of metallic iron (JCPDS 03-065-4899) [289], were found in

Co-Fe-800. Interestingly, no diffraction peaks from metallic cobalt appeared in Co-Fe-800 sample, which may be due to the diffraction intensity of iron are much stronger than cobalt and the diffraction peaks for cobalt emerged with that of iron. In addition, the structures of Co-Fe-T were also measured by XRD (Figure 5.7c). All of them exhibited the same two peaks at 44.5° and 65.5°, indicating the existence of metallic iron in all the composites. Moreover, these two peaks become sharper and more intense with increasing the carbonisation temperature from 600 to 1000 °C, implying an increase of iron crystallinity and iron particle size.

The Raman spectrum of xCo-yFe-800 series composites are shown in Figure 5.8a. All the samples revealed the characteristic D and G bands of carbon at 1350 and 1595 cm^{-1}, which correspond to disordered amorphous carbon and sp^2 hybridised graphitic carbon [290], respectively. However, two peaks located at 2690 cm^{-1} and 2900 cm^{-1} that correspond to the 2D band and G+D band in xCo-yFe-800 series samples, could not be observed in sample Co-800, indicating the existence of a synergistic effect between iron and cobalt that can prompt the formation of a graphitised nanostructure with carbon onions. Moreover, the Co-Fe-T series composites were also measured by Raman spectrum and shown in Figure 5.8b. Sample Co-Fe-600 only showed a weak peak at around 1340 cm^{-1}, implying a very small amount of disordered amorphous carbon existed in it (as further confirmed by TGA-MS). However, the two sample Co-Fe-800 and Co-Fe-1000 displayed sharp peaks at 1350 and 1595 cm^{-1}, indicating that both graphitic carbon and disordered amorphous carbon are presented in these two samples. Moreover, two peaks located at 2690 and 2900 cm^{-1} in sample Co-Fe-800 and Co-Fe-1000, indicating the formation of graphitised structure in both samples. The peaks for Co-Fe-1000 are more intense and sharper, implying a higher graphitisation level and the graphitised nanostructure increases with the increasing of carbonisation temperature.

The thermal stabilities of the as-synthesised xCo-yFe-800 series samples were evaluated *via* heating in air atmosphere and monitored by TGA-MS. As shown in Figure 5.9a, all the samples displayed a weak weight loss below 100 °C, owing to the removal of the adsorbed H_2O in the composites. Then, a major weight loss event happened at 300 °C for all the composites and the percentage of weight loss increases with the increase of the Co: Fe ratio,

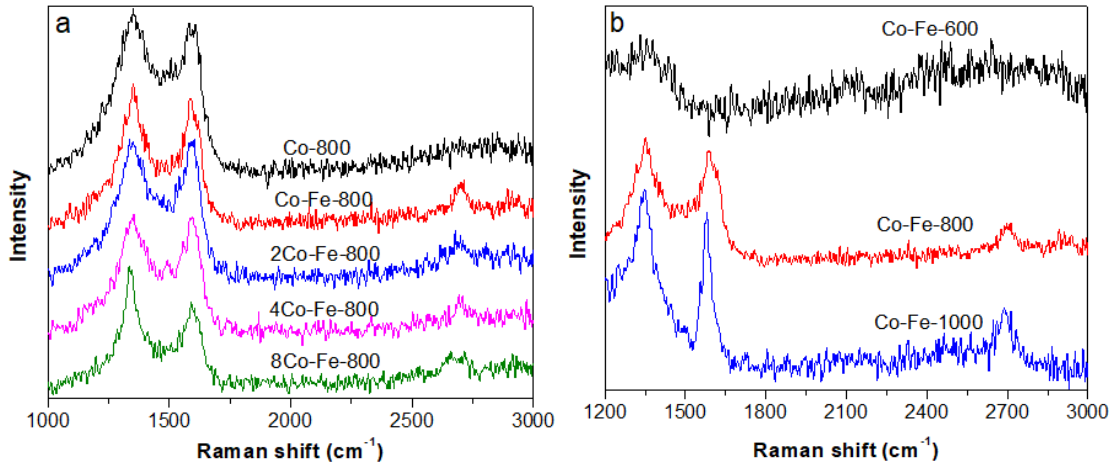

Figure 5. 8 Raman spectra of (a) xCo-yFe-800 series composites and (b) Co-Fe-T series composites

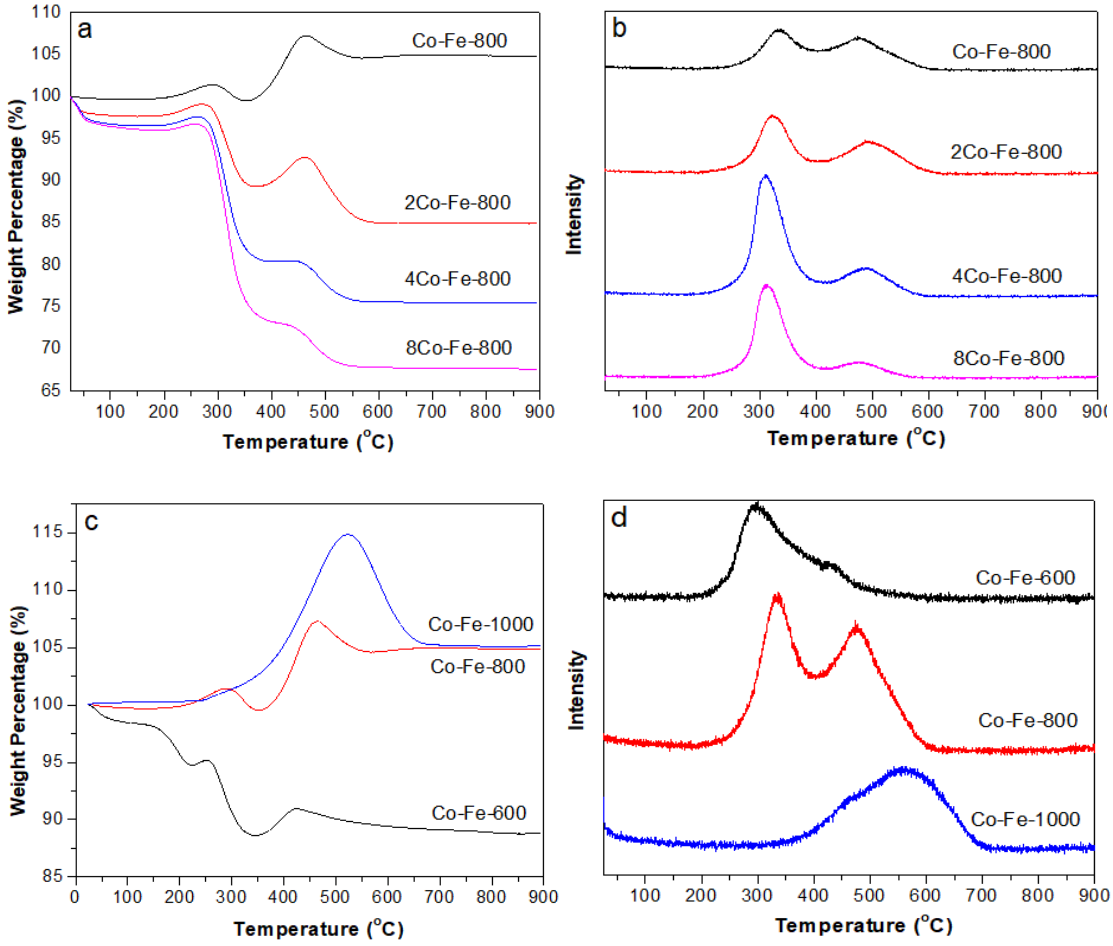

Figure 5. 9 (a, c) TGA and their corresponding MS curves of (b, d) MS signals of CO2 for xCo-yFe-800 and Co-Fe-T series composites, respectively

implying the burning off the formed carbon species. Then, there was a weight increase event at 390 °C that may be due to the oxidation of metal species to high valence state of iron ion, followed by another major weight loss event at 490 °C, which corresponds to the chemical transformation from metal (iron)

carbide to oxide. These weigh loss events could be further confirmed by the MS signals of CO_2 emission in these samples, as shown in Figure 5.9b. The intensity of CO_2 increased at the first event and then decreased at the second one with the increasing ratio of Co: Fe, further indicating the burning off formed carbons and the chemical oxidation of iron carbide at 300 and 490 °C, respectively. In addition, three as-synthesised composites of Co-Fe-600, Co-Fe-800 and Co-Fe-1000 were also measured by TGA-MS and shown in Figure 5.9c. Interestingly, Co-Fe-600 exhibited two major weight loss evens at 200 and 300 °C, suggesting the decomposition of un-converted organic linkers and the burning of the formed carbon, respectively. In contrast, Co-Fe-1000 exhibited a big weigh increase event in the temperature range of 250-560 °C, due to the oxidation of both metals to oxides, and followed by a major weight loss event at 560 °C, suggesting the chemical transformation of metal carbide to metal oxides and the burn off carbon species in air. In the MS result shown in Figure 5.9d, there is only one CO_2 emission peak at 300 °C for Co-Fe-600, indicating that only small amount of carbon existed in this sample, which is consistent to the Raman spectrum (shown in Figure 5.8). In comparison, the CO_2 emission peak appeared at around 570 °C for Co-Fe-1000, implying that the CO_2 is from the burn off carbon and the chemical conversion of metal carbide to oxides in the composite. For sample Co-Fe-800, both iron carbide and porous carbon are presented in this composite.

5.3 Electrocatalytic performance of cobalt-iron/ N-doped porous carbon composites

5.3.1 Oxygen evolution reaction

The electrocatalytic activities of the as-synthesised xCo-yFe-T series composites for oxygen evolution reaction (OER) were evaluated in O_2-saturated 1M KOH (pH=14) electrolyte using a three electrodes system with scan rate of 5 mVs^{-1}. Owing to the effect of ohmic resistance (iR), the as-measured current did not reflect the intrinsic behaviour of the tested samples. Therefore, before OER measurement, all the samples were subjected to initial current for iR correction. The OER performance of the catalytic materials derived from Co: Fe ratio of 1: 0, 1: 1, 2: 1, 4: 1 and 8: 1 carbonised in Argon atmosphere at 800 °C were first measured by steady-state linear sweep voltammetry on a rotating disk electrode and the results are shown in

Table 5. 1 OER performances of xCo-yFe-T series composites

Catalyst	Onset potential (V vs. RHE)	Potential (V vs. RHE) @ current density of 10 mA cm^{-2}	Tafel slope (mV/dec)
Co-800	1.56	1.61	59.2
8Co-Fe-800	1.52	1.58	58.8
4Co-Fe-800	1.49	1.56	52.5
2Co-Fe-800	1.46	1.53	47.7
Co-Fe-800	1.44	1.48	45.2
Co-Fe-600	1.46	1.50	63.6
Co-Fe-1000	1.43	1.50	38.4

Figure 5.10a. Samples Co-Fe-800, 2Co-Fe-800 and 4Co-Fe-800 exhibited excellent onset potential of 1.44, 1.46 and 1.49 V, respectively, which are all much higher than that of reference material IrO_2/C (1.5 V), while 8Co-Fe-800 and Co-800 showed lower onset potential of 1.52 and 1.56 V, respectively. Moreover, all the samples achieved current density of 10 mA cm^{-2} at small overpotential of 1.48, 1.53, 1.56, 1.58 and 1.61 V for Co-Fe-800, 2Co-Fe-800, 4Co-Fe-800, 8Co-Fe-800 and Co-800, respectively, which are all lower than the value of 1.63 V for IrO_2 and other reported bimetal electrocatalysts including NiFe, CoNi and CoSe. It is believed that the introduction of iron can trigger synergistic effects between cobalt and iron particles and result in bi-functional performances of the materials, which will efficiently enhance the OER activities. Meanwhile, the Tafel slope results, which derived from the polarisation curves are shown in Figure 5.10b. Compared with the Tafel slope values of 2Co-Fe-800 (47.7 mV/dec), 4Co-Fe-800 (52.5 mV/dec), 8Co-Fe-800 (58.8 mV/dec), Co-800 (59.2 mV/dec) and IrO_2 (82 mV/dec), the sample Co-Fe-800 displayed the smallest value of 45.2 mV/dec, indicating its remarkable OER reaction rate. Based on the above results, the OER performance of samples with Co: Fe =1: 1 exhibited excellent electrochemical activities, hence Co-Fe-T series composites obtained under different carbonisation temperatures were further evaluated. The polarisation curve of Co-Fe-T and IrO_2/C were shown in Figure 5.10c. Obviously, Co-Fe-1000 exhibited the lowest onset potential of 1.43 V, which was 10 mV and 30 mV lower than that of Co-Fe-800 and Co-Fe-600,

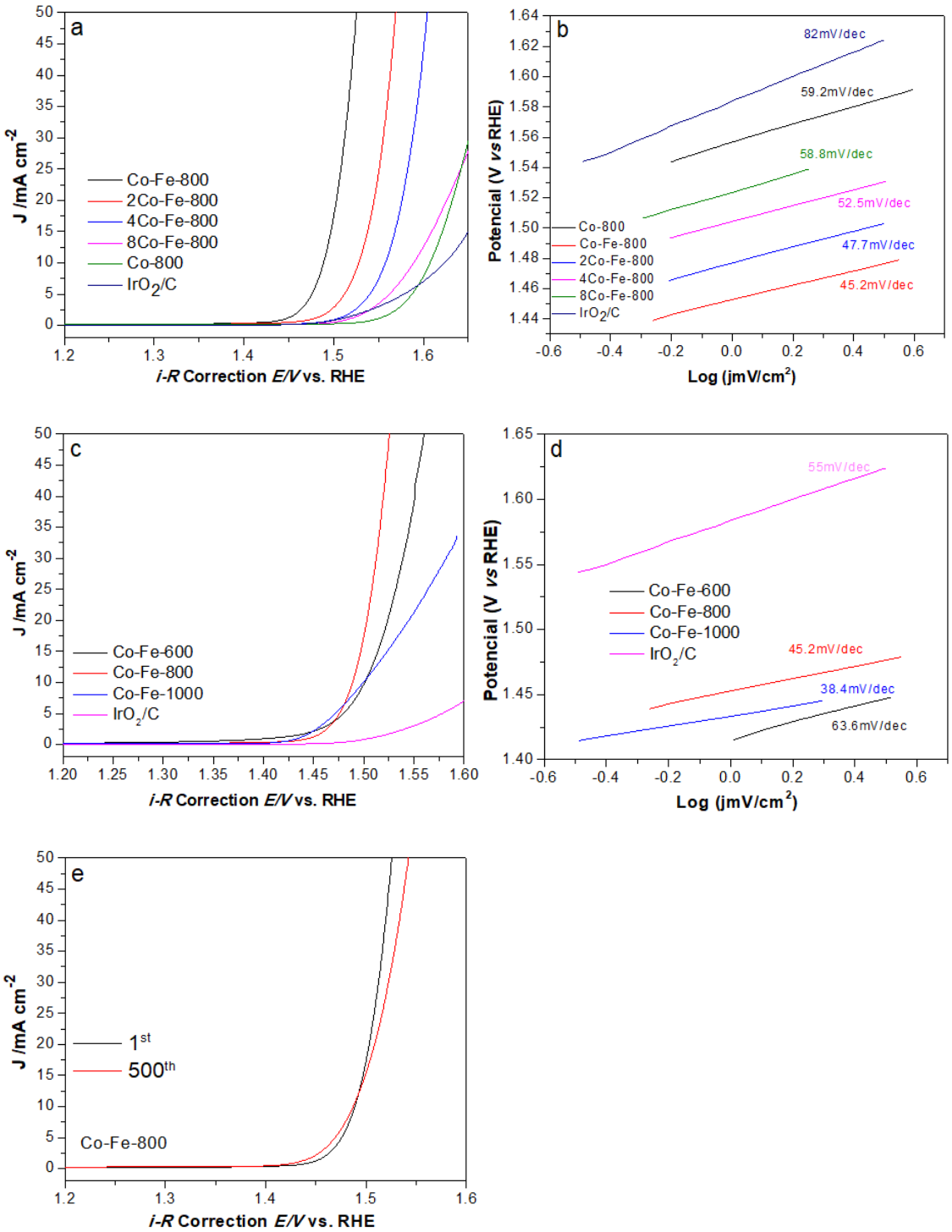

Figure 5. 10 Polarisation curves for OER on (a) xCo-yFe-800 series composites and IrO_2/C and (b) their Tafel plot (c) Co-Fe-T series composites and IrO_2/C and (d) their Tafel plot (e) durability test for Co-Fe-800

respectively. However, potential of 1.48 V was acquired to reach the current density of 10 mA cm^{-2} for Co-Fe-800, which was 20 mV lower than both Co-Fe-1000 and Co-Fe-600. Moreover, only a potential of 1.52 V is required for sample Co-Fe-800 to reach the current density of 50 mA cm^{-2}, while the values of 1.56 V and >1.6 V are needed for sample Co-Fe-1000 and Co-Fe-600 to

realise the same current density, respectively. In addition, the Tafel slope (shown in Figure 5.10d and Table 5.1) values were 38.4, 45.2 and 63.6 mV/dec for Co-Fe-1000, Co-Fe-800 and Co-Fe-600, respectively. It is likely that part of bimetal particles contained in Co-Fe-1000 were easily oxidised during the OER process to form divalent state metal oxides which may accelerate the OER reaction rate; however, these metal particles are lacking of high density active sites, and consequently the samples cannot reach high current density at a fixed potential compared with sample Co-Fe-800. Additionally, the chronoamperometric test of Co-Fe-800 was also carried out and shown in Figure 5.10e. Excitingly, after 500^{th} times scanning at the scan rate of 5 mVs^{-1}, sample Co-Fe-800 exhibited even lower onset potential than the initial one, which may be due to the increase of oxidised cobalt ions during the LSV scanning of the composites that formed more active oxides species on the surface of the samples.

5.3.2 Hydrogen evolution reaction

The HER performance of xCo-yFe-T series composites were all evaluated in 1M KOH electrolyte and the iR-corrected linear sweep voltammetry curves are shown in Figure 5.11a. The samples 2Co-Fe-800, 4Co-Fe-800 and 8Co-Fe-800 exhibited very similar onset potentials at around 0.23 V, which is higher than that of Co-Fe-800 (0.21 V) and much lower than the value of Co-800 (0.28 V). Meanwhile, both 4Co-Fe-800 and 8Co-Fe-800 realised a current density of 10 mA cm^{-2} at a same overpotential of 275 mV, which is 5 mV and 20 mV higher than the value of 2Co-Fe-800 and Co-Fe-800, respectively, while 65 mV lower than that of Co-800. Moreover, to achieve the current density of 50 mA cm^{-2} and 100 mA cm^{-2}, overpotential of 325 and 350 mV were required for sample Co-Fe-800, which exhibited the best HER performance than others. Based on the LSV curves of the HER performance of the samples, their Tafel slope were calculated and summarised. In Figure 5.11b and Table 5.2, the Tafel slope value of 94 mV/dec was obtained for sample Co-Fe-800 and other samples like 2Co-Fe-800, Co-800, 4Co-Fe-800 and Co-800 exhibited the Tafel slopes in the range of 96-101 mV/dec. Obviously, the introduction of iron can produce a synergistic effect with cobalt and this could optimise their electronic structure. Meanwhile, the samples with Co: Fe ratio of 1: 1 exhibited remarkable HER performance compared with other Co: Fe ratio in alkaline media. Based on this

result, the HER performance of Co-Fe-T series composites were further measured. From Figure 5.11c, we can find that both Co-Fe-600 and Co-Fe-800 exhibited the same onset potential of 0.21 V, which is much lower than that of 0.33 V for Co-Fe-1000.

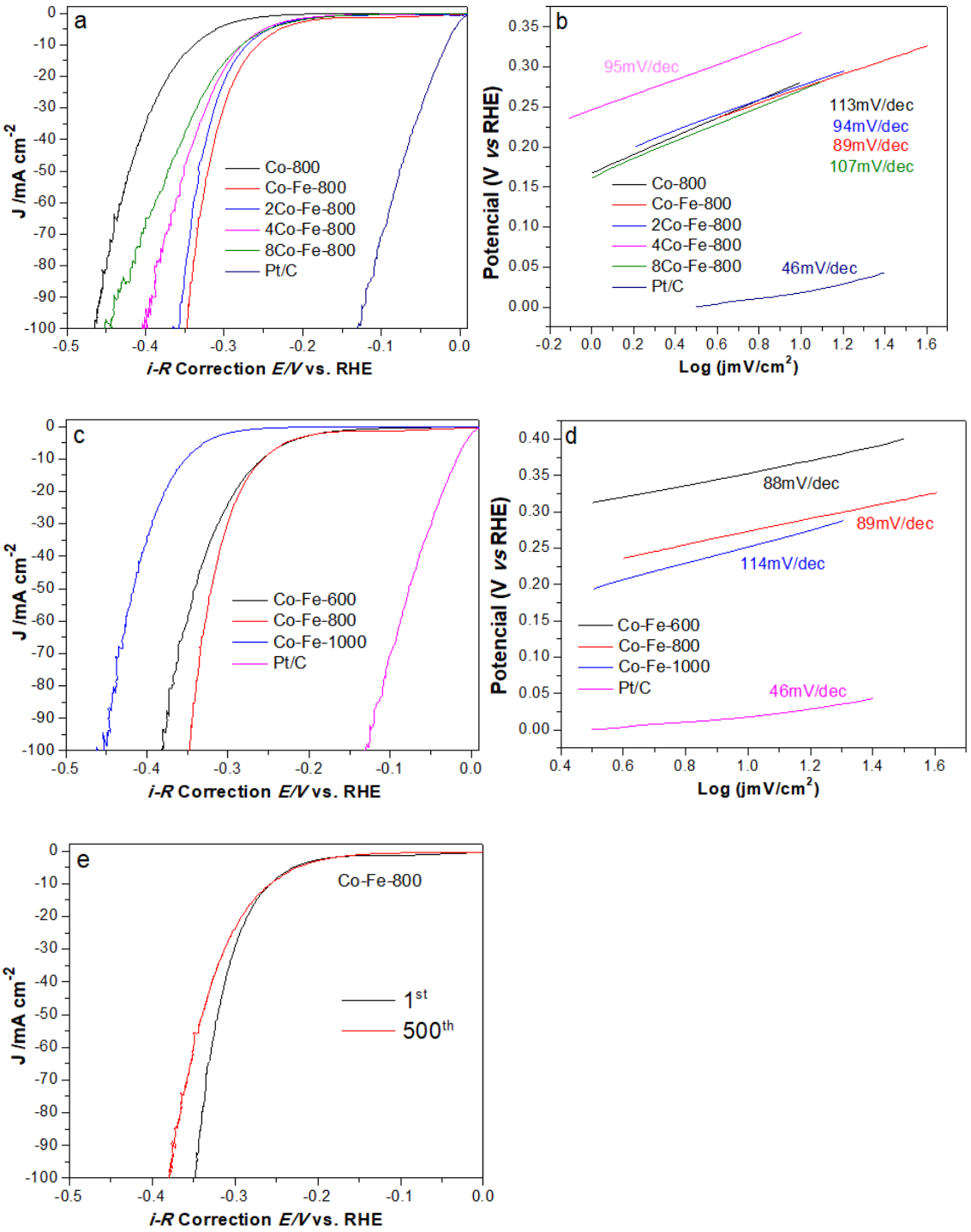

Figure 5. 11 Polarisation curves for HER on (a) xCo-yFe-800 series composites and Pt/C and (b) their Tafel plot (c) Co-Fe-T series composites and Pt/C and (d) their Tafel plot (e) durability test for Co-Fe-800; Measured in 1 M KOH electrolyte

Interestingly, both of them can also achieve a current density of 10 mA cm^{-2} at a same overpotential of 255 mV, whereas 350 mV is required for Co-Fe-1000. However, the overpotential of 325 and 350 mV are needed for sample Co-Fe-800 to achieve a current density of 50 and 100 mA cm^{-2}; in contrast, 345 and 380 mV were required for sample Co-Fe-600. Tafel slope results for those samples are shown in Figure 5.11d. The slope value of both samples Co-Fe-600 and Co-Fe-800 was 89 mV/dec, which is much lower than that of sample Co-Fe-1000 (114 mV/dec). From the above HER results, it indicated that much high level of active sites may exist in both Co-Fe-600 and Co-Fe-800, and the metal ions in the samples were readily reduced by the *in-situ* formed carbon, therefore, exhibiting the similar onset potentials and slope values. However, due to the relative low amount of carbon contained in the sample Co-Fe-600, it cannot reach a high current density in comparison with Co-Fe-800. Owing to the existence of metal carbide particles in the sample, Co-Fe-1000 exhibited weak HER activities during the test. In addition, the chronoamperometric test was measured and shown in Figure 5.11e. After 500^{th} scanning cycles, Co-Fe-800 exhibited a similar I-V curve to its initial one and only drop 30 mV at the current density of 10 mA cm^{-2}.

Table 5. 2 HER performances of xCo-yFe-T series composites. Measured in 1M KOH and 0.5M H_2SO_4 electrolyte

Catalyst	HER Measured in 1M KOH electrolyte			HER Measured in 0.5M H_2SO_4 electrolyte		
	Onset potential (V vs. RHE)	Overpotential (V vs. RHE) @ current density of 10mA cm^{-2}	Tafel slopte (mV/dec)	Onset potential (V vs. RHE)	Overpotential (V vs. RHE) @ current density of 10mA cm^{-2}	Tafel slopte (mV/dec)
Co-800	0.28	0.335	113	0.28	0.37	97
8Co-Fe-800	0.23	0.27	107	0.34	0.4	101
4Co-Fe-800	0.23	0.27	95	0.34	0.41	99
2Co-Fe-800	0.23	0.265	94	0.28	0.36	96
Co-Fe-800	0.21	0.25	89	0.26	0.34	94

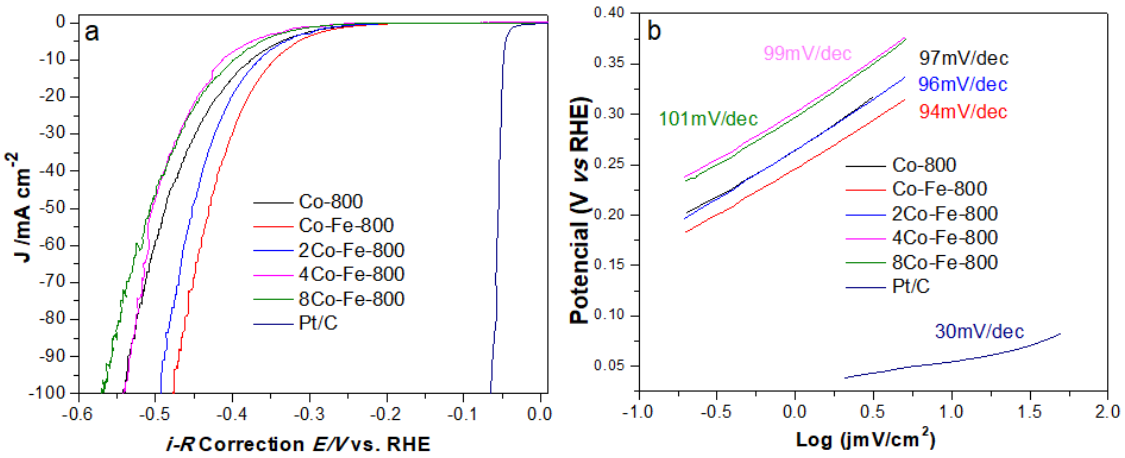

Figure 5. 12 Polarisation curves for HER on (a) xCo-yFe-800 series composites and Pt-C and (b) their Tafel plot; Measured in 0.5 M H_2SO_4 electrolyte

The HER performance of xCo-yFe-800 series composites were also assessed in acid electrolyte (0.5M H_2SO_4 solution). As shown in Figure 5.12a, we can find the polarisation curve recorded for sample Co-Fe-800 showed the lowest onset potential of 0.26 V. In contrast, other samples exhibited higher onset potentials (shown in Table 5.2) ranging from 0.28 to 0.34 V. It should be noted that an overpotential of 0.34 V was required for Co-Fe-800 to achieve the current density of 10 mA cm^{-2}, which is slightly lower than others ranging from 0.36 to 0.41 V. Meanwhile, the Tafel slopes of the samples (shown in Figure 5.12b) also reflected their HER activity. The Co-Fe-800 displayed the lowest slope value of 94 mV/dec, while the others' slope values were ranging from 96 to 101 mV/dec. Based on these experimental results, it is clear that the iron contained samples not only exhibited superior OER/HER activities in alkaline media, but also showed good HER performance in acid electrolyte. More importantly, both the ratio of Co: Fe and carbonisation temperature can be optimised and the sample Co-Fe-800 exhibited the best overall water splitting activities among all catalysts.

5.4 Characterisations of cobalt-iron/ N-doped porous carbon/ graphene composites

From the previous work, the bimetal cobalt and iron and N doped porous carbon nanocomposites, especially the Co-Fe-800 sample express a good electrocatalytic performance. Based on this result, graphene was introduced into above system to improve the electrochemical performance for the reason of its excellent electrical conductivity, high surface area, and good chemical and environmental stability. In addition, N doped graphene will create some heteroatomic defects, which also enhance the conductivity at the electrolyte interface. In the following part, the graphene based bimetal cobalt and iron series sample results will be presented.

The chemical environment and structure of as-synthesised composites of Co-Fe-5G-T were investigated by XPS (Figure 5.13a). From the spectrum of C 1s (Figure 5.13b), all samples showed three doublets at 284.5, 285.3 and 286.4 eV, which are corresponding to the sp^2 hybridised graphitic, C=N and C-O/ C-N [260] component, respectively, indicating the formation of graphitic structure in all of them. In the spectrum of Co 2p (Figure 5.13c), four doublets at 779.7, 781.2 and 796.2 eV could be found, which were consistent to the presence of Co $2p_{3/2}$ in composites. Another two more peaks appeared at 786 and 803.2 eV, corresponding to coordination Co $2p_{1/2}$ and satellite components, due to the presence of cobalt ions [283]. Interestingly, two peaks at 781.3 eV (Co-C) could be found in sample Co-Fe-5G-800 and Co-Fe-5G-1000, but did not display in Co-Fe-5G-600, may be attributed to the formation of stoichiometric cobalt iron carbides during high-temperature annealing process [284-286]. From the spectrum of Fe 2p (Figure 5.13d), all samples exhibited doublets at 707.5, 709.8 and 723.4 eV, which were corresponding to Fe $2p_{1/2}$. Apart from that, three different peaks located at 711.8, 713.6 and 725.3 eV, were consistent to the presence of Fe $2p_{3/2}$ and satellite components in all samples [283]. Furthermore, the N 1s spectrum (Figure 5.13e) for all samples deconvoluted into four different peaks at 392.8, 399.1, 400.1 and 401.8 eV, corresponding to pyridinic-N, Co-N, pyrrolic-N and graphitic-N, respectively. It has been found that the N-doped carbon materials can enhance electrochemical properties and improve the onset potential in OER and HER. Based on the results from XPS, the Co-Fe-5G-800 are consisting of C, Co, Fe and N.

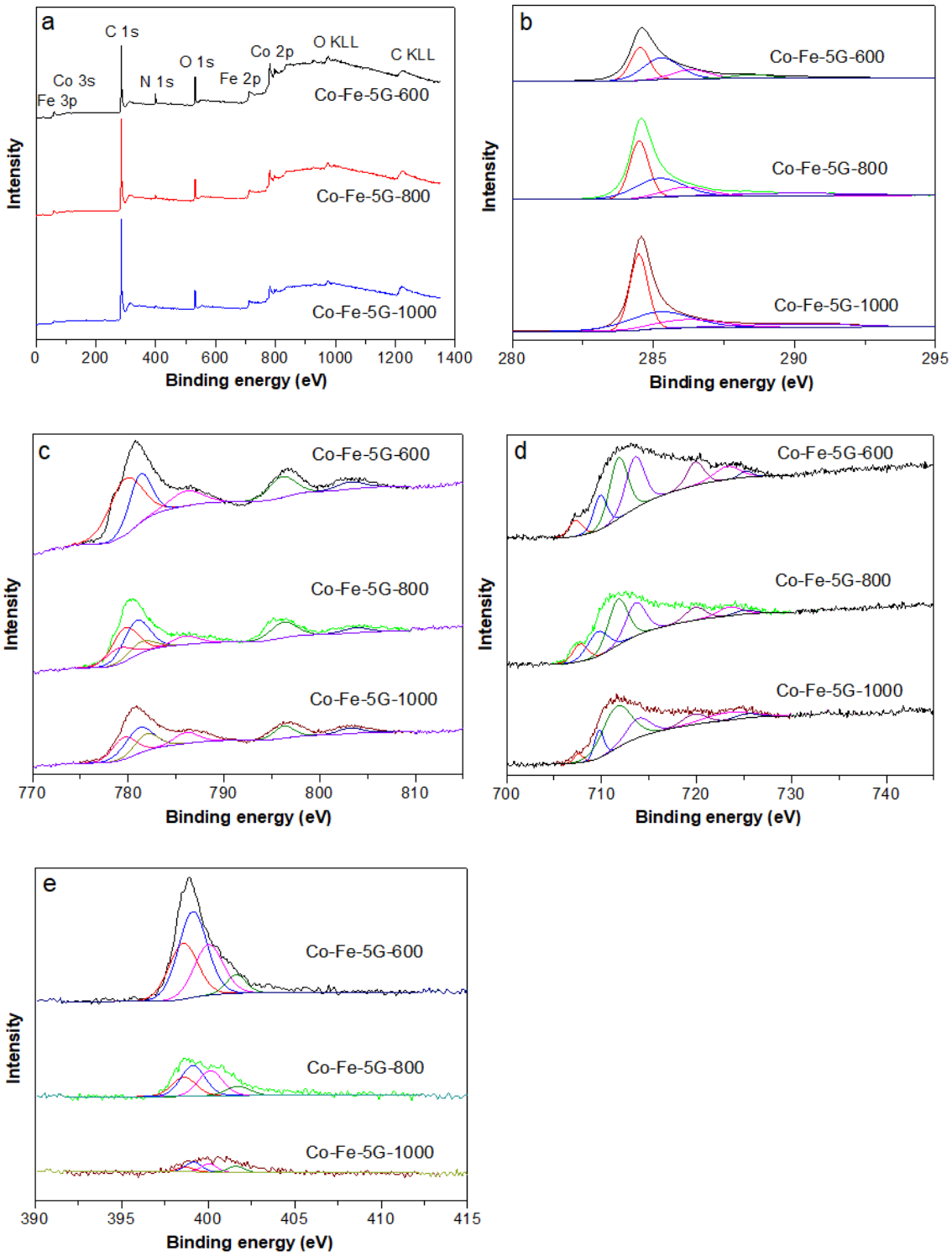

Figure 5. 13 (a) Element survey by XPS and fine XPS spectrum of (b) C 1s, (c) Co 2p, (d) Fe 2p, (e) N 1s for Co-Fe-5G-600, Co-Fe-5G-800 and Co-Fe-5G-1000

The XRD patterns of Fe-substituted GO/ZIF67 precursors are shown in Figure 5.14a. All precursor composites exhibited the same peaks located at 10.2°, 12.5°, 18°, 26.9°, corresponding to (002), (112), (222), and (134) planes of ZIF-67 [288], respectively, indicating the structure of ZIF-67 was not dramatically damaged by the addition of GO and iron species into the synthesis gel. After

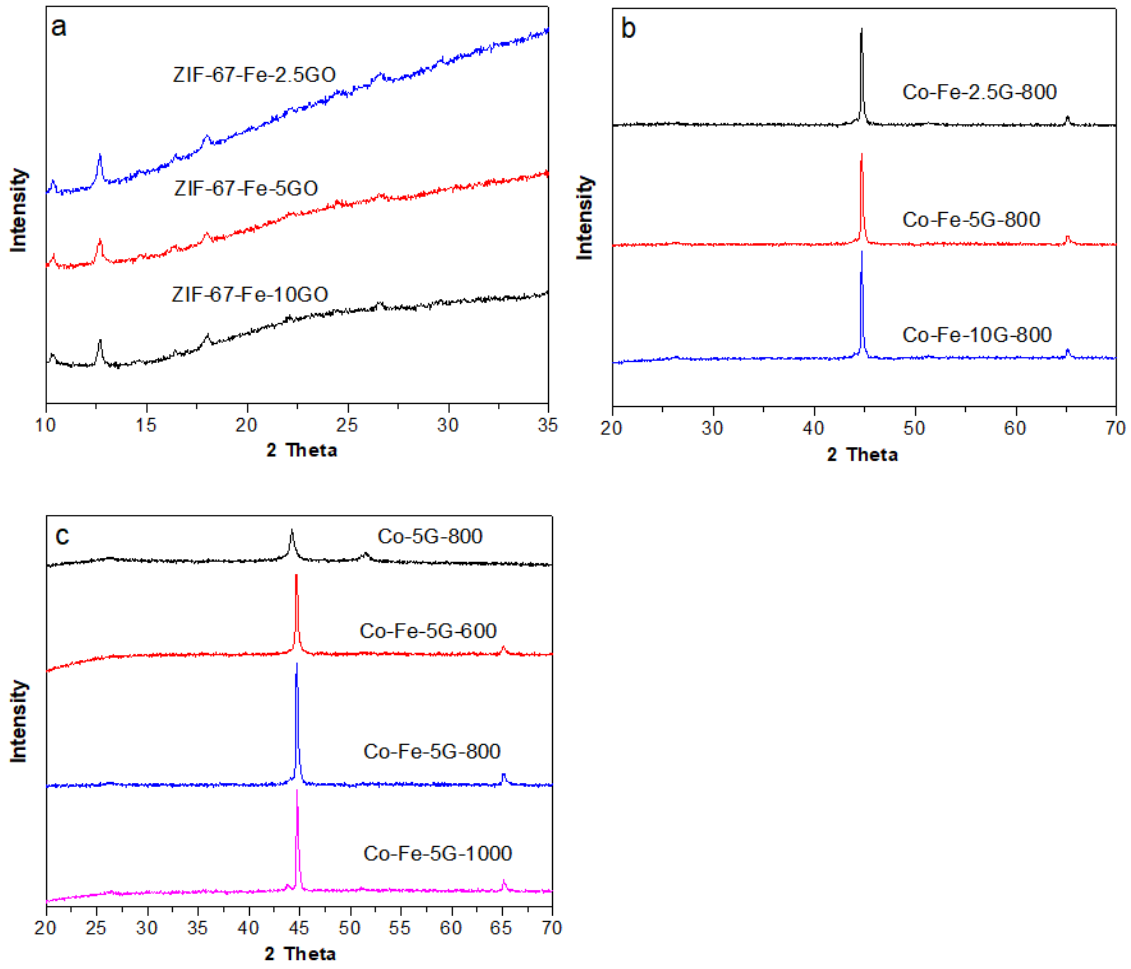

Figure 5. 14 XRD patterns of (a) Fe-substituted GO/ZIF-67 composites (b) Co-Fe-zG-800 series composites and (c) Co-Fe-5G-T series composites and Co-5G-800

the carbonisation process, the XRD patterns of Co-Fe-zG-800 series composites are shown in Figure 5.14b. As what was discussed about the xCo-yFe-800 XRD results before, we could not find any peak of metal cobalt in Co-Fe-800 due to the strong diffraction intensity of iron. Therefore, only two peaks located at 44.5 and 65.5° corresponding to iron (110) and (200) (JCPDS 03-065-4899) [289] diffraction planes could be found in Co-Fe-zG-800. Obviously, the different amount of introduced graphene in the composites have no effect on the crystallinity of the composites. Moreover, a very weak peak located at 26° appeared in all samples maybe because of the graphene contained in the composites. In addition, the XRD patterns of Co-Fe-5G-T and Co-5G-800 are shown in Figure 5.14c. Similar to above observance, all the iron-containing samples exhibited two strong diffraction peaks at 44.5 and 65.5° corresponding to iron (110) and (200) planes, two other peaks of sample Co-5G-800 appeared at 44 and 52°, corresponding to cobalt (111) and (200) (JCPDS 15-0806) [291] diffraction planes. With the increase of carbonisation temperature, the two

diffraction peaks of metal iron became sharper and more intense, which indicates an increase of iron crystalline and its particle sizes.

The Raman spectra of Co-Fe-zG-800 series composites are shown in Figure 5.15a. All of them revealed the characteristic D and G bands of carbon at 1350 and 1595 cm^{-1}, which correspond to disordered amorphous carbon and sp^2 hybridised graphitic carbon, respectively. Furthermore, two peaks could be found at around 2690 cm^{-1} and 2900 cm^{-1}, indicating the formation of graphitised structure in all the composites. The Raman spectrum of Co-Fe-5G-T series composites and Co-5G-800 are shown in Figure 5.15b. Both D and G bands could be found in sample Co-5G-800, Co-Fe-5G-800 and Co-Fe-5G-1000. In contrast, two weak peaks appeared at D and G bands in sample Co-Fe-5G-600, indicated that only a small amount of graphene and rare carbon achieved after the heating process, which was also confirmed by XPS and TGA-MS results.

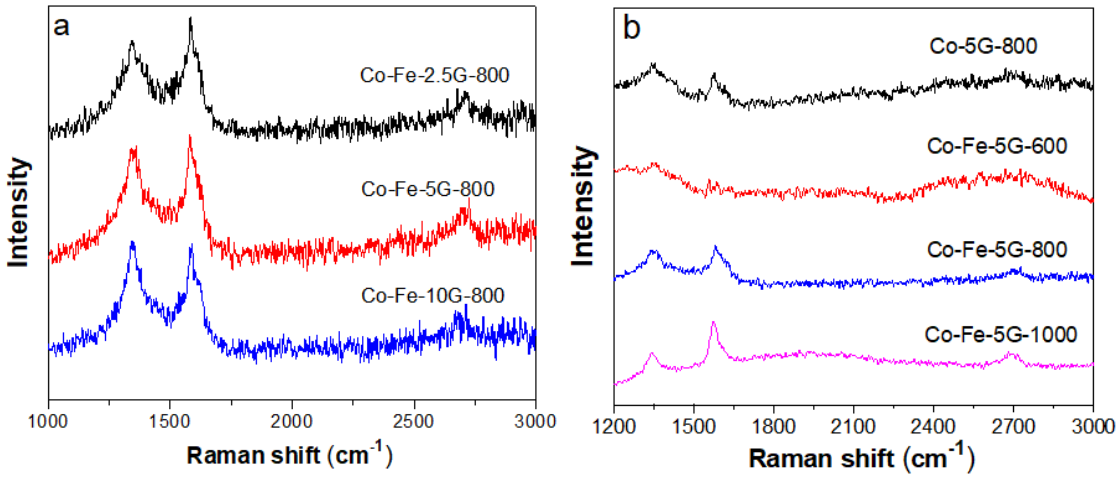

Figure 5. 15 Raman spectra of (a) Co-Fe-zG-800 series composites and (b) Co-Fe-5G-T series composites and Co-5G-800

The thermal stabilities of the as-synthesised Co-Fe-zG-800 series composites were measured by TGA-MS. As shown in Figure 5.16a, all samples showed weak weight loss below 100 °C due to the removal of the adsorbed H_2O or moisture in the composites, followed by a weight increase event between 200 and 300 °C, owing to the oxidation of metal in composites. Then, another weight increase event at 390 °C, may be due to the oxidation of metal ions to high valence state, followed by a major weight loss at around 490 °C, which is corresponding to chemical conversion of metal carbide to metal oxide and CO_2. Their emission signals of CO_2 are shown in Figure 5.16b. Obviously, the CO_2

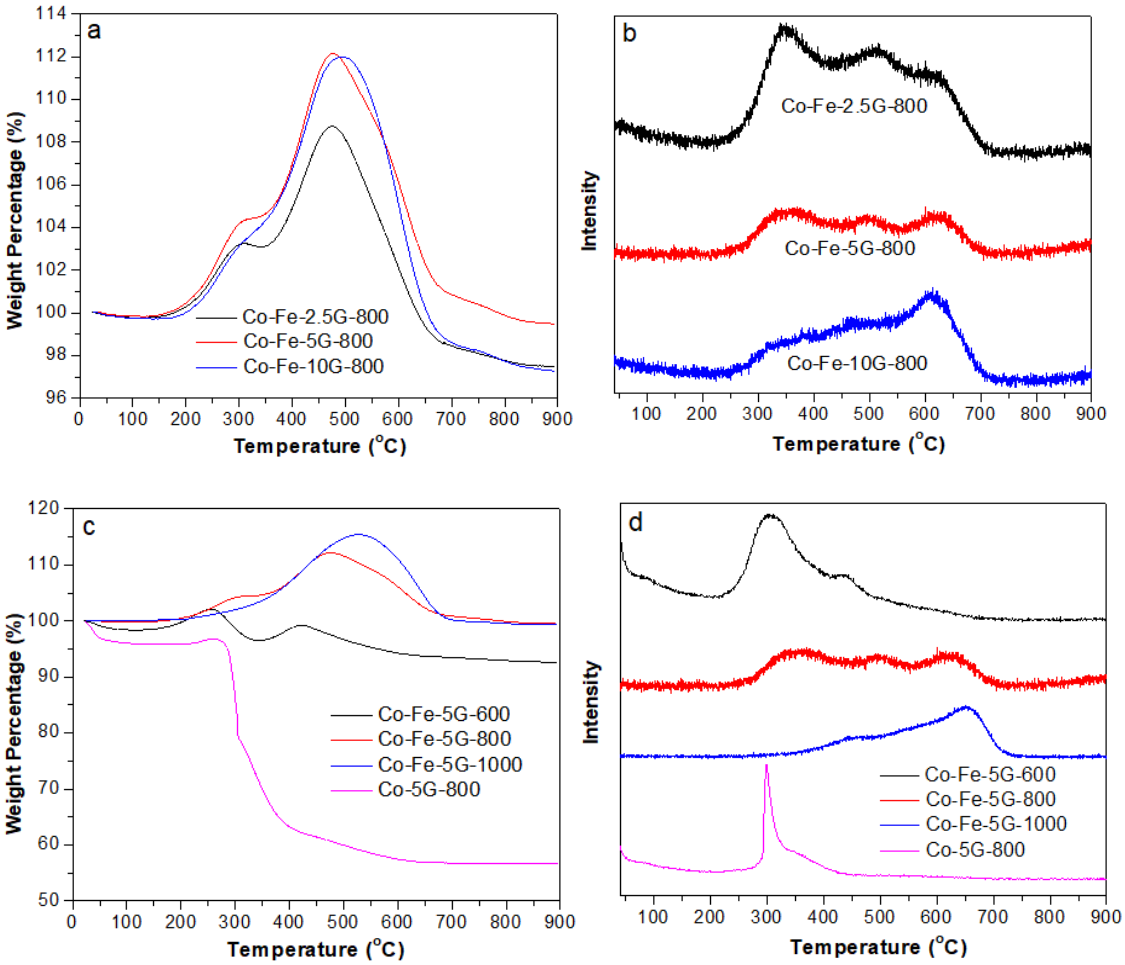

Figure 5. 16 (a, c) TGA and their corresponding MS curves of (b, d) CO2 for the Co-Fe-zG-800 series composites and Co-Fe-5G-T series composites/ Co-5G-800, respectively

emission could be detected in the range of 300 to 700 °C, indicating metal carbide, porous carbon and graphene were all formed during the carbonisation treatment in all three samples. Interestingly, Co-Fe-2.5G-800 showed high intensity of CO_2 peak at around 350 °C, and Co-Fe-5G-800 displayed the equally CO_2 intensity at 350 and 620 °C, while Co-Fe-10G-800 exhibited high intensity of CO_2 peak at around 620 °C. It suggests that graphene oxide in the as-synthesised samples could influence the component of composites due to the existence of functional groups in it. Thus, the component could be optimised by controlling the content of graphene oxide adding into the precursors during the synthesis of the Fe-substituted GO/ZIF-67 precursors. In addition, the thermal stability of the as-synthesised Co-Fe-5G-T series composites and Co-5G-800 were also measured by TGA-MS (shown in Figure 5.16c). In previous result of Co-Fe-600 (shown in Figure 5.9b), two major weight loss evens happened at 200 and 300 °C, owing to the decomposition of un-converted organic linkers and the burning of the formed carbon, respectively. However,

only one major weight loss event around 300 °C could be found, corresponding to the burning off the formed carbon. The Co-Fe-5G-1000 exhibited similar weight loss evens with Co-Fe-1000, indicating the graphene oxide solution did not influence the formation of metal carbide. Taking both TGA and MS results of sample Co-5G-800 in consideration, it can be found that a major weight loss event happened at 300 °C and its CO_2 emission peak appear around 300 °C, implying only carbon was formed during the carbonisation process.

The morphologies of the as-synthesised composites were characterised by scanning electron microscopy (SEM). SEM images of Co-Fe-zG-800 and Co-5G-800 are shown in Figure 5.17a-f. Obviously, the particles were nanocrystals with polyhedral shape and well dispersed in composites (shown in Figure 5.17a, c and e). Actually, the average particle size decreased from around 130 nm to 80 nm with the increase of graphene content in the composites. GO or graphene layers are not observable in the composites, indicating GO were completely converted to graphene and well embedded in the composites. As discussed in TGA-MS results, some functional groups of graphene oxide contained in precursor Fe-substituted GO/ZIF-67 may inhibit the growth of crystals. Meanwhile, the coordination of iron ions and GO sheet can also prevent the aggregation of crystals. In addition, the SEM images of Co-Fe-600, Co-Fe-1000 and Co-5G-800 are also presented in Figure 5.17g-l, respectively. Co-Fe-5G-600 showed the similar crystal size with more aggregated particles than sample Co-Fe-5G-800, which indicates the formation of weak crystallisation in relative low carbonisation temperature. However, Co-Fe-5G-1000 displayed large crystal size with circular structure, suggesting the relative high carbonisation temperature results in the change of the morphologies of the resulting materials. Comparing with Co-Fe-5G-800, some large particles with octahedral crystal structure could be found in sample Co-5G-800, further implying that the carbonisation temperature do influence the morphology of the samples and the synergistic effect between cobalt and iron in composites may exist.

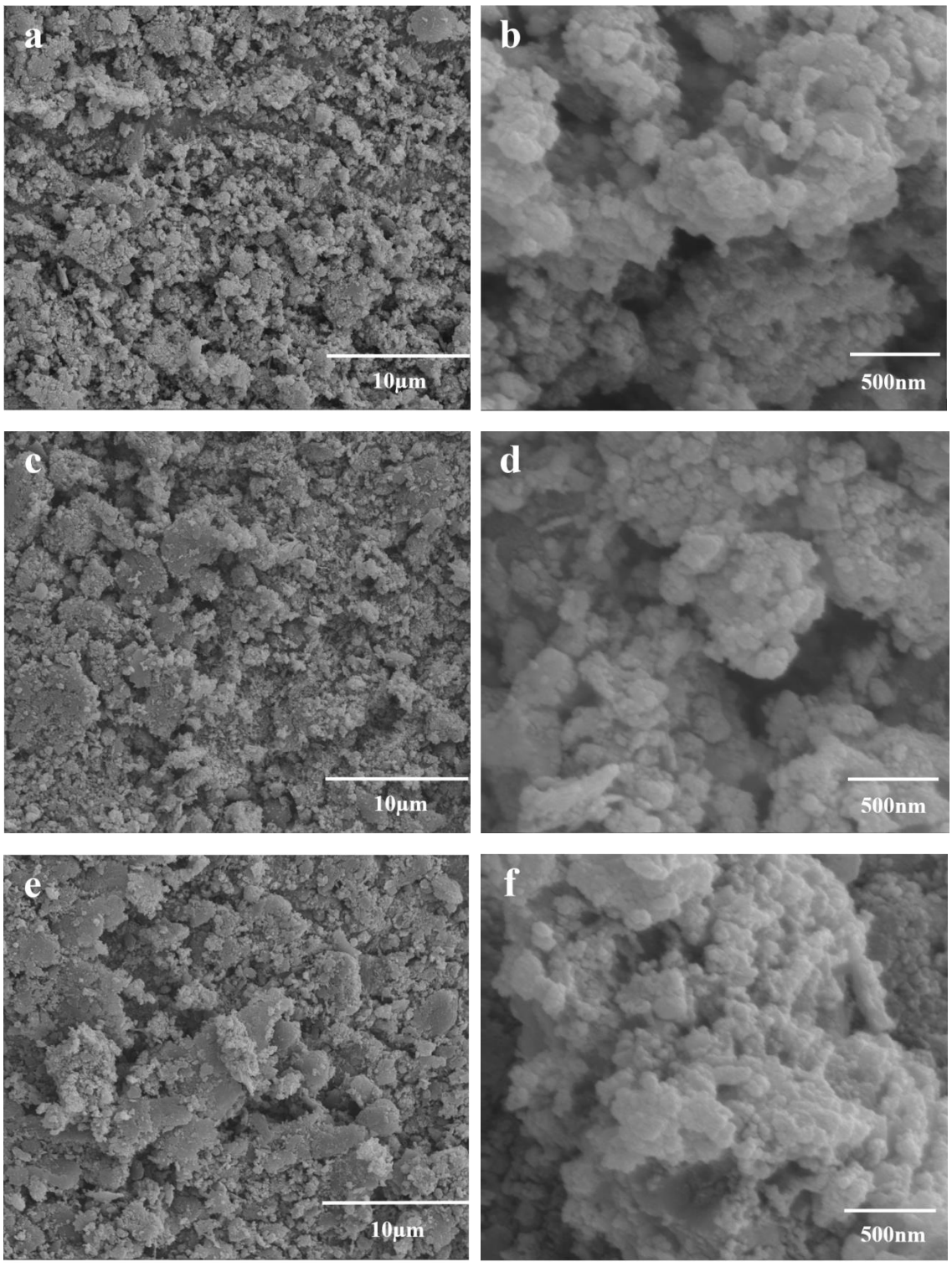
a
10μm
b
500nm
c
10μm
d
500nm
e
10μm
f
500nm

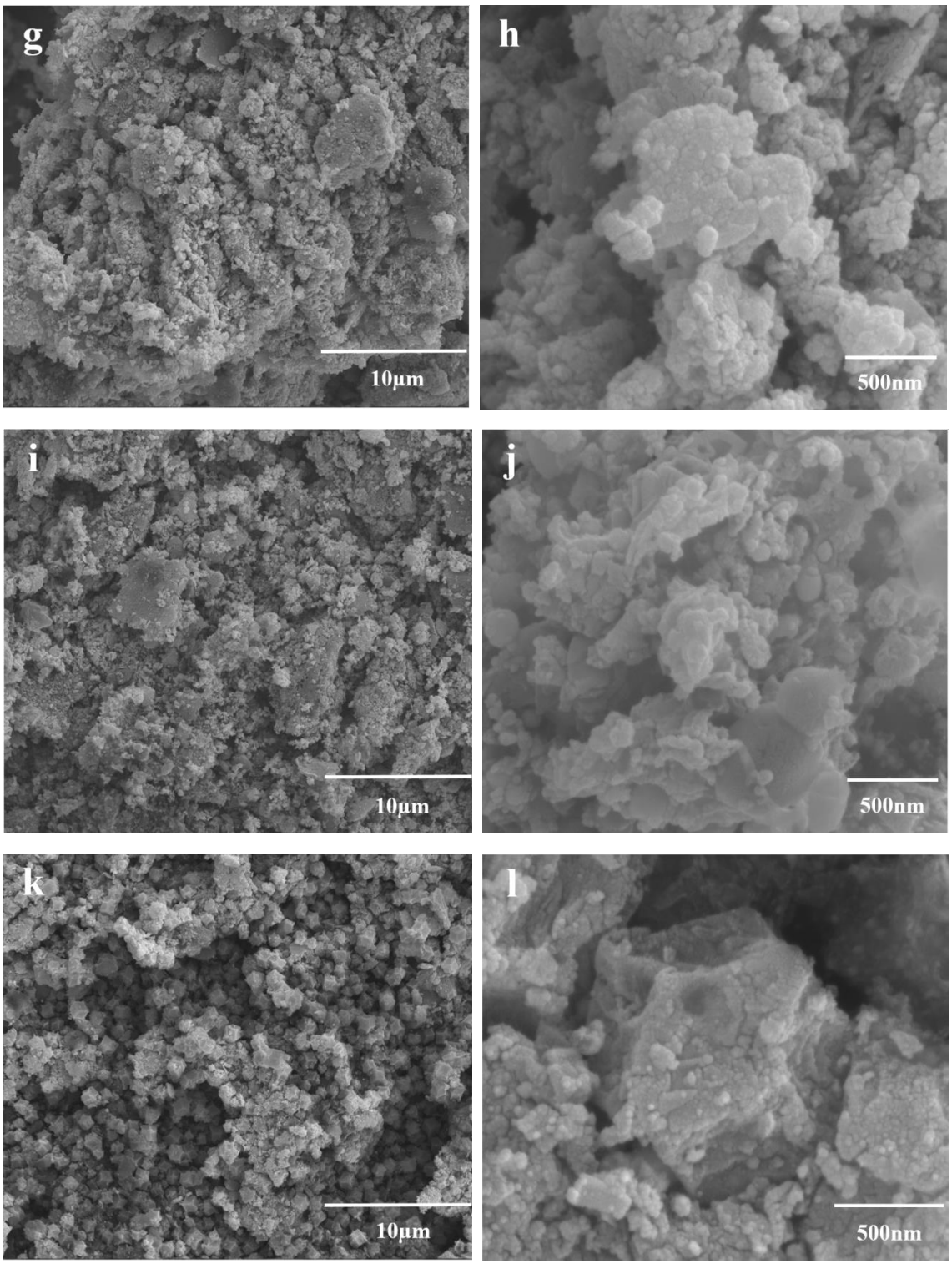

Figure 5. 17 SEM images of the (a, b) Co-Fe-2.5G-800 (c, d) Co-Fe-5G-800 (e, f) Co-Fe-10G-800 (g, h) Co-Fe-5G-600 (i, j) Co-Fe-5G-1000 (k, l) Co-5G-800

The morphologies and microstructure of the as-synthesised Co-Fe-zG-800 are further investigated by TEM (shown in Figure 5.18). All three composites showed spherical-like particles after the carbonisation at 800 °C. There was no single metal/ metal carbide particles could be easily found and most of them were well embedded into composites and surrounded with carbon and

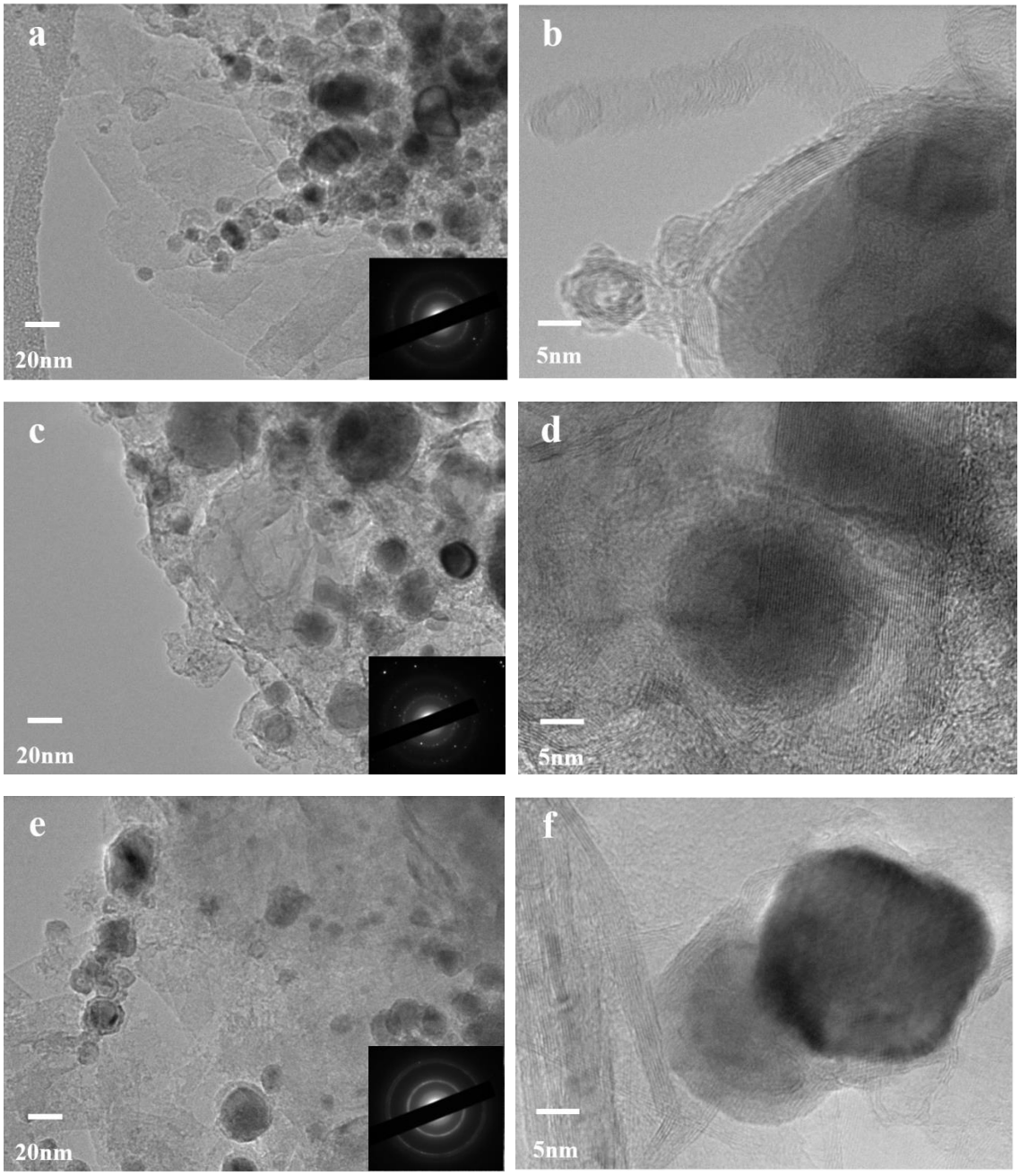

Figure 5. 18 TEM images of (a, b) Co-Fe-2.5G-800 (c, d) Co-Fe-5G-800 and (e, f) Co-Fe-10G-800. Inset in (a, c and e) is SAED patterns for corresponding composites

graphene. It should be noticed that the graphene could be serving as bridges between metal / carbide contained porous carbon materials. From the low magnification images (shown in Figure 5.18a, c and e), the average particle size decreased from 28 to 18 nm with the increase of graphene content. In the high resolution TEM image of Co-Fe-2.5G-800 (shown in Figure 5.18b), carbon nanotubes with the length around 40 nm and carbon onion surrounded with metal particles could be easily found, implying carbon nanotubes and carbon onions were *in-situ* formed by the catalytic role of cobalt and iron in the graphene contained composites. Moreover, as shown in Figure 5.18d & f,

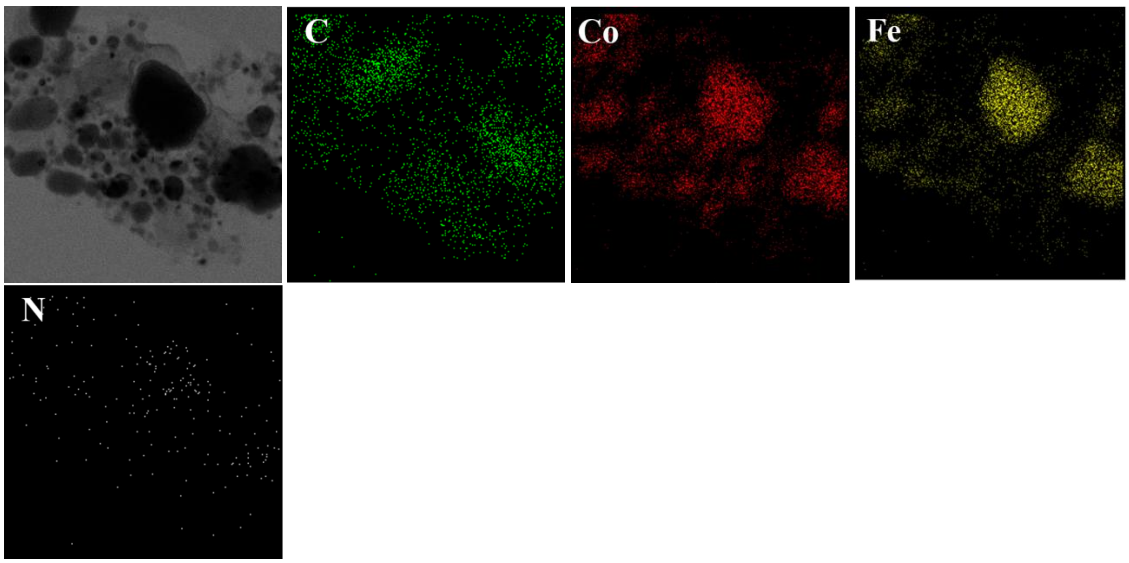

Figure 5. 19 TEM images and element mappings (C, Co, Fe and N) for Co-Fe-5G-800

particles were surrounded with porous carbon and covered/ attached with several sheets of graphene. The selected area electron diffraction (SAED) patterns, shown in the inset of Figure 5.18a & c, clearly showed the bright scattered dots contributed from the crystalline metal nanoparticles while the dimmed diffraction rings were from the amorphous porous carbon matrix. Based on these results, it is believed that Co-Fe-zG-800 composites were partially graphitised nanostructure; meanwhile, graphene is transferred from GO and well embedded in composites after the heat process. In addition, the element mapping (Figure 5.19) of Co-Fe-5G-800 exhibited similar C, Co, Fe and N patterns with the selected TEM area, indicating all elements were uniformly distributed in all the composites.

5.5 Electrocatalytic performance of cobalt-iron/ N-doped porous carbon/ graphene composites

5.5.1 Oxygen evolution reaction

The electrocatalytic activities of the as-synthesised Co-Fe-zG-800 series catalysts were evaluated in O_2- saturated 1M KOH (pH=14) electrolyte using three electrodes system with a scan rate of 5 mVs^{-1}. Obviously, all Co-Fe-zG-800 catalysts exhibited excellent OER activities with much higher onset potential than the value of reference material IrO_2/C (1.5 V). As shown in Figure 5.20a and Table 5.3, both Co-Fe-5G-800 and Co-Fe-2.5G-800 displayed the lowest onset potential of 1.41 V, which is 20 and 30 mV lower than the values of Co-Fe-10G-800 and Co-Fe-800, respectively. Impressively, only a potential of 1.45 V is required for Co-Fe-5G-800 to achieve a current density of 10 mA cm^{-2}, which is 10, 20 and 30 mV lower than that of Co-Fe-2.5G-800, Co-Fe-10G-800 and Co-Fe-800, respectively. Meanwhile, the Tafel slope results of these for OER were shown in Figure 5.20b. Sample Co-Fe-5G-800 exhibited the lowest slope value of 40.3 mV/dec and others displayed the values ranging from 43.7 to 45.2 mV/dec, which are all much lower than the value of 82 mV/dec of reference sample IrO_2/C. Moreover, the polarisation curves of Co-Fe-5G-T and Co-5G-800 were measured and shown in Figure 5.20c. As one can see that the onset potential of Co-Fe-5G-800 was 1.41 V, which is similar to those values of Co-Fe-5G-600 and Co-Fe-5G-1000, but much lower than that of Co-5G-800 (1.46 V). Significantly, the sample Co-Fe-5G-800 can realise a current density of 10 mA cm^{-2} at a potential of 1.45 V, which is comparable to 1.47, 1.475 and 1.48 V of other samples. The calculated Tafel slope value based on their LSV scanning (shown in Figure 5.20d) were 40.3, 45, 64 and 78 mV/dec for sample Co-Fe-5G-800, Co-Fe-5G-1000, Co-Fe-5G-600 and Co-5G-800, respectively. Additionally, the chronoamperometric test of the representative sample Co-Fe-5G-800 was measured and shown in Figure 5.20e. After 500^{th} times scanning with a scan rate of 5 mVs^{-1}, Co-Fe-5G-800 only showed 40 mV shift of onset and overpotential increase, indicating the high durability performance of Co-Fe-5G-800 in OER. Based on these results, it is believed that the introduction of graphene can efficiently enhance OER activities of resulting samples. The graphene with excellent conductivity could serve as bridges between metal /carbide contained porous carbon materials to improve the conductivity and the

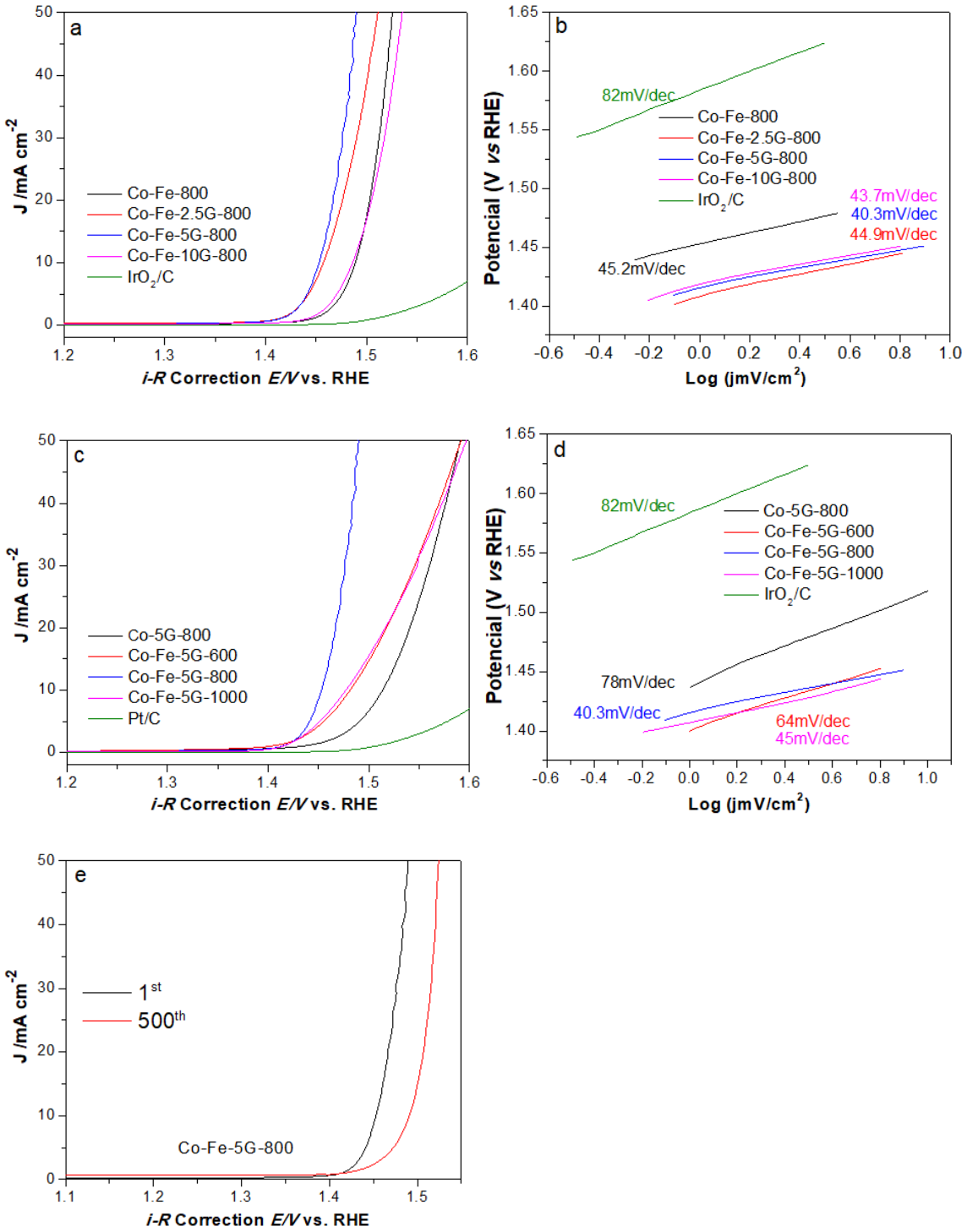

Figure 5. 20 Polarisation curves for OER on (a) Co-Fe-zG-800 series composites and IrO_2/C and (b) their Tafel plot; (c) Co-Fe-5G-T series composites, Co-5G-800 and IrO_2/C (d) their Tafel plot; (e) durability test for Co-Fe-5G-800

graphene is doped by N species during the carbonisation process, which could not only offers more active sites for catalytic reaction, but also provides anchoring sites for catalytic nanoparticle deposition. Due to the existence of multi-metal valence states in the samples and the optimised graphene contained, sample Co-Fe-5G-800 exhibited the best OER activities among all

studied samples. Furthermore, the graphene together with the formed porous carbons in the composites can provide carbon shells to protect the oxidation of metal/ carbide, thus, a superior OER stabilities were achieved by Co-Fe-5G-800.

Table 5. 3 OER performances of Co-Fe-zG-T series composites

Catalyst	Onset potential (V vs. RHE)	Potential (V vs. RHE) @ current density of 10 mA cm^{-2}	Tafel slope (mV/dec)
Co-5G-800	1.46	1.51	78
Co-Fe-800	1.44	1.48	45.2
Co-Fe-2.5G- 800	1.41	1.56	44.9
Co-Fe-5G- 800	1.41	1.45	40.3
Co-Fe-10G- 800	1.43	1.47	43.7
Co-Fe-5G- 600	1.42	1.475	64
Co-Fe-5G- 1000	1.42	1.47	45

5.5.2 Hydrogen evolution reaction

The Co-Fe-zG-800 series composites exhibited not only good performance in OER, but also in HER. All the samples were evaluated in 1M KOH electrolyte and the iR-corrected linear sweep voltammetry curves were shown in Figure 5.21a. Due to the effect of iron, all the LSV curves for the samples had a slight decrease between 0 to -0.1 V. The polarisation curves recorded with Co-Fe-5G-800 and Co-Fe-2.5G-800 displayed the same onset potential of 0.17 V, which is lower than the value of 0.21 and 0.24 V for Co-Fe-10G-800 and Co-Fe-800, respectively. Interestingly, both Co-Fe-5G-800 and Co-Fe-2.5G-800 can achieve a current density of 10 mA cm^{-2} at the same overpotential of 190 mV, which was 30 and 70 mV lower than Co-Fe-10G-800 and Co-Fe-800, respectively. However, to reach the current density of 50 and 100 mA cm^{-2}, overpotential of 255 and 280 mV were required for the Co-Fe-5G-800, which suggested much better HER activities for sample Co-Fe-5G-800 than other samples. Their Tafel plots were shown in Figure 5.21b and the best slope value was 83 mV/dec for Co-Fe-5G-800 and the values for Co-Fe-2.5G-800, Co-5G-800 and Co-Fe-10G-800 were in the range of 88-90 mV/dec. To get some insight of the effect of heating temperature on the electrochemical performances, the HER activities of Co-Fe-5G-T series samples and Co-5G-800 were also measured and shown in Figure 5.21c. Obviously, the sample Co-Fe-5G-800

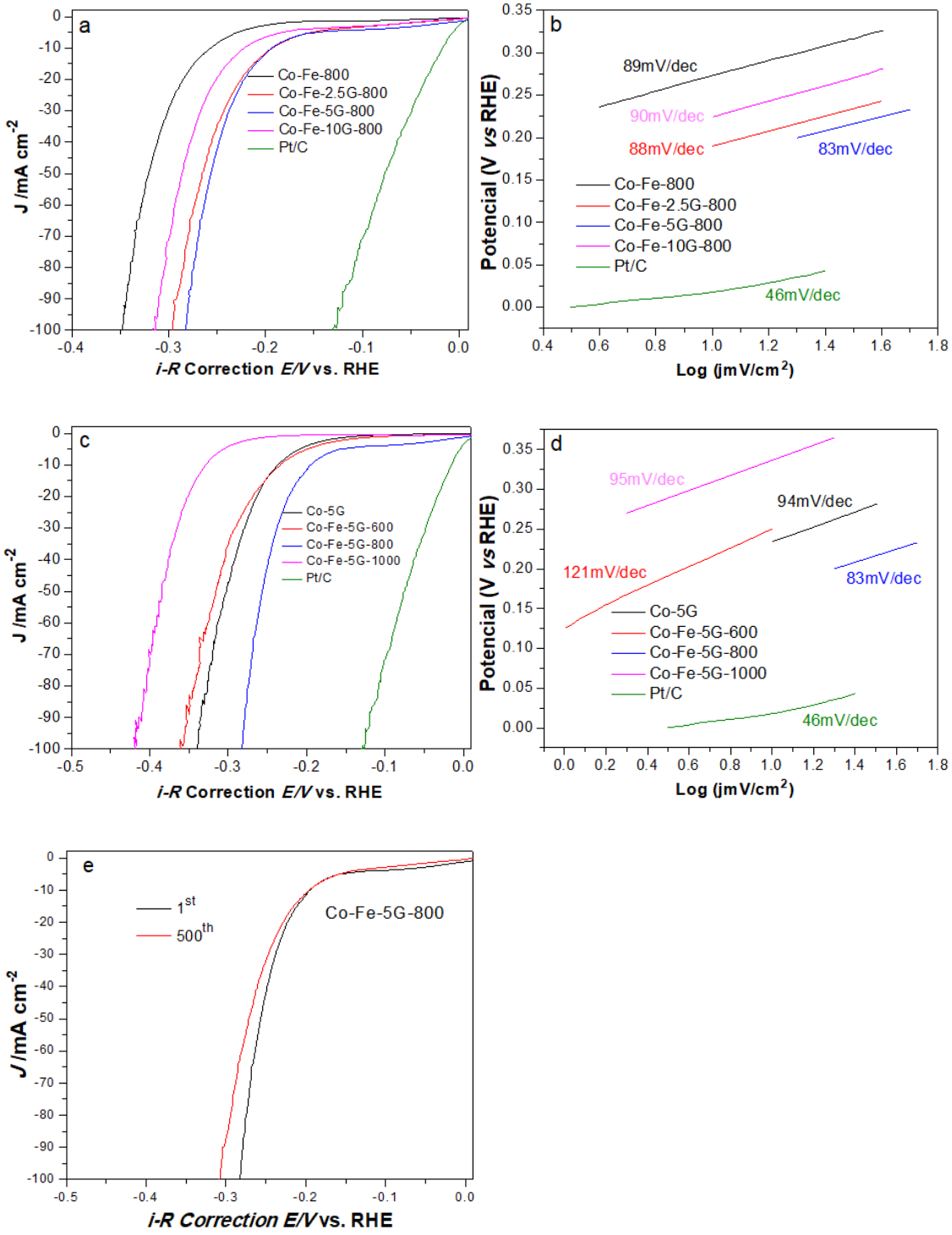

Figure 5. 21 Polarisation curves for HER on (a) Co-Fe-zG-800 series composites and Pt/C and (b) their Tafel plot (c) Co-Fe-5G-T series composites, Co-5G-800 and Pt/C and (d) their Tafel plot (e) durability test for Co-Fe-5G-800; Measured in 1M KOH electrolyte

showed the best onset potential of 0.17 V and overpotential of 0.19 V at the current density of 10 mA cm^{-2}. In comparison, the sample Co-Fe-5G-600 and Co-5G-800 exhibited the same onset potential of 0.2 V and the same overpotential of 0.23 V at the current density of 10 mA cm^{-2}, which are both much higher than Co-Fe-5G-1000 (shown in Table 5.4). The Tafel plots are

recorded in Figure 5.21d. The Tafel slope value was 83 mV/dec for Co-Fe-5G-800, which is smaller than those values of other samples: Co-5G-800 (94 mV/dec), Co-Fe-5G-600 (121 mV/dec) and Co-Fe-5G-1000 (95 mV/dec), further confirming that among the tested samples, Co-Fe-5G-800 was the most active materials for HER in KOH solution The catalytic stability towards HER was also tested and presented in Figure 5.21e. The sample Co-Fe-5G-800 exhibited similar I-V curve to its initial one with only 2 mV negative shift to reach 10 mA cm^{-2} after 500 continuous potential cycles, suggesting a remarkable stability of this catalyst for HER.

The HER performances of the as-synthesised Co-Fe-zG-800 series composites were also measured in acidic media (shown in Figure 5.22 and Table 5.4). Obviously, all graphene contained samples showed better HER performance than those without graphene, implying the important promoting role of graphene in the composites due to their excellent conductivity of the introduced graphene. Sample Co-Fe-2.5G-800 exhibited the lowest onset potential of 0.15 V, which is 50, 100 and 110 mV lower than Co-Fe-5G-800, Co-Fe-10G-800 and Co-Fe-800, respectively. To reach the current density of 10 mA cm^{-2}, only an overpotential of 0.24 V was required for Co-Fe-2.5G-800, which is obviously lower than those values of Co-Fe-5G-800 (0.27 V), Co-Fe-10G-800 (0.31 V) and Co-Fe-800 (0.34 V) to achieve the same current density. Moreover, the Tafel slope (Figure 5.22b) value of Co-Fe-2.5G-800 went down to 90 mV/dec, which is slightly lower than 94 mV/dec for both Co-Fe-5G-800 and Co-Fe-800, and 107 mV/dec for Co-Fe-10G-800, suggesting that the high level of superfluous graphene introduced may have blocked the access pathways between of cations or anions between the electrodes and the electrolytic solution. Based on the observed HER activities of studied samples both in alkaline and acidic electrolyte solution, it is believed that the improved HER performance can be contributed to the introduction of graphene into the samples which provides more access pathways and promotes electron transfer between the catalysts surface and reaction intermediates. Meanwhile, high level of multi-valence states metal active sites were formed in the samples during carbonisation at high temperature, therefore, the sample Co-Fe-5G-800 exhibited superior OER/HER performance for overall water splitting among all the studied composites.

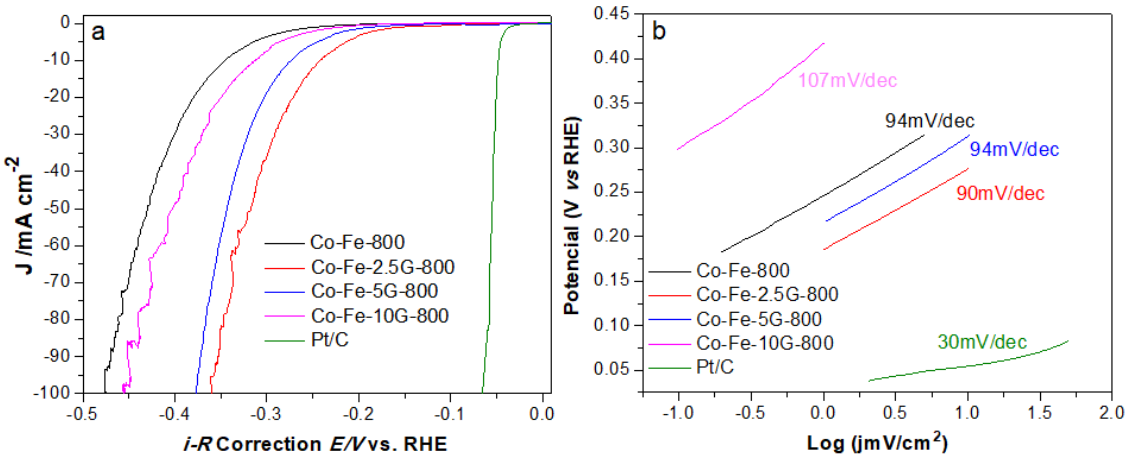

Figure 5. 22 Polarisation curves for HER on (a) Co-Fe-zG-800 series composites and Pt/C and (b) their Tafel plot; Measured in 0.5 M H_2SO_4 electrolyte

Table 5. 4 HER performances of Co-Fe-zG-T series composites. Measured in 1M KOH and 0.5M H_2SO_4 electrolyte

	HER Measured in 1M KOH electrolyte			HER Measured in 0.5M H_2SO_4 electrolyte		
Catalyst	Onset potential (V vs. RHE)	Overpotential (V vs. RHE) @ current density of 10mA cm^{-2}	Tafel slopte (mV/dec)	Onset potential (V vs. RHE)	Overpotential (V vs. RHE) @ current density of 10mA cm^{-2}	Tafel slopte (mV/dec)
Co-Fe-800	0.24	0.26	89	0.26	0.34	94
Co-Fe-2.5G-800	0.17	0.19	88	0.15	0.24	90
Co-Fe-5G-800	0.17	0.19	83	0.2	0.27	94
Co-Fe-10G-800	0.21	0.22	90	0.25	0.31	107
Co-5G-800	0.2	0.23	94			
Co-Fe-5G-600	0.2	0.23	121			
Co-Fe-5G-1000	0.28	0.33	95			

5.6 Electrocatalytic performance of cobalt-iron oxides/ porous carbon/ graphene composites

In previous study, the composites derived from the carbonisation of Fe-substituted ZIF-67 and Fe-substituted GO/ZIF-67 in Argon environment were well analysed and their electrochemical activities were evaluated. On the other hand, cobalt oxide and iron oxide were both reported as good catalysts in OER/ HER. However, to the best of our knowledge, there is no research have been performed to investigate the electrochemical activities of tri-functional cobalt-iron oxide with porous carbon and graphene. Therefore, in this part, the overall water splitting abilities of cobalt-iron oxide/carbon/graphene series catalysts will be investigated.

5.6.1 Oxygen evolution reaction

To obtain xCoO-yFeO-zG-350 series composites, the previous obtained xCo-yFe-zG series samples (0.3 g) were loaded into tube furnace on an alumina boat in the air. The furnace was set to a target temperature (350 °C) with a ramp rate of 10 °C/min in air for 1 hour. The obtained composites were named as xCoO-yFeO-zG-350.

The OER electrocatalytic activities of the as-synthesised xCoO-yFeO-zG-350 composites were evaluated in O_2- saturated 1 M KOH (pH=14) electrolyte by using three electrodes system with a scan rate of 5 mVs^{-1}. As shown in Figure 5.23a and Table 5.5, CoO-FeO-350 displayed an onset potential of 1.57 V, which is similar to that value of CoO-350. In contrast, all graphene contained samples exhibited obviously lower onset potential of 1.52, 1.53 and 1.54 V, corresponding to CoO-FeO-5G-350, CoO-FeO-2.5G-350 and CoO-FeO-10G-350, respectively. Clearly, CoO-FeO-5G-350 displayed the best OER performance in this series samples. Moreover, graphene contained samples achieved a lower OER overpotential than those without graphene over the whole potential range (shown in Table 5.5), implying that graphene offered more active sites for catalytically reaction and enhance the OER performance of the resulting composites. In addition, in comparison of the Tafel plots (Figure 5.23b and Table 5.5), the lowest slope value of 50.5 mV/dec for CoO-FeO-5G-350 and 52-55.2 mV/dec for other samples, further indicating that CoO-FeO-

5G-350 is the most active electrocatalyst for OER in the studied oxide series samples.

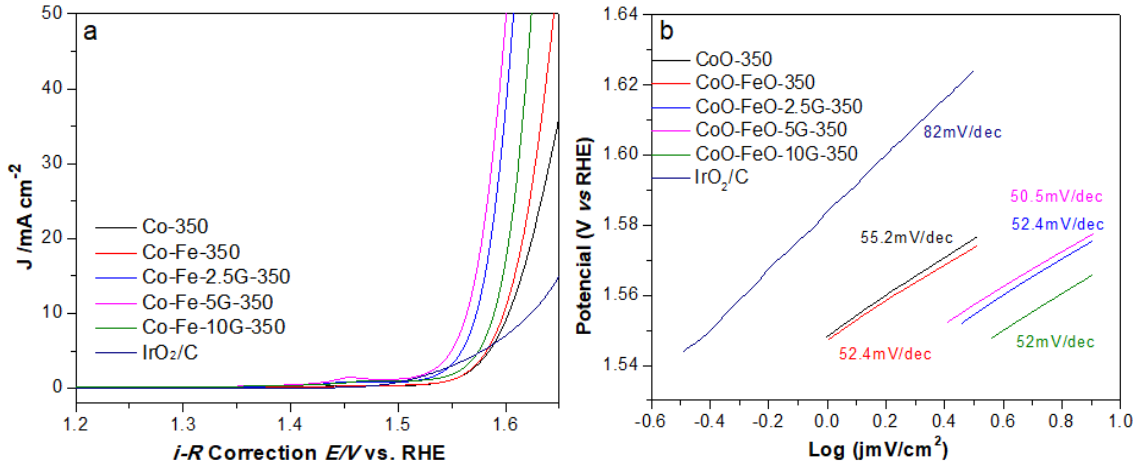

Figure 5. 23 Polarisation curves for OER on (a) xCoO-yFeO-zG-350 series composites and IrO2/C and (b) their Tafel plot

5.6.2 Hydrogen evolution reaction

The electrocatalytic HER performance of xCoO-yFeO-zG-350 series composites were measured by iR corrected linear sweep voltammetry (LSV) on a rotating disk electrode (RDE) in N_2- saturated 1M KOH. In Figure 5.24a and Table 5.5, the lowest onset potential of 0.17 V was achieved by sample CoO-FeO-5G-350, which is much lower than those values of CoO-FeO-350 (0.25 V) and CoO-350 (0.42 V). Notably, overpotentials of 0.22, 0.29 and 0.31 V are required to realise a current density of 10, 50 and 100 mA cm^{-2} for CoO-FeO-5G-350. In Figure 5.24b, the slope values were in the range of 74.8 to 79.3 mV/dec for graphene containing samples, which are much lower than the slope values of graphene-free samples with 100.7 and 102.4 mV/dec for CoO-FeO-350 and CoO-350, respectively. Obviously, all graphene contained samples exhibited remarkable OER/ HER activities for overall water splitting. It is believed that the introduction of iron and graphene play a significant promoting role to enhance the electrocatalaytic performances of cobalt oxide.

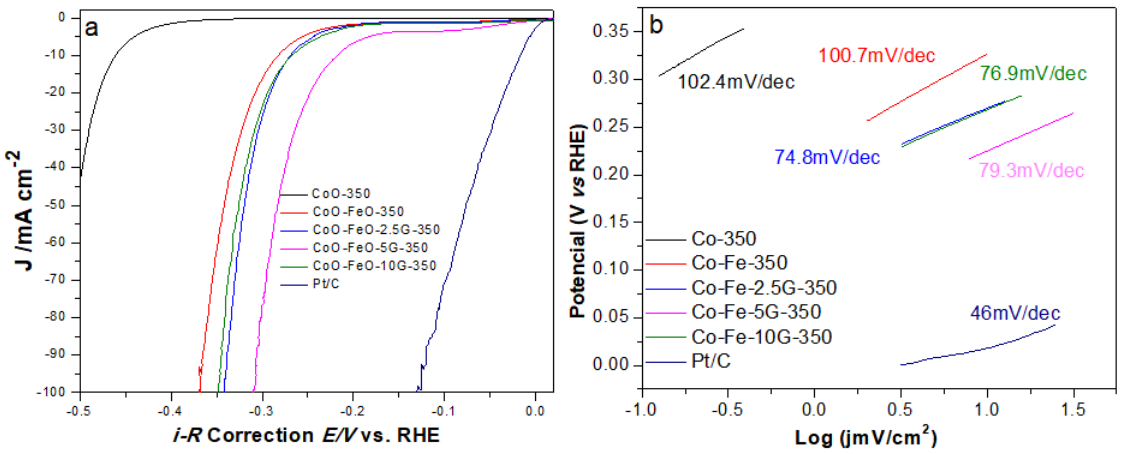

Figure 5. 24 Polarisation curves for HER on (a) xCoO-yFeO-zG-350 series composites and Pt/C and (b) their Tafel plot. Measured in 1 M KOH electrolyte

Table 5. 5 OER and HER performances of the xCo-yFe-zG-350 series composites. Measured in 1M KOH electrolyte

	OER Measured in 1M KOH electrolyte			HER Measured in 1M KOH electrolyte		
Catalyst	Onset potential (V vs. RHE)	Overpotential (V vs. RHE) @ current density of 10mA cm^{-2}	Tafel slopte (mV/dec)	Onset potential (V vs. RHE)	Overpotential (V vs. RHE) @ current density of 10mA cm^{-2}	Tafel slopte (mV/dec)
CoO-350	1.58	1.61	55.2	0.42	0.46	102.4
CoO-FeO-350	1.57	1.6	52.4	0.25	0.29	100.7
CoO-FeO-2.5G-350	1.53	1.57	52.4	0.23	0.24	74.8
CoO-FeO-5G-350	1.52	1.56	50.5	0.17	0.27	79.3
CoO-FeO-10G-350	1.54	1.59	52	0.22	0.27	76.9

5.7 Summary

In summary, both bi-metallic cobalt-iron/ N-doped porous carbon and bi-metallic cobalt-iron/ N-doped porous carbon/ graphene series samples were successfully synthesised from Fe-substituted ZIF-67 and Fe-substituted GO/ZIF-67 *via* a facile one-step carbonisation process. Due to the synergistic

effect between cobalt and iron, the crystalline structure of metal particles, the high porosity of the materials and the homogeneous dispersion of N in the resulting composites, xCo-yFe-800 series samples exhibit remarkable electrochemical activities and superior durability for OER and HER. Moreover, graphene reinforced xCo-yFe-zG-800 series samples show a significantly enhanced OER and HER activities for overall water splitting due to the high conductivity, more active sites and more electron transfer of graphene. Finally, their oxidised derivative CoO-FeO-zG-350 series sample also exhibit exceptional electrochemical activity for water splitting.

Chapter 6：Bi-metallic cobalt and iron sulfides/ N, S co-doped porous carbon/ graphene composites and their electrocatalytic applications

6.1 Introduction

With the increasing energy demands and environmental pollution resulting from the burn off fossil fuels, there is a great interest to develop clean and sustainable energy conversion and storage technologies [292-293]. Therefore, the overall water splitting into oxygen and hydrogen has been considered as a promising alternative to currently fossil fuels owing to its clean and efficient approach to generate high purity of H_2 fuel [292]. Great efforts, therefore, have been devoted to developing low-cost alternatives, such as transition metal sulfide based materials, including CoS [294-295], MoS_2 [296], WS_2 [297-298], NiS_x [299-300] and FeS_2 [280, 301], which have gained noticeable attention as alternative electrocatalysts for HER and OER, that are measured in acid and alkaline media, respectively, due to their low-cost and high catalytic activity. However, the current prevailing strategies often utilise the incompatible integration of the two catalysts which inevitably results in mediocre performance for complete water splitting [302-303]. It is therefore highly imperative to develop electrocatalysts that can be used for both HER and OER in the same electrolyte to achieve efficient overall water splitting.

Recently, many studies revealed that a new method to enhance the activity for overall water splitting is making additional metal doping into the intrinsic metal catalyst. For example, ZnCo [304], NiCo [305], CuCo [306] sulfides have been widely studied and exhibited efficient electrochemical activity for water splitting in a wide pH range. However, to the best of our knowledge, there are rare studies are focused on bimetal Co-Fe sulfide composites for water splitting, especially using metal organic framworks (MOFs) as precursors to prepare bimetallic sulfide nanocomposites. Due to the special crystal structure of MOFs, metal, metal sulfide or metal oxide would be formed after the thermal treatment in argon, hydrogen sulfide or air atmosphere. Therefore, MOFs are widely regarded as excellent precursors to prepare porous carbon based metal sulfide

nanocomposites, which will give an enhancement to electrochemical activities. In addition, graphene has been widely reported as good catalytic supporting material due to its excellent electrical conductivity, high surface area, and good chemical and environmental stability [9, 307]. With these advantages, the superior electrical conductivity of graphene can significantly improve the electrochemical performance of catalysts.

In this chapter, a facile method for the preparation of the cobalt-iron sulfide embedded in N, S co-doped porous carbon and graphene from the simultaneously sulfurisation and carbonisation of Fe-substituted GO/ZIF-67 will be presented. Owing to the rich content of Co-N and Fe-N, Fe-substituted ZIF-67 was chosen as the precursor. The resultant 2CoS-FeS-800 composites exhibited the best OER/HER activities among bimetal Co-Fe sulfides samples with different Co: Fe ratios. On the basis of those results, graphene contained sample 2CoS-FeS-5G-800 showed an improved electrocatalytic activity in water splitting.

6.2 Characterisations of the bi-metallic sulfides derived from Fe substituted ZIF-67

The crystal structures of the as-synthesised Fe-substituted ZIF-67 with different ratio of cobalt to iron, were investigated by XRD (Figure 6.1a). All precursor composites exhibited the same peaks located at 10.2°, 12.5°, 14.5°, 16.4°, 18°, 24.5°, 25.8°, 26.9°, corresponding to (002), (112), (022), (013), (222), (223), (224) and (134) planes of ZIF-67 samples [244], respectively. The XRD spectrum of sulfurised and carbonised xCoS-yFeS-800 series composites were shown in Figure 6.1b. It is completely different from the sodalite structure of the Fe-substituded-ZIF-67 precursor, the as-synthesised xCoS-yFeS-800 composites displayed four main peaks at 31°, 35.5°, 47° and 55°, corresponding to (100), (101), (102) and (110) (JCPDS 75-0605) diffraction planes of cobalt sulfide [308], respectively. These four peaks became more intense and sharper with the increase of the ratio of Fe: Co and the peaks of Co_3S_4 could not be detected, suggesting the existence of a synergistic effect between iron and cobalt in the hybrid composites and indicating the well crystallinity of cobalt sulfide. Only some very weak diffraction peaks from iron species located at 28°, 41°, 58° and 65°, corresponding to (111), (211), (222) and (321) (JCPDS 42-1340) diffraction planes of pyrite [309], respectively, were detected in the CoS-FeS-800, maybe

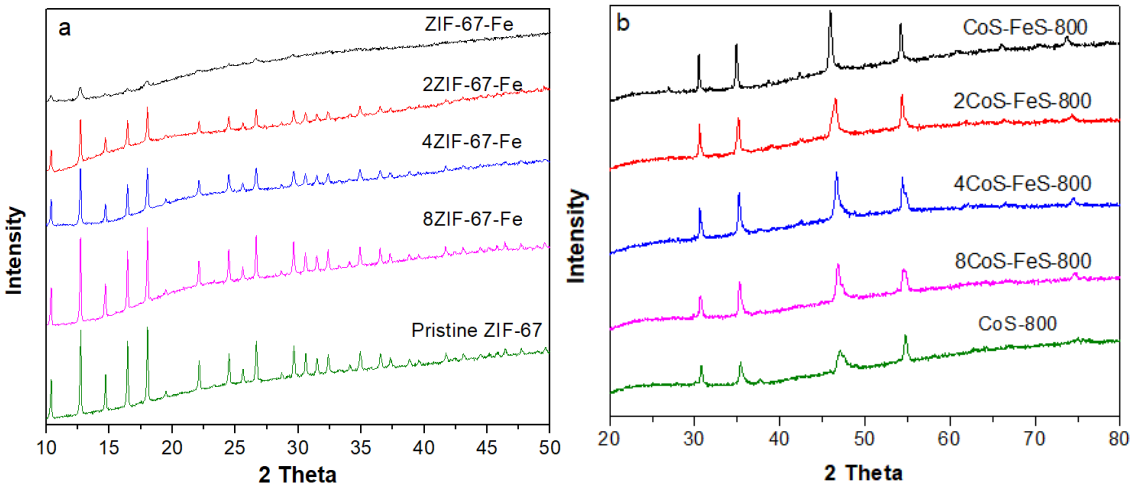

Figure 6. 1 XRD patterns of (a) as-synthesised Fe-substituted ZIF-67 composites (b) xCoS-yFeS-800 series composites

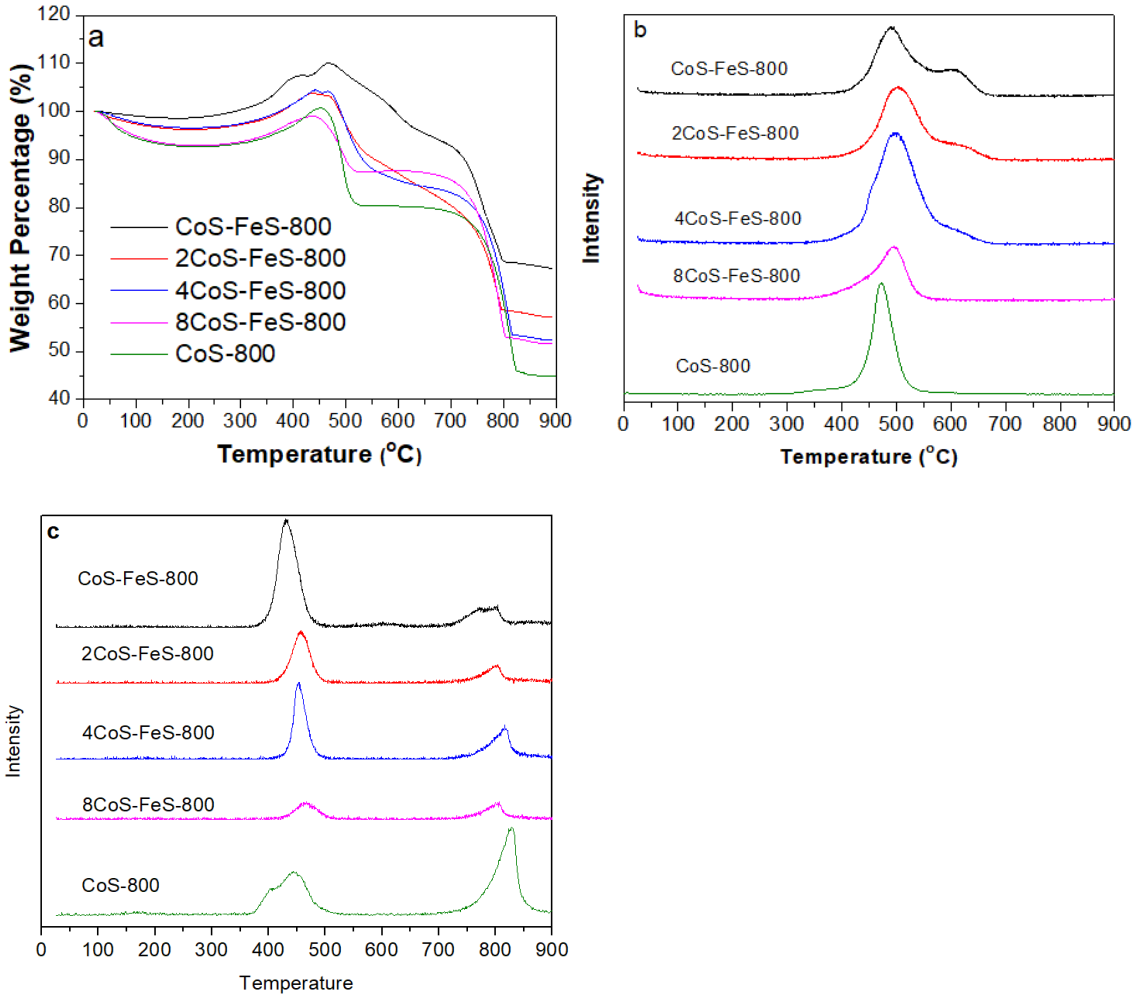

Figure 6. 2 (a) TGA and their corresponding MS curves of (b) CO_2 and (c) SO_2 for xCoS-yFeS-800 series composites

due to the diffraction intensity of cobalt sulfide were much higher than that of iron sulfide. Both cobalt sulfide and iron sulfide are electrocatalysts and beneficial to the electrochemical activities, thus it is interesting to understand

the electrochemical performances of bimetal sulfides in such a complicated system.

The thermal stabilities of the as-synthesised xCoS-yFeS-800 series composites were evaluated by TGA-MS while being heated in air atmosphere (Figure 6.2a). Due to the adsorbed H_2O in the composites, all composites exhibited a weak weight loss event before 100 °C. Then, a small weight increase event happened in the range of 300-450 °C for all composites, owing to the oxidation of cobalt and iron sulfide to high valence state, followed by two major weight loss events at 460-550 °C and 780 °C for all composites, corresponding to the burn off the porous carbon in air and decomposition of cobalt/ iron sulfides. Both of the two weight loss events could be further confirmed by the emission of CO_2 and SO_2 in the MS signals (Figure 6.2b & c). In Figure 6.2c, peaks at 350-500 °C were due to the burn off S dope carbon, which is accompanied with the formation of SO_2 and the signs of peaks at 750-850 °C were due to the conversion of metal sulfide to metal oxides.

To investigate carbonaceous materials, Raman spectroscopy is the most common and powerful technique. The Raman spectra of xCoS-yFeS-800 series composites are shown in Figure 6.3. All the composites revealed the characteristic D and G bands of carbon at 1350 and 1595 cm^{-1}, respectively. The D band is an indication of less disordered carbon and the G band is a symbol of monocrystalline and sp^2 hybridised carbon [270]. In addition, two very weak peaks located at 2700 cm^{-1} (2D band) and 2950 cm^{-1} (G+D band) in iron-containing composites, however, they could not be found in CoS-800, indicating that the existence of graphitised nanostructure with carbon onions and carbon nanotube in the iron-containing samples. The appearance of D, G, 2D and G+D band in xCoS-yFeS-800 series composites, suggests the formation of amorphous carbon and graphitised nanostructure during the carbonisation and sulfurisation process.

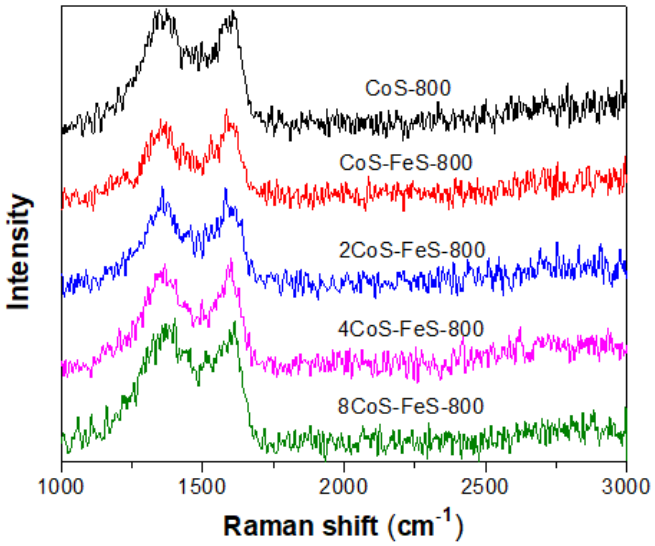

Figure 6. 3 Raman spectra of xCoS-yFeS-800 series composites

The X-ray photoelectron spectroscopy (XPS) analysis was utilised to investigate the chemical state of the representative as-synthesised 2CoS-FeS-800 composite. As shown in Figure 6.4a, element survey clearly illustrated the presence of C, Co, Fe, S and N in the representative 2CoS-FeS-800 sample. The XPS spectra for each element are presented in Figure 6.4b-f. A strong peak with binding energy at 284.5 eV was observed in the high resolution C 1s XPS spectrum (Figure 6.4b), indicating the formation of sp^2 graphitic structure [260], which could improve the electron transfer and be beneficial to the OER/HER activities. Additionally, the spectrum could be deconvoluted into three peaks located at 285.3, 286.4 and 288.6 eV, which may correspond to C=N, C-N and C-S [250-253], respectively. The spectrum of Co 2p (Figure 6.4c) for the as-synthesised composite exhibited the presence of two peaks at 779.7 and 781.2 eV, which are consistent with the presence of Co $2p_{3/2}$, implying the existence of Co^{2+} oxidation state [261, 310]. Two peaks located at 786 and 800.3 eV indicated the octahedrolly coordination Co^{2+} in cobalt and Co $2p_{1/2}$ satellite components. Furthermore, except the Co^{2+} oxidation state, another two weak doublets appeared at 779.1 and 781.9 eV, which imply the existence of Co^{3+} oxidation state in the composite. In Fe 2p spectrum (Figure 6.4d), the sample 2CoS-FeS-800 exhibited three peaks at 709.8, 715.5 and 723.4 eV, corresponding to Fe (II) $2p_{2/3}$ and Fe^{2+} [311-312]. Apart from Fe^{2+} oxidation state, it also showed three doublets located at 711.8, 713.6 and 725.3 eV, which are characteristic of Fe $2p_{2/3}$ (Fe^{3+} oxide states), implying the co-existence of Fe^{3+} and Fe^{2+} oxidation state in the composite [311-312]. The S 2p spectrum shown in Figure 6.4e exhibited the

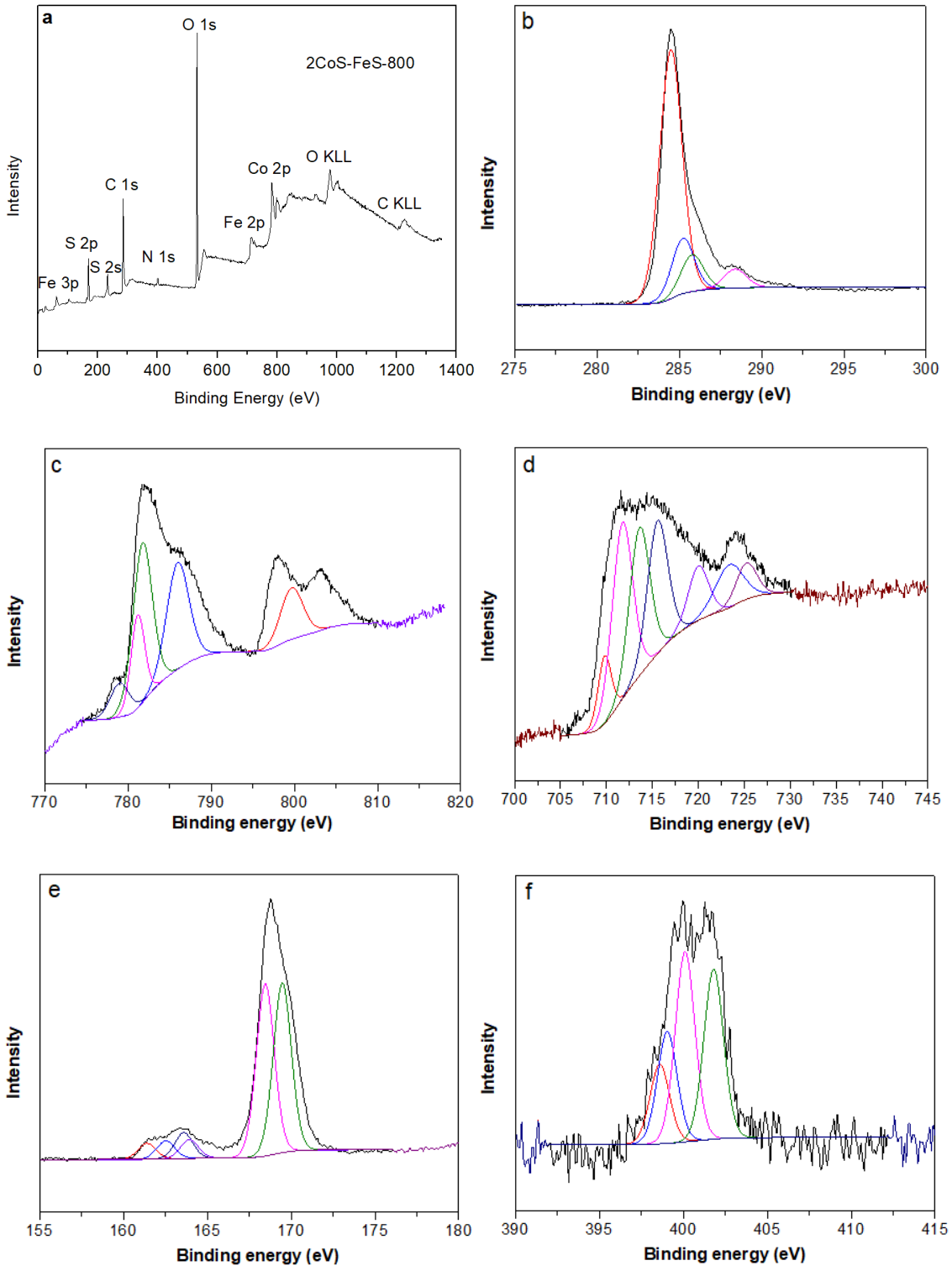

Figure 6. 4 (a) Element survey by XPS and XPS spectrum of (b) C 1s, (c) Co 2p, (d) Fe 2p, (e) S 2p and (f) N 1s for 2CoS-FeS-800

presence of two peaks at 162.5 and 163.6 eV, that are corresponding to the S 2p $_{3/2}$ and S 2p $_{1/2}$ doublets with a binding energy separation of 1.1 eV, corresponding to the S^{2-} species of metal sulfides [255, 313]. Two peaks could be found at around 162.8 and 163.9 eV, suggesting the existence of C-S-C bonding and S (0) [252, 267], respectively. Additionally, two peaks at 168.5 and

169.5 eV suggested that they are assigned to the S $2p_{3/2}$ and S $2p_{1/2}$ peaks of oxidised S species, such as sulfate groups [314], which could be due to the partially oxidation of sulfur in air [300]. It is believed that it can be dissolved in the solution, thus, the effect of sulfide compound on the OER/HER activities could be negligible. In N 1s spectrum (Figure 6.4f), four peaks located at 397.8, 399.1, 400.1 and 401.8 eV could be detected, corresponding to the pyridinic-N, Co-N, pyrrolic-N and graphitic-N [257-258], respectively. Owing to the volatility of N and S species in high temperature heat treatment, therefore, low content of N and S remain in the composite. In XPS analysis, it is clear that 2CoS-FeS-800 composite composes of Co^{2+}, Co^{3+}, Fe^{2+}, Fe^{3+} and S^{2-} states. Additionally, the X-ray diffraction is also consistent with the XPS analysis, indicating Co-Fe bimetallic sulfides have been successfully prepared from one-step carbonisation and sulfurisation process, which lead to the formation of CoS / FeS supported on N, S co-doped carbon composites.

The morphologies of the as-synthesised composites were characterised by scanning electron microscopy (SEM). As shown in Figure 6.5a-j, the particle size of xCo-yFe-800 composites can be controlled by adjusting the ratio of Co: Fe. The CoS-800 exhibited a distorted rhombic dodecahedron shapes after high temperature sulfurisation. With the introduction of small content of iron, some large dodecahedron and octahedron particles with average size of 2 μm appeared in 8CoS-FeS-800 and 4CoS-FeS-800, suggesting the potential existence of pyrite and pyrrhotite. However, with further increasing of the iron content in the composite, not a single large particle could be found and both 2CoS-FeS-800 and CoS-FeS-800 samples exhibited typically metal sulfide crystals morphology with average size growing up to 100 nm. This interesting phenomenon could indicate there is a synergistic effect between cobalt and iron and synthesised composites morphology are controlled by the ratio of Co: Fe.

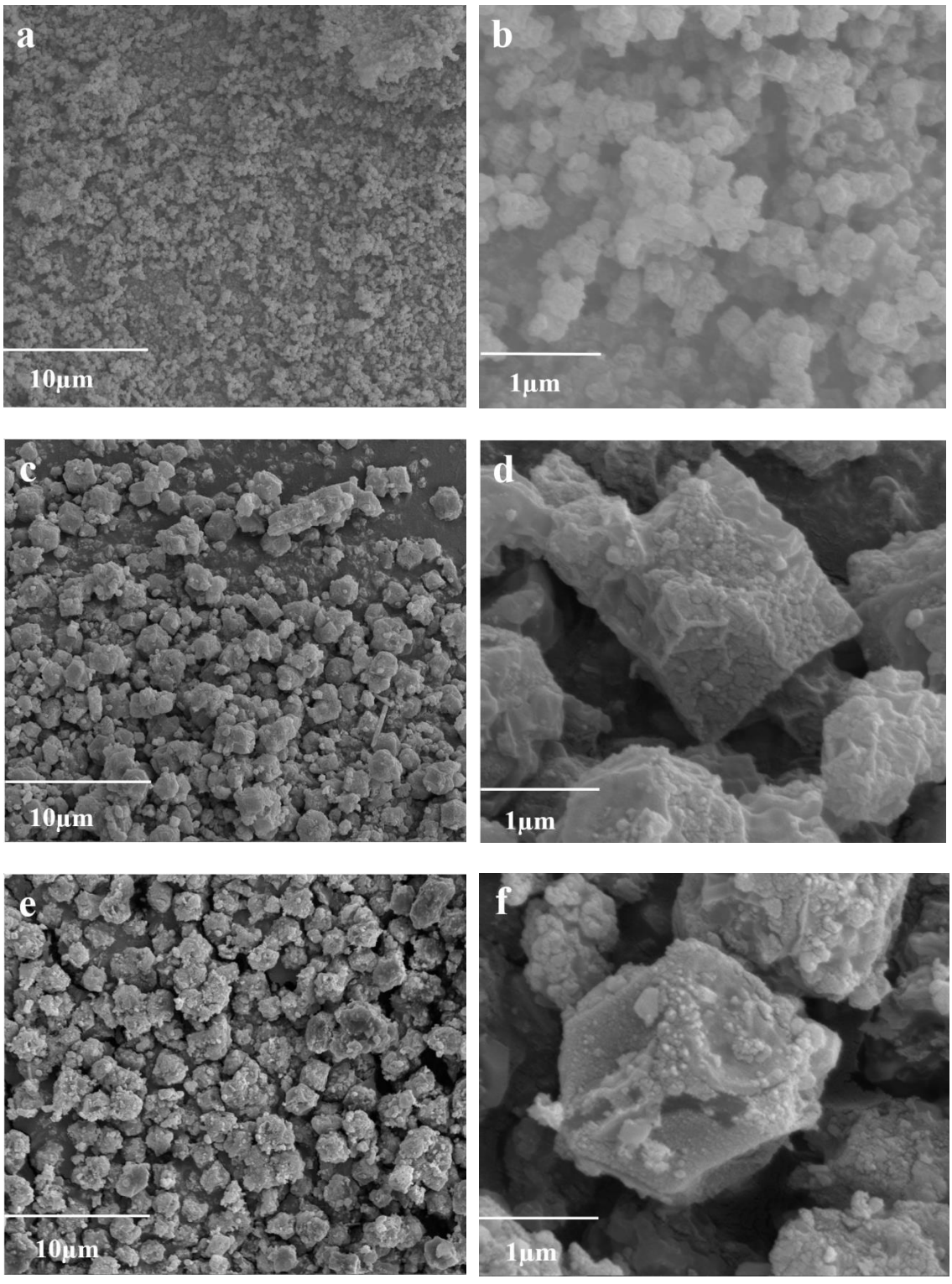
a
10µm
b
1µm
c
10µm
d
1µm
e
10µm
f
1µm

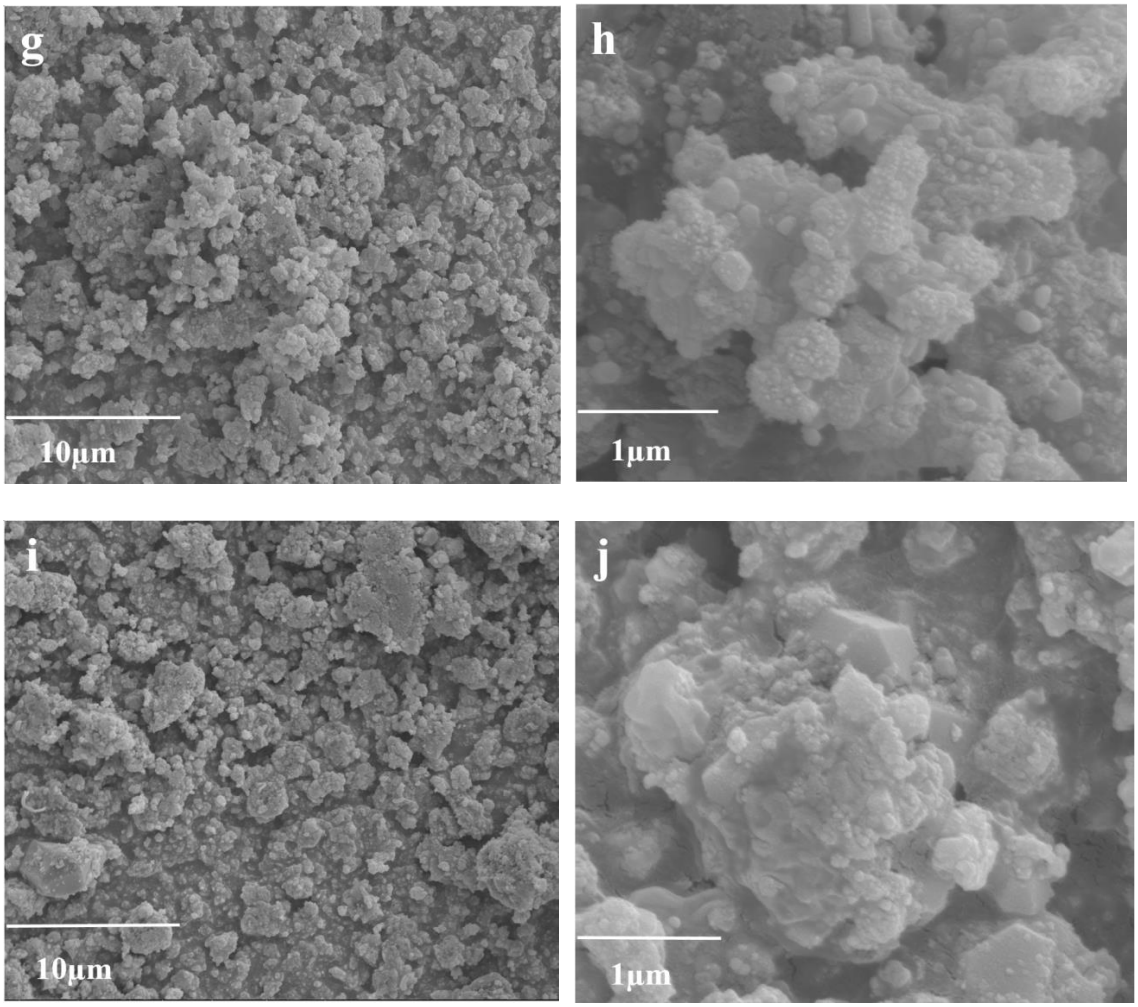

Figure 6. 5 SEM images of the (a, b) CoS-800 (c, d) 8CoS-FeS-800 (e, f) 4CoS-FeS-800 (g, h) 2CoS-FeS-800 (i, j) CoS-FeS-800

To further investigate the morphologies, transmission electron microscopy (TEM) was carried out to characterise the representative 2CoS-FeS-800 composite. As presented in Figure 6.6a&b, the resulting nanocomposite exhibited spherical-like particles owing to the shrinkage during the carbonisation and sulfurisation at 800 °C. From the low magnification images, we can find the original rhombic dodecahedron particle shape of precursor was completely damaged with the average particle size around 20 nm, suggesting the addition of iron may affect and modulate the structure of nanocomposite. As shown in Figure 6.6b, some amorphous carbon could be found around particles. Interestingly, a dark nanotube with the length around 15 nm appeared in the high resolution image, indicating the existence of a synergistic effect between cobalt and iron sulphide, which is again in agreement with the Raman spectrum results of graphitised nanostructure. Moreover, the corresponding selected area electron diffraction (SAED) patterns (shown in inset of Figure 6.6a) clearly revealed that the bright

scattered dots are contributed from the crystalline nanoparticles while the dimmed diffraction rings are from the amorphous porous carbon matrix. In order

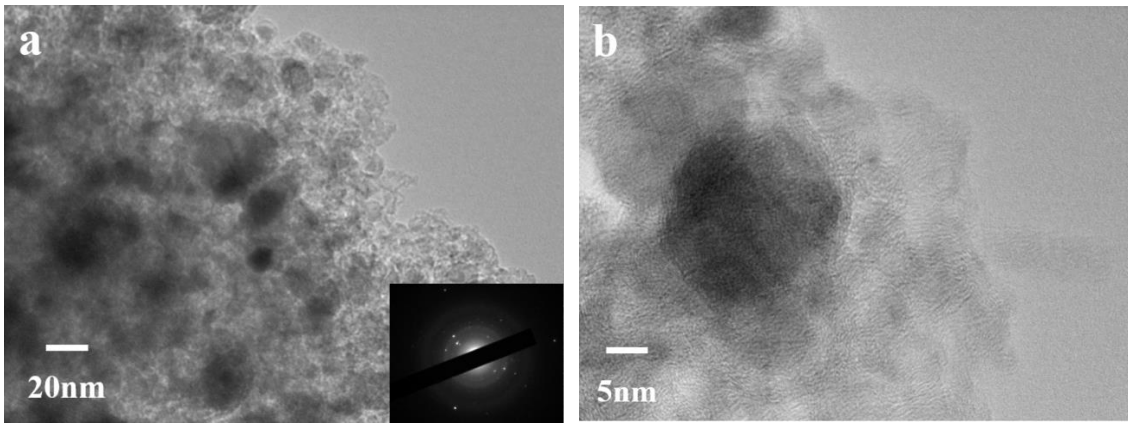

Figure 6. 6 TEM images of 2CoS-FeS-800. Inset in (a) is SAED patterns for corresponding composite

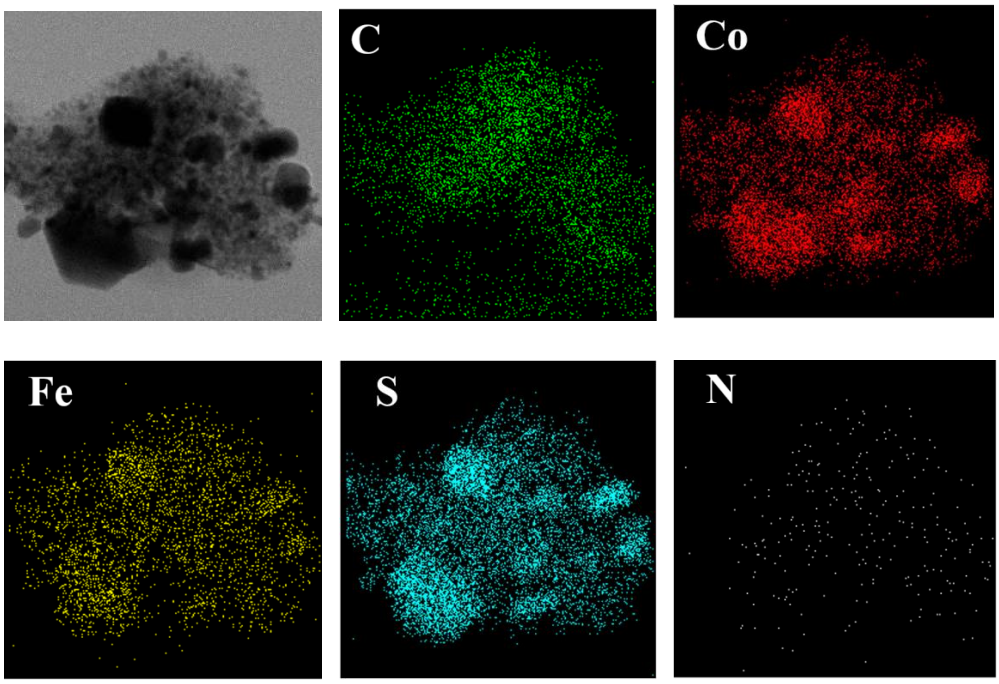

Figure 6. 7 TEM images and element mappings (C, Co, Fe, S and N) for 2CoS-FeS-800

to ascertain the distribution of cobalt sulfide and iron sulfide particles in 2CoS-FeS-800 composite, the elemental mapping of a representative sample were measured *via* EDX and the results were shown in Figure 6.7. The element Co, Fe, S exhibited similar elemental mapping patterns with dark area in the TEM images, implying a uniform dispersion of cobalt/iron sulfide particles in the carbon matrix. In addition, element C and N were also detected in the result, where C content is much more than that of N, maybe duo to the volatility of N species during high temperature treatment.

6.3 Electrocatalytic applications of the bi-metallic sulfides derived from Fe substituted ZIF-67

6.3.1 Hydrogen evolution reaction

The HER catalytic activities of xCoS-yFeS-800 sulfurised and carbonised in 800 °C composites were all evaluated in 1M KOH electrolyte and the iR corrected linear sweep voltammetry curves are shown in Figure 6.8a. Owing to the effect of ohmic resistance, the as-measured current was not the intrinsic behaviour. Therefore, an iR correction was applied to all initial current for analysis. Both CoS-FeS-800 and 4CoS-FeS-800 exhibited the same onset potential of 0.18 V, which is 0.01 V higher than 2CoS-FeS-800 and 0.04 V lower than 8CoS-FeS-800 and CoS-800. In order to afford a current density of 10 mA cm^{-2}, the lowest overpotential of 220 mV was required for 2CoS-FeS-800, while 230, 250, 270 and 272 mV were needed for 4CoS-FeS-800, CoS-FeS-800, 8CoS-FeS-800 and CoS-800, respectively. The excellent HER activities were also appeared in their Tafel slope results. As shown in Figure 6.8b and Table 6.1, sample 2CoS-FeS-800 showed the lowest slope value of 95.7 mV/dec, while other values were in range of 97.2-130.7 mV/dec for 4CoS-FeS-800, CoS-FeS-800, 8CoS-FeS-800 and CoS-800, respectively. Obviously, the introduction of iron can produce a synergistic effect with cobalt sulfide during the sulfurisation and carbonisation process, which could optimise their electronic structure of carbon in order to enhance the electron transformation. Among all composites, the 2CoS-FeS-800 exhibited the best HER activities compared with other Co: Fe ratio samples in alkaline media. In addition, chronoamperometric test was performed and results were shown in Figure 6.8c. Sample 2CoS-FeS-800 showed a similar I-V curve after 500 scan cycles with a scan rate of 5 mVs^{-1}, while the 500^{th} curve displayed the same overpotential at the current density of 10 mA cm^{-2} and it was even better than the initial one, which displayed decreased potential of 25 and 40 mV at the current density of 50 and 100 mA cm^{-2}, maybe due to the partially metal ions were reduced to low valence state during the scanning and displaying remarkable HER activities.

Additionally, the HER performance of xCoS-yFeS-800 series composites were also assessed in acidic electrolyte (0.5M H_2SO_4). As shown in Figure 6.9a, the polarisation curve recorded with sample 2CoS-FeS-800, 4CoS-FeS-800 and

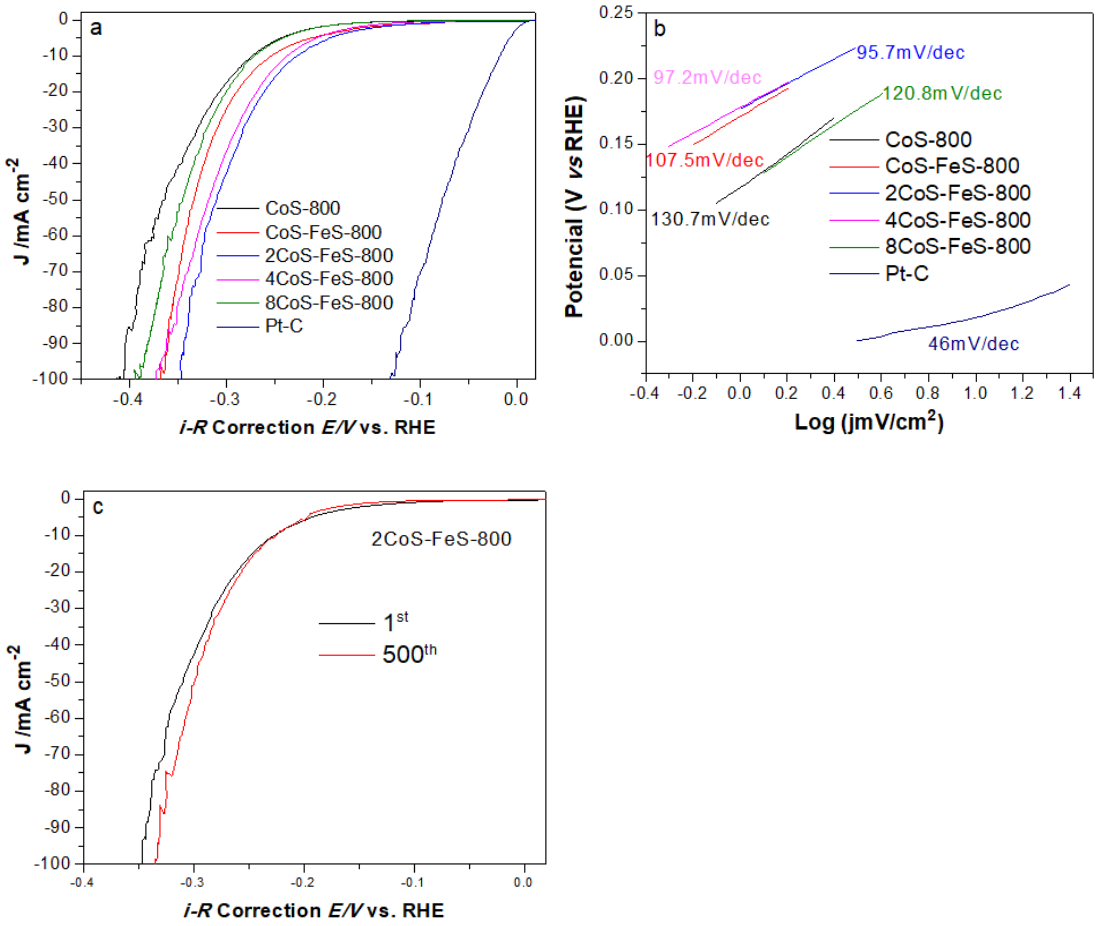

Figure 6. 8 Polarisation curves for HER on (a) xCoS-yFeS-800 series composites and Pt-C and (b) their Tafel plot and (c) durability test for 2CoS-FeS-800. Measured in 1 M KOH electrolyte

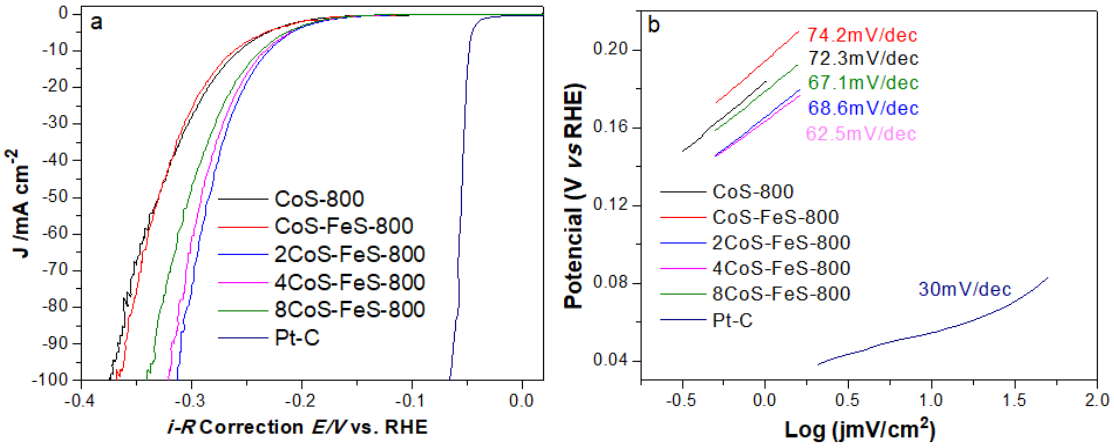

Figure 6. 9 Polarisation curves for HER on (a) xCoS-yFeS-800 series composites and Pt-C and (b) their Tafel plot. Measured in 0.5 M H_2SO_4 electrolyte

8CoS-FeS-800 showed the same onset potential of 0.18 V and exhibited overpotentials of 225, 230 and 235 mV, respectively, to reach the current density of 10 mA cm^{-2}. In contrast, both CoS-FeS-800 and CoS-800 exhibited lower HER activity (same onset potential of 0.2 V). Furthermore, their Tafel slope results were shown in Figure 6.9b. The 2CoS-FeS-800 displayed the

Table 6. 1 HER performances of the xCoS-yFeS-800 series composites. Measured in 1M KOH and 0.5M H_2SO_4 electrolyte

Catalyst	Onset potential (mV vs. RHE)		Over potential (mV vs. RHE)@ 10 mA cm^{-2}		Tafel slope (mV dec^{-1})	
	0.5 M H_2SO_4	1 M KOH	0.5 M H_2SO_4	1 M KOH	0.5 M H_2SO_4	1 M KOH
CoS-800	200	220	265	272	72.3	130.7
CoS-FeS-800	200	180	270	250	74.2	107.5
2CoS-FeS-800	180	170	225	220	68.6	95.7
4CoS-FeS-800	180	180	230	230	62.5	97.2
8CoS-FeS-800	180	220	235	270	67.1	120.8
Pt-C	61	10	62	30	30	46

lowest slope value of 62.5 mV/dec, while the slope values for others ranged from 67.1 to 74.2 mV/dec. Obviously, the iron-contained composites not only exhibited superior water splitting activities in alkaline media, but also showed an excellent HER activity in acidic solution. More importantly, the sample 2CoS-FeS-800 exhibited the best overall water splitting activities among all the studied composites. The HER performances both in acidic and alkaline media for xCoS-yFeS-800 and Pt-C samples are all summarised in Table 6.1.

6.3.2 Oxygen evolution reaction

The electrocatalytic activities of the as-synthesised xCo-yFe series composites were also evaluated in O_2- saturated 1 M KOH (pH=14) solution by using three electrodes system with a scan rate of 5 mVs^{-1}. As shown in Figure 6.10a, the composites with different Co: Fe ratios were all treated in H_2S atmosphere at 800 °C and measured by steady-state linear sweep voltammetry (LSV) on a rotating disk electrode (RDE). In details, the sample CoS-800 showed an onset potential of 1.5 V, which is the same value as the reference IrO_2/C. However, a potential of 1.56 V was required to reach the current density of 10 mA cm^{-2} for sample CoS-800, while 1.63 V was required for IrO_2/C. In comparison, all the iron-containing composites exhibited much better OER activities than CoS-800.

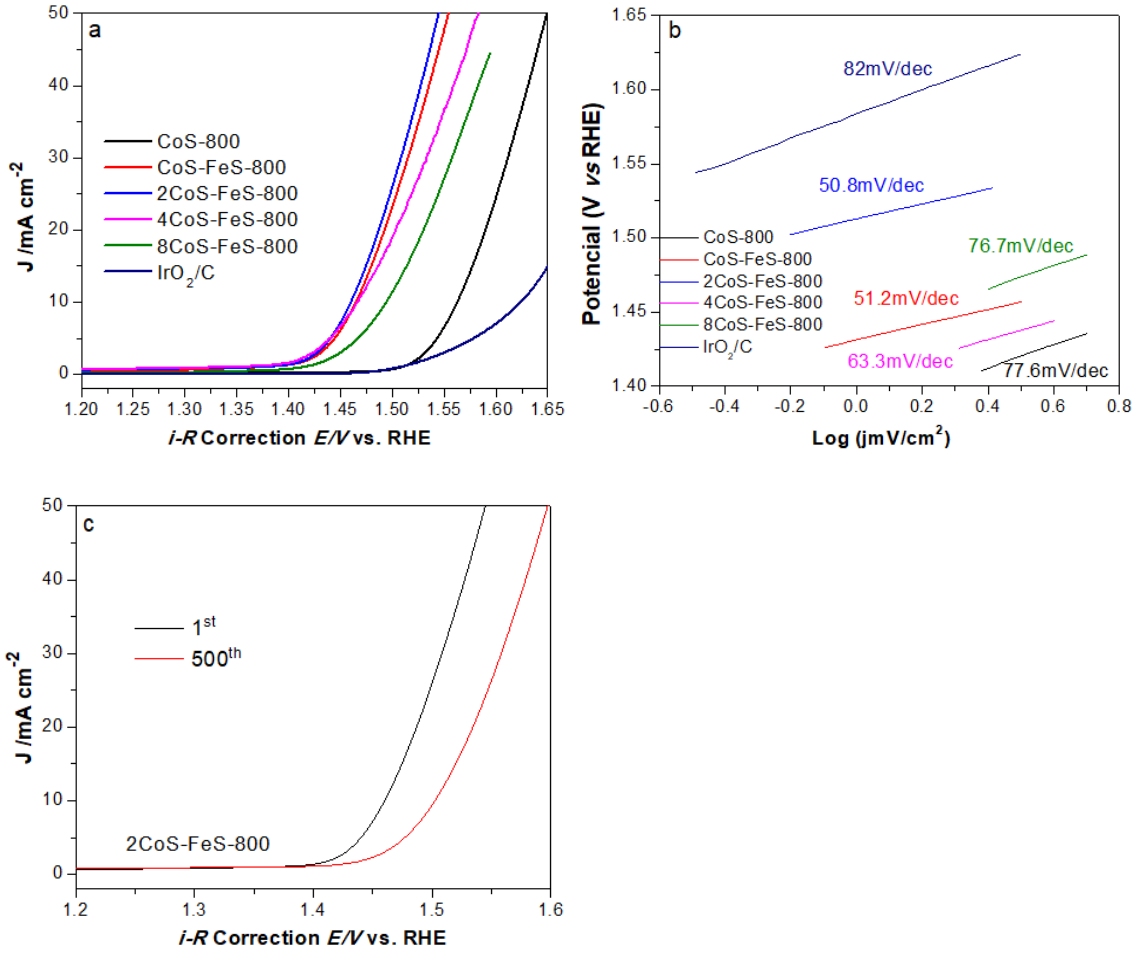

Figure 6. 10 Polarisation curves for OER on (a) xCoS-yFeS-800 series composites and IrO_2/C and (b) their Tafel plot and (c) durability test for 2CoS-FeS-800

Table 6. 2 OER performances of the xCoS-yFeS-800 series composites

Catalyst	Onset potential (V vs. RHE)	Potential (V vs. RHE) @ current density of 10 mA cm^{-2}	Tafel slopte (mV/dec)
CoS-800	1.50	1.56	77.6
CoS-FeS-800	1.42	1.45	52.1
2CoS-FeS-800	1.42	1.445	50.8
4CoS-FeS-800	1.42	1.45	63.3
8CoS-FeS-800	1.43	1.49	76.7
IrO_2/C	1.5	1.61	82

The 2CoS-FeS-800 sample demonstrated an onset potential of 1.42 V, which is very similar to that of CoS-FeS-800 and 4CoS-FeS-800, but 10 mV lower than that of 8CoS-FeS-800. It is believed that the introduction of iron will form the bi-functional catalyst and the promoting effect between cobalt and iron will efficiently enhance the OER activities. Moreover, all iron containing composites can achieve a current density of 10 mA cm^{-2} at small potentials of 1.445, 1.45, 1.45 and 1.49 V for 2CoS-FeS-800, CoS-FeS-800, 4CoS-FeS-800 and 8CoS-FeS-800, respectively, which are much lower than 1.63 V for IrO_2/C and other reported bimetal sulfide electrocatalysts including NiS-FeS and CoS-NiS. In addition, the Tafel slope results were shown in Figure 6.10b and Table 6.2. The 2CoS-FeS-800 displayed the smallest value of 50.8 mV/dec, which is higher than those of CoS-FeS-800 (51.2 mV/dec), 4CoS-FeS-800 (63.3 mV/dec), 8Co-Fe-800 (76.7 mV/dec), CoS-800 (77.6 mV/dec) and IrO_2 (82 mV/dec), further indicating its remarkable OER performance. Comparing the onset potential and the overpotential to achieve current density of 10 mA cm^{-2} of these catalysts with reference IrO_2/C, one can easily find that the ratio of Co: Fe =2:1 composites exhibited the best OER activities among all Co-Fe ratios. Based on these results, the chronoamperometric test of 2CoS-FeS-800 was carried out and shown in Figure 6.10c. After 500 times scanning at the scan rate of 5 mVs^{-1}, it exhibited a similar LSV curve with 0.05 V onset potential shift higher than initial one, which may be due to partially oxidation of carbon matrix and sulfide nanoparticles at high voltage.

6.4 Characterisations of the bi-metallic sulfides derived from Fe substituted GO/ZIF-67

From previous work, the bimetal cobalt and iron sulfide and N, S co-doped porous carbon composites exhibited good electrocatalytic performance. In the following part, graphene will be introduced into above system to improve the electrocatalytic performance owing to its high surface area and good electrical conductivity. Furthermore, N, S co-doped graphene will create some heteroatomic defects, which also enhance the conductivity at the interface.

The XRD patterns of the as-synthesised Fe-substituted GO/ZIF-67 composites are shown in Figure 6.11a. All samples exhibited strong diffraction peaks at 10.2°, 12.5°, 14.5°, 16.4°, 18°, 24.5°, 25.8°, 26.9°, corresponding to (002), (112), (022), (013), (222), (223), (224) and (134) planes [244], respectively, which

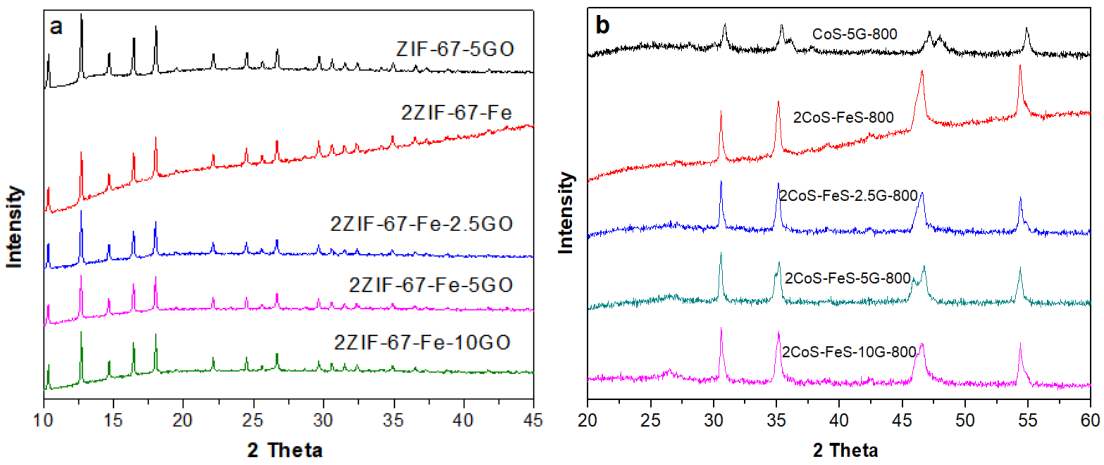

Figure 6. 11 XRD patterns of (a) 2Co-Fe-zGO and (b) 2CoS-FeS-zG-800 series composites

indicates that the introduction of iron ions and GO into the synthesis gel did not break the inherent crystalline structure of ZIF-67. It is interesting to note that the XRD peaks for GO could not be found in the XRD patterns, suggesting that the amount of GO added to the composites was relatively low and the XRD peaks for GO may be overlapped with ZIF-67 at 2θ=10.2°. After the sulfurisation and carbonisation process, bimetallic sulfide with graphene nanocomposites were achieved. XRD patterns of 2CoS-FeS-yG-800 series composites are presented in Figure 6.11b for further investigation of their crystal structure. All samples exhibited a wide diffraction peak at around 20-30°, which was considered to be attributed to carbon or graphene (further confirmed by Raman spectrum). Obviously, four peaks located at 31°, 35.5°, 47° and 55°, corresponding to (100), (101), (102) and (110) (JCPDS 75-0605) diffraction planes of cobalt sulfide [308], respectively, could be found in all samples, which indicates the existence of cobalt sulfide with hexagonal structure in the composites. There were no obvious diffraction peaks from iron species in the XRD, maybe due to the small amount of iron substituted into cobalt sulfide. In addition, a peak was found at 2θ=26° in all samples, suggesting the formation of graphitic carbon, which is beneficial to the electrochemical activities.

Thermal stabilities of the as-synthesised 2CoS-FeS-zG-800 series composites were measured by TGA-MS (shown in Figure 6.12). All composites showed a minor weight loss before 100 °C due to the removal of adsorbed H_2O in the composites, followed by a weight increase event between 200 and 450 °C, which may be caused by the oxidation of metal sulfides in the composites. For all iron-contained composites, they not only exhibited two major weight loss

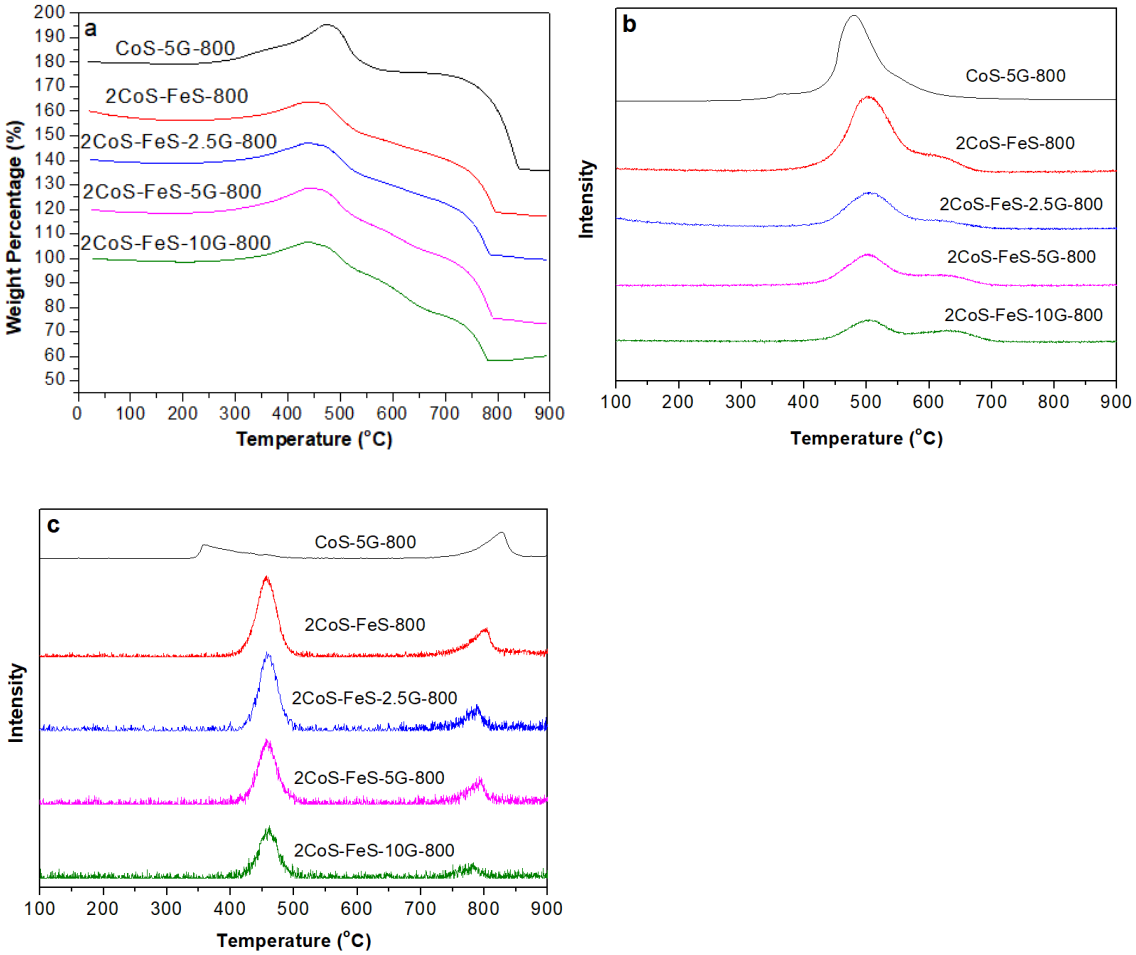

Figure 6. 12 (a) TGA and their corresponding MS curves of (b) CO_2 and (c) SO_2 for 2CoS-FeS-zG-800 series composites

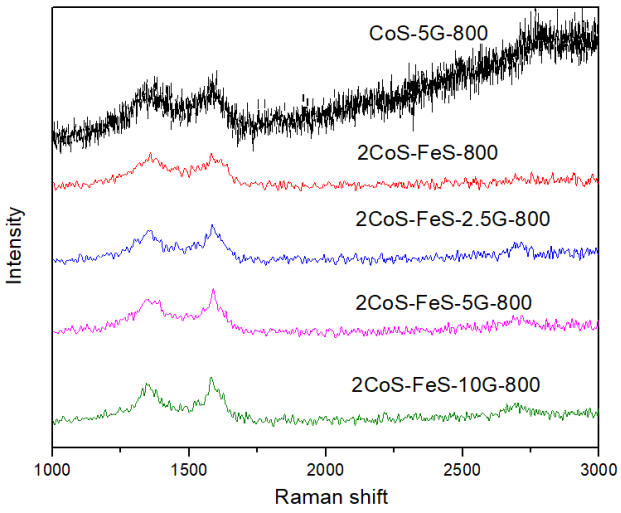

Figure 6. 13 Raman spectra of the 2CoS-FeS-zG-800 series composites

evens around 450-500 °C and 730-770 °C, corresponding to the burn off of the S doped carbon matrix and transfer of bimetallic sulfides to bimetallic oxides (confirmed by emission of CO_2 and SO_2 in MS signals), but also showed a slight

weight loss event between 630 and 680 °C. In contrast, only two major weight loss events could be observed for CoS-5G-800. In addition, the CO_2 emission intensity increased between 570 to 700 °C with the increase of graphene content, which could indicate the formation of graphitised structure carbon and further confirm the existence of graphene in the composite.

The Raman spectrum of Co-Fe-zG-800 series samples are shown in Figure 6.13. All samples displayed the characteristic D and G bands of carbon at 1350 and 1595 cm^{-1}, which correspond to disordered carbon and sp^2 hybridised graphitic carbon, respectively. Interestingly, all graphene-contained samples exhibited a peak around 2700 cm^{-1}, which indicates graphitised structure in the composites and the graphene were achieved from GO during the heat process.

The X-ray photoelectron spectroscopy (XPS) analysis was applied to investigate the chemical state of the as-synthesised 2CoS-FeS-5G composites. As shown in Figure 6.14a, element survey indicates the presence of C, Co, Fe, S and N in the representative 2CoS-FeS-5G sample. From Figure 6.14b, three peaks could be found at 285.3, 286.4 and 288.6 eV, corresponding to the C=N, C-N and C-S bond [250-253], respectively. the peak with binding energy located at 284.5 eV suggested the formation of sp^2 graphitic structure [260]. In the spectrum of Co 2p (Figure 6.14c), the sample exhibited two doublets at 786 and 800.3 eV, which indicate the octahedrolly coordination Co^{2+} in cobalt and Co $2p_{1/2}$ satellite components. Apart from that, two peaks could also be found at 779.7 and 781.2 eV, which are consistent with the presence of Co $2p_{3/2}$, implying the existence of Co^{2+} oxidation state [261, 310]. In addition, two weak doublets appeared at 779.1 and 781.9 eV, which implies the existence of Co^{3+} oxidation state in the composite. The spectrum of Fe 2p (Figure 6.14d) exhibited three peaks located at 709.8, 715.5 and 723.4 eV may be attributed to Fe (II) $2p_{2/3}$ satellite and Fe^{2+} [311-312]. Two doublets located at 711.8 and 713.6 eV, were consistent with Fe $2p_{3/2}$ (Fe^{3+} oxide states) and satellite components in the sample [311-312]. In S 2p spectrum shown in Figure 6.14e, the sample 2CoS-FeS-5G-800 displayed two peaks with binding energy at 162.5 and 163.6 eV owing to the S $2p_{3/2}$ and S $2p_{1/2}$ doublets with a binding energy separation of 1.1 eV, corresponding to the S^{2-} species of metal sulfides [255, 313]. Moreover, two peaks could be found at around 162.8 and 163.9 eV, may be due to the formation of S-C bonding [252]. In addition, binding energy at 168.5 and 169.4 eV were assigned to the S $2p_{3/2}$

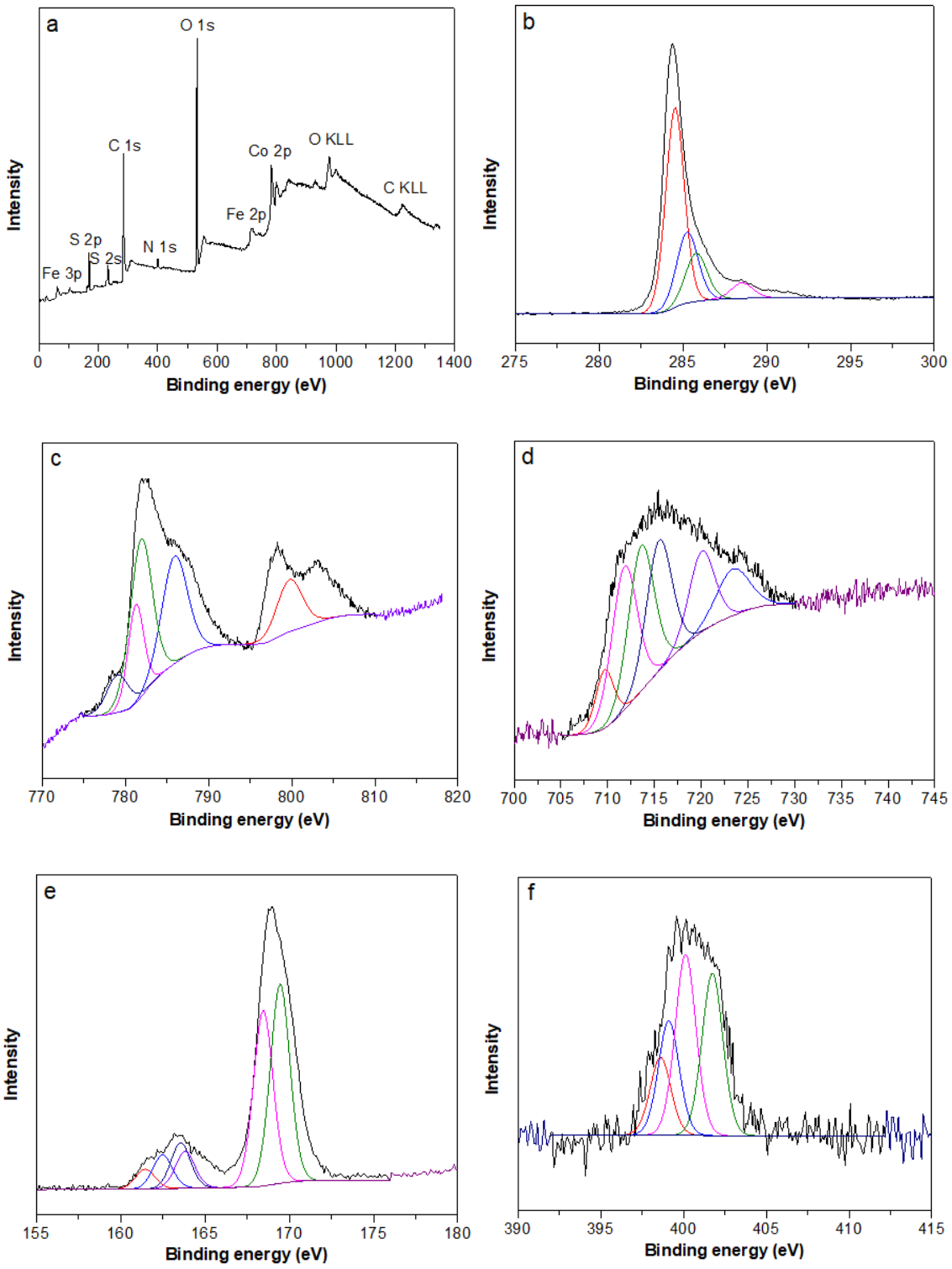

Figure 6. 14 (a) Element survey by XPS and XPS spectrum of (b) C 1s, (c) Co 2p, (d) Fe 2p, (e) S 2p and (f) N 1s for 2CoS-FeS-800

and S 2p $_{1/2}$ peaks of oxidised S species, such as sulfate groups [314], which could be due to the partially oxidation of sulfur in air [300]. Furthermore, the main peaks located at 397.8, 399.1, 400.1 and 401.8 eV corresponding to the pyridinic-N, Co-N, pyrrolic-N and graphitic-N [257-258], respectively, could be detected for N 1s spectrum in Figure 6.14f. The pyridinic-N and graphitic-N are

beneficial to OER/HER processes, which could enhance the onset potential and limit current. Owing to the volatility of N and S species in high temperature heat treatment, therefore, low content of N and S remains in the composite. From XPS analysis, we could conclude that sample 2CoS-FeS-5G-800 is composed of Co^{2+}, Co^{3+}, Fe^{2+}, Fe^{3+} and S^{2-} states. Combining XPS analysis, Raman spectrum and TEM results together, it can be concluded that Co-Fe sulfide have been successfully prepared *via* one-step carbonisation and sulfurisation process and CoS/FeS nanoparticles were supported on N, S co-doped carbon and/or graphene matrices.

The morphologies of the as-synthesised composites were characterised by scanning electron microscopy (SEM). Images of 2CoS-FeS-zG-800 series samples are shown in Figure 6.15a-f. Obviously, particles are all well dispersed in the composites. With the increase of graphene weight content from 2.5% to 10%, and the particles in the composites exhibited polyhedral shapes (shown in Figure 6.15a, c and e) with average crystal sizes decreasing from 150 to 90 nm. It is believed that the crystal sizes of bimetallic sulfide could be adjusted by controlling over the content of graphene in the composites, because the functional groups contained in Fe-substituted GO/ZIF-67 precursor will inhibit the growth of crystals.

The structures and morphologies of 2CoS-FeS-zG-800 series samples are further investigated by transmission electron microscopy (TEM). As shown in Figure 6.16a-f, the resulting composites did not hold the original shapes and morphology of precursors which was completely damaged after sulfurisation and carbonisation process at 800 °C. Since the GO solution could be beneficial to the dispersion, graphene contained composites exhibited better embedded particles than those without graphene. No single CoS or FeS particle could be found and most CoS and FeS particles were well embedded into composites and surrounded with carbon or graphene with particle size around 15 nm. From Figure 6.16b, it can be easily found that several graphene sheets are attached at the edge of the nanoparticles. It is believed that graphene were successfully formed and well dispersed into the composite, which not only could serve as bridges between bimetal sulfides and the contained porous carbon materials, but also offer more conductive approaches to enhance the electrochemical activities. Interestingly, an obvious carbon nanotube around 50 nm could be

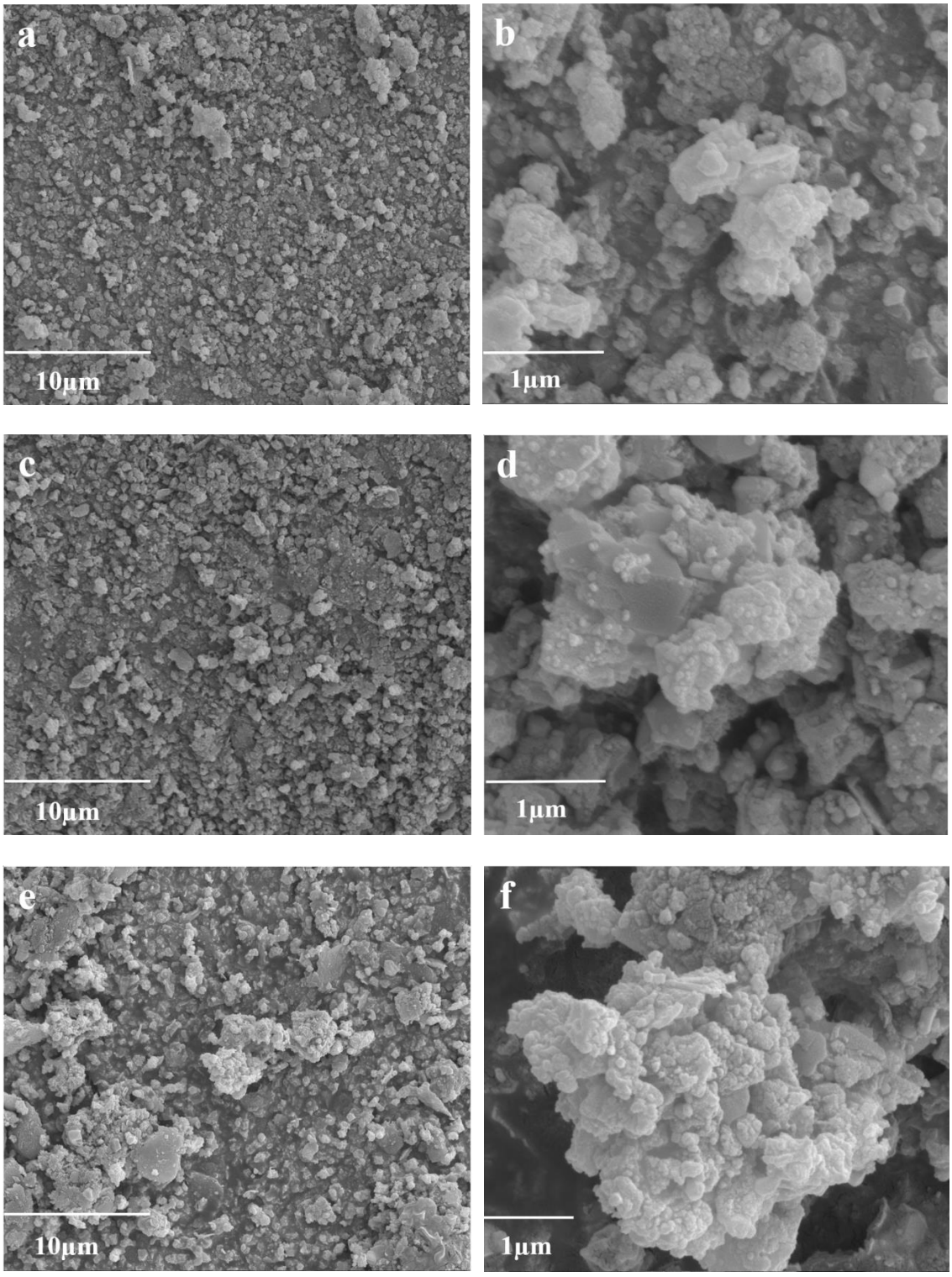

Figure 6. 15 SEM images of the (a, b) 2CoS-FeS-2.5G-800 (c, d) 2CoS-FeS-5G-800 (e, f) 2CoS-FeS-10G-800

observed in Figure 6.16d, which indicates the existence of synergistic effect between cobalt and iron. Moreover, the metal sulfide particles surrounded by carbon onions and carbon shells could be found in all composite particles, which can offer more active sites and electron transfer pathways to improve OER/HER activities for water splitting. The selected area electron diffraction

(SAED) patterns, shown in inset of Figure 6.16a, c and e, clearly displayed bright scattered dots are contributed from the crystalline nanoparticles while the dimmed diffraction rings are from the amorphous porous carbon matrix. In addition, the elemental mapping (2CoS-FeS-5G-800) of C, Co, Fe, S and N exhibited similar patterns with the selected TEM area, shown in Figure 6.17, indicating all elements were uniformed distributed in all composites.

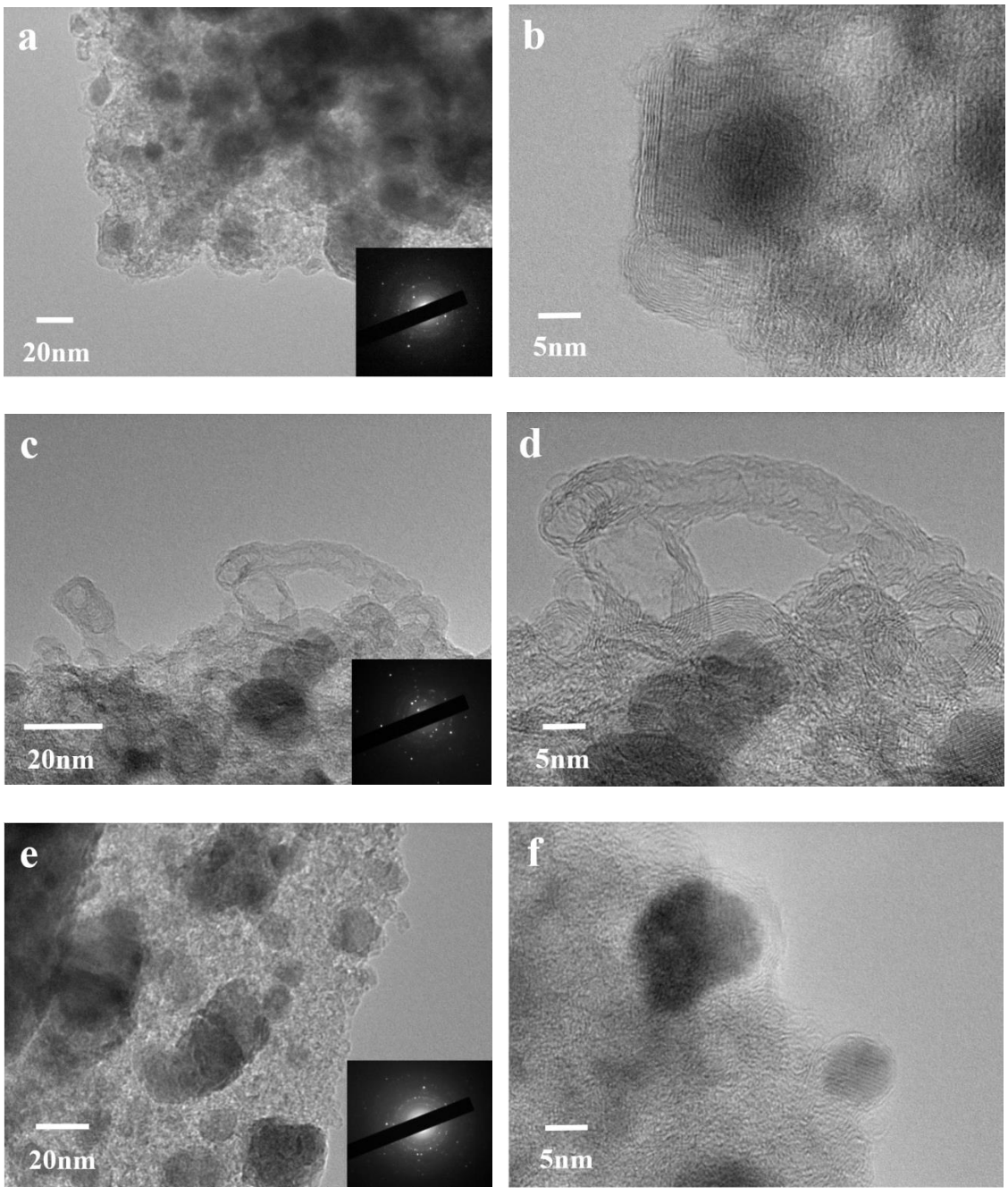

Figure 6. 16 TEM images of (a, b) 2CoS-FeS-2.5G-800 (c, d) 2CoS-FeS-5G-800 and (e, f) 2CoS-FeS-10G-800. Inset in (a, c and e) are SAED patterns for corresponding composites

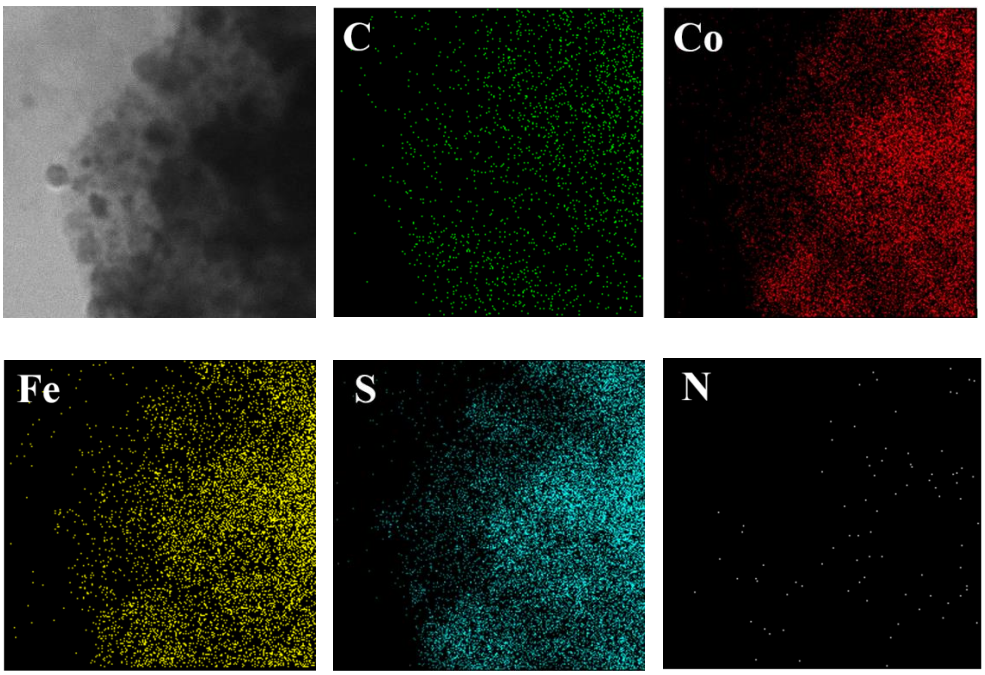

Figure 6. 17 TEM images and element mappings (C, Co, Fe, S and N) for 2CoS-FeS-5G-800

6.5 Electrocatalytic applications of bi-metallic sulfides derived from Fe substituted GO/ZIF-67

6.5.1 Hydrogen evolution reaction

In previous study, the sample 2CoS-FeS-800 exhibited the best OER and HER activities among all composites with different Co: Fe ratio. Therefore, the electrocatalytic activities of 2CoS-FeS-zG-800 series samples will be analysed. The HER performance of 2CoS-FeS-zG-800 series composites in 1M KOH electrolyte was evaluated and iR-corrected linear sweep voltammetry curves of the samples are presented in Figure 6.18a. All the samples exhibited a rapid catalytic current increase when voltage scanning beyond 0.15 V with the lowest onset potential of 0.125 V for 2CoS-FeS-5G-800. In contrast, 2CoS-FeS-10G-800, 2CoS-FeS-2.5G-800 and 2CoS-FeS-800 displayed a similar onset potential of 0.14 V, which is much lower than the value for the sample without iron sulfide. To afford a current density of 10 mA cm^{-2}, an overpotential of 190 mV (lowest) was required for 2CoS-FeS-5G-800, while similar overpotential of 200, 220 and 230 mV were needed for sample 2CoS-FeS-10G-800, 2CoS-FeS-2.5G-800 and 2CoS-FeS-800, respectively. However, CoS-5G-800 showed a very pool result with overpotential of 270 mV, implying the significant enhancing effect of iron sulfide in HER activities. This big difference also happened in their

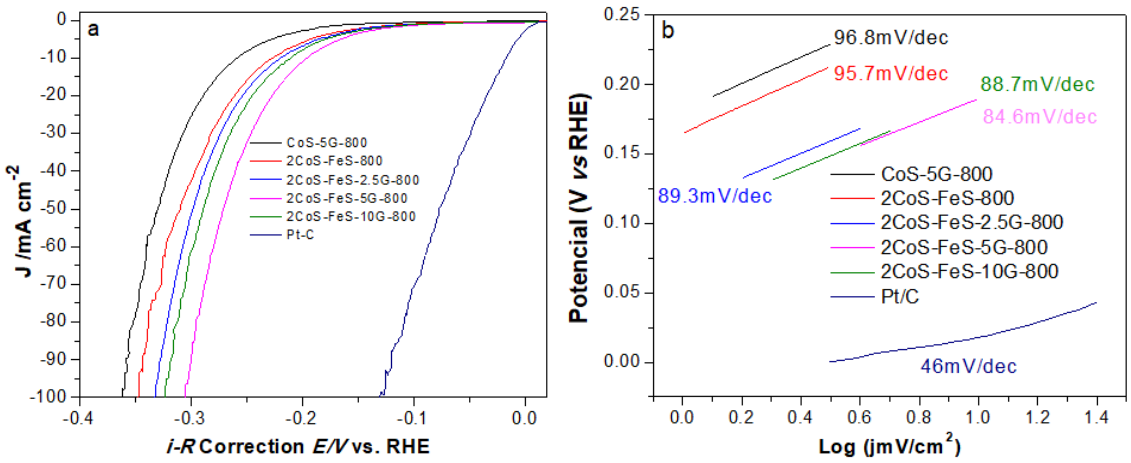

Figure 6. 18 Polarisation curves for HER on (a) 2CoS-FeS-zG-800 series composites and Pt-C and (b) their Tafel plot. Measured in 1 M KOH electrolyte

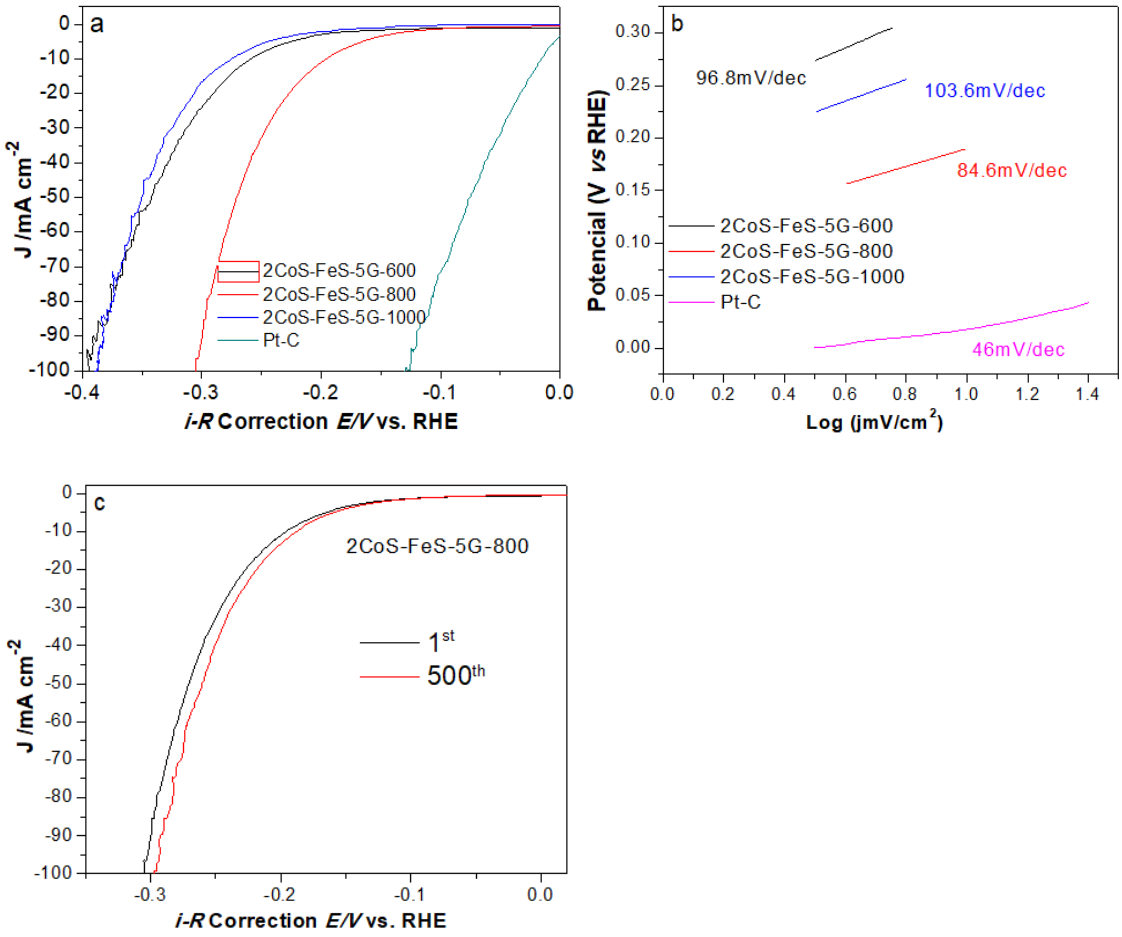

Figure 6. 19 Polarisation curves for HER on (a) 2CoS-FeS-5G-T series composites and Pt-C and (b) their Tafel plot and (c) durability test for 2CoS-FeS-5G-800. Measured in 1 M KOH electrolyte

Tafel slope results. From Figure 6.18b and Table 6.3, sample 2CoS-FeS-5G-800 showed the lowest slope value of 84.6 mV/dec, which is slightly lower than the value of 88.7 and 89.3 mV/dec for 2CoS-FeS-10G-800 and 2CoS-FeS-

Table 6. 3 HER performances of the 2CoS-FeS-zG-800 series composites. Measured in 1M KOH and 0.5M H_2SO_4 electrolyte

Catalyst	Onset potential (mV vs. RHE)		Over potential (mV vs. RHE)@ 10 mA cm^{-2}		Tafel slope (mV dec^{-1})	
	0.5 M H_2SO_4	1 M KOH	0.5 M H_2SO_4	1 M KOH	0.5 M H_2SO_4	1 M KOH
CoS-5G-800	350	200	420	270	90.3	96.8
2CoS-FeS-800	150	180	275	230	67.1	95.7
2CoS-FeS-2.5G-800	150	140	232	220	60.2	89.3
2CoS-FeS-5G-800	150	125	230	190	59.7	84.6
2CoS-FeS-10G-800	150	140	250	200	63.6	88.7
Pt-C	61	10	62	30	30	46

2.5G-800, respectively. In contrast, graphene-free sample 2CoS-FeS-800 exhibited value of 95.7 mV/dec, which is much higher than those of graphene-contained samples, further indicating that graphene played an important role in enhancing HER performance. Additionally, the HER activities of 2CoS-FeS-5G-T series composites obtained from different carbonisation/ sulfurisation temperature were also measured and shown in Figure 6.19a. Obviously, 2CoS-FeS-5G-800 exhibited the lowest onset and overpotential of 125 mV and 190 mV, whereas 2CoS-FeS-5G-600 and 2CoS-FeS-5G-1000 exhibited much higher onset potential of 200mV and 210mV respectively, and overpotential of 260 mV and 280 mV respectively, at the current density of 10 mA cm^{-2}. Their Tafel slopes were calculated and shown in Figure 6.19b, where slope values were 103.6 mV/dec and 124 mV/dec for 2CoS-FeS-5G-600 and 2CoS-FeS-5G-1000 respectively, much higher than that of 2CoS-FeS-5G-800 (84.6 mV/dec). Furthermore, the chronoamperometric test of 2CoS-FeS-5G-800 was measured and shown in Figure 6.19c. The 2CoS-FeS-5G-800 exhibited outstanding durability with same onset potential and only 10 mV negative shift of the overpotential to reach 10 mA cm^{-2} after 500 continuous potential cycle tests**.** It is obviously that graphene, converted from GO in the composite precursors, can provide more access pathways and improve electron transfer between the

catalyst surface and reaction intermediates. In addition, a synergistic effect between cobalt sulfide and iron sulfide, and many high density and multi valence states metal active sites in the composites were obtained during the sulfurisation and carbonisation process at 800 °C. As a result, the combining effects of graphene and iron sulfide enhance the HER performance and the composite materials exhibited outstanding activities for the overall water splitting.

Besides, the HER performance of 2CoS-FeS-zG-800 series composites were also assessed in acidic electrolyte (0.5M H_2SO_4) media. As shown in Figure 6.20a, the polarisation curves for 2CoS-FeS-5G-800, 2CoS-FeS-2.5G-800, 2CoS-FeS-10G-800 and 2CoS-FeS-800 showed a similar onset potential of ~0.15 V and exhibited the overpotential of 230, 232, 250 and 275 mV respectively, to reach the current density of 10 mA cm^{-2}. In contrast, CoS-5G-800 displayed a much higher onset potential of 0.35 V and the overpotential of 0.42 V. Furthermore, all the graphene contained samples exhibited similar Tafel plots with the lowest slope value of 59.7 mV/dec for sample 2CoS-FeS-5G-800, while the slope values for other samples ranged from 60.2 to 90.3 mV/dec, respectively. It is interesting to note that sample 2CoS-FeS-5G-800 not only showed the lowest onset/overpotential in alkaline media, but also exhibited the best HER activities in acidic solution. Therefore, the composite with Co: Fe ratio of 2: 1 and containing 5% graphene exhibited the best overall water splitting activities among all the composites.

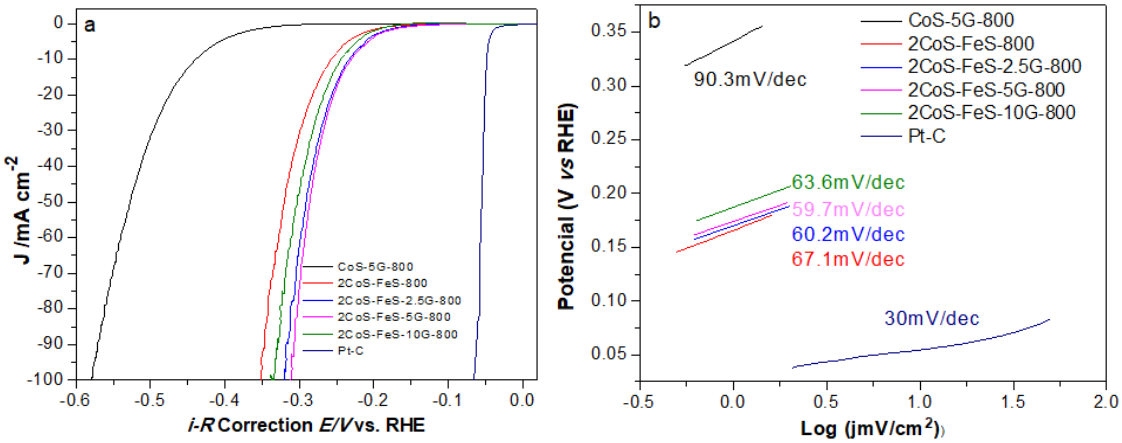

Figure 6. 20 Polarisation curves for HER on (a) 2CoS-FeS-zG-800 series composites and Pt-C and (b) their Tafel plot and 2CoS-FeS-5G-800. Measured in 0.5 M H_2SO_4 electrolyte

6.5.2 Oxygen evolution reaction

As shown in Figure 6.21, 2CoS-FeS-zG-800 composites showed excellent OER activities and exhibited much lower onset potential (1.38-1.40 V) than sample CoS-5G-800 (1.48 V) and reference material IrO_2/C (1.5 V), indicating the introduction of iron could improve the OER activities of the studied materials. The 2CoS-FeS-5G-800 exhibited the lowest onset potential of 1.38 V, which is the same value as 2CoS-FeS-2.5G-800 and 20 mV lower than that of 2CoS-FeS-10G-800 and 2CoS-FeS-800. In comparison, all graphene-contained samples expressed lower onset potentials than 2CoS-FeS-800 without graphene, indicating that graphene in the composites could enhance the OER activities of the materials. The operating potential to achieve a current density of 10 mA cm^{-2} was also compared with the studied samples. The sample 2CoS-FeS-5G-800 needed an overpotential of 1.44 V to realise the current density of 10 mA cm^{-2}, which is comparable to the value of 1.46 V for 2CoS-FeS-2.5G-800, 2CoS-FeS-10G-800 and 2CoS-FeS-800 (shown in Table 6.4). Meanwhile, as the Tafel slope result shown in Figure 6.21b, the 2CoS-FeS-5G-800 exhibited the lowest slope value of 40.3 mV/dec and other samples displayed slope values ranging from 43.7 to 45.2 mV/dec, which were all much lower than that of 82 mV/dec for IrO_2/C. Furthermore, the durability of the catalyst is evaluated and displayed in Figure 6.21c. The 2CoS-FeS-5G-800 showed a similar I-V curve after 500 times scanning with a scan rate of 5 mVs^{-1}, while the 500^{th} curve displayed a 80 mV lower overpotential at the current density of 10 mA cm^{-2} and 50 mV lower onset potential than the initial one.

Table 6. 4 OER performances of the 2CoS-FeS-yG-800 series composites

Catalyst	Onset potential (V vs. RHE)	Overpotential (V vs. RHE) @ current density of 10mA cm^{-2}	Tafel slope (mV/dec)
CoS-5G-800	1.48	1.54	59.5
2CoS-FeS-800	1.40	1.46	50.8
2CoS-FeS-2.5G-800	1.38	1.46	50.5
2CoS-FeS-5G-800	1.38	1.44	50.3
2CoS-FeS-10G-800	1.40	1.46	55.5

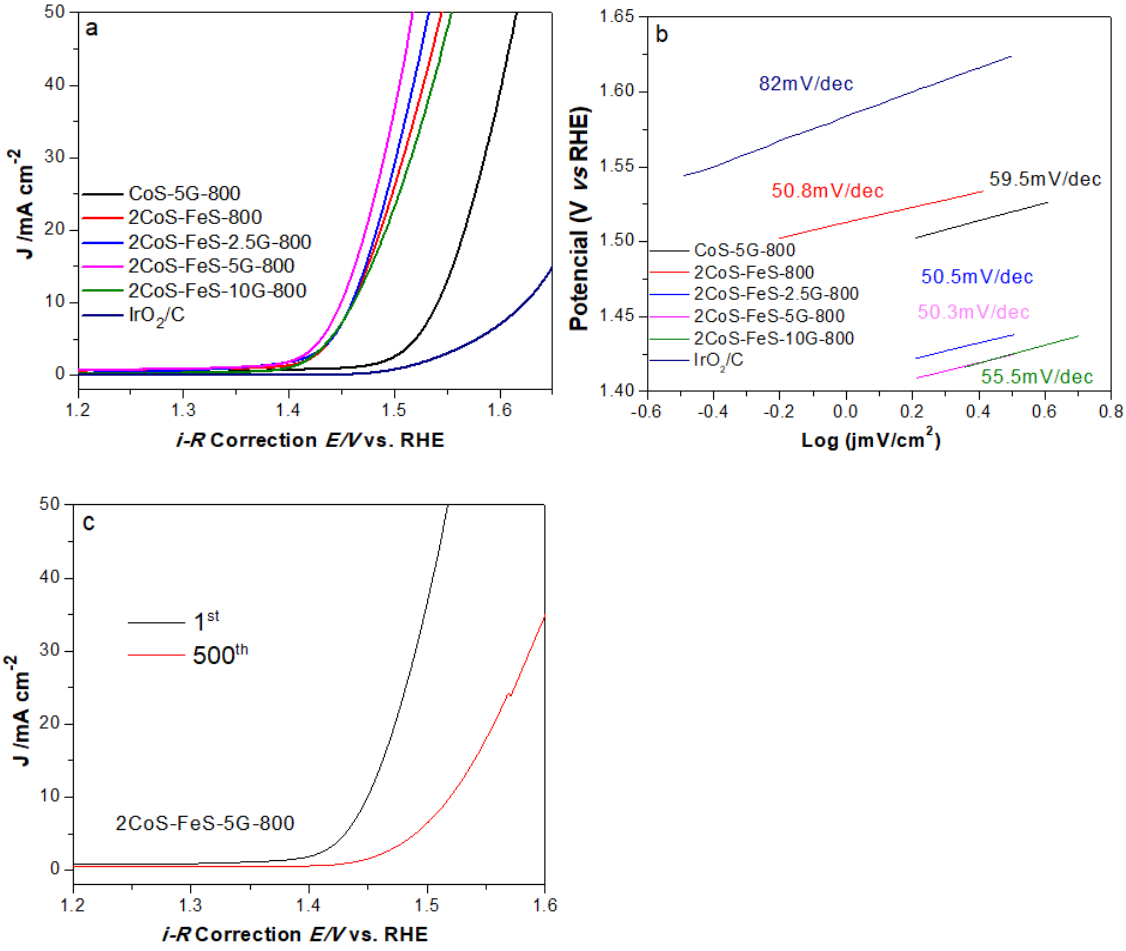

Figure 6. 21 Polarisation curves for OER on (a) 2CoS-FeS-yG-800 series composites and IrO_2/C and (b) their Tafel plot and (c) durability test for 2CoS-FeS-5G-800

6.6 Summary

In summary, Fe-substituted ZIF-67 and Fe-substituted GO/ZIF-67 were successfully synthesised and their derivatives obtained *via* carbonised/sulfurised in Argon/H_2S atmosphere were also well prepared. The physiochemical properties of the two series composites xCoS-yFeS-800 and 2CoS-FeS-zG-800 were discussed and fully analysed by various Characterisation techniques. XPS, XRD, TGA and TEM results have all confirmed cobalt/iron sulfide nanoparticles were homogenously dispersed in *in-situ* formed porous carbon and graphene matrix and synergistic interaction between cobalt sulfide and iron sulfide particles existed in the obtained composites. Furthermore, graphene contained composites exhibited excellent electrochemical activities both in OER and HER, and the composite 2CoS-FeS-5G-800 is one of the promising electrode materials for water splitting.

Chapter 7: Conclusions and future work

In conclusion, simple and cost-efficient synthesis of GO/ZIFs based composites and their graphene reinforced derivatives have been successfully developed and these derivatives showed excellent performances in electrocatalytic fields. This thesis presents the synthesis of a series of ZIFs and ZIF derivatives, such as ZIF-67, GO/ZIF-67, cobalt sulfide/N, S co-doped porous carbon derived from ZIF-67, cobalt sulfide/N, S co-doped porous carbon/graphene derived from GO/ZIF-67, cobalt-nickel sulfide/N, S co-dopoed porous carbon/graphene derived from Ni-substituted GO/ZIF-67, cobalt-iron/N dopoed porous carbon/graphene derived from Fe-substituted GO/ZIF-67, cobalt-iron oxides/N-doped porous carbon/graphene derived from Fe-substituted GO/ZIF-67 and cobalt-iron sulfide/N, S co-dopoed porous carbon/graphene derived from Fe-substituted GO/ZIF-67. The crystal structures, morphologies, thermal stabilities and textural properties of these as-synthesised nanocomposites were characterised. Furthermore, the excellent applications, including gas adsorption, electrocatalytic oxygen reduction reaction, oxygen evolution reaction, hydrogen evolution reaction and water splitting have also been reported. Therefore, the PhD objectives have been achieved.

In Chapter 4, a process featured the sulfurisation of GO/ZIF-67 precursors was demonstrated to be a facile one-step method to prepare graphene containing cobalt sulfide/N, S co-doped porous carbon. A variety of characterisation techniques were conducted to study the physico-chemical properties of the resulting CoS-C-G composites. It was found that cobalt sulfide nanoparticles were homogenously dispersed in carbon matrix and N, S elements were successfully doped into porous carbon and graphene. Compared with the CoS-C composite, the graphene containing CoS-C-G composites exhibit outstanding electrocatalytic performance not only in ORR with higher onset potential and a four-electron pathway, but also in OER with a smaller overpotential and remarkable durability, showing that the introduction of graphene in the composites holds the key to obtain the increased electrical conductivity and ion transfer rate. All these findings indicate that CoS-C-G is highly promising electrode material in many energy-related applications. Additionally, bi-metallic nickel promoted cobalt sulfide/N, S co-dopoed porous carbon and graphene catalyst was also successfully prepared through a simple one-step

carbonisation and sulfurisation process by using Ni-substituted GO/ZIF-67 as precursors. The produced homogeneously cobalt/nickel sulfide nanoparticles were uniformly dispersed within the functionalised nanoporous carbon matrix and N, S elements were well doped into porous carbon and graphene. Possessing the Ni substitution, N, S co-doping and the presence of graphene, the resulting sample 4CoS-NiS-5G-800 exhibited remarkable OER electrochemical activities with low oneset/overpotential in alkaline electrolyte media as well as a good HER activities over a wide pH range.

In Chapter 5, both homogeneous dispersed bi-metallic cobalt-iron/N-doped porous carbon and bi-metallic cobalt-iron/N-doped porous carbon/graphene series nanocomposites as high-performance bifunctional electrocatalysts towards OER and HER were successfully synthesised from Fe-substituted ZIF-67 and Fe-substituted GO/ZIF-67, respectively, by using a facile and efficient synthesis approach. As a result, xCo-yFe-800 series nanocomposites displayed remarkable electrocatalytic activities and superior durability, owing to the synergistic effect between cobalt and iron, the crystalline structure of metal particles, the high porosity of corresponding materials as well as the homogeneous dispersion of N in the resulting composites. In comparison, graphene-reinforced xCo-yFe-zG-800 series samples demonstrated a significantly enhanced electrocatalytic activities for overall water splitting as a result of the combining effect of increased electrical conductivity, more active sites and higher electron transfer rate of graphene. In addition, Chapter 5 also demonstrates a series of bi-metallic cobalt-iron/N-doped porous carbon/graphene composites synthesised by oxidation in air at 350 °C of Co-Fe/N-doped carbon/graphene. The formed Co-Fe oxides/N-doped carbon/graphene composite shows not only exceptionally electrochemical activity for water splitting, but also ability to provide anchoring sites for catalytically active metal oxide nanoparticles to deposit.

In Chapter 6, the efficient synthesis method of simultaneous sulfurisation and carbonisation has been presented for the preparation of both cobalt-iron sulfide/S, N co-doped porous carbon and cobalt-iron sulfide/N, S co-doped porous carbon/graphene from precursors of Fe-substituted ZIF-67 and Fe-substituted GO/ZIF-67, respectively. The effect of different Co: Fe ratios on the electrocatalytic activities was discussed. Among the as-synthesised

nanocomposites, sample 2CoS-FeS-800 showed excellent OER and HER activities for overall water splitting. Therefore, it comes to the conclusion that the introduction of graphene is the reason behind the improved electrocatalytic activity of 2CoS-FeS-5G-800 in water splitting.

Based on the results above we have achieved in this thesis, some suggestions and recommendations for further work is offered as follows:

- GO/ZIF-67 series nanocomposites have been successfully prepared via a one-step in-situ synthesis method, which are excellent precursors to produce graphene reinforced transition metal component nanocomposites. Porous carbon can provide high surface area with micropores, while, porous graphene can give an enhancement to electrical conductivity and electron transfer rate. Thus, it would be interesting to synthesise the different GO-containing ZIFs nanomaterials via the similar method.
- Bi-metallic derivatives have been obtained from Ni or Fe substituted GO/ZIF-67, and subsequently exhibited remarkable electrochemical performance, duo to the synergistic effect of bi-metals. It will be very interesting to develop other bi-metal or even tri-metal GO/ZIFs based systems with the addition of metals like Mo and W. The products would be potentially excellent electrode materials which are useful in applications like supercapacitors and lithium ion batteries.
- Thanks to the doping effect of nitrogen and sulfur, ZIF-67 derivatives demonstrate excellent electrocatalytic performance in this thesis work. Therefore, doping effect in similar systems is an interesting topic worth exploration and potentially generate highly exciting results.
- Even bi-metallic derivatives exhibit improved electrocatalytic performance, according to findings made in this work, there are still challenges remain. It is very necessary to find out the mechanisms of synergistic effect in bi-metals and elements doping effect in composites. Morover, although porous graphene and porous-graphene-based materials exhibit good properties and potential to be employed in many applications, the theoretical studies such as inherent properties of porous graphene, the control of pore size distribution, and the realisation of large-scale production are still extensive required in the future.

References

1. B. Chen; Yang, Z.; Zhu, Y.; Xia, Y., *Journal of Materials Chemistry A* 2014, **2**, 16811-16831.
2. B. Wang; Côté, A. P.; Furukawa, H.; O'Keeffe, M.; Yaghi, O. M., *Nature* 2008, **453**, 207.
3. A. Phan; Doonan, C. J.; Uribe-Romo, F. J.; Knobler, C. B.; O'Keeffe, M.; Yaghi, O. M., *Accounts of Chemical Research* 2010, **43**, 58-67.
4. X. Lu; Hao, G.-P.; Sun, X.; Kaskel, S.; Schmidt, O. G., *Journal of Materials Chemistry A* 2017, **5**, 6284-6291.
5. W. Ju; Bagger, A.; Hao, G.-P.; Varela, A. S.; Sinev, I.; Bon, V.; Roldan Cuenya, B.; Kaskel, S.; Rossmeisl, J.; Strasser, P., *Nature Communications* 2017, **8**, 944.
6. J. Liu; Zhu, D.; Guo, C.; Vasileff, A.; Qiao, S.-Z., *Advanced Energy Materials* 2017, 1700518.
7. J. C. Tan; Bennett, T. D.; Cheetham, A. K., *Proceedings of the National Academy of Sciences* 2010, **107**, 9938-9943.
8. A. K. Geim, *Science* 2009, **324**, 1530-1534.
9. Y. Sun; Wu, Q.; Shi, G., *Energy & Environmental Science* 2011, **4**, 1113-1132.
10. L. Jiang; Fan, Z., *Nanoscale* 2014, **6**, 1922-1945.
11. M. A. Worsley; Pauzauskie, P. J.; Olson, T. Y.; Biener, J.; Satcher, J. H.; Baumann, T. F., *Journal of the American Chemical Society* 2010, **132**, 14067-14069.
12. Z.-S. Wu; Ren, W.; Gao, L.; Zhao, J.; Chen, Z.; Liu, B.; Tang, D.; Yu, B.; Jiang, C.; Cheng, H.-M., *ACS Nano* 2009, **3**, 411-417.
13. Z. Fan, *Carbon* 2012, **v. 50**, pp. 1699-1703-2012 v.50 no.4.
14. S. Stankovich; Dikin, D. A.; Dommett, G. H. B.; Kohlhaas, K. M.; Zimney, E. J.; Stach, E. A.; Piner, R. D.; Nguyen, S. T.; Ruoff, R. S., *Nature* 2006, **442**, 282-286.
15. K. S. Park; Ni, Z.; Côté, A. P.; Choi, J. Y.; Huang, R.; Uribe-Romo, F. J.; Chae, H. K.; O'Keeffe, M.; Yaghi, O. M., *Proceedings of the National Academy of Sciences* 2006, **103**, 10186-10191.
16. X.-C. Huang; Lin, Y.-Y.; Zhang, J.-P.; Chen, X.-M., *Angewandte Chemie International Edition* 2006, **45**, 1557-1559.

17. J. Cravillon; Münzer, S.; Lohmeier, S.-J.; Feldhoff, A.; Huber, K.; Wiebcke, M., *Chemistry of Materials* 2009, **21**, 1410-1412.
18. S. K. Nune; Thallapally, P. K.; Dohnalkova, A.; Wang, C.; Liu, J.; Exarhos, G. J., *Chemical Communications* 2010, **46**, 4878-4880.
19. S. R. Venna; Carreon, M. A., *Journal of the American Chemical Society* 2010, **132**, 76-78.
20. R. Ameloot; Gobechiya, E.; Uji-i, H.; Martens, J. A.; Hofkens, J.; Alaerts, L.; Sels, B. F.; De Vos, D. E., *Advanced Materials* 2010, **22**, 2685-2688.
21. Y.-Q. Tian; Zhao, Y.-M.; Chen, Z.-X.; Zhang, G.-N.; Weng, L.-H.; Zhao, D.-Y., *Chemistry – A European Journal* 2007, **13**, 4146-4154.
22. M. G. Walter; Warren, E. L.; McKone, J. R.; Boettcher, S. W.; Mi, Q.; Santori, E. A.; Lewis, N. S., *Chemical Reviews* 2010, **110**, 6446-6473.
23. C. C. L. McCrory; Jung, S.; Ferrer, I. M.; Chatman, S. M.; Peters, J. C.; Jaramillo, T. F., *Journal of the American Chemical Society* 2015, **137**, 4347-4357.
24. F. Song; Hu, X., *Nature Communications* 2014, **5**, 4477.
25. Y. Yan; Xia, B. Y.; Zhao, B.; Wang, X., *Journal of Materials Chemistry A* 2016, **4**, 17587-17603.
26. M. E. Davis, *Nature* 2002, **417**, 813-821.
27. S. A. Moggach; Bennett, T. D.; Cheetham, A. K., *Angewandte Chemie* 2009, **121**, 7221-7223.
28. D. Fairen-Jimenez; Moggach, S. A.; Wharmby, M. T.; Wright, P. A.; Parsons, S.; Düren, T., *Journal of the American Chemical Society* 2011, **133**, 8900-8902.
29. G.-P. Hao; Sahraie, N. R.; Zhang, Q.; Krause, S.; Oschatz, M.; Bachmatiuk, A.; Strasser, P.; Kaskel, S., *Chemical Communications* 2015, **51**, 17285-17288.
30. J. Liu; Zhu, D.; Guo, C.; Vasileff, A.; Qiao, S.-Z., *Advanced Energy Materials* 2017, **7**, 1700518.
31. N. Cheng; Ren, L.; Xu, X.; Du, Y.; Dou, S. X., *Advanced Energy Materials* 2018, **8**, 1801257.
32. P. G. Bruce; Freunberger, S. A.; Hardwick, L. J.; Tarascon, J.-M., *Nature Materials* 2011, **11**, 19.

33. Y. V. Kaneti; Dutta, S.; Hossain, M. S. A.; Shiddiky, M. J. A.; Tung, K.-L.; Shieh, F.-K.; Tsung, C.-K.; Wu, K. C.-W.; Yamauchi, Y., *Advanced Materials* 2017, **29**, 1700213.
34. H. Wu; Zhou, W.; Yildirim, T., *Journal of the American Chemical Society* 2007, **129**, 5314-5315.
35. R. Banerjee; Phan, A.; Wang, B.; Knobler, C.; Furukawa, H.; O'Keeffe, M.; Yaghi, O. M., *Science* 2008, **319**, 939-943.
36. H. Hayashi; Côté, A. P.; Furukawa, H.; O'Keeffe, M.; Yaghi, O. M., *Nature Materials* 2007, **6**, 501.
37. R. Banerjee; Furukawa, H.; Britt, D.; Knobler, C.; O'Keeffe, M.; Yaghi, O. M., *Journal of the American Chemical Society* 2009, **131**, 3875-3877.
38. R. E. Morris, *Angewandte Chemie International Edition* 2008, **47**, 442-444.
39. J.-P. Zhang; Zhu, A.-X.; Lin, R.-B.; Qi, X.-L.; Chen, X.-M., *Advanced Materials* 2011, **23**, 1268-1271.
40. Y. Ban; Li, Y.; Liu, X.; Peng, Y.; Yang, W., *Microporous and Mesoporous Materials* 2013, **173**, 29-36.
41. D. Peralta; Chaplais, G.; Simon-Masseron, A.; Barthelet, K.; Pirngruber, G. D., *Microporous and Mesoporous Materials* 2012, **153**, 1-7.
42. J. Cravillon; Nayuk, R.; Springer, S.; Feldhoff, A.; Huber, K.; Wiebcke, M., *Chemistry of Materials* 2011, **23**, 2130-2141.
43. Y. Pan; Liu, Y.; Zeng, G.; Zhao, L.; Lai, Z., *Chemical Communications* 2011, **47**, 2071-2073.
44. J. Qian; Sun, F.; Qin, L., *Hydrothermal synthesis of zeolitic imidazolate framework-67 (ZIF-67) nanocrystals*. 2012; Vol. 82, p 220–223.
45. A. F. Gross; Sherman, E.; Vajo, J. J., *Dalton Transactions* 2012, **41**, 5458-5460.
46. J. Yao; He, M.; Wang, K.; Chen, R.; Zhong, Z.; Wang, H., *CrystEngComm* 2013, **15**, 3601-3606.
47. F.-K. Shieh; Wang, S.-C.; Leo, S.-Y.; Wu, K. C.-W., *Chemistry – A European Journal* 2013, **19**, 11139-11142.
48. E. R. Parnham; Morris, R. E., *Accounts of Chemical Research* 2007, **40**, 1005-1013.
49. E. R. Cooper; Andrews, C. D.; Wheatley, P. S.; Webb, P. B.; Wormald, P.; Morris, R. E., *Nature* 2004, **430**, 1012-1016.

50. G. A. V. Martins; Byrne, P. J.; Allan, P.; Teat, S. J.; Slawin, A. M. Z.; Li, Y.; Morris, R. E., *Dalton Transactions* 2010, **39**, 1758-1762.
51. B. Seoane; Zamaro, J. M.; Tellez, C.; Coronas, J., *CrystEngComm* 2012, **14**, 3103-3107.
52. Q. Shi; Chen, Z.; Song, Z.; Li, J.; Dong, J., *Synthesis of ZIF-8 and ZIF-67 by Steam-Assisted Conversion and an Investigation of Their Tribological Behaviors*. 2011.
53. J.-B. Lin; Lin, R.-B.; Cheng, X.-N.; Zhang, J.-P.; Chen, X.-M., *Chemical Communications* 2011, **47**, 9185-9187.
54. M. J. Cliffe; Mottillo, C.; Stein, R. S.; Bučar, D.-K.; Friščić, T., *Chemical Science* 2012, **3**, 2495-2500.
55. J. F. Fernández-Bertrán; Hernández, M. P.; Reguera, E.; Yee-Madeira, H.; Rodriguez, J.; Paneque, A.; Llopiz, J. C., *Journal of Physics and Chemistry of Solids* 2006, **67**, 1612-1617.
56. T. Friščić; Halasz, I.; Beldon, P. J.; Belenguer, A. M.; Adams, F.; Kimber, S. A. J.; Honkimäki, V.; Dinnebier, R. E., *Nature Chemistry* 2013, **5**, 145.
57. P. J. Beldon; Fábián, L.; Stein, R. S.; Thirumurugan, A.; Cheetham, A. K.; Friščić, T., *Angewandte Chemie International Edition* 2010, **49**, 9640-9643.
58. J. Yao; Wang, H., *Chemical Society Reviews* 2014, **43**, 4470-4493.
59. H. Bux; Liang, F.; Li, Y.; Cravillon, J.; Wiebcke, M.; Caro, J., *Journal of the American Chemical Society* 2009, **131**, 16000-16001.
60. E. Haldoupis; Nair, S.; Sholl, D. S., *Journal of the American Chemical Society* 2010, **132**, 7528-7539.
61. N. Masciocchi; Attilio Ardizzoia, G.; Brenna, S.; Castelli, F.; Galli, S.; Maspero, A.; Sironi, A., *Chemical Communications* 2003, 2018-2019.
62. K. Müller-Buschbaum, *Zeitschrift für Naturforschung B*, 2006; **61**, 792.
63. A. Huang; Bux, H.; Steinbach, F.; Caro, J., *Angewandte Chemie International Edition* 2010, **49**, 4958-4961.
64. A. Huang; Dou, W.; Caro, J., *Journal of the American Chemical Society* 2010, **132**, 15562-15564.
65. L. Li; Yao, J.; Chen, R.; He, L.; Wang, K.; Wang, H., *Microporous and Mesoporous Materials* 2013, **168**, 15-18.
66. X. Dong; Huang, K.; Liu, S.; Ren, R.; Jin, W.; Lin, Y. S., *Journal of Materials Chemistry* 2012, **22**, 19222-19227.

67. R. Zhao; Xia, W.; Lin, C.; Sun, J.; Mahmood, A.; Wang, Q.; Qiu, B.; Tabassum, H.; Zou, R., *Carbon* 2017, **114**, 284-290.
68. M. Jiang; Cao, X.; Zhu, D.; Duan, Y.; Zhang, J., *Electrochimica Acta* 2016, **196**, 699-707.
69. L.-L. Feng; Yu, G.; Wu, Y.; Li, G.-D.; Li, H.; Sun, Y.; Asefa, T.; Chen, W.; Zou, X., *Journal of the American Chemical Society* 2015, **137**, 14023-14026.
70. H. Hu; Han, L.; Yu, M.; Wang, Z.; Lou, X. W., *Energy & Environmental Science* 2016, **9**, 107-111.
71. X. Liang; Zheng, B.; Chen, L.; Zhang, J.; Zhuang, Z.; Chen, B., *ACS Applied Materials & Interfaces* 2017, **9**, 23222-23229.
72. H. Li; Qian, X.; Xu, C.; Huang, S.; Zhu, C.; Jiang, X.; Shao, L.; Hou, L., *ACS Applied Materials & Interfaces* 2017, **9**, 28394-28405.
73. X. Li; Fang, Y.; Lin, X.; Tian, M.; An, X.; Fu, Y.; Li, R.; Jin, J.; Ma, J., *Journal of Materials Chemistry A* 2015, **3**, 17392-17402.
74. Y. Hou; Li, J.; Wen, Z.; Cui, S.; Yuan, C.; Chen, J., *Nano Energy* 2015, **12**, 1-8.
75. W. Xia; Zhu, J.; Guo, W.; An, L.; Xia, D.; Zou, R., *Journal of Materials Chemistry A* 2014, **2**, 11606-11613.
76. B. Chen; Ma, G.; Kong, D.; Zhu, Y.; Xia, Y., *Carbon* 2015, **95**, 113-124.
77. Y. Pan; Lai, Z., *Chemical Communications* 2011, **47**, 10275-10277.
78. M. E. Davis, *Accounts of Chemical Research* 1993, **26**, 111-115.
79. C. Chizallet; Lazare, S.; Bazer-Bachi, D.; Bonnier, F.; Lecocq, V.; Soyer, E.; Quoineaud, A.-A.; Bats, N., *Journal of the American Chemical Society* 2010, **132**, 12365-12377.
80. U. P. N. Tran; Le, K. K. A.; Phan, N. T. S., *ACS Catalysis* 2011, **1**, 120-127.
81. L. T. L. Nguyen; Le, K. K. A.; Phan, N. T. S., *Chinese Journal of Catalysis* 2012, **33**, 688-696.
82. F. X. Llabrés i Xamena; Casanova, O.; Galiasso Tailleur, R.; Garcia, H.; Corma, A., *Journal of Catalysis* 2008, **255**, 220-227.
83. L. T. L. Nguyen; Le, K. K. A.; Truong, H. X.; Phan, N. T. S., *Catalysis Science & Technology* 2012, **2**, 521-528.
84. S. B. Kalidindi; Esken, D.; Fischer, R. A., *Chemistry – A European Journal* 2011, **17**, 6594-6597.

85. J. Zakzeski; Dębczak, A.; Bruijnincx, P. C. A.; Weckhuysen, B. M., *Applied Catalysis A: General* 2011, **394**, 79-85.
86. C.-Y. Sun; Qin, C.; Wang, X.-L.; Su, Z.-M., *Expert Opinion on Drug Delivery* 2013, **10**, 89-101.
87. C.-Y. Sun; Qin, C.; Wang, X.-L.; Yang, G.-S.; Shao, K.-Z.; Lan, Y.-Q.; Su, Z.-M.; Huang, P.; Wang, C.-G.; Wang, E.-B., *Dalton Trans.* 2012; **41**, 6906-6909.
88. N. Liédana; Galve, A.; Rubio, C.; Téllez, C.; Coronas, J., *ACS Applied Materials & Interfaces* 2012, **4**, 5016-5021.
89. W. Ma; Jiang, Q.; Yu, P.; Yang, L.; Mao, L., *Analytical Chemistry* 2013, **85**, 7550-7557.
90. S. Liu; Xiang, Z.; Hu, Z.; Zheng, X.; Cao, D., *Journal of Materials Chemistry* 2011, **21**, 6649-6653.
91. V. Manuel Aceituno Melgar; Kim, J.; Roslee Othman, M., *Journal of Industrial and Engineering Chemistry*. 2015, **28**.
92. S. Wang; Hou, Y.; Lin, S.; Wang, X., *Nanoscale* 2014, **6**, 9930-9934.
93. Q. Xu; Li, H.; Yue, F.; Chi, L.; Wang, J., *New Journal of Chemistry* 2016, **40**, 3032-3035.
94. E. A. Flügel; Lau, V. W.-h.; Schlomberg, H.; Glaum, R.; Lotsch, B. V., *Chemistry – A European Journal* 2016, **22**, 3676-3680.
95. L. Huang; He, M.; Chen, B.-b.; Cheng, Q.; Hu, B., *ACS Applied Materials & Interfaces* 2017, **9**, 2550-2559.
96. A. Aijaz; Fujiwara, N.; Xu, Q., *Journal of the American Chemical Society* 2014, **136**, 6790-6793.
97. S. Kattel; Wang, G., *Journal of Materials Chemistry A* 2013, **1**, 10790-10797.
98. B. Chen; Li, R.; Ma, G.; Gou, X.; Zhu, Y.; Xia, Y., *Nanoscale* 2015, **7**, 20674-20684.
99. V. Ganesan; Ramasamy, P.; Kim, J., *International Journal of Hydrogen Energy* 2017, **42**, 5985-5992.
100. Y. Guo; Tang, J.; Qian, H.; Wang, Z.; Yamauchi, Y., *Chemistry of Materials* 2017, **29**, 5566-5573.
101. D. Ji; Peng, S.; Fan, L.; Li, L.; Qin, X.; Ramakrishna, S., *Journal of Materials Chemistry A* 2017, **5**, 23898-23908.

102. B. You; Jiang, N.; Sheng, M.; Gul, S.; Yano, J.; Sun, Y., *Chemistry of Materials* 2015, **27**, 7636-7642.
103. X. Li; Jiang, Q.; Dou, S.; Deng, L.; Huo, J.; Wang, S., *Journal of Materials Chemistry A* 2016, **4**, 15836-15840.
104. N. L. Torad; Hu, M.; Ishihara, S.; Sukegawa, H.; Belik, A. A.; Imura, M.; Ariga, K.; Sakka, Y.; Yamauchi, Y., *Small* 2014, **10**, 2096-2107.
105. H.-L. Jiang; Liu, B.; Lan, Y.-Q.; Kuratani, K.; Akita, T.; Shioyama, H.; Zong, F.; Xu, Q., *Journal of the American Chemical Society* 2011, **133**, 11854-11857.
106. W. Chaikittisilp; Hu, M.; Wang, H.; Huang, H.-S.; Fujita, T.; Wu, K. C. W.; Chen, L.-C.; Yamauchi, Y.; Ariga, K., *Chemical Communications* 2012, **48**, 7259-7261.
107. N. L. Torad; Salunkhe, R. R.; Li, Y.; Hamoudi, H.; Imura, M.; Sakka, Y.; Hu, C.-C.; Yamauchi, Y., *Chemistry – A European Journal* 2014, **20**, 7895-7900.
108. H. Yi; Wang, H.; Jing, Y.; Peng, T.; Wang, X., *Journal of Power Sources* 2015, **285**, 281-290.
109. M. Yao; Zhao, X.; Jin, L.; Zhao, F.; Zhang, J.; Dong, J.; Zhang, Q., *Chemical Engineering Journal* 2017, **322**, 582-589.
110. B. Liu; Shioyama, H.; Akita, T.; Xu, Q., *Journal of the American Chemical Society* 2008, **130**, 5390-5391.
111. S. Lim; Suh, K.; Kim, Y.; Yoon, M.; Park, H.; Dybtsev, D. N.; Kim, K., *Chemical Communications* 2012, **48**, 7447-7449.
112. A. J. Amali; Sun, J.-K.; Xu, Q., *Chemical Communications* 2014, **50**, 1519-1522.
113. D. Hulicova; Yamashita, J.; Soneda, Y.; Hatori, H.; Kodama, M., *Chemistry of Materials* 2005, **17**, 1241-1247.
114. J. Chmiola; Yushin, G.; Dash, R.; Gogotsi, Y., *Journal of Power Sources* 2006, **158**, 765-772.
115. S. Ma; Goenaga, G. A.; Call, A. V.; Liu, D.-J., *Chemistry – A European Journal* 2011, **17**, 2063-2067.
116. J. Tang; Salunkhe, R. R.; Liu, J.; Torad, N. L.; Imura, M.; Furukawa, S.; Yamauchi, Y., *Journal of the American Chemical Society* 2015, **137**, 1572-1580.

117. R. R. Salunkhe; Bastakoti, B. P.; Hsu, C.-T.; Suzuki, N.; Kim, J. H.; Dou, S. X.; Hu, C.-C.; Yamauchi, Y., *Chemistry – A European Journal* 2014, **20**, 3084-3088.
118. X.-h. Xia; Tu, J.-p.; Zhang, Y.-q.; Mai, Y.-j.; Wang, X.-l.; Gu, C.-d.; Zhao, X.-b., *RSC Advances* 2012, **2**, 1835-1841.
119. R. R. Salunkhe; Tang, J.; Kamachi, Y.; Nakato, T.; Kim, J. H.; Yamauchi, Y., *ACS Nano* 2015, **9**, 6288-6296.
120. W. Xia; Qu, C.; Liang, Z.; Zhao, B.; Dai, S.; Qiu, B.; Jiao, Y.; Zhang, Q.; Huang, X.; Guo, W.; Dang, D.; Zou, R.; Xia, D.; Xu, Q.; Liu, M., *Nano Letters* 2017, **17**, 2788-2795.
121. D. P. Dubal; Suarez-Guevara, J.; Tonti, D.; Enciso, E.; Gomez-Romero, P., *Journal of Materials Chemistry A* 2015, **3**, 23483-23492.
122. Z.-S. Wu; Winter, A.; Chen, L.; Sun, Y.; Turchanin, A.; Feng, X.; Müllen, K., *Advanced Materials* 2012, **24**, 5130-5135.
123. Y. Xu; Lin, Z.; Huang, X.; Liu, Y.; Huang, Y.; Duan, X., *ACS Nano* 2013, **7**, 4042-4049.
124. B. G. Choi; Chang, S.-J.; Kang, H.-W.; Park, C. P.; Kim, H. J.; Hong, W. H.; Lee, S.; Huh, Y. S., *Nanoscale* 2012, **4**, 4983-4988.
125. M. F. El-Kady; Strong, V.; Dubin, S.; Kaner, R. B., *Science* 2012, **335**, 1326-1330.
126. Y. Xie; Liu, Y.; Zhao, Y.; Tsang, Y. H.; Lau, S. P.; Huang, H.; Chai, Y., *Journal of Materials Chemistry A* 2014, **2**, 9142-9149.
127. X. Deng; Zhu, S.; Li, J.; Ma, L.; He, F.; Liu, E.; He, C.; Shi, C.; Li, Q.; Zhao, N., *Nanoscale* 2017, **9**, 6478-6485.
128. H. Hu; Guan, B.; Xia, B.; Lou, X. W., *Journal of the American Chemical Society* 2015, **137**, 5590-5595.
129. H. Hu; Guan, Bu Y.; Lou, Xiong W., *Chem* 2016, **1**, 102-113.
130. H. Du; Li, J.; Zhang, J.; Su, G.; Li, X.; Zhao, Y., *The Journal of Physical Chemistry C* 2011, **115**, 23261-23266.
131. M. Zhou; Zhai, Y.; Dong, S., *Analytical Chemistry* 2009, **81**, 5603-5613.
132. F. Bonaccorso; Sun, Z.; Hasan, T.; Ferrari, A. C., *Nature Photonics* 2010, **4**, 611.
133. T. H. Han; Huang, Y.-K.; Tan, A. T. L.; Dravid, V. P.; Huang, J., *Journal of the American Chemical Society* 2011, **133**, 15264-15267.

134. Z.-L. Wang; Xu, D.; Wang, H.-G.; Wu, Z.; Zhang, X.-B., *ACS Nano* 2013, **7**, 2422-2430.
135. Y. Hernandez; Nicolosi, V.; Lotya, M.; Blighe, F. M.; Sun, Z.; De, S.; McGovern, I. T.; Holland, B.; Byrne, M.; Gun'Ko, Y. K.; Boland, J. J.; Niraj, P.; Duesberg, G.; Krishnamurthy, S.; Goodhue, R.; Hutchison, J.; Scardaci, V.; Ferrari, A. C.; Coleman, J. N., *Nature Nanotechnology* 2008, **3**, 563.
136. D.-e. Jiang; Cooper, V.; Dai, S., *Nano letters* 2009, **9**, 4019-24.
137. H. C. Schniepp; Li, J.-L.; McAllister, M. J.; Sai, H.; Herrera-Alonso, M.; Adamson, D. H.; Prud'homme, R. K.; Car, R.; Saville, D. A.; Aksay, I. A., *The Journal of Physical Chemistry B* 2006, **110**, 8535-8539.
138. S. Niyogi; Bekyarova, E.; Itkis, M. E.; McWilliams, J. L.; Hamon, M. A.; Haddon, R. C., *Journal of the American Chemical Society* 2006, **128**, 7720-7721.
139. J. Ha; Park, S.; Kim, D.; Ryu, J.; Lee, C.; Hong, B. H.; Hong, Y., *Organic Electronics* 2013, **14**, 2324-2330.
140. X. Michalet; Pinaud, F. F.; Bentolila, L. A.; Tsay, J. M.; Doose, S.; Li, J. J.; Sundaresan, G.; Wu, A. M.; Gambhir, S. S.; Weiss, S., *Science* 2005, **307**, 538-544.
141. B. D. Zdravkov; Čermák, J. J.; Šefara, M.; Janků, J., *Central European Journal of Chemistry* 2007, **5**, 385-395.
142. C. Liang; Li, Z.; Dai, S., *Angewandte Chemie International Edition* 2008, **47**, 3696-3717.
143. T. Kyotani, *Control of pore structure in carbon. Carbon 38 (2): 269-286*. 2000, **38**, 269-286.
144. P. Russo; Hu, A.; Compagnini, G., *Nano-Micro Letters* 2013, **5**, 260-273.
145. K. S. Novoselov; Geim, A. K.; Morozov, S. V.; Jiang, D.; Katsnelson, M. I.; Grigorieva, I. V.; Dubonos, S. V.; Firsov, A. A., *Nature* 2005, **438**, 197-200.
146. H. Bi; Sun, S.; Huang, F.; Xie, X.; Jiang, M., *Journal of Materials Chemistry* 2012, **22**, 411-416.
147. W. Chen; Yan, L., *Nanoscale* 2011, **3**, 3132-3137.
148. X. Li; Huang, X.; Liu, D.; Wang, X.; Song, S.; Zhou, L.; Zhang, H., *The Journal of Physical Chemistry C* 2011, **115**, 21567-21573.
149. Y. Ma; Chen, Y., *National Science Review* 2014, **2**, 40-53.

150. Z. Chen; Ren, W.; Gao, L.; Liu, B.; Pei, S.; Cheng, H.-M., *Nature Materials* 2011, **10**, 424.
151. Y. Xu; Sheng, K.; Li, C.; Shi, G., *ACS Nano* 2010, **4**, 4324-4330.
152. W. Chen; Li, S.; Chen, C.; Yan, L., *Advanced materials (Deerfield Beach, Fla.)* 2011, **23**, 5679-5683.
153. H.-P. Cong; Ren, X.-C.; Wang, P.; Yu, S.-H., *ACS Nano* 2012, **6**, 2693-2703.
154. F. Liu; Seo, T. S., *Advanced Functional Materials* 2010, **20**, 1930-1936.
155. D. Wang; Kou, R.; Choi, D.; Yang, Z.; Nie, Z.; Li, J.; Saraf, L. V.; Hu, D.; Zhang, J.; Graff, G. L.; Liu, J.; Pope, M. A.; Aksay, I. A., *ACS Nano* 2010, **4**, 1587-1595.
156. X. Cao; Shi, Y.; Shi, W.; Lu, G.; Huang, X.; Yan, Q.; Zhang, Q.; Zhang, H., *Small* 2011, **7**, 3163-3168.
157. X. Li; Zhao, T.; Wang, K.; Yang, Y.; Wei, J.; Kang, F.; Wu, D.; Zhu, H., *Langmuir : the ACS journal of surfaces and colloids* 2011, **27**, 12164-12171.
158. C. Wang; Xu, J.; Yuen, M.-F.; Zhang, J.; Li, Y.; Chen, X.; Zhang, W., *Advanced Functional Materials* 2014, **24**, 6372-6380.
159. J.-C. Yoon; Lee, J.-S.; Kim, S.-I.; Kim, K.-H.; Jang, J.-H., *Scientific Reports* 2013, **3**, 1788.
160. Z. Tang; Shen, S.; Zhuang, J.; Wang, X., *Angewandte Chemie International Edition* 2010, **49**, 4603-4607.
161. Y. Zhu; Murali, S.; Stoller, M. D.; Ganesh, K. J.; Cai, W.; Ferreira, P. J.; Pirkle, A.; Wallace, R. M.; Cychosz, K. A.; Thommes, M.; Su, D.; Stach, E. A.; Ruoff, R. S., *Science* 2011, **332**, 1537-1541.
162. L. Zhang; Zhang, F.; Yang, X.; Long, G.; Wu, Y.; Zhang, T.; Leng, K.; Huang, Y.; Ma, Y.; Yu, A.; Chen, Y., *Scientific Reports* 2013, **3**, 1408.
163. W. Peng; Liu, S.; Sun, H.; Yao, Y.; Zhi, L.; Wang, S., *Journal of Materials Chemistry A* 2013, **1**, 5854-5859.
164. X. Zhao; Hayner, C. M.; Kung, M. C.; Kung, H. H., *ACS Nano* 2011, **5**, 8739-8749.
165. Q. Xi; Chen, X.; Evans, D. G.; Yang, W., *Langmuir* 2012, **28**, 9885-9892.
166. Z. Fan; Zhao, Q.; Li, T.; Yan, J.; Ren, Y.; Feng, J.; Wei, T., *Carbon* 2012, **50**, 1699-1703.

167. J. Li; Chung, T.-F.; Chen, Y. P.; Cheng, G. J., *Nano Letters* 2012, **12**, 4577-4583.
168. X. Xie; Zhou, Y.; Bi, H.; Yin, K.; Wan, S.; Sun, L., *Scientific Reports* 2013, **3**, 2117.
169. Y. Zhu; Li, L.; Zhang, C.; Casillas, G.; Sun, Z.; Yan, Z.; Ruan, G.; Peng, Z.; Raji, A.-R. O.; Kittrell, C.; Hauge, R. H.; Tour, J. M., *Nature Communications* 2012, **3**, 1225.
170. Y. Li; Li, Z.; Shen, P. K., *Advanced Materials* 2013, **25**, 2474-2480.
171. Y. Liu; Ma, Y.; Guang, S.; Ke, F.; Xu, H., *Carbon* 2015, **83**, 79-89.
172. M. Bieri; Treier, M.; Cai, J.; Aït-Mansour, K.; Ruffieux, P.; Gröning, O.; Gröning, P.; Kastler, M.; Rieger, R.; Feng, X.; Müllen, K.; Fasel, R., *Chemical Communications* 2009, 6919-6921.
173. Y. Li; Zhou, Z.; Shen, P.; Chen, Z., *Chemical Communications* 2010, **46**, 3672-3674.
174. M. Treier; Pignedoli, C. A.; Laino, T.; Rieger, R.; Müllen, K.; Passerone, D.; Fasel, R., *Nature Chemistry* 2010, **3**, 61.
175. M. D. Fischbein; Drndić, M., *Applied Physics Letters* 2008, **93**, 113107.
176. G. F. Schneider; Kowalczyk, S. W.; Calado, V. E.; Pandraud, G.; Zandbergen, H. W.; Vandersypen, L. M. K.; Dekker, C., *Nano Letters* 2010, **10**, 3163-3167.
177. A. Du; Zhu, Z.; Smith, S. C., *Journal of the American Chemical Society* 2010, **132**, 2876-2877.
178. M. Hatanaka, *Chemical Physics Letters* 2010, **488**, 187-192.
179. J. Zhou; Wang, Q.; Sun, Q.; Chen, X. S.; Kawazoe, Y.; Jena, P., *Nano Letters* 2009, **9**, 3867-3870.
180. A. Nourbakhsh; Cantoro, M.; Vosch, T.; Pourtois, G.; Clemente, F.; van der Veen, M. H.; Hofkens, J.; Heyns, M. M.; De Gendt, S.; Sels, B. F., *Nanotechnology* 2010, **21**, 435203.
181. S. Y. Zhou; Gweon, G. H.; Fedorov, A. V.; First, P. N.; de Heer, W. A.; Lee, D. H.; Guinea, F.; Castro Neto, A. H.; Lanzara, A., *Nature Materials* 2007, **6**, 770.
182. H. Chang; Cheng, J.; Liu, X.; Gao, J.; Li, M.; Li, J.; Tao, X.; Ding, F.; Zheng, Z., *Chemistry – A European Journal* 2011, **17**, 8896-8903.
183. R. Balog; Jørgensen, B.; Nilsson, L.; Andersen, M.; Rienks, E.; Bianchi, M.; Fanetti, M.; Lægsgaard, E.; Baraldi, A.; Lizzit, S.; Sljivancanin, Z.;

Besenbacher, F.; Hammer, B.; Pedersen, T. G.; Hofmann, P.; Hornekær, L., *Nature Materials* 2010, **9**, 315.

184. M. Vanević; Stojanović, V. M.; Kindermann, M., *Physical Review B* 2009, **80**, 045410.
185. M. De La Pierre; Karamanis, P.; Baima, J.; Orlando, R.; Pouchan, C.; Dovesi, R., *The Journal of Physical Chemistry C* 2013, **117**, 2222-2229.
186. F. Cervantes-Sodi; Csányi, G.; Piscanec, S.; Ferrari, A. C., *Physical Review B* 2008, **77**, 165427.
187. C. Lee; Wei, X.; Kysar, J. W.; Hone, J., *Science* 2008, **321**, 385-388.
188. A. A. Balandin; Ghosh, S.; Bao, W.; Calizo, I.; Teweldebrhan, D.; Miao, F.; Lau, C. N., *Nano Letters* 2008, **8**, 902-907.
189. C. Faugeras; Faugeras, B.; Orlita, M.; Potemski, M.; Nair, R. R.; Geim, A. K., *ACS Nano* 2010, **4**, 1889-1892.
190. G. Brunetto; Galvao, D. S., *MRS Proceedings* 2014, **1658**, mrsf13-1658-rr07-20.
191. Y. Matsuda; Tahir-Kheli, J.; Goddard, W. A., *The Journal of Physical Chemistry Letters* 2010, **1**, 2946-2950.
192. I. W. Frank; Tanenbaum, D. M.; Zande, A. M. v. d.; McEuen, P. L., *Journal of Vacuum Science & Technology B:* 2007, **25**, 2558-2561.
193. W. Cai; Moore, A. L.; Zhu, Y.; Li, X.; Chen, S.; Shi, L.; Ruoff, R. S., *Nano Letters* 2010, **10**, 1645-1651.
194. H. W. Ha; Choudhury, A.; Kamal, T.; Kim, D.-H.; Park, S.-Y., *ACS Applied Materials & Interfaces* 2012, **4**, 4623-4630.
195. M. Mecklenburg; Schuchardt, A.; Mishra, Y. K.; Kaps, S.; Adelung, R.; Lotnyk, A.; Kienle, L.; Schulte, K., *Advanced Materials* 2012, **24**, 3486-3490.
196. S. Murali; Potts, J. R.; Stoller, S.; Park, J.; Stoller, M. D.; Zhang, L. L.; Zhu, Y.; Ruoff, R. S., *Carbon* 2012, **50**, 3482-3485.
197. J. Schrier, *The Journal of Physical Chemistry Letters* 2010, **1**, 2284-2287.
198. J. Xiao; Mei, D.; Li, X.; Xu, W.; Wang, D.; Graff, G. L.; Bennett, W. D.; Nie, Z.; Saraf, L. V.; Aksay, I. A.; Liu, J.; Zhang, J.-G., *Nano Letters* 2011, **11**, 5071-5078.
199. V. Stengl; Bakardjieva, S.; Grygar, T. M.; Bludská, J.; Kormunda, M., *Chemistry Central journal* 2013, **7**, 41-41.

200. A. Hu; Peng, P.; Alarifi, H.; Zhang, X. Y.; Guo, J. Y.; Zhou, Y.; Duley, W. W., *Journal of Laser Applications* 2012, **24**, 042001.
201. P. Simon; Gogotsi, Y., *Nature Materials* 2008, **7**, 845.
202. E. Frackowiak; Béguin, F., *Carbon* 2001, **39**, 937-950.
203. M. Endo; Takeda, T.; Kim, Y.; Koshiba, K.; Ishii, K., *Carbon letters* 2001; **1**, 3-4
204. D. Qu; Shi, H., *Journal of Power Sources* 1998, **74**, 99-107.
205. Y.-C. Yong; Dong, X.-C.; Chan-Park, M. B.; Song, H.; Chen, P., *ACS Nano* 2012, **6**, 2394-2400.
206. D. Yu; Dai, L., *The Journal of Physical Chemistry Letters* 2010, **1**, 467-470.
207. K. H. An; Kim, W. S.; Park, Y. S.; Moon, J.-M.; Bae, D. J.; Lim, S. C.; Lee, Y. S.; Lee, Y. H., *Advanced Functional Materials* 2001, **11**, 387-392.
208. M. D. Stoller; Park, S.; Zhu, Y.; An, J.; Ruoff, R. S., *Nano Letters* 2008, **8**, 3498-3502.
209. Y. Zhu; Murali, S.; Stoller, M. D.; Velamakanni, A.; Piner, R. D.; Ruoff, R. S., *Carbon* 2010, **48**, 2118-2122.
210. L. L. Zhang; Zhao, X.; Stoller, M. D.; Zhu, Y.; Ji, H.; Murali, S.; Wu, Y.; Perales, S.; Clevenger, B.; Ruoff, R. S., *Nano Letters* 2012, **12**, 1806-1812.
211. Z. Li; Liu, Z.; Sun, H.; Gao, C., *Chemical Reviews* 2015, **115**, 7046-7117.
212. Z.-S. Wu; Yang, S.; Sun, Y.; Parvez, K.; Feng, X.; Müllen, K., *Journal of the American Chemical Society* 2012, **134**, 9082-9085.
213. M. J. Allen; Tung, V. C.; Kaner, R. B., *Chemical Reviews* 2010, **110**, 132-145.
214. J. K. Lee; Smith, K. B.; Hayner, C. M.; Kung, H. H., *Chemical Communications* 2010, **46**, 2025-2027.
215. J. D. Roy-Mayhew; Bozym, D. J.; Punckt, C.; Aksay, I. A., *ACS Nano* 2010, **4**, 6203-6211.
216. M.-Y. Yen; Hsiao, M.-C.; Liao, S.-H.; Liu, P.-I.; Tsai, H.-M.; Ma, C.-C. M.; Pu, N.-W.; Ger, M.-D., *Carbon* 2011, **49**, 3597-3606.
217. X. Li; Zhu, H.; Wang, K.; Cao, A.; Wei, J.; Li, C.; Jia, Y.; Li, Z.; Li, X.; Wu, D., *Advanced Materials* 2010, **22**, 2743-2748.
218. W. Yuan; Shi, G., *Journal of Materials Chemistry A* 2013, **1**, 10078-10091.

219. W. Yuan; Chen, J.; Shi, G., *Materials Today* 2014, **17**, 77-85.
220. P. N. Dyer; Richards, R. E.; Russek, S. L.; Taylor, D. M., *Solid State Ionics* 2000, **134**, 21-33.
221. J. Chen; Li, Y.; Huang, L.; Jia, N.; Li, C.; Shi, G., *Advanced Materials* 2015, **27**, 3654-3660.
222. C. T. Nguyen; Beskok, A., *Physical Chemistry Chemical Physics* 2019, **21**, 9483-9494.
223. D. Cohen-Tanugi; Grossman, J. C., *Nano Letters* 2012, **12**, 3602-3608.
224. T. A. N. Peiris. *Materials Science* 2014.
225. H. Abudayyeh. Synthesis and Analysis of ZnO Nanowires. 2012.
226. R. A. Halvorson; Vikesland, P. J., *Environ Sci Technol* 2010, **44**, 7749-7755.
227. S. Mahshid; Luo, S.; Yang, L.; Mahshid, S. S.; Askari, M.; Dolati, A.; Cai, Q., *Journal of nanoscience and nanotechnology* 2011, **11**, 6668-75.
228. M. Armand; Tarascon, J.-M., *Nature* 2008, **451**, 652-657.
229. B. Dunn; Kamath, H.; Tarascon, J.-M., *Science* 2011, **334**, 928-935.
230. D. He; Cheng, K.; Li, H.; Peng, T.; Xu, F.; Mu, S.; Pan, M., *Langmuir* 2012, **28**, 3979-3986.
231. N. Markovic; Schmidt, T.; Stamenkovic, V.; Ross, P., *FUEL CELLS-WEINHEIM-* 2001, **1**, 105-116.
232. H. A. Gasteiger; Kocha, S. S.; Sompalli, B.; Wagner, F. T., *Applied Catalysis B: Environmental* 2005, **56**, 9-35.
233. C. C. McCrory; Jung, S.; Peters, J. C.; Jaramillo, T. F., *Journal of the American Chemical Society* 2013, **135**, 16977-16987.
234. D. He; Xiong, Y.; Yang, J.; Chen, X.; Deng, Z.; Pan, M.; Li, Y.; Mu, S., *Journal of Materials Chemistry A* 2015.
235. S. Mao; Wen, Z.; Huang, T.; Hou, Y.; Chen, J., *Energy & Environmental Science* 2014, **7**, 609-616.
236. J. Zhang; Zhao, Z.; Xia, Z.; Dai, L., *Nature nanotechnology* 2015, **10**, 444-452.
237. S. Mao; Wen, Z.; Huang, T.; Hou, Y.; Chen, J., *Energy & Environmental Science* 2014, **7**, 609-616.
238. B. Chen; Li, R.; Ma, G.; Gou, X.; Zhu, Y.; Xia, Y., *Nanoscale* 2015, **7**, 20674-20684.

239. Y. Sun; Liu, C.; Grauer, D. C.; Yano, J.; Long, J. R.; Yang, P.; Chang, C. J., *Journal of the American Chemical Society* 2013, **135**, 17699-17702.
240. B. Chen; Ma, G.; Zhu, Y.; Wang, J.; Xiong, W.; Xia, Y., *Journal of Power Sources* 2016, **334**, 112-119.
241. Y. Yang; Fei, H.; Ruan, G.; Tour, J. M., *Advanced Materials* 2015, **27**, 3175-3180.
242. K. V. Babu; Kumar, G. V. S.; Satyanarayana, G.; Sailaja, B.; Sailaja Lakshmi, C. C., *Journal of Science: Advanced Materials and Devices* 2018, **3**, 236-242.
243. K. Vijaya Babu; Satyanarayana, G.; Sailaja, B.; Santosh Kumar, G. V.; Jalaiah, K.; Ravi, M., *Results in Physics* 2018, **9**, 55-62.
244. F. Bai; Xia, Y.; Chen, B.; Su, H.; Zhu, Y., *Carbon* 2014, **79**, 213-226.
245. Z. Wang; peng, s.; Hu, Y.; Li, L.; Yan, T.; Yang, G.; Dongxiao, J.; Srinivasan, M.; Pan, Z.; Ramakrishna, S., *Journal of Materials Chemistry A* 2017.
246. S. Gadipelli; Zhao, T.; Shevlin, S. A.; Guo, Z., *Energy & Environmental Science* 2016, **9**, 1661-1667.
247. T. H. Yoon; Johnson, S. B.; Musgrave, C. B.; Brown Jr, G. E., *Geochimica et Cosmochimica Acta* 2004, **68**, 4505-4518.
248. T.-M. Wu; Lin, Y.-W.; Liao, C.-S., *Carbon* 2005, **43**, 734-740.
249. L. Lai; Potts, J. R.; Zhan, D.; Wang, L.; Poh, C. K.; Tang, C.; Gong, H.; Shen, Z.; Lin, J.; Ruoff, R. S., *Energy & Environmental Science* 2012, **5**, 7936-7942.
250. J. Wang; Cui, W.; Liu, Q.; Xing, Z.; Asiri, A. M.; Sun, X., *Advanced Materials* 2016, **28**, 215-230.
251. S. Yang; Zhi, L.; Tang, K.; Feng, X.; Maier, J.; Müllen, K., *Advanced Functional Materials* 2012, **22**, 3634-3640.
252. S.-A. Wohlgemuth; White, R. J.; Willinger, M.-G.; Titirici, M.-M.; Antonietti, M., *Green Chemistry* 2012, **14**, 1515-1523.
253. Y. Dong; Pang, H.; Yang, H. B.; Guo, C.; Shao, J.; Chi, Y.; Li, C. M.; Yu, T., *Angewandte Chemie International Edition* 2013, **52**, 7800-7804.
254. J. F. Marco; Gancedo, J. R.; Gracia, M.; Gautier, J. L.; Rios, E. I.; Palmer, H. M.; Greaves, C.; Berry, F. J., *Journal of Materials Chemistry* 2001, **11**, 3087-3093.

255. T. A. J. Loh; Chua, D. H. C.; Wee, A. T. S., *Scientific Reports* 2015, **5**, 18116.
256. J. Huang; Wang, X.; Li, J.; Cao, L.; Xu, Z.; Wei, H., *J. Alloys Compd.* 2016, 60-66.
257. Y. Hou; Wen, Z.; Cui, S.; Ci, S.; Mao, S.; Chen, J., *Advanced Functional Materials* 2015, **25**, 872-882.
258. J. R. Pels; Kapteijn, F.; Moulijn, J. A.; Zhu, Q.; Thomas, K. M., *Carbon* 1995, **33**, 1641-1653.
259. H. Wang; Liang, Y.; Gong, M.; Li, Y.; Chang, W.; Mefford, T.; Zhou, J.; Wang, J.; Regier, T.; Wei, F.; Dai, H., *Nature Communications* 2012, **3**, 917.
260. D. J. Li; Maiti, U. N.; Lim, J.; Choi, D. S.; Lee, W. J.; Oh, Y.; Lee, G. Y.; Kim, S. O., *Nano Letters* 2014, **14**, 1228-1233.
261. S.-J. Bao; Li, Y.; Li, C. M.; Bao, Q.; Lu, Q.; Guo, J., *Crystal Growth & Design* 2008, **8**, 3745-3749.
262. W. Zhou; Wu, X.-J.; Cao, X.; Huang, X.; Tan, C.; Tian, J.; Liu, H.; Wang, J.; Zhang, H., *Energy & Environmental Science* 2013, **6**, 2921-2924.
263. X.-J. Lv; She, G.-W.; Zhou, S.-X.; Li, Y.-M., *RSC Advances* 2013, **3**, 21231-21236.
264. Q. Liu; Zhang, J., *CrystEngComm* 2013, **15**, 5087-5092.
265. Q. Liu; Jin, J.; Zhang, J., *ACS Applied Materials & Interfaces* 2013, **5**, 5002-5008.
266. T. A. J. Loh; Chua, D. H. C.; Wee, A. T. S., *Sci. Rep.* 2015, **5**, 18116.
267. Z. Yang; Yao, Z.; Li, G.; Fang, G.; Nie, H.; Liu, Z.; Zhou, X.; Chen, X. a.; Huang, S., *ACS Nano* 2012, **6**, 205-211.
268. J. Wang; Ma, R.; Zhou, Z.; Liu, G.; Liu, Q., *Sci. Rep.* 2015, **5**, 9304.
269. G. Li; Sun, J.; Hou, W.; Jiang, S.; Huang, Y.; Geng, J., *Nature Commun.* 2016, **7**, 10601.
270. A. C. Ferrari, *Solid State Communications* 2007, **143**, 47-57.
271. S. Chu; Majumdar, A., *Nature* 2012, **488**, 294.
272. S. Cobo; Heidkamp, J.; Jacques, P.-A.; Fize, J.; Fourmond, V.; Guetaz, L.; Jousselme, B.; Ivanova, V.; Dau, H.; Palacin, S.; Fontecave, M.; Artero, V., *Nature Materials* 2012, **11**, 802.
273. F. Song; Hu, X., *Nature Communications* 2014, **5**, 4477.

274. J. Tian; Liu, Q.; Cheng, N.; Asiri, A. M.; Sun, X., *Angewandte Chemie International Edition* 2014, **53**, 9577-9581.
275. T. Liu; Liu, Q.; Asiri, A. M.; Luo, Y.; Sun, X., *Chemical Communications* 2015, **51**, 16683-16686.
276. L. Trotochaud; Young, S. L.; Ranney, J. K.; Boettcher, S. W., *Journal of the American Chemical Society* 2014, **136**, 6744-6753.
277. C. G. Morales-Guio; Mayer, M. T.; Yella, A.; Tilley, S. D.; Grätzel, M.; Hu, X., *Journal of the American Chemical Society* 2015, **137**, 9927-9936.
278. C. C. L. McCrory; Jung, S.; Peters, J. C.; Jaramillo, T. F., *Journal of the American Chemical Society* 2013, **135**, 16977-16987.
279. R. Gao; Li, Z.; Zhang, X.; Zhang, J.; Hu, Z.; Liu, X., *ACS Catalysis* 2016, **6**, 400-406.
280. B. C. M. Martindale; Reisner, E., *Advanced Energy Materials* 2016, **6**, 1502095.
281. S. Yang; Zhi, L.; Tang, K.; Feng, X.; Maier, J.; Müllen, K., *Advanced Functional Materials* 2012, **22**, 3634-3640.
282. Y. Dong; Pang, H.; Yang, H. B.; Guo, C.; Shao, J.; Chi, Y.; Li, C. M.; Yu, T., *Angewandte Chemie International Edition* 2013, **52**, 7800-7804.
283. M. D. Meganathan; Mao, S.; Huang, T.; Sun, G., *Journal of Materials Chemistry A* 2017, **5**, 2972-2980.
284. M. Fan; Zhu, C.; Feng, Z.-Q.; Yang, J.; Liu, L.; Sun, D., *Nanoscale* 2014, **6**, 4882-4888.
285. K. M. Ismail; Badawy, W. A., *Journal of Applied Electrochemistry* 2000, **30**, 1303-1311.
286. H. Huang; Feng, X.; Du, C.; Wu, S.; Song, W., *Journal of Materials Chemistry A* 2015, **3**, 4976-4982.
287. Y. Hou; Wen, Z.; Cui, S.; Ci, S.; Mao, S.; Chen, J., *Advanced Functional Materials* 2015, **25**, 872-882.
288. R. Liu; Zhao, Y.; Huang, R.; Zhao, Y.; Zhou, H., *CrystEngComm* 2010, **12**, 4091-4094.
289. Y. Yu; Jung, H. J.; Je, M.; Choi, H.; Yong Choi, M., *Chemosphere* 2016; **155**, 250-256.
290. M. J. Matthews; Pimenta, M. A.; Dresselhaus, G.; Dresselhaus, M. S.; Endo, M., *Physical Review B* 1999, **59**, R6585-R6588.

291. K. Simeonidis; Martínez-Boubeta, C.; Iglesias, O.; Cabot, A.; Angelakeris, M.; Mourdikoudis, S.; Tsiaoussis, I.; Delimitis, A.; Dendrinou-Samara, C.; Kalogirou, O., *Phys. Rev.* 2011, **84**, 144430
292. F. M. Sapountzi; Gracia, J. M.; Weststrate, C. J.; Fredriksson, H. O. A.; Niemantsverdriet, J. W., *Progress in Energy and Combustion Science* 2017, **58**, 1-35.
293. S. P. S. Badwal; Giddey, S. S.; Munnings, C.; Bhatt, A. I.; Hollenkamp, A. F., *Frontiers in chemistry* 2014, **2**, 79-79.
294. M. Chauhan; Reddy, K. P.; Gopinath, C. S.; Deka, S., *ACS Catalysis* 2017, **7**, 5871-5879.
295. Y. Liu; Li, Q.; Si, R.; Li, G.-D.; Li, W.; Liu, D.-P.; Wang, D.; Sun, L.; Zhang, Y.; Zou, X., *Advanced Materials* 2017, **29**, 1606200.
296. I. S. Amiinu; Pu, Z.; Liu, X.; Owusu, K. A.; Monestel, H. G. R.; Boakye, F. O.; Zhang, H.; Mu, S., *Advanced Functional Materials* 2017, **27**, 1702300.
297. S. Peng; Li, L.; Zhang, J.; Tan, T. L.; Zhang, T.; Ji, D.; Han, X.; Cheng, F.; Ramakrishna, S., *Journal of Materials Chemistry A* 2017, **5**, 23361-23368.
298. L. Ju; Dai, Y.; Wei, W.; Li, M.; Huang, B., *Applied Surface Science* 2018, **434**, 365-374.
299. P. Luo; Zhang, H.; Liu, L.; Zhang, Y.; Deng, J.; Xu, C.; Hu, N.; Wang, Y., *ACS Applied Materials & Interfaces* 2017, **9**, 2500-2508.
300. N. Jiang; Tang, Q.; Sheng, M.; You, B.; Jiang, D.-e.; Sun, Y., *Catalysis Science & Technology* 2016, **6**, 1077-1084.
301. F. Kong; Fan, X.; Kong, A.; Zhou, Z.; Zhang, X.; Shan, Y., *Advanced Functional Materials* 2018, **28**, 1803973.
302. L.-M. Cao; Hu, Y.-W.; Tang, S.-F.; Iljin, A.; Wang, J.-W.; Zhang, Z.-M.; Lu, T.-B., *Advanced science (Weinheim, Baden-Wurttemberg, Germany)* 2018, **5**, 1800949-1800949.
303. L. Chen; Shi, J., *Journal of Materials Chemistry A* 2018, **6**, 13538-13548.
304. P. Zhang; Guan, B. Y.; Yu, L.; Lou, X. W., *Angewandte Chemie International Edition* 2017, **56**, 7141-7145.
305. Z. Peng; Jia, D.; Al-Enizi, A. M.; Elzatahry, A. A.; Zheng, G., *Advanced Energy Materials* 2015, **5**, 1402031.
306. Z. Yang; Chen, C.-Y.; Liu, C.-W.; Li, C.-L.; Chang, H.-T., *Advanced Energy Materials* 2011, **1**, 259-264.

307. Y. J. Yun; Ah, C. S.; Hong, W. G.; Kim, H. J.; Shin, J.-H.; Jun, Y., *Nanoscale* 2017, **9**, 11439-11445.
308. J. Joshi; Kanchan, D.; Joshi, M.; Jethva, H. O.; Parikh, K., *Materials Research Bulletin* 2017, **93**, 63-73.
309. Z. Hu; Zhang, K.; Zhu, Z.; Tao, Z.; Chen, J., *J. Mater. Chem. A* 2015, **3**, 12898-12904.
310. J. F. Marco; Gancedo, J. R.; Gracia, M.; Gautier, J. L.; Ríos, E. I.; Palmer, H. M.; Greaves, C.; Berry, F. J., *Journal of Materials Chemistry* 2001, **11**, 3087-3093.
311. T. Yamashita; Hayes, P., *Applied Surface Science* 2008, **254**, 2441-2449.
312. A. P. Grosvenor; Kobe, B. A.; Biesinger, M. C.; McIntyre, N. S., *Surface and Interface Analysis* 2004, **36**, 1564-1574.
313. G. Li; Sun, J.; Hou, W.; Jiang, S.; Huang, Y.; Geng, J., *Nature Communications* 2016, **7**, 10601.
314. J. Wang; Ma, R.; Zhou, Z.; Liu, G.; Liu, Q., *Scientific Reports* 2015, **5**, 9304.